QUANTITATIVE PROTON RELAXOMETRY IN THE ROTATING FRAME WITH MAGNETIC RESONANCE IMAGING

By

Jared Guthrie Cobb

Dissertation

Submitted to the Faculty of the

Graduate School of Vanderbilt University

in partial fulfillment of the requirements

for the degree of

DOCTOR OF PHILOSOPHY

in

Biomedical Engineering

December, 2011

Nashville, Tennessee

Approved:

Professor John C. Gore

Professor J. Christopher Gatenby

Professor Daniel F. Gochberg

Professor Mark M. Does

Professor Bruce M. Damon

ACKNOWLEDGEMENTS

I would like to express my gratitude to Prof. John Gore for his thoughtfulness and support in guiding me through the process of crafting my dissertation. In addition, I would like to thank my committee members, Profs. Dan Gochberg, Bruce Damon, Mark Does, and Chris Gatenby, each of whom contributed to my progress sometimes with small nudges and sometimes with swift kicks. I would also like to express my appreciation to my previous advisors, Profs. Cynthia Paschal and Paul King who helped me with my early graduate studies.

I would also like to acknowledge my colleagues, Mary Loveless, Adam Hortch, Jingping Xie, and Ke Li, who each helped to enlighten my scientific knowledge in their own way.

Finally, I would like to thank my parents, grandparents, brother, and of course my dear Cheryl and Graham, on whom I relied for quiet and unconditional support.

LIST OF FIGURES

Figure 1: A typical $T_{1\rho}$ experiment. Magnetization precession and decay under spin-locking conditions. The M_0 vector is first nutated into the transverse plane by a 90-degree pulse. A long, low power SL pulse is applied, locking magnetization to the B_1 field. The M vector decays with the rate $R_{1\rho}$. Finally, a 90-degree pulse returns the magnetization vector to the Z-axis, where the $T_{1\rho}$ prepped signal may be read by any imaging sequence. 7

Figure 2: Schematic depiction of chemical exchange between two proton pools. The two environments communicate via chemical exchange at appropriate sites with the rates k_{ba} and k_{ab}. 15

Figure 3: Schematic depiction of diffusive exchange. Water protons diffuse freely through water surrounding susceptibility agents. These agents induce a magnetic field that causes spins to dephase as they traverse the local environment. 20

Figure 4: A. Simulated proton spectrum demonstrating the CEST technique with off-resonance RF saturation. B. Simulated CEST z-spectrum showing the location of a metabolite peak separated from water by some frequency offset ($\delta\omega$). This demonstrates a great advantage of CEST, namely that the metabolite peak need not be clearly discernable in a proton spectrum (4.a.) to be used to generate contrast... 23

Figure 5: a. Acrylamide monomer (AC), b. N,N'=methylene-bis-acrylamide monomer (BIS). c. A typical structural element in cross-linked polyacrylamide gel (PAG). .. 26

Figure 6: Base molecular structures for A. Poly-L-Lysine (PLK), B. Poly-L-Arginine (PLR), and C. Poly-L-Threonine (PLT). Note the differences in available

exchangeable NH groups (Blue) and OH groups (Red). The images reference the corresponding National Center for Biological Information (PubChem) CID numbers. 28

Figure 7: Sugars in order of increasing complexity. Note that the polysaccharides are cross-linked at OH sites, removing a potential exchanging site. The images reference the corresponding National Center for Biological Information (PubChem) CID numbers. 29

Figure 8: A. Chemical structure of Iohexol. B. Chemical structure of Iopamidol. Note the differences in available NH and OH exchange sites. 31

Figure 9: Adult articular cartilage layers. Note the distinctive orientation of the Radial Layer as opposed to the less organized Superficial and Middle zones. 33

Figure 10: PDW-TSE image of epiphyseal cartilage layers in a 10YO M at 3T. Arrow A points to the clear demarcation of the growth plate. Note that the articular surface (Arrow B) is difficult to distinguish from the large epiphyseal cartilage zones (light regions). 36

Figure 11: Three and four pulse SL clusters to reduce the effects of B_1 and B_0 inhomogeneity. 11.a. demonstrates a SL pulse with phase reversal half way through, thus rewinding accrued phase in the presence of inhomogeneous B_1. 11.b. includes a 180-degree refocusing pulse to reduce the effects of B_0 inhomogeneity. 11.c. This pulse is similar to 11.b but may be applied at any excitation angle α. 41

TABLE OF CONTENTS

Page

ACKNOWLEDGEMENTS ii

LIST OF FIGURES iii

Chapter

I. FACTORS CONTRIBUTING TO ROTATING FRAME RELAXATION IN COMPLEX TISSUE 1

OBJECTIVE 1
SPECIFIC AIMS 2
BACKGROUND AND LITERATURE REVIEW 4
RELAXATION THEORY 9
$R_{1\rho}$ relaxation in a one-pool model 10
$R_{1\rho}$ relaxation in a two-pool model 11
Factors Influencing Spin Lock Contrast 12
Factors Influencing CEST Contrast 22
MODEL BIOMOLECULES AND TISSUES 24
Polyacrylamide Gels 25
Peptides, Sugars and Proteins 27
Iohexol as an Exchange-Rate Based Contrast Agent 30
Models to explore Diffusion and Susceptibility 31
Cartilage Constituents 32
EXPERIMENTAL METHODS 37
Pulse Sequences to measure T1ρ 37
Pulse Sequence to Measure CEST Contrast 42
Imaging Technique Limitations and Caveats 43
DATA ANALYSIS METHODS 44
Analysis of T1ρ Measurements 44
Analysis of CEST Data 46
SUMMARY 46
REFERENCES 48

II. $T_{1\rho}$ MAPPING OF PEDIATRIC EPIPHYSEAL AND ARTICULAR CARTILAGE IN THE KNEE 63

ABSTRACT 63
INTRODUCTION 65
MATERIALS AND METHODS 68
RESULTS 72
DISCUSSION AND CONCLUSIONS 76

REFERENCES 81

III. CONTRIBUTIONS OF CHEMICAL EXCHANGE
TO $T_{1\rho}$ DISPERSION IN A TISSUE MODEL 87

ABSTRACT 87
INTRODUCTION 88
THEORY 91
$R_{1\rho}$ relaxation in a one-pool model 91
$R_{1\rho}$ relaxation in a two-pool model 92
METHODS 96
Rotating-Frame Relaxation Simulations 96
Experimental Studies 97
Gel Phantom Preparation 98
MRI Measurements 99
RESULTS 101
Simulation Results 101
Fitting to Chopra Model 105
DISCUSSION AND CONLCUSIONS 109
Exchange Dependence on Polymer Side Chains 110
pH Dependence 112
Fitting Methods Compared 115
Conclusions 116
REFERENCES 118

IV. EXCHANGE-MEDIATED CONTRAST AGENTS
FOR SPIN-LOCK IMAGING 122

ABSTRACT 122
INTRODUCTION 123
METHODS 126
NMR Experiments 126
Imaging Experiments 127
Theory and Data Analysis 127
RESULTS 130
DISCUSSION AND CONCLUSION 137
REFERENCES 144

V. EXCHANGE-MEDIATED CONTRAST MECHANISMS
FOR CEST AND SPIN-LOCK IMAGING.
PART I: THEORY AND SIMULATIONS 149

ABSTRACT 149
THEORY 159
CEST and Spin-Locking Simulations 161

METHODS 163
Computer Simulations 163
RESULTS 164
DISCUSSION 175
CONCLUSIONS 182
REFERENCES 184

VI. EXCHANGE-MEDIATED CONTRAST MECHANISMS FOR CEST AND SPIN-LOCK IMAGING. PART II: EXPERIMENTAL STUDIES ON MODEL SYSTEMS 189

ABSTRACT 189
INTRODUCTION 190
METHODS 195
Experimental Studies 195
Data Analysis 198
RESULTS 201
CEST and SL Results for Polypeptides 201
CEST and SL Results for Sugars 204
Imaging Results 215
DISCUSSION 220
CONCLUSIONS 232
REFERENCES 233

VII. CONTRIBUTIONS OF CHEMICAL AND DIFFUSIVE EXCHANGE TO $T_{1\rho}$ DISPERSION 238

ABSTRACT 238
INTRODUCTION 239
THEORY 244
METHODS 246
Simulations of Diffusive and Chemical Exchange Effects on $R_{1\rho}$ 246
Materials 248
NMR Experiments 249
Data Analysis 249
RESULTS 251
Simulation Results 251
Experimental Results 258
DISCUSSION AND CONCLUSIONS 263
APPENDIX 272
REFERENCES 275

VIII. CONCLUSIONS 279

SUMMARY OF MANUSCRIPTS 279
APPLICATIONS OF ROTATING FRAME RELAXATION MEASUREMENTS IN BIOLOGY AND MEDICINE 285
FUTURE STUDIES 287
PROTECTION OF RESEARCH SUBJECTS 289
SOCIETAL IMPLICATIONS 290
APPENDICES 293
Appendix 1: Role of the Student in the Manuscript 293
Appendix 2: Relaxation Simulations 294
Appendix 3: Experimental Materials and Ancillary Data 297
Appendix 4: MATLAB Code 300
Bloch Simulation Code: 300
Noise Generation 305
Model Fitting 307
Spectroscopic Dispersion Analysis 309
Imaging Dispersion Analysis 311
Philips T1ρ Mapping 314
Gochberg Subtraction Method 316

CHAPTER I

FACTORS CONTRIBUTING TO ROTATING FRAME RELAXATION IN COMPLEX TISSUE

OBJECTIVE

This thesis describes a series of studies that attempt to move beyond qualitative measurements with magnetic resonance imaging (MRI) towards a more quantitative understanding of the mechanisms by which protons relax in heterogeneous tissues. The aims seek to explain how molecular and cellular properties of tissue constituents influence specific proton relaxation processes and how they may be employed to generate useful and novel contrast in images. The experiments described will emphasize measurements of spin-lattice relaxation in the rotating frame, known as $T_{1\rho}$ relaxation, with spin locking techniques and their interpretation. These methods have been used previously to examine low frequency molecular interactions in cartilage (1-4), breast tissue (5), brain (6-12), muscle (13), and also in mouse tumor models (14-17). At high field $T_{1\rho}$ relaxation may provide new opportunities for studies of proton exchange at biologically relevant exchange rates. By furthering knowledge about the factors that affect rotating frame relaxation, new methods may be developed that are sensitive to growth, maturation, or disease processes in tissue.

SPECIFIC AIMS

The studies described were developed to address three Specific Aims:

Aim I. To develop quantitative techniques for measuring $T_{1\rho}$ relaxation and to implement these on clinical and pre-clinical imaging systems. Quantitative $T_{1\rho}$ measurements will be made in model tissue systems such as polymer gels and cartilage constituents. This aim will determine the feasibility of acquiring quantitative data *in vivo*, will provide reference relaxation and quantitative model parameter values for various tissues, and may provide unique empirical information regarding the mechanisms affecting $T_{1\rho}$ contrast.

Aim II. To quantify the contributions of different relaxation mechanisms, such as chemical exchange, novel experiments to better understand the complex behavior of $T_{1\rho}$ contrast in heterogeneous tissues will be employed in model systems. Tissue phantoms of various concentrations of macromolecules (bovine serum albumin, polypeptides, cartilage components, and polysaccharides) will be studied for changes in measured $T_{1\rho}$ vs. spin-lock strength, resulting in a phenomenon known as $T_{1\rho}$ dispersion (1). By fitting these data to an appropriate model, measurements of the relative contribution of chemical exchange may be estimated (16,18,19). These studies will demonstrate the effects of macromolecular content, chemical exchange parameters, field strength, and other factors on $T_{1\rho}$ contrast in model tissue systems. Moreover, these studies will also demonstrate how novel parametric images emphasizing protons with specific exchange rates may be selectively imaged. The results will also be compared to chemical exchange saturation transfer (CEST) imaging with which $T_{1\rho}$ imaging shares some complementary features.

Aim III. An additional potential relaxation mechanism of interest is the effect of water diffusion in the presence of dephasing gradients arising from local susceptibility differences ($\Delta\chi$) that may mimic chemical exchange effects. Quantitative $T_{1\rho}$ measurements will be investigated in a model susceptibility agent system of dextran microspheres (Sephadex®) to determine if diffusion through these gradients contributes to rotating frame relaxation or dispersion. The sensitivity of $T_{1\rho}$ imaging to susceptibility agents of different sizes and in different chemical environments will be evaluated. Susceptibility effects caused by agents such as calcium or iron deposits in the brain have been associated with several disease processes, e.g. multiple sclerosis (MS), Parkinson's disease (PD), or Alzheimer's disease (AD) (20-22). Data from the model Sephadex system will be of help in understanding the possible role of susceptibility effects in diseased tissues *in vivo* on spin lock measurements.

BACKGROUND AND LITERATURE REVIEW

As one of the few clinical imaging modalities not to use ionizing radiation, Magnetic Resonance Imaging (MRI) is as a compelling resource for biomedical research. Its relative safety coupled with a rich variety of available research techniques makes it an ideal platform for performing studies on human tissues. The elucidation of the physics governing MRI date back to the work of Bloch and Purcel who first coupled quantum mechanics theory to nuclear spin physics in the late 1940s, giving rise to the field of nuclear magnetic resonance (NMR) (23). Since then, foundational techniques have been developed to generate novel information about the structure and function of biologic tissue, revolutionizing the fields of chemistry, physics, and biology. The novel application of a spatially varying magnetic field over a sample in the 1970s by Lauterbur and others created the ability to gather spatial information by separating the frequency components of the resulting signal (24). This development led to the realization that as a non-invasive imaging modality, MRI could be safely applied to humans, providing diagnostically useful tomographic information. Many of the subsequent research efforts in this field have focused on developing meaningful contrast mechanisms for use in image formation.

The most widely used mechanisms for generating contrast in MRI are based on the spin-lattice and spin-spin relaxation processes of nuclei within a sample. The spin-lattice relaxation rate, or $1/T_1 = R_1$, is associated with the time required for nuclei to return to ~63% of their initial magnetization state after excitation with a radio frequency (RF) pulse while in a static magnetic field. The spin-lattice relaxation rate is determined by the

process of excited spins transferring energy to their neighbors or, as originally measured in solids, the surrounding crystal lattice. If two tissues have sufficiently different T_1 values, this difference may be exploited to generate useful contrast. For example, the T_1s of gray and white matter in brain at 1.5 T are ~950 ms and ~600 ms respectively (25). With appropriate imaging parameters, this time difference may be used to generate an image where gray and white matter may be clearly differentiated. The spin-spin relaxation rate or $1/T_2 = R_2$, is associated with the time required for nuclei to decay to ~37% of their initial transverse magnetization state after RF excitation. The spin-spin relaxation rate is determined by the rate at which different spins within an excited sample lose phase coherence. This dephasing process is predominantly determined by local variations in precession frequency among the spins. T_1 and T_2 times are very similar for liquid samples; however, in tissues, T_2 times are reduced to be about an order of magnitude less than T_1 times. For example, the T_2s of gray and white matter at 1.5 T are about 100 and 80 ms respectively. The time constants T_1 and T_2, along with the density of spins within a sample, are the primary determinants of imaging contrast.

Changes in these relaxation times may be reflected in image contrast where the scan parameters have been manipulated to emphasize T_1 or T_2 differences in a tissue in a process known as contrast weighting. Thus a T_2-weighted image was produced to emphasize tissues with large T_2 differences. However, these differences are rarely evaluated quantitatively in a clinical setting for diagnostic use. Quantitative imaging has proven useful for elucidating the underlying biophysical or chemical mechanisms for T_1 and T_2 changes in model tissue systems. For example, Keonig et al. elucidated a possible

mechanism for changes observed in T_1 relaxation in protein solutions with varying main fields (26). Changes in T_2 have been attributed to changes in protein structure, conformation, and interactions with water in tissues as described by Hills et al. (27). By seeking a more complete and quantitative description of these tissues models, hypotheses may be developed to probe for signal alterations as a function of physiological state, disease state, damage, or other perturbation.

In addition to T_1 and T_2, which are laboratory frame relaxation times, contrast may also be generated in the rotating frame. The first experiments measuring rotating frame relaxation are attributed to Torrey, Redfield, and Lee and Goldburg (28-30), and were developed to probe low-frequency interactions between bound and free water in metal ion solutions at low field (B_0). Recently, these techniques have been adapted to exploit the interactions of protons in macromolecules and bulk water in biologic systems at high field, where the increased frequency separation between chemical species begins to dominate rotating frame relaxation. Quantitative measurements of rotating frame relaxation can, in principle, yield insights into the time scale of molecular motions, the sizes of different proton pools, rates of chemical and diffusive exchange processes, protein sizes and concentrations, and other attributes which will be discussed in depth later (2,31-33). This thesis contains experiments linked by the overarching goal of obtaining a better understanding of the underlying mechanisms of proton relaxation in the rotating frame in tissues and tissue models.

The MRI methods used to probe rotating frame relaxation are generally referred to as spin locking techniques. Spin locking is achieved by the application of an RF pulse that is designed to "lock" magnetization to an applied B_1 field. Using conventional nomenclature (Figure 1), typically, magnetization is first nutated away from B_0 by some angle θ by the application of an RF pulse (B_1 field) about the x-axis. A long, low-power spin-locking pulse is then applied on resonance along the y-axis and magnetization begins to precess in the rotating frame about the B_1 field. This pulse "locks" a certain bandwidth of spins to this B_1 field, thus preventing spins from dephasing, originating the term spin-locking (SL). Magnetization that relaxes during spin locking is referred to as occurring in the ρ-domain. Analogous to R_1 and R_2 ($1/T_1$ and $1/T_2$) relaxation in the laboratory frame, relaxation in the rotating frame is referred to by the longitudinal and transverse rates $R_{1\rho}$ or $R_{2\rho}$.

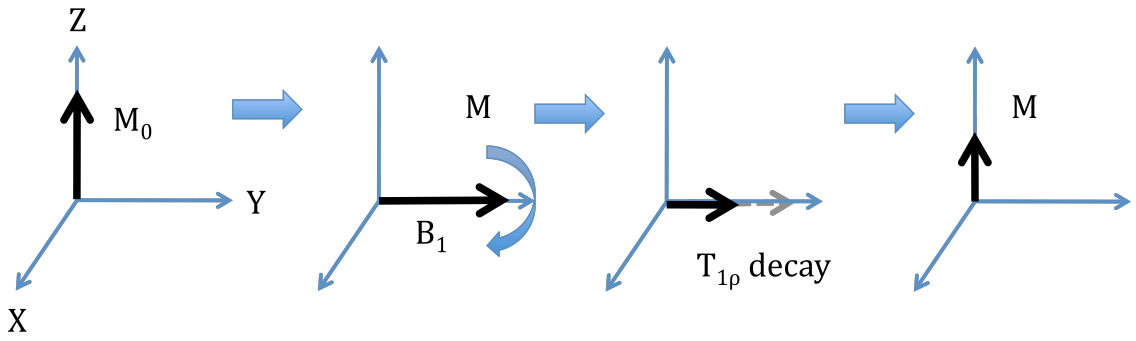

Figure 1: A typical $T_{1\rho}$ experiment. Magnetization precession and decay under spin-locking conditions. The M_0 vector is first nutated into the transverse plane by a 90-degree pulse. A long, low power SL pulse is applied, locking magnetization to the B_1 field. The M vector decays with the rate $R_{1\rho}$. Finally, a 90-degree pulse returns the magnetization vector to the Z-axis, where the $T_{1\rho}$ prepped signal may be read by any imaging sequence.

The physical principles that govern R_1 and R_2 relaxation also govern ρ-domain relaxation and will be discussed in depth later. Measurements of monoexponential spin-lattice relaxation in protein solutions and tissues are well documented, but values of $R_{1\rho}$ depend on the applied B_1 field. Thus, if the locking field is varied, the measured $R_{1\rho}$ rates will change, resulting in $R_{1\rho}$ dispersion as a function of the applied B_1 field. The shape of the dispersion curve depends on several factors including molecular motions, dipolar interactions, diffusion, and proton exchange processes that modulate the local magnetic fields experienced by protons on the time scale of the precession in the rotating frame (2,31).

$T_{1\rho}$ dispersion has been previously measured in an attempt to detect slow exchange dynamics or low frequency molecular motions at low field (B_0). At low field, rotating frame relaxation is dominated by dipolar effects resulting from low-frequency interactions between adjacent molecules (1). However, at high fields the increased separation of resonance frequencies between water and other chemical species such as amides gives rise to greater contributions to rotating frame relaxation dispersion from chemical exchange. These chemical exchange processes are of interest not only for their effects on $R_{1\rho}$ but also on R_2 and as modulators of saturation transfer contrast (CEST) (34,35). There have been few studies undertaken that attempt to quantify these processes or to derive parameters which describe them in biological samples. For example, the relative influences of macromolecular composition on chemical exchange, cross relaxation, and diffusion effects on $T_{1\rho}$ dispersion have not been reported. Cross-relaxation in the rotating frame may allow for exchanging protons to be affected by non-

exchanging protons in macromolecules via through space dipolar coupling, where dispersion could reflect motions on the time scale of the Rabi frequency (γB_1). Such effects are reduced when the line width of the macromolecular protons is much greater than the locking frequency, as is typically the case in tissues, and they may be eliminated by locking at the magic angle (31). A greater understanding of these features in tissue models may inform the development of methods to generate and interpret novel quantitative image contrast. The aims will explore these relaxation effects in the rotating frame of reference in several tissue models and biologically relevant macromolecules. This knowledge may further enlighten the use of imaging methods to diagnose, and monitor the progress of disease in abnormal tissues.

RELAXATION THEORY

Consideration of the molecular origins of proton relaxation has been an active area of research for over 50 years. The quantification of different molecular, chemical, and physical processes still constitutes an area of active study, as there is no consensus on their relative contributions to proton relaxation in heterogeneous tissues. However, general formalisms have been developed and successfully utilized to report quantitative data regarding individual contributions to proton relaxation under specific conditions. When describing these processes, it is customary to begin with equations governing relaxation in a single pool of protons and then add complexity until the model adequately reflects the experimental data (36).

$R_{1\rho}$ relaxation in a one-pool model

In a simple one-pool model as described by Hills and others (32,37), the rotating frame relaxation rate is governed by the randomly fluctuating local magnetic fields of dipolar interactions among protons (38). If the time scale of fluctuations is given by correlation time τ_c, $R_{1\rho}$ (= $1/T_{1\rho}$) can be described by:

$$R_{1\rho,dip} = 0.2A\left[3J(\omega_1,\tau_c) + 5J(\omega_0,\tau_c) + 2J(4\omega_0,\tau_c)\right] \qquad [1]$$

where ω_0 is the Larmor frequency, $\omega_1 = \gamma B_1$ is the applied RF field frequency, J describes the spectral density function, $J(n\omega, \tau_c) = \tau_c / (1+n\omega^2\tau_c^2)$, and

$$A = (\mu_0 / 4\pi)^2 * (h / 2\pi)^2 * \gamma 4I(I+1) / r^6$$

where μ_0 is the permeability of space, γ the gyromagnetic ratio, h is Plank's constant, I is the spin number (½) and r is the inter-nuclear distance.

As ω_1 approaches ω_0, $R_{1\rho}$ approaches R_1; as ω_1 approaches 0, $R_{1\rho}$ approaches R_2. $R_{1\rho}$ thus displays frequency dispersion between a maximum value of R_2 and a minimum value of R_1. When $(\omega_1\tau_c)^2 << 1$ and $\omega_1 << \omega_0$,

$$R_{1\rho} = R_1 \cos^2\theta + R_2 \sin^2\theta \qquad [2]$$

where θ is the tilt angle of the effective locking field (tan θ = ω_1/δ, and δ = offset from resonance).

$R_{1\rho}$ relaxation in a two-pool model

Often the behaviors of polymerized gels and tissues can be appropriately described in terms of a two-pool system in which the first pool is a liquid pool of free water (noted as pool "a") and a second pool (noted as pool "b") includes non-exchanging protons on the polymer. Clearly more elaborate multi-pool models can be developed, such as those that include an intermediate pool or hydration layer with intermediate characteristics but similar chemical shift. In addition, chemical exchange between water and labile protons in the solute may occur at specific sites such as hydroxyl ($^-$OH) and amino (NH^+) groups (39). These solutes resonate at a different frequency from water ($\delta\omega_0$), and thus contribute an additional dephasing term to rotating frame relaxation. For practical locking field strengths on or near resonance

$$R_{1\rho} = R_1 \cos^2\theta + \left(R_2^0 + p_a p_b \Delta\omega_b^2 \frac{r_b}{r_b^2 + \omega_1^2} \right) \sin^2\theta \qquad [3]$$

where p_a and p_b are the relative pool sizes (a = free, b = exchanging) where $p_a + p_b = 1$, $\Delta\omega_b$ is the frequency difference between the two pools, and r_b is the exchange rate and R_2^0 is the transverse relaxation rate without exchange.

The chemical exchange contribution to $T_{1\rho}$ may be described by the Bloch equations that have been modified to include exchange terms. These are sometimes referred to as the Bloch–McConnell equations (40). Chopra et al. (18) modified the Bloch equations and showed how, under specific conditions, an experiment measuring $R_{1\rho}$ at different locking field strengths (B_1) may be used to determine exchange rates. Chopra's methods will be explored further in the analysis section. Chemical exchange is postulated to dominate rotating frame relaxation at high fields, and thus experiments exploring this process will form the bulk of the work reported. However, there are other processes that are of interest, and each will be briefly introduced below.

Factors Influencing Spin Lock Contrast

Relaxation in the presence of long continuous wave (*cw*) irradiation is governed by many complex interactions. Redfield made the first experiments with this technique to reduce dephasing effects in solids and the theory was later translated into liquids and other biological tissues (1,29,31). Early measurements of rotating frame relaxation were shown to vary with locking field, the phenomenon known as $T_{1\rho}$ dispersion. If the B_1 field strength is set to zero ($\gamma B_1 = 0$ Hz), $T_{1\rho}$ is substantially equivalent to T_2. If the locking field is hypothetically increased to the strength of the main field, $T_{1\rho}$ will approach T_1. This allows the contrast to be selectively modulated between T_1- and T_2-weighting within the limits of the imaging system (32). $T_{1\rho}$ dispersions are often interpreted as reflecting the timescales of local motions in polymers and macromolecules, and indeed the presence of segmental motions in long chain molecules or macromolecular rotations may be

important influences on the difference between $T_{1\rho}$ and R_2 (2,29). However, theory predicts that exchange processes are also potentially important and to not require macromolecules to be present. For example, even in pure water, very weak dispersion pattern has been observed near 1 kHz. It is thought that this is due to chemical exchange of protons with naturally abundant $H_2{}^{17}O$ in water (41). This weak effect is often ignored for experiments at high field. For tissue models containing hydroxyl and amide groups, their abundance, exchange rates, and intrinsic relaxation properties are likely to be important.

Dipolar interactions between bound water and highly structured macromolecules such as collagen have been shown to contribute to $T_{1\rho}$ relaxation under specific conditions (2,3). When the movement of water molecules becomes sufficiently restricted, as is the case when in contact with highly structured molecules, the relaxation rates R_1, R_2 and $R_{1\rho}$ become frequency-dependent. In addition, the contribution of residual dipolar interactions (RDI) to relaxation is dependent on the orientation of the sample to B_0. At an angle of 0° or 180° to B_0, the RDI in a sample are maximized, and they approach a minimum at the "magic angle" of ~54.7° (42). One notable occurrence of this phenomenon is in musculoskeletal imaging where collagen fibers in tendons are aligned near the magic angle and result in a local increase in signal on T_2-weighted images (42,43). In a manner similar to the methods Koenig et al. used to measure T_1 dispersion, three and four pool models of this type of relaxation have been proposed to measure the relative contribution of dipolar effects to relaxation in the rotating frame (26,31,44). A corresponding method of directly measuring the contribution of dipolar cross-relaxation

to $T_{1\rho}$ with SIR-$T_{1\rho}$-FSE has been proposed by Hills (31). Selective inversion may produce bi-exponential recovery in the rotating frame where the fast rate corresponds to the dipolar cross-relaxation rate. Hills demonstrated that the dipolar cross-relaxation component is only a minor contributor to $R_{1\rho}$ relaxation, imparting only a small scalar offset to chemical exchange induced dispersion (31). Alternately, spin-locking techniques may be employed at low locking field, thus reducing the effects of low frequency RDIs, leaving contributions to $R_{1\rho}$ relaxation only from chemical exchange (43). However, other processes such as diffusion may in principle also contribute to $R_{1\rho}$ relaxation at low locking field, making it difficult to separate these relaxation effects.

Measurements of $T_{1\rho}$ have been shown to be highly sensitive to the effects of chemical exchange, resulting in a variation in $T_{1\rho}$ with applied locking field. These methods are analogous to the use of the Carr-Purcell-Meiboom-Gill (CPMG) method to investigate dispersions in T_2 (45). In CPMG sequences, as the rate of 180 degree pulses is increased, dephasing caused by chemical exchange is more effectively refocused, resulting in an increase in measured T_2. Similarly, in spin-locking experiments only isochromats carrying a resonant frequency less than the Rabi frequency (γB_1) will be "locked" to the applied B_1 field and thus not experience dephasing effects (32,46). The effects of chemical exchange in proteins, sugars, and other macromolecules are well studied with other MRI techniques, yet there is no consensus on their contribution to $T_{1\rho}$ dispersion. This lack of prior data is a prime motivation for the current work.

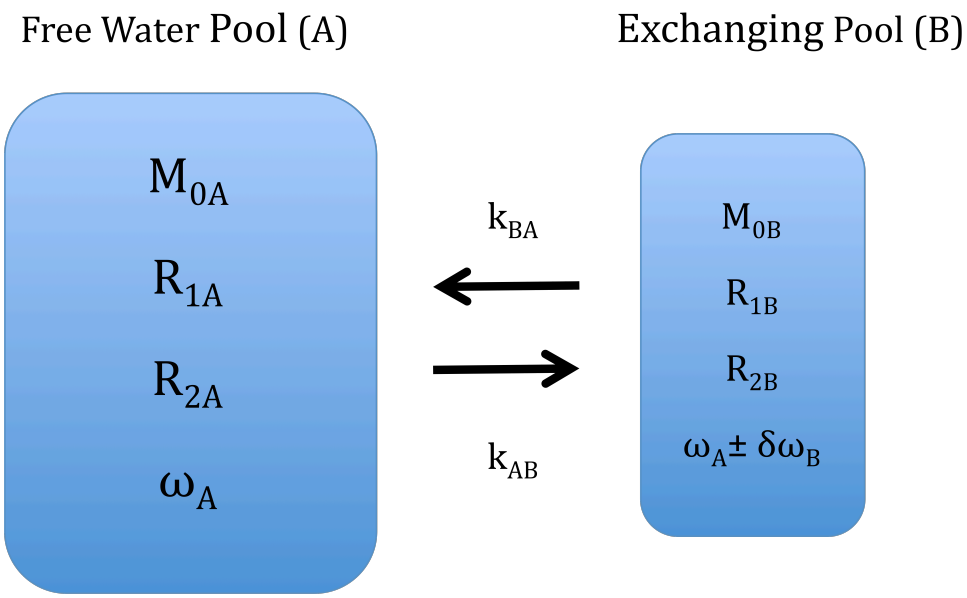

Figure 2: Schematic depiction of chemical exchange between two proton pools. The two environments communicate via chemical exchange at appropriate sites with the rates k_{ba} and k_{ab}.

Figure 2 illustrates a two-pool system in exchange for the case of a small pool of exchangeable solute protons (b) and a large pool for bulk water protons (a). The MRI parameters for these pools and the chemical exchange processes between them are also shown. The following terms are defined as: $\omega_A = 2\pi*\gamma B0$, $\omega_1 = 2\pi*\gamma B_1$, where γ is the gyromagnetic ratio for protons, B_0 is the main field strength, and B_1 is the applied rf field, and $\delta\omega = \omega-\omega_A$ is the frequency offset between water and the exchanging species. The Bloch equations modified for exchange can be written as:

$$\frac{dM_{xb}}{dt} = -\delta\omega_b M_{yb} - R_{2b} M_{xb} - k_{ba} M_{xb} + k_{ab} M_{xa} \qquad [4]$$

$$\frac{dM_{yb}}{dt} = -\delta\omega_b M_{xb} + \omega_1 M_{zb} - R_{2b} M_{yb} - k_{ba} M_{yb} + k_{ab} M_{ya} \qquad [5]$$

$$\frac{dM_{zb}}{dt} = -\omega_1 M_{yb} - R_{1b}\left(M_{zb} - M_{0b}\right) - k_{ba}M_{zb} + k_{ab}M_{za} \qquad [6]$$

$$\frac{dM_{xa}}{dt} = -\delta\omega_a M_{ya} - R_{2a}M_{xa} + k_{ba}M_{xb} - k_{ab}M_{xa} \qquad [7]$$

$$\frac{dM_{ya}}{dt} = \delta\omega_a M_{xa} + \omega_1 M_{za} - R_{2a}M_{ya} + k_{ba}M_{yb} - k_{ab}M_{ya} \qquad [8]$$

$$\frac{dM_{za}}{dt} = -\omega_1 M_{ya} - R_{1a}\left(M_{za} - M_{0a}\right) + k_{ba}M_{zb} - k_{ab}M_{za} \qquad [9]$$

Here R_1 and R_2 are the relaxation rates, M_0 is the equilibrium magnetization of each pool, and k_{ba} and k_{ab} are the proton exchange rates from pool b to a and from a to b respectively. The system obeys the law of conservation of mass, so $k_{ba}M_{0b} = k_{ab}M_{0a}$ is also true. Many investigators have attempted to simplify these equations into concise analytical solutions using a series of assumptions for a two-pool system (16,18,19). In addition, Trott and Palmer modeled more than two exchanging pools in a similar fashion to work in multi-site exchange in CEST experiments by Woessner et al (33,47).

Experimental data may be fit to these analytic expressions and subsequently used to estimate the contribution of chemical exchange to $R_{1\rho}$ relaxation in selected tissue models (16,18,31,48). For example, Virta et al. reported no significant dispersion in BSA with pH variation at very low field (0.1T) and with large spin locking field strengths of 2-8 kHz, and he proposed that cross-relaxation may dominate measured $T_{1\rho}$ values under these conditions (1). However, Duvvuri et al. suggested that in model cartilage systems at higher field (2T) under lower frequency spin locking (<1 kHz), proton exchange between NH^+ and ^-OH groups dominates dispersion effects (2). Hills attributes the increase in

chemical exchange mediated dispersion at high field to the larger resonance frequency offset ($\delta\omega$) between water and exchanging protons on macromolecules (31). As the main field frequency (B_0) increases the value of $\delta\omega$ between exchanging species increases, thus allowing chemical exchange to increasingly dominate proton relaxation. However, proton exchange fails to completely account for dispersion data in more rigid or desiccated tissues where water content falls below 50% of the total weight, and the additional contributions of dipolar cross-relaxation, diffusion, or tissue microstructure may be needed to fully explain a particular system (32). The relative contributions of these relaxation pathways have not been fully elucidated in model tissues and are the subject of some of the work described below.

In addition to chemical exchange, additional potential contributions to $T_{1\rho}$ relaxation may also arise from the diffusion of spins through heterogeneous fields, which may induce a dispersive effect due to either resonance frequency or susceptibility differences between different locations. As the locking field strength is increased, dephasing caused by diffusion processes may be theoretically reduced, which should result in an increase in measured $T_{1\rho}$. Similar effects have been noted in low frequency T_2 dispersions in BSA and in hydrated Sephadex bead suspensions (49,50), but it is unknown to what degree these low frequency dispersions also effect $T_{1\rho}$ relaxation. Quantitative $T_{1\rho}$ imaging may have a role in imaging local changes in susceptibility agents such as from amyloid plaques, which are small iron-rich lesions that begin to appear in many late-stage neurological disorders. Lesions typically range in size from 20 μm in mouse models up to 200 μm in human tissues. These lesions can be imaged with T_2, T_2* or susceptibility-

weighted imaging techniques (21,51,52). It is possible to image plaques directly due to the magnetic disturbance induced by the iron load of the plaque dephasing spins in the surrounding tissue and thus giving the appearance of a particle of up to 50 times its size (53). Previous studies at Vanderbilt have shown that $T_{1\rho}$ may also detect such lesions, possibly because the iron causes the spinlock to be off resonance or because of other effects on water dynamics.

We consider two cases of interest. Namely, $T_{1\rho}$ relaxation in the presence of gradient fields imparted by susceptibility agents ($\Delta\chi$) or main field inhomogeneities (ΔB_0), and second, the effects of combined chemical exchange and diffusion through susceptibility gradients on $T_{1\rho}$ relaxation.

Conceptually, diffusion between two regions of different susceptibility is very similar to chemical exchange; the latter is usually considered to involve instantaneous changes in frequency whereas the former comprises a continuous dephasing effect. In biological media where the intrinsic diffusion coefficient D is of the order 2×10^{-5} cm^2s^{-1}, the time on average required to move 2 μm is 1 msec. If the static field experienced by water molecules varies significantly on this spatial scale, we may expect to observe significant $R_{1\rho}$ dispersion around locking fields of 1 kHz, well within the regime readily accessible in practical MRI experiments. When the scale is much larger, dispersion will occur at correspondingly lower frequencies.

One simple model comprises a uniform space containing spheres of different susceptibility. Within each sphere the static field is uniform but exterior to each the field

is non-uniform. Water may diffuse within the spheres and exchange to the exterior spaces. If diffusion is fast enough that both spatial regions are thoroughly sampled in a time short as compared to differences in their resonant frequency or intrinsic relaxation times such diffusive exchange may be approximated as slow chemical exchange with a rate ~D/r^2 assuming a bulk water diffusion coefficient (D) and a mean bead radius (r) (49,54). When the rate of diffusion is much slower and the exchange rate is less than the frequency difference, nuclei do not sample all spatial areas. This results in different degrees of dephasing and more complex multi-exponential relaxation (49).

A second diffusion-related process is water diffusion through locally induced field gradients caused by susceptibility differences (55). As the bulk magnetic susceptibility of water and particles such as Ca^{++} or Fe^{++} are different, their placement in a large static field induces magnetic field gradients as shown in Figure 3. Within such a heterogeneous medium, the decay of transverse magnetization is accelerated, but the precise effects depend on several factors including the sizes of the field perturbations, their spatial extent and geometry, the rate of spin diffusion in their vicinity, and the pulse sequence. For example, this is the dominant relaxation mechanism enabling functional magnetic resonance imaging (fMRI) (55) wherein the $\Delta\chi$ originate from vessels with deoxyhemoglobin. The effects of paramagnetic iron, deoxyhemoglobin, and gadolinium (Gd) have been extensively studied via standard gradient- and spin-echo imaging techniques for a variety of vessel geometries (55-57). One theoretical description that affords useful insights into how these factors interplay is the Anderson-Weiss Mean Field approach previously applied to MRI by Kennan et al. (57,58). Spin-lattice relaxation in

the rotating frame with rate $R_{1\rho}$ is sensitive to variations in the local magnetic field experienced by nuclei that vary on the time scale of an applied radiofrequency spin-locking field that is under experimental control. This phenomenon will be explored with experiments on susceptibility agents in Chapter VII.

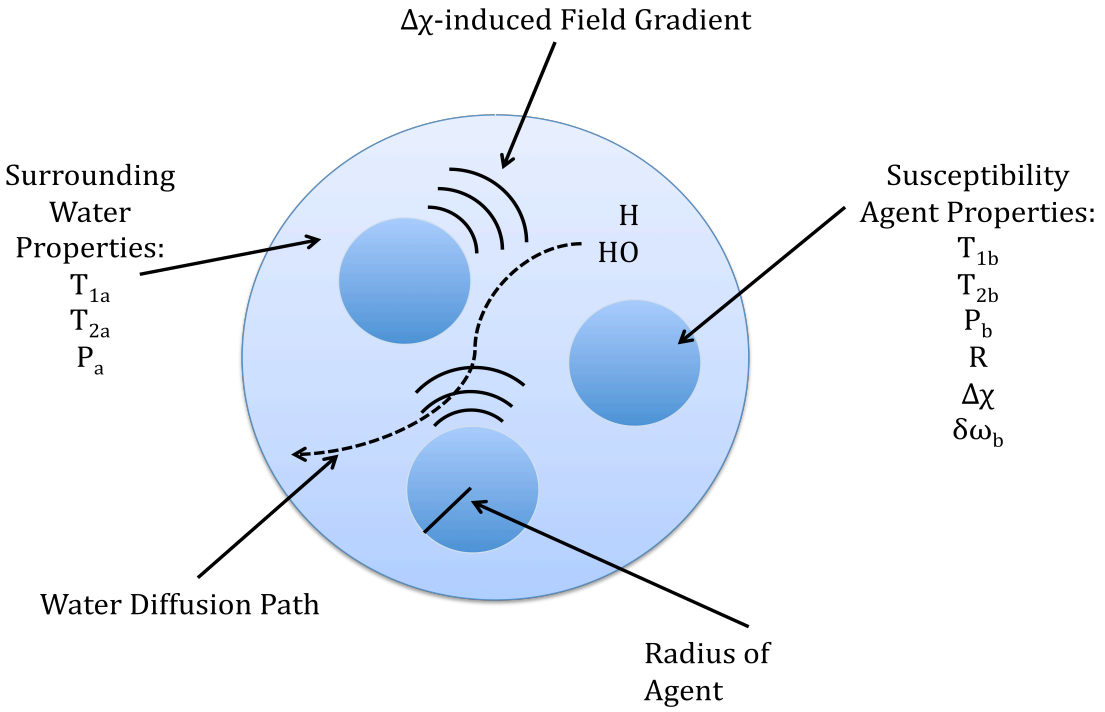

Figure 3: Schematic depiction of diffusive exchange. Water protons diffuse freely through water surrounding susceptibility agents. These agents induce a magnetic field that causes spins to dephase as they traverse the local environment.

In principle, it may be possible to quantitatively measure $T_{1\rho}$ and deduce parameters about the size of the susceptibility perturbation or to enhance contrast from Δχ agents using appropriate spin locking techniques. For example, in sphere-shaped objects, the gradients occur externally to the particles, and Eq. 10 gives the average field gradient generated,

$$G_{avg} = \mu_0 B_0 \Delta\chi / (4R) \qquad [10]$$

where μ_0 is the magnetic permeability of free space, B_0 is the main field strength, $\Delta\chi$ is the magnetic susceptibility difference between substances, and R is the object radius (59). For transverse relaxation, this mechanism contributes an additional diffusion-related term shown in Eq 11.

$$R_{2,obs} = R_2 + D(\gamma G \tau)^2/3 \qquad [11]$$

where R_2 is the intrinsic spin-spin relaxation rate, D is the diffusion coefficient, γ is the gyromagnetic ratio, G is the induced field gradient, and τ is the interval between refocusing pulses in a CPMG measurement that defines the time scale for irreversible spin dephasing.

For rotating frame relaxation we can identify τ instead as the inverse of the locking frequency $\tau = (\gamma B_1)^{-1}$ so that an equivalent expression for rotating relaxation may be expressed as Eq 12.

$$R_{1\rho} = R_{1\rho}^0 + \frac{DG^2}{3B_1^2} \qquad [12]$$

where $R_{1\rho}$ is the rotating frame relaxation rate, $R_{1\rho}^{\infty}$ is the rotating frame relaxation rate at 0 Hz locking field ($R_{1\rho}^0 = R_2$), and B_1 is the applied locking field strength.

Hills et al. attribute a midpoint of a region of dispersion to the relevant mean diffusive or chemical exchange rate (49). This analysis method will be used on model systems of susceptibility agents in Chapter VII.

Factors Influencing CEST Contrast

Chemical exchange saturation transfer (CEST) methods are of interest in this work as they provide an alternate method to generate contrast from chemical exchange effects. Additionally, the characteristic experimental limitations of spin locking and CEST are such that each can provide complementary information about specific model systems, and their features are explored in a later chapter. CEST contrast is generated by RF saturation of an exchanging species, which is then transferred to water, greatly reducing the relative magnitude of the water MR signal as shown in Figure 4. The change in water signal and image contrast depends on the exchange rate and the concentrations of the exchanging species among other factors. The saturation pulse must be applied at the resonant frequency of the labile proton, but the signal change does not, in the ideal case of perfectly selective RF saturation, explicitly depend on the magnitude of the chemical shift.

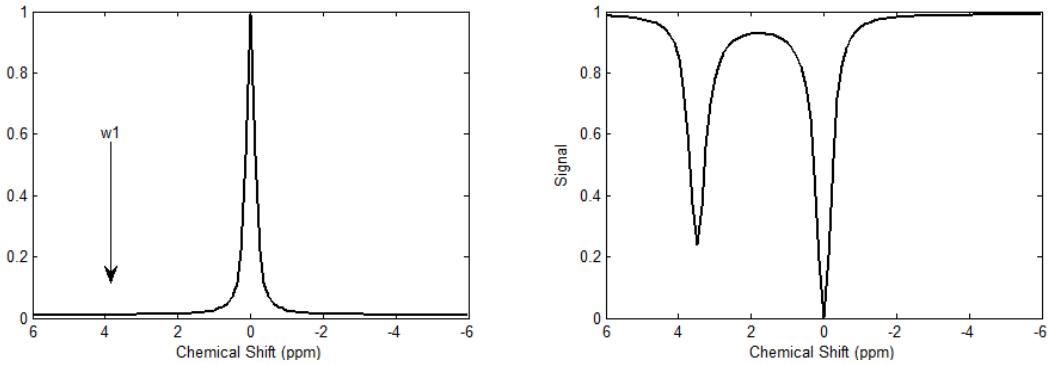

Figure 4: A. Simulated proton spectrum demonstrating the CEST technique with off-resonance RF saturation. B. Simulated CEST z-spectrum showing the location of a metabolite peak separated from water by some frequency offset (δω). This demonstrates a great advantage of CEST, namely that the metabolite peak need not be clearly discernable in a proton spectrum (4.a.) to be used to generate contrast.

To obtain CEST contrast, typically, an RF pulse is applied at an offset frequency (typically several ppm, δω) as referenced to the water peak (ω_0 = 0 ppm), and after saturated protons exchange with the water the reduced signal is then acquired. The off-resonance irradiation pulse may then be swept across a range of frequencies surrounding the water peak forming a "z-spectrum" of the resulting signal intensity at each obtained frequency step. If this spectrum is then normalized to a non-saturated image acquired on-resonance (M_0), the magnetization transfer ratio (MTR) is generated as shown in Eq. 13. Peaks in this z-spectrum identify resonance frequency offsets of specific exchanging species. However, the applied pulse may also alter the water signal because of direct saturation or non-specific magnetization transfer (60) with other broad resonances, and so generally two images are acquired for CEST imaging. Each image is acquired at the opposite frequency offset (± ppm of metabolite resonance of interest). The difference in the normalized saturation contrast on opposite sides of the water peak is referred to as the

magnetization transfer ratio asymmetry (MTR_{asym}) generated from Eq. 14, where $\delta\omega$ is the resonant frequency offset, and ω_0 is the reference water frequency.

$$MTR = 1 - \frac{S(\delta)}{S(0)} \qquad [13]$$

$$MTR_{asym} = \frac{S(-\delta) - S(+\delta)}{S(0)} \qquad [14]$$

The design performance and applications of CEST methods have been recently reviewed (61,62). In the context of this work, established CEST methods will be compared with spin-locking techniques to evaluate the relative strengths and weaknesses of each technique for use in specific tissues and model systems.

MODEL BIOMOLECULES AND TISSUES

Simple molecules and polymer gels are useful to explore relaxation processes in biologically relevant systems. Samples of these materials are used in the following experiments as they possess many of the properties of complex tissue, but they are more easily modified in terms of composition or pH to assess NMR relaxation processes. The types of model systems used in the following chapters will be briefly introduced below, with detailed descriptions presented in the following chapters. In addition to these simple systems, the opportunity arose to test spin-locking methods in a population of children with immature cartilage, for which $T_{1\rho}$ values have not been previously reported. A more

complete description of the relaxation properties of this complex tissue is provided as journal formatting precluded a more comprehensive literature review within that chapter.

Polyacrylamide Gels

Simple systems of biopolymers such as agarose or bovine serum albumin (BSA) possess many of the relaxation properties of more complex tissues, and they give insight into the important component processes of relaxation. Unfortunately there are limitations on the degree to which these can be manipulated to probe specific features. Instead, therefore, to begin quantitative studies of $T_{1\rho}$, we have selected a simple polymer system of polyacrylamide gels (PAG) that can be more easily manipulated and varied to investigate the effects of chemical exchange or other magnetization transfer pathways on rotating frame relaxation. Specifically, these were chosen due to their amide (NH^{+}) functional groups that are believed to be conduits for relaxation, and because their rigidity and pH can be varied without changing important elements of the composition. These gels have previously been studied for their relaxation properties by other methods (63). The structures of monomer acrylamide (AC), cross-linking agent (BIS), and potential gel structure are illustrated in Fig. 5.

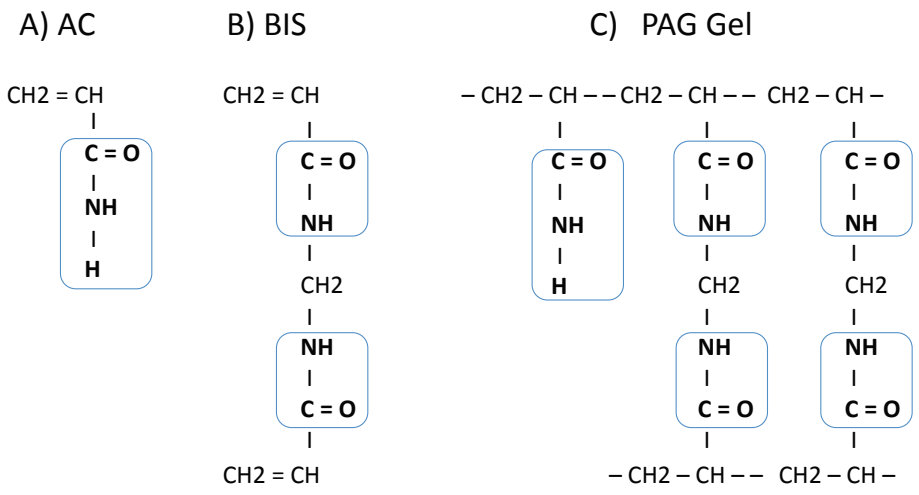

Figure 5: a. Acrylamide monomer (AC), b. N,N'=methylene-bis-acrylamide monomer (BIS). c. A typical structural element in cross-linked polyacrylamide gel (PAG).

The cross-linking agent BIS is essentially two acrylamide molecules joined via a methylene group, and forms bridges between acrylamide chains in the polymer. A common feature to the acrylamide and BIS monomers are the amide groups, which are circled in Figure 5. This structural group is common to many amino acids, and contributes to base-catalyzed exchange due to the oxygen's proximity to the NH^+ group.

Amides are of particular interest to proton exchange studies with NMR as they are typically governed by slow exchange processes (< 400 Hz) (64,65). These groups have been extensively researched in the high-resolution structural NMR literature, as they are of great importance to peak assignment in studies of proteins and peptides. These studies

led to the observation that molecular structures adjacent to the amide exchange sites have an important role in determining the intrinsic proton exchange rates for those sites. The work of Molday and Bai (65,66) shows that the nearest neighbors often govern the exchange rate in a predictable manner. Specifically for amides, the presence of polar side chains act to withdraw electrons, thus making the exchanging side relatively more acidic, and thus susceptible to base-catalyzed exchange (66). This observation is important because it suggests that exchange rate may be a more selective parameter to identify specific groups that are otherwise similar.

Peptides, Sugars and Proteins

Peptides are small polymers of simple amino acid chains that are linked by a peptide bond. Multiple peptide bonds may be used to link peptides together to create polypeptides. Polypeptides carry many of the same properties as proteins, but are usually much shorter in length and in general are distinguished from proteins by their ability to be created synthetically (67). Polypeptides are of great importance to a number of cell processes including DNA and RNA replication, cell signaling, cell metabolism, and also as potential synthetic antibodies and reporter agents. In the context of MRI, polypeptides may constitute a new class of endogenous contrast agent due to the presence of exchanging protons on the peptide chain such as amines or hydroxyls. These polypeptides have recently been utilized in this capacity as a non-paramagnetic MR reporter gene *in vivo*, by engineering a xenograft of brain tumor cells that express an artificial lysine-rich protein (68). The polypeptides poly-L-lysine (PLK), poly-L-arginine (PLR), and poly-L-threonine (PLT), shown in Figure 6, have been recently identified

from a large assay of polypeptides as being particularly sensitive to CEST methods by McMahon et al. (69), so these substances will be used in the following experiments.

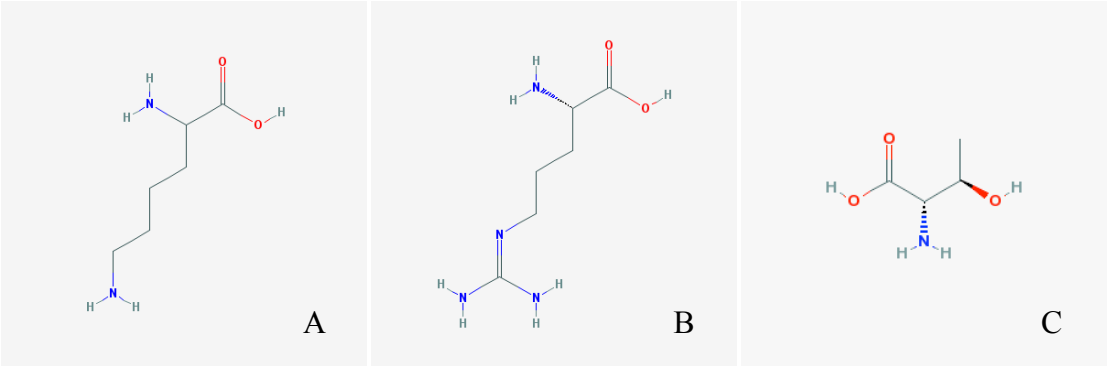

Figure 6: Base molecular structures for A. Poly-L-Lysine (PLK), B. Poly-L-Arginine (PLR), and C. Poly-L-Threonine (PLT). Note the differences in available exchangeable NH groups (Blue) and OH groups (Red). The images reference the corresponding National Center for Biological Information (PubChem) CID numbers.

6.a. Lysine (CID: 5962) sub-unit of poly-L-lysine with exchangeable amide (RC(O)NR'R) groups that resonate collectively near 3.69 ppm from water (0 ppm).

6.b. Arginine (CID: 6322) sub-unit of poly-L-arginine with exchanging guadinyl NH^+ (gNH_2) groups.

6.c. Threonine (CID: 6288) sub-unit of poly-L-threonine with exchanging NH^+ and ^-OH groups.

Endogenous sugars such as the monosaccharide glucose are also of great interest to the study of chemical exchange processes with MRI due to their large number of exchanging hydroxyl protons. These simple sugars are present in the brain, liver, skeletal muscle, and other organs in concentrations as high as 15 to 20% (wt/wt) (70,71). Simple sugars may be joined together with a glycosidic bond to form a disaccharide such as the commonly

known sucrose. This concept may be further extended with multiple glycosidic bonds to generate polysaccharides of biologic importance such as glycogen that is present in high concentrations in skeletal muscle (72) and especially in liver (73), or dextran that is often used as a biologically compatible coating for metal imaging probes. Chondroitin sulfate (CS) is a type of glycosaminoglycan, a particular type of polysaccharide that combines N-acetylgalactosamine and glucuronic acid. Like glycogen, a CS chain may be hundreds of units long. CS is often found in close conjunction with proteins and has numerous exchanging $^{-}$OH and a single NH^{+} group and has been recently used to generate CEST contrast (74). CS is also thought to be a dominant contributor to SL contrast *in vivo* (2,3) and its potential role in cartilage degeneration will be discussed later. The sugars used in the following experiments are given in Figure 7 in increasing order of complexity.

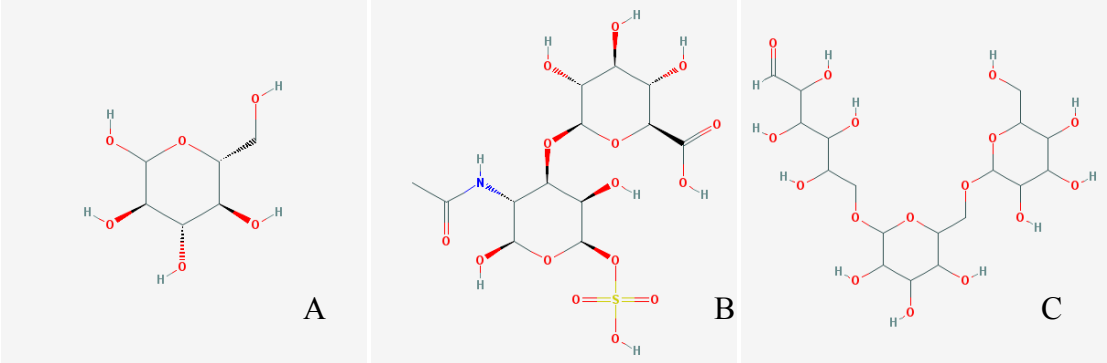

Figure 7: Sugars in order of increasing complexity. Note that the polysaccharides are cross-linked at OH sites, removing a potential exchanging site. The images reference the corresponding National Center for Biological Information (PubChem) CID numbers.

7.a. Glucose molecule (CID: 5793) with 3 distinct hydroxyl ($^{-}$OH) exchanging sites.

7.b. Chondroitin Sulfate (CID: 24766), a sulfated glycosaminoglycan that carries multiple exchanging $^{-}$OH and a single NH^{+} site.

7.c. Dextran (CID: 4125253), a poly-glucose molecule that is formed from multiple glycosidic linkages at the α-1,6 or α-1,3 sites on the glucose sub-unit and carries exchanging $^{-}$OH sites that resonate near 1.2 ppm.

Iohexol as an Exchange-Rate Based Contrast Agent

A commonly used family of X-ray contrast agents has recently been identified for potential use as an exchange-based exogenous agent for MRI (75). Specifically, the agent Iopamidol has been used to generate novel image contrast from CEST techniques. We intend to determine if a similar molecule, Iohexol (CAS Num: 66108-95-0), may be used to generate contrast with spin locking techniques. Iohexol is used clinically in a variety of angiographic and neurologic screening protocols due to the presence of iodine. Iohexol also carries two NH^{+} and six $^{-}$OH functional groups that impart it with suitable MR properties for use as an exchange-based contrast agent. Note that the structure of Iohexol is different from Iopamidol. Iopamidol has three available NH^{+} and five $^{-}$OH sites (See Figure 8). We demonstrate how appropriate spin-locking techniques can be used to produce novel contrast in the presence of Iohexol in a later chapter.

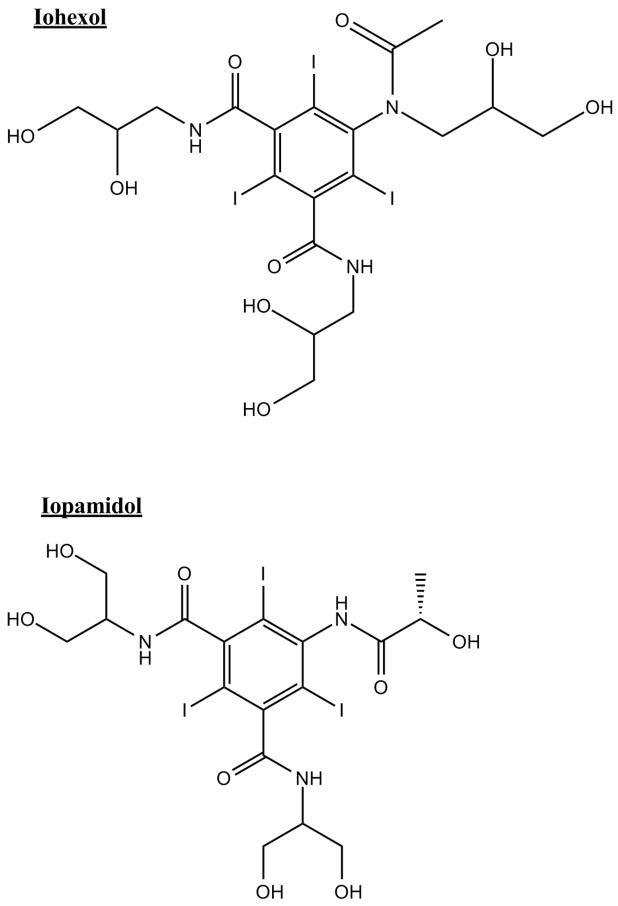

Figure 8: A. Chemical structure of Iohexol. B. Chemical structure of Iopamidol. Note the differences in available NH and OH exchange sites.

Models to explore Diffusion and Susceptibility

Spherical beads provide a useful model system to explore susceptibility effects, as they simplify the geometric dependence of relaxation effects considerably. As mentioned, we aim to determine the role of diffusion with and without chemical exchange on rotating frame relaxation. Sephadex beads provide a suitable system to explore these effects as they are spherical, and they consist of cross-linked dextran that have chemically

exchanging hydroxyl groups. They are available commercially in a variety of sizes and cross-link densities. The beads are permeable to the extent that water may freely diffuse between the inner dextran and outside water pools. In addition to the Sephadex beads, latex beads of similar diameter will be used as a control substance as they are impermeable to water, and thus should not exhibit relaxation due to chemical exchange. It is unknown to what extent spin locking techniques are sensitive to diffusion and chemical exchange effects in these systems, and they will be evaluated extensively in a later chapter.

Cartilage Constituents

Cartilage has several unique features that impart it with interesting proton relaxation properties. It features a high concentration of fibrous collagen structures, a relatively high density, and is present *in vivo* in distinct, thin layers (76). These attributes make cartilage difficult to image with standard clinical sequences and thus a candidate for investigation with alternative contrast methods such as with spin locking. Healthy cartilage is important to proper biomechanical function, and poor cartilage quality is associated with a variety of diseases including osteoarthritis (OA) (3,77,78).

Cartilage is composed of a semi-solid matrix of water (65-80%), proteoglycan (~5%), and collagen (15-20%), and other proteins (~2%) (79). This collagen is predominantly type II (hyaline cartilage), and is present in long triple-helical fibers (3). Proteoglycan (PG) content is of particular interest for its potential role in cartilage degenerative processes. Proteoglycans are highly charged macromolecules comprised of a large

concentration of glycosaminoglycans (GAGs) (80). These GAGs in turn are composed of carboxyl and sulfate groups that are strongly bound together. These highly compacted molecules create an area of locally negative charge and are measured in terms of a fixed charge density (FCD). This negative charge results in an increased affinity for positively charged Na^+ cations and a drop in Cl^- anions in the extracellular space (81). Thus, for healthy normal collagen, there should be a strong correlation among Na^+ and GAG and FCD. Indeed, histological and biomechanical studies correlate FCD with GAG concentration, and demonstrate a loss of compressive stiffness with along with a drop in FCD and GAG (82-87). The collagen content serves a variety of biomechanical purposes *in vivo*, including: providing shock absorption, imparting flexibility, and smoothing joint motions (88).

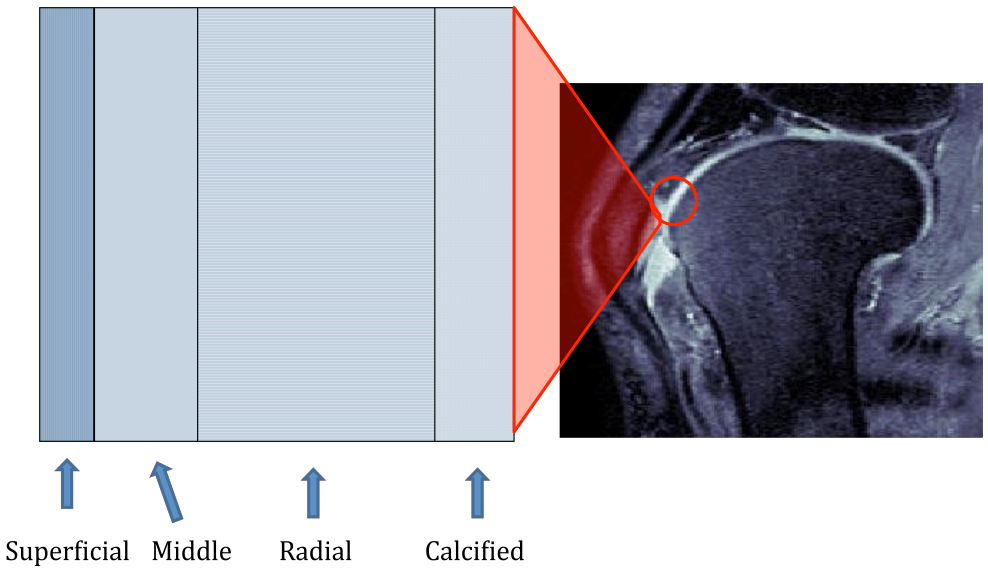

Figure 9: Adult articular cartilage layers. Note the distinctive orientation of the Radial Layer as opposed to the less organized Superficial and Middle zones.

Typically GAG, and thus Na^+ concentration increases with depth away from the articular surface as demonstrated by a number of studies (77,79,81). This is due in part to the structure of articular cartilage. Normal cartilage tissue occurs in four layers that are typically between two and five millimeters in total depth (See Figure 9) (88-91).

Beginning with the articular surface, the first layer is the superficial zone. This layer has two sub-layers the first of which is composed of collagen fibers that are parallel to the articular surface and contain flattened chondrocytes, which produce and regulate extracellular matrix (ECM) (88). The second sub-layer consists of fibers that are perpendicular to the surface. Overall, the superficial zone is densely packed with collagen fibers, but contains a high concentration of water and a relatively low concentration of PG. The next layer is the intermediate layer and is composed of larger chondrocytes and unordered ECM. Here PG content is increased and water content further decreased. Proceeding outward, the next layer is the radial zone, which is characterized by fibers that are arranged perpendicular to the articular surface. Here the water content is lowest and the PG content highest. This area then transitions to the calcified zone where there is a marked drop in PG and collagen as the tissue ossifies.

Quantitative measurements of $T_{1\rho}$ may, in principle, be used to assess cartilage quality. Articular cartilage has been studied *in vivo* for correlation of $T_{1\rho}$ changes with osteoarthritis (OA) degenerative processes (3,4,92). Osteoarthritis can be broadly categorized as a spectrum of degenerative diseases that alter the physical and chemical properties of cartilage. Most likely, symptoms of OA occur due to a complex interplay of

mechanical stress injury played out over a time frame as long as several decades coupled with the inability of chondrocytes to regenerate the extracellular matrix and maintain proper joint function. Early OA changes are associated with the loss of PG, although early-state molecular degradation is not typically seen on clinical imaging sequences (3,4,77,93). This may provide an opportunity for $T_{1\rho}$-weighted imaging to identify early-stage cartilage disease. $T_{1\rho}$ changes may correlate with changes in proteoglycan content, theoretically yielding changes in chemical exchange rates and macromolecular pool sizes. A competing technique known as Gadolinium-enhanced magnetic resonance imaging of cartilage (dGEMRIC) is also sensitive to PG loss, but requires the use of exogenous contrast (81). Spin locking techniques to assess cartilage quality have been used in research studies, but have so far remained outside of routine clinical practice. This lack of adoption may be attributed to a prominent criticism that states that the degradation model of cartilage with trypsin digest is subject to errors that mask a definitive correlation of $T_{1\rho}$ with GAG content (77,85,94).

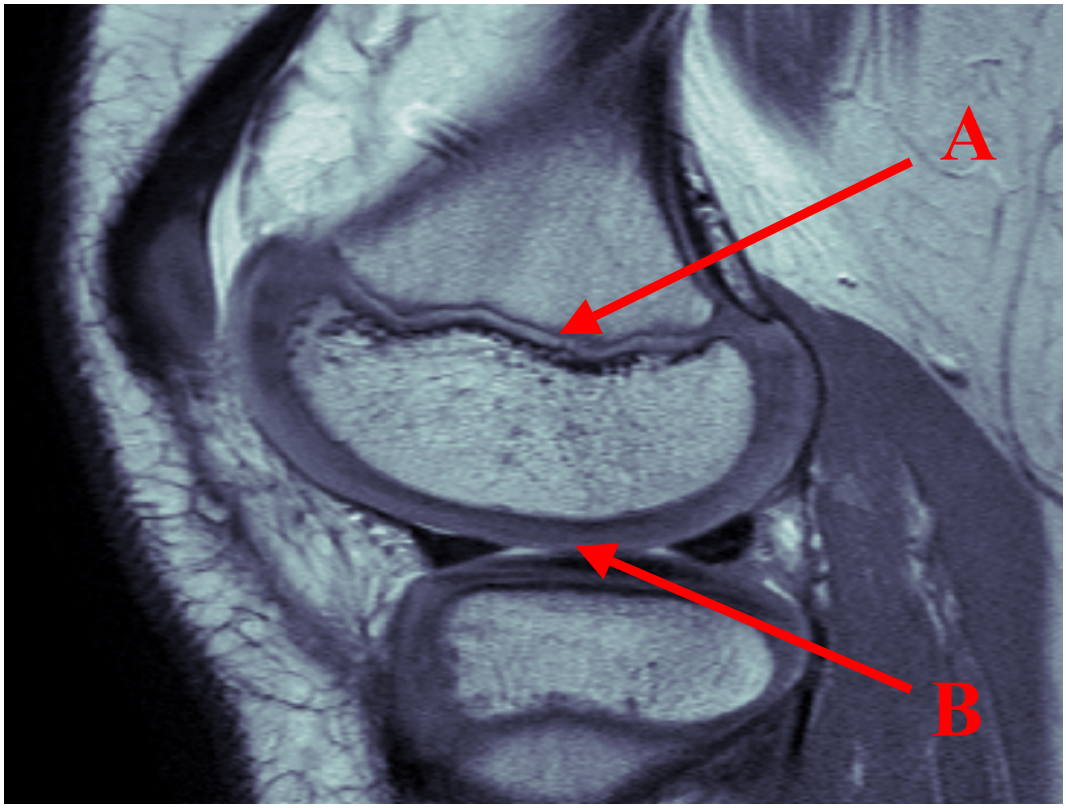

Figure 10: PDW-TSE image of epiphyseal cartilage layers in a 10YO M at 3T. Arrow A points to the clear demarcation of the growth plate. Note that the articular surface (Arrow B) is difficult to distinguish from the large epiphyseal cartilage zones (light regions).

$T_{1\rho}$-weighted imaging has been extensively used to investigate adult articular cartilage; however, similar measurements have not been performed in immature epiphyseal cartilage. Epiphyseal cartilage is found at the ends of long bones between the joint and the primary growth plate in children (See Figure 10). The epiphysis is initially completely comprised of cartilage with a high concentration of GAG (95,96). Typically by adolescence, the epiphysis completely ossifies. The ossification process is characterized by a degradation of GAG macromolecules and the hypertrophy of chondrocytes scattered in the epiphysis, reducing the amount of bound water. This transformation gives rise to

higher signal on T_2-weighted images (97). This process potentially makes epiphyseal cartilage suitable for study of water exchange dynamics via $T_{1\rho}$-weighted imaging. A small cohort of children who still have a large percentage of epiphyseal cartilage were recruited to have $T_{1\rho}$ quantification performed at the end of their clinically indicated study. The details of this experiment are given in a later chapter.

EXPERIMENTAL METHODS

Pulse Sequences to measure $T_{1\rho}$

Spin-lock contrast ($T_{1\rho}$-weighting) may be imparted to an image with a variety of pulse sequences, but usually $T_{1\rho}$-weighted contrast is achieved by one of two methods. The first is the addition of a spin-lock (SL) "cluster" of pulses before an imaging sequence (98-100). The typical cluster shown in Figure 1 consists of a 90-degree pulse that nutates the longitudinal magnetization vector into the transverse plane, followed by a long, pseudo-continuous wave (*cw*) pulse that may be applied for durations up to several hundreds of milliseconds.

The long B_1 pulse is applied in the direction of the nutated magnetization vector, causing spins to precess about this transverse axis. Longitudinal magnetization will decay in the rotating reference frame with time constant $T_{1\rho}$, and transverse magnetization will decay with time constant $T_{2\rho}$ (29). As mentioned, this rate is dependent on the B_1 value of the applied *cw* pulse. After the prescribed spin-lock time (TSL) has elapsed, another 90-degree pulse returns the magnetization vector to alignment to the Z-axis. Any residual

transverse magnetization is then spoiled, and any imaging sequence may then be performed to read out the $T_{1\rho}$-weighted magnetization (See Figure 1).

The second category of methods utilizes a pulse train of adiabatic pulses to generate ρ-domain contrast. Under appropriate conditions, a feature of adiabatic pulses is that relaxation is governed by $R_{1\rho}$ and $R_{2\rho}$ (17,101,102). However, this approach results in significantly greater power deposition as measured by specific absorption rate (SAR). This increased power requirement and other technical factors make this type of pulse sequence difficult to implement on clinical scanners, and the extraction of quantitative measurements is less straightforward. Sierra et al. (16) have also shown that the adiabatic and *cw* methods are substantially equivalent for measuring proton relaxation, so the experiments proposed here will utilize the simpler *cw* methods.

The original 3-pulse cluster as utilized by Redfield et al. to investigate $T_{1\rho}$ dispersion in metal ion solutions is very sensitive to B_1 and B_0 inhomogeneities especially at low values of applied B_1 (100). If we follow the magnetization vector using rotation matrices as adapted from Witschey et al. and Borthakur et al. (100,103), we can understand the source and implications of B_1 and B_0 inhomogeneity in the context of $T_{1\rho}$-weighted imaging. Beginning at thermal equilibrium suppose $\underline{M}$ represents the magnetization vector sum of isochromats whose line width is less than γB_1.

$$\underline{M} = [M_x' = 0, M_y' = 0, M_z' = 1]$$

If first we apply a short duration rotation of angle θ about the x-axis to tip the magnetization towards the transverse plane, then the magnetization is

$$[M_x' = 0, M_y' = \sin(\theta), M_z' = \cos(\theta)]$$

A long duration spin-locking pulse is then applied along the y-axis for duration TSL. Magnetization will then begin to precess about this applied B_1 field in the rotating frame as described previously. This precession imparts a rotation turn angle measured as $\alpha = \gamma B_1 * TSL$. The resulting magnetization vector can then be described by:

$$M_x' = -\cos(\theta)*\sin(\alpha)*e^{-TSL/\ T2\rho}$$

$$M_y' = \sin(\theta)*e^{-TSL/\ T1\rho}$$

$$M_z' = \cos(\theta)*\cos(\alpha)*e^{-TSL/\ T2\rho}$$

Another θ pulse about the x-axis with phase shifted by 180° returns the prepped magnetization to the +z-axis, yielding:

$$M_x' = -\cos(\theta)*\sin(\alpha)*e^{-TSL/\ T2\rho}$$

$$M_y' = \sin(\theta)\ *e^{-TSL/\ T1\rho} - \sin(\theta)\ \cos(\theta)\ \sin(\alpha)*e^{-TSL/\ T2\rho}$$

$$M_z' = \sin^2(\theta)\ *e^{-TSL/\ T1\rho} + \cos^2(\theta)*\cos(\alpha)*e^{-TSL/\ T2\rho}$$

If a crusher gradient is applied, spoiling the residual transverse magnetization, and if the excitation flip angle (θ) is equal to 90°, M_z is reduced to a much simpler expression:

$$M_z' = M_0 e^{-TSL/T1\rho}$$

It is often impossible or impractical to achieve a perfect 90° excitation, or to generate a uniform B_1 field. This results in a distribution of flip angles across the sample, and as a result some isochromats will not experience the prescribed 90° pulse. These errors will typically manifest themselves in an image as banding artifacts (104).

In an attempt to reduce artifacts induced by B_0 and B_1 inhomogeneities, certain modifications of the *cw* pulse sequence have been attempted. The first set of developments were derived from Solomon's rotary echo techniques (105). A four-pulse cluster tends to compensate for B_1 inhomogeneity by reversing the phase of the applied spin-lock pulse half way through its application (See Figure 11.a). This corrects for accumulated phase variations from imperfect B_1 fields. After the first half of the cluster, the magnetization vector is:

$$M_x' = -\cos(\theta)*\sin(\alpha/2)*e^{-TSL/2*T2\rho}$$

$$M_y' = \sin(\theta) *e^{-TSL/2*T1\rho}$$

$$M_z' = \cos(\theta)*\cos(\alpha/2)*e^{-TSL/2*T2\rho}$$

During the second half of the SL pulse the phase is rewound, so the M vector loses its dependence on α, so the net effect is:

$$M_x' = 0$$

$$M_y' = \sin(\theta)*e^{-TSL/T1\rho}$$

$$M_z' = \cos(\theta)*e^{-TSL/T2\rho}$$

Zeng et al. and Witschey et al. introduced additional improvements by inserting a 180-degree inversion pulse half way through the applied spin-lock pulse (100,106) as shown in Figure 11.b and 11.c. These five-pulse clusters compensate for non-uniformities in the B_0 field as long as $B_1 > \Delta B_0$. This condition can usually be met even at high fields as the typical background ΔB_0 is ≤ ~100 Hz in tissue and it is easy to ensure that B_1 is prescribed to be greater than this value (107). This technique represents the current method of choice for clinical $T_{1\rho}$-weighted imaging due to its simplicity of implementation as compared with the adiabatic approaches discussed previously.

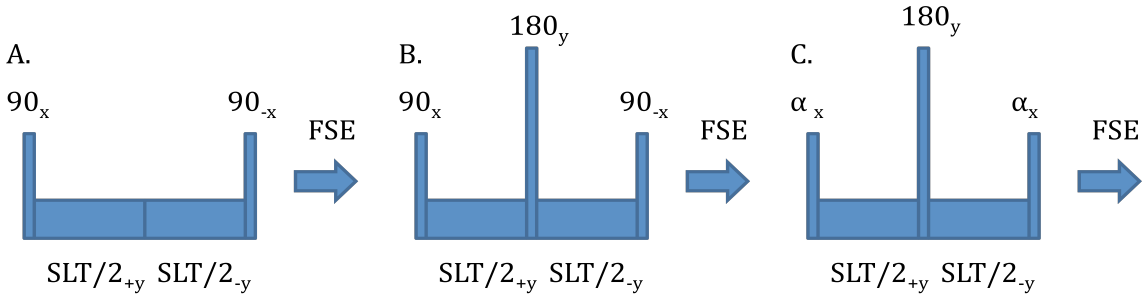

Figure 11: Three and four pulse SL clusters to reduce the effects of B_1 and B_0 inhomogeneity. 11.a. demonstrates a SL pulse with phase reversal half way through, thus rewinding accrued phase in the presence of inhomogeneous B_1. 11.b. includes a 180-degree refocusing pulse to reduce the effects of B_0 inhomogeneity. 11.c. This pulse is similar to 11.b but may be applied at any excitation angle α.

Pulse Sequence to Measure CEST Contrast

CEST contrast generation shares much in common with magnetization transfer (MT) contrast techniques first used in an imaging context by Sled and Pike (108). MT attempts to saturate the broad line width of semi-solid metabolites, which is then transferred to the water pool in a manner that generates useful contrast. A number of MT techniques have been subsequently developed, including *cw*, pulsed, on- and off-resonance techniques (109-111). CEST methods are very similar conceptually, but attempt to saturate only a narrow band of frequencies centered on a metabolite of interest as opposed to a broad line width with MT experiments. These techniques have been reviewed recently by Zhou et al. and van Zijl et al. (61,62). RF power selection and optimization for CEST pulses is of great importance, and the subject of recent research (112). Typically, the power and duration of the RF pulse is optimized empirically to improve the saturation efficiency observed from a particular metabolite. This process must be done for each sample of interest, as CEST contrast is a function of resonance frequency offset and the chemical exchange regime of the sample. As mentioned previously, typically an RF pulse is applied at an offset frequency (typically several ppm, $\delta\omega$) as referenced to the water peak (ω_0 = 0 ppm), and after saturated protons exchange with the water the reduced signal is acquired. The off-resonance irradiation pulse may then be swept across a range of frequencies surrounding the water peak forming a "z-spectrum" of the resulting signal intensity at each obtained frequency step. The scan parameters may then be empirically optimized to improve the clarity of the water and metabolite peaks, and these data may then be used to generate the MTR and MTR_{asym} as described in the data analysis section.

Imaging Technique Limitations and Caveats

Several practical limitations affect $T_{1\rho}$ and CEST imaging techniques. These typically include: specific absorption rate (SAR) limits for clinical imaging, banding artifacts and chemical shift artifacts due to complex off-resonance excitation and rotations respectively in the presence of B_0 and B_1 inhomogeneities. The SL cluster is generally performed at γB_1 (113) ranging from a few hundred Hz to two kHz for clinical imaging systems to stay within the SAR limits while still maintaining reasonable scan times. Studies with preclinical imaging systems have been performed with locking fields up to ~30 kHz (31,44). CEST RF pulses are typically an order of magnitude lower than SL pulses, however they are generally also much longer in duration (several sec vs. tens or hundreds of msec). Therefore, in order to remain within clinical SAR limits, long repetition times are required, thus making imaging less efficient. The focus of these aims will be on developing techniques that may ultimately be of clinical significance; therefore study of the lower range of frequency interactions will be emphasized.

At higher field, SAR becomes the dominant obstacle to clinical $T_{1\rho}$ imaging. The repetition time (TR) needed to stay within the SAR envelope becomes large enough to preclude imaging at multiple B_1 values during a clinical imaging session. SAR issues have been addressed with a variety of k-space segmentation techniques including banding, keyhole methods, and parallel imaging. The k-space segmentation techniques are typically characterized by utilizing low-power SLA for distant k-space lines and full power SLA for centric acquisitions. These techniques may reduce SAR by up to 40%, thereby reducing the minimum TR for each acquisition and significantly enhancing the

prospects of utilizing $T_{1\rho}$-weighted imaging clinically. These types of techniques add around a 2% error to the measured $T_{1\rho}$ time constant (114). Parallel imaging techniques have been applied to spin-lock imaging and have shown similar promise for utility in $T_{1\rho}$ mapping (115).

DATA ANALYSIS METHODS

Analysis of $T_{1\rho}$ Measurements

The first aim will demonstrate three parameter $T_{1\rho}$ mapping as performed by fitting signal intensity to a monoexponential decay function (Eq. 15) on a pixel-by-pixel basis to create a map of this relaxation parameter:

$$S(TSL) = M_0 \exp\frac{-TSL}{T_{1\rho}} + C \quad [15]$$

where S is the signal as a function of TSL, TSL is the spin-lock time (ms), M_0 is the signal intensity with no applied locking pulse, and C is a constant accommodating differences in proton density.

$T_{1\rho}$ dispersion data may be fit with a variety of models to estimate chemical exchange parameters. Chopra et al. (18) considered the general case in which exchanging nuclei experience different relaxation rates as well as chemical shifts when moving between phases, which is more appropriate for biopolymers which exhibit strong dipolar relaxation effects. Chopra et al. modified the Bloch equations and showed how, under

specific conditions, an experiment measuring $R_{1\rho}$ at different locking field strengths (γB_1) may be used to determine solvent exchange rate. Over the limited range of locking frequencies usually available in MR imaging systems, there are negligible variations in the dipolar contributions to longitudinal relaxation, so Chopra's equation may adequately describe rotating frame relaxation in a two-pool system as given in Eq. 16.

$$R_{1\rho} = R_{2f} + p_b r_b \left(R_{2b} \left(R_{2b} + r_b \right)^{-1} \right) \left\{ \frac{\left(R_{1b} + r_b \right) \left(R_{2b} + r_b + \frac{\Delta\omega_b^2}{R_{2b}} \right) + \omega_1^2}{\left(R_{1b} + r_b \right) \left(R_{2b} + r_b + \frac{\Delta\omega_b^2}{R_{2b} + r_b} \right) + \omega_1^2} \right\} \quad [16]$$

In Eq. 16, R_{2a} is the relaxation rate of free water, p_b is the ratio of exchangeable sites, r_b is the exchange rate from the bound to free water pools, R_{1b} and R_{2b} are the relaxation rates of the bound sites, ω_1 is the spin lock amplitude, and the chemical shift is given as $\Delta\omega_b$.

By substituting expressions for the limits of weak ($R_{1\rho}^0$) and strong ($R_{1\rho}^\infty$) locking fields into Eq. 16, the expression for the observed $R_{1\rho}$ reduces to:

$$R_{1\rho} = \left\{ \frac{R_2 + \frac{\left(R_{1\rho}^\infty * \omega_1^2 \right)}{S_\rho^2}}{1 + \frac{\omega_1^2}{S_\rho^2}} \right\} \qquad [17]$$

where $S_\rho^2 = (R_{1b} + r_b) / (R_{2b} + r_b) * \{ (R_{2b} + r_b)^2 + \Delta\omega_b^2 \}$. A non-linear least-squares fit of the variation of $R_{1\rho}$ with ω_1 to Eq. 17 may be used to obtain best fits of R_2, $R_{1\rho}^{\infty}$, and S_ρ^2 for cases where $r_b > R_{1b}, R_{2b}$.

Then a study of $R_{1\rho}$ vs. ω_1 may be used to estimate exchange rates if $\Delta\omega_b$ is known (or negligible). Here, chemical shift values are taken from the maximum point of the measured CEST MTR asymmetry. This approach has been used previously in an attempt to quantify proteoglycans in bovine articular cartilage (4).

Analysis of CEST Data

CEST z-spectra will be obtained for the samples under investigation, and then the magnetization transfer ratio and MTR_{asym} calculated using Eqs. 13 and 14.

SUMMARY

Spin locking is a potentially rich source of data from a sample of interest due to the technique's sensitivity to a large number of MRI parameters. The specific contributors to rotating frame relaxation are not well understood. This work comprises a series of studies that attempt to move beyond qualitative measurements with spin locking techniques towards a more quantitative understanding of the mechanisms by which protons relax in heterogeneous tissues. The experiments attempt to explain how molecular and cellular properties of model tissue systems influence proton relaxation in the rotating frame and how they may be employed to generate useful contrast in images. The experiments will emphasize quantitative measurements of spin-lattice relaxation in the rotating frame,

model fitting to extract exchange rates, and image subtraction techniques used to generate novel contrast.

REFERENCES

1. Virta A, Komu M, Kormano M. T-1 rho of protein solutions at very low fields: Dependence on molecular weight, concentration, and structure. Magnet Reson Med 1997;37(1):53-57.
2. Duvvuri U, Goldberg AD, Kranz JK, Hoang L, Reddy R, Wehrli FW, Wand AJ, Englander SW, Leigh JS. Water magnetic relaxation dispersion in biological systems: the contribution of proton exchange and implications for the noninvasive detection of cartilage degradation. Proc Natl Acad Sci U S A 2001;98(22):12479-12484.
3. Akella SV, Regatte RR, Gougoutas AJ, Borthakur A, Shapiro EM, Kneeland JB, Leigh JS, Reddy R. Proteoglycan-induced changes in T1rho-relaxation of articular cartilage at 4T. Magn Reson Med 2001;46(3):419-423.
4. Regatte RR, Akella SV, Borthakur A, Reddy R. Proton spin-lock ratio imaging for quantitation of glycosaminoglycans in articular cartilage. J Magn Reson Imaging 2003;17(1):114-121.
5. Santyr GE, Henkelman RM, Bronskill MJ. Spin locking for magnetic resonance imaging with application to human breast. Magn Reson Med 1989;12(1):25-37.
6. Grohn OH, Lukkarinen JA, Silvennoinen MJ, Pitkanen A, van Zijl PC, Kauppinen RA. Quantitative magnetic resonance imaging assessment of cerebral ischemia in rat using on-resonance T(1) in the rotating frame. Magn Reson Med 1999;42(2):268-276.

7. Kettunen MI, Grohn OH, Lukkarinen JA, Vainio P, Silvennoinen MJ, Kauppinen RA. Interrelations of T(1) and diffusion of water in acute cerebral ischemia of the rat. Magn Reson Med 2000;44(6):833-839.

8. Aronen HJ, Perkio J. Dynamic susceptibility contrast MRI of gliomas. Neuroimaging Clin N Am 2002;12(4):501-523.

9. Grohn OH, Makela HI, Lukkarinen JA, DelaBarre L, Lin J, Garwood M, Kauppinen RA. On- and off-resonance T(1rho) MRI in acute cerebral ischemia of the rat. Magn Reson Med 2003;49(1):172-176.

10. Kettunen MI, Grohn OH, Kauppinen RA. Quantitative T1rho NMR spectroscopy of rat cerebral metabolites in vivo: effects of global ischemia. Magn Reson Med 2004;51(5):875-880.

11. Borthakur A, Gur T, Wheaton AJ, Corbo M, Trojanowski JQ, Lee VM, Reddy R. In vivo measurement of plaque burden in a mouse model of Alzheimer's disease. J Magn Reson Imaging 2006;24(5):1011-1017.

12. Haris M, McArdle E, Fenty M, Singh A, Davatzikos C, Trojanowski JQ, Melhem ER, Clark CM, Borthakur A. Early marker for Alzheimer's disease: hippocampus T1rho (T(1rho)) estimation. J Magn Reson Imaging 2009;29(5):1008-1012.

13. Virta A, Komu M, Lundbom N, Kormano M. T1 rho MR imaging characteristics of human anterior tibial and gastrocnemius muscles. Acad Radiol 1998;5(2):104-110.

14. Markkola AT, Aronen HJ, Paavonen T, Hopsu E, Sipila LM, Tanttu JI, Sepponen RE. T1 rho dispersion imaging of head and neck tumors: a comparison to spin

lock and magnetization transfer techniques. J Magn Reson Imaging 1997;7(5):873-879.

15. Poptani H, Duvvuri U, Miller CG, Mancuso A, Charagundla S, Fraser NW, Glickson JD, Leigh JS, Reddy R. T1rho imaging of murine brain tumors at 4 T. Acad Radiol 2001;8(1):42-47.

16. Sierra A, Michaeli S, Niskanen JP, Valonen PK, Grohn HI, Yla-Herttuala S, Garwood M, Grohn OH. Water spin dynamics during apoptotic cell death in glioma gene therapy probed by T1rho and T2rho. Magn Reson Med 2008;59(6):1311-1319.

17. Jokivarsi KT, Niskanen JP, Michaeli S, Grohn HI, Garwood M, Kauppinen RA, Grohn OH. Quantitative assessment of water pools by T 1 rho and T 2 rho MRI in acute cerebral ischemia of the rat. J Cereb Blood Flow Metab 2009;29(1):206-216.

18. Chopra S, Mcclung RED, Jordan RB. Rotating-Frame Relaxation Rates of Solvent Molecules in Solutions of Paramagnetic-Ions Undergoing Solvent Exchange. J Magn Reson 1984;59(3):361-372.

19. Trott O, Palmer AG, 3rd. R1rho relaxation outside of the fast-exchange limit. J Magn Reson 2002;154(1):157-160.

20. Haacke EM, Cheng NY, House MJ, Liu Q, Neelavalli J, Ogg RJ, Khan A, Ayaz M, Kirsch W, Obenaus A. Imaging iron stores in the brain using magnetic resonance imaging. Magn Reson Imaging 2005;23(1):1-25.

21. Chamberlain R, Reyes D, Curran GL, Marjanska M, Wengenack TM, Poduslo JF, Garwood M, Jack CR, Jr. Comparison of amyloid plaque contrast generated by

T2-weighted, T2*-weighted, and susceptibility-weighted imaging methods in transgenic mouse models of Alzheimer's disease. Magn Reson Med 2009;61(5):1158-1164.

22. Filippi M, Agosta F. Imaging biomarkers in multiple sclerosis. J Magn Reson Imaging 2010;31(4):770-788.

23. Bloch F. Nuclear Induction. Physical Review 1946;70(7-8):460.

24. Lauterbu.Pc. Image Formation by Induced Local Interactions - Examples Employing Nuclear Magnetic-Resonance. Nature 1973;242(5394):190-191.

25. Haacke EM. Magnetic resonance imaging : physical principles and sequence design. New York: Wiley; 1999. xxvii, 914 p. p.

26. Koenig SH, Brown RD, 3rd, Ugolini R. A unified view of relaxation in protein solutions and tissue, including hydration and magnetization transfer. Magn Reson Med 1993;29(1):77-83.

27. Hills BP, Takacs SF, Belton PS. The Effects of Proteins on the Proton Nmr Transverse Relaxation-Times of Water .1. Native Bovine Serum-Albumin. Mol Phys 1989;67(4):903-918.

28. Torrey HC. Transient Nutations in Nuclear Magnetic Resonance. Physical Review 1949;76(8):1059.

29. Redfield AG. Nuclear Magnetic Resonance Saturation and Rotary Saturation in Solids. Physical Review 1955;98(6):1787.

30. Lee M, Goldburg WI. Nuclear-Magnetic-Resonance Line Narrowing by a Rotating Rf Field. Physical Review 1965;140(4A):1261–1271.

31. Hills BP. The Proton-Exchange Cross-Relaxation Model of Water Relaxation in Biopolymer Systems .2. The Sol and Gel States of Gelatin. Mol Phys 1992;76(3):509-523.

32. Hills B. Magnetic resonance imaging in food science. New York: Wiley; 1998.

33. Trott O, Palmer AG. Theoretical study of R-1p rotating-frame and R-2 free-precession relaxation in the presence of n-site chemical exchange. J Magn Reson 2004;170(1):104-112.

34. Gore JC, Brown MS, Zhong J, Mueller KF, Good W. NMR relaxation of water in hydrogel polymers: a model for tissue. Magn Reson Med 1989;9(3):325-332.

35. Zhou JY, Payen JF, Wilson DA, Traystman RJ, van Zijl PCM. Using the amide proton signals of intracellular proteins and peptides to detect pH effects in MRI. Nat Med 2003;9(8):1085-1090.

36. Halle B. The physical basis of model-free analysis of NMR relaxation data from proteins and complex fluids. J Chem Phys 2009;131(22):224507.

37. Slichter CP. Principles of magnetic resonance. Berlin ; New York: Springer; 1996. xi, 655 p. p.

38. Bloembergen N, Purcell EM, Pound RV. Relaxation Effects in Nuclear Magnetic Resonance Absorption. Physical Review 1948;73(7):679.

39. Englander SW, Downer NW, Teitelbaum H. Hydrogen exchange. Annu Rev Biochem 1972;41:903-924.

40. McConnell HM. Reaction Rates by Nuclear Magnetic Resonance. The Journal of Chemical Physics 1958;28(3):430-431.

41. Knispel RR, Pintar MM. Temperature dependence of the proton exchange time in pure water by NMR. Chemical Physics Letters 1975;32(2):238-240.

42. Krasnosselskaia LV, Fullerton GD, Dodd SJ, Cameron IL. Water in tendon: orientational analysis of the free induction decay. Magn Reson Med 2005;54(2):280-288.

43. Akella SV, Regatte RR, Wheaton AJ, Borthakur A, Reddy R. Reduction of residual dipolar interaction in cartilage by spin-lock technique. Magn Reson Med 2004;52(5):1103-1109.

44. Hills BP. The Proton-Exchange Cross-Relaxation Model of Water Relaxation in Biopolymer Systems. Mol Phys 1992;76(3):489-508.

45. Carver JP, Richards RE. General 2-Site Solution for Chemical Exchange Produced Dependence of T2 Upon Carr-Purcell Pulse Separation. J Magn Reson 1972;6(1):89-&.

46. Rabi II, Ramsey NF, Schwinger J. Use of Rotating Coordinates in Magnetic Resonance Problems. Reviews of Modern Physics 1954;26(2):167.

47. Woessner DE, Zhang S, Merritt ME, Sherry AD. Numerical solution of the Bloch equations provides insights into the optimum design of PARACEST agents for MRI. Magn Reson Med 2005;53(4):790-799.

48. Chen EL, Kim RJ. Magnetic Resonance Water Proton Relaxation in Protein Solutions and Tissue: T-1p Dispersion Characterization. Plos One 2010;5(1).

49. Hills BP, Wright KM, Belton PS. Nmr-Studies of Water Proton Relaxation in Sephadex Bead Suspensions. Mol Phys 1989;67(1):193-208.

50. Hills BP, Takacs SF, Belton PS. The Effects of Proteins on the Proton Nmr Transverse Relaxation-Time of Water .2. Protein Aggregation. Mol Phys 1989;67(4):919-937.

51. Faber C, Zahneisen B, Tippmann F, Schroeder A, Fahrenholz F. Gradient-echo and CRAZED imaging for minute detection of Alzheimer plaques in an APPV717I x ADAM10-dn mouse model. Magn Reson Med 2007;57(4):696-703.

52. Haacke EM, Ayaz M, Khan A, Manova ES, Krishnamurthy B, Gollapalli L, Ciulla C, Kim I, Petersen F, Kirsch W. Establishing a baseline phase behavior in magnetic resonance imaging to determine normal vs. abnormal iron content in the brain. J Magn Reson Imaging 2007;26(2):256-264.

53. Shapiro EM, Skrtic S, Sharer K, Hill JM, Dunbar CE, Koretsky AP. MRI detection of single particles for cellular imaging. Proc Natl Acad Sci U S A 2004;101(30):10901-10906.

54. Beall PT, Amtey SR, Kasturi SR. NMR data handbook for biomedical applications. New York: Pergamon Press; 1984. xviii, 198 p. p.

55. Kennan RP, Zhong J, Gore JC. Intravascular susceptibility contrast mechanisms in tissues. Magn Reson Med 1994;31(1):9-21.

56. Majumdar S, Zoghbi S, Pope CF, Gore JC. Quantitation of MR relaxation effects of iron oxide particles in liver and spleen. Radiology 1988;169(3):653-658.

57. Kennan RP, Zhong J, Gore JC. On the relative importance of paramagnetic relaxation and diffusion-mediated susceptibility losses in tissues. Magn Reson Med 1991;22(2):197-203; discussion 213-195.

58. Anderson PW, Weiss PR. Exchange Narrowing in Paramagnetic Resonance. Reviews of Modern Physics 1953;25(1):269.

59. Glasel JA, Lee KH. Interpretation of Water Nuclear Magnetic-Resonance Relaxation-Times in Heterogeneous Systems. J Am Chem Soc 1974;96(4):970-978.

60. Wolff SD, Balaban RS. Magnetization transfer contrast (MTC) and tissue water proton relaxation in vivo. Magn Reson Med 1989;10(1):135-144.

61. Zhou JY, van Zijl PCM. Chemical exchange saturation transfer imaging and spectroscopy. Prog Nucl Mag Res Sp 2006;48(2-3):109-136.

62. van Zijl PCM, Yadav NN. Chemical exchange saturation transfer (CEST): What is in a name and what isn't? Magnet Reson Med 2011;65(4):927-948.

63. Kennan RP, Richardson KA, Zhong JH, Maryanski MJ, Gore JC. The effects of cross-link density and chemical exchange on magnetization transfer in polyacrylamide gels. J Magn Reson Ser B 1996;110(3):267-277.

64. Wüthrich K. NMR of proteins and nucleic acids. New York: Wiley; 1986. xv, 292 p.

65. Molday RS, Englande.Sw, Kallenrg. Primary Structure Effects on Peptide Group Hydrogen-Exchange. Biochemistry-Us 1972;11(2):150-&.

66. Bai YW, Milne JS, Mayne L, Englander SW. Primary Structure Effects on Peptide Group Hydrogen-Exchange. Proteins 1993;17(1):75-86.

67. Twyman RM, Wisden W. Advanced molecular biology : a concise reference. Oxford, UK. New York, NY: Bios Scientific Publishers. Springer; 1999. xi, 499.

68. Gilad AA, McMahon MT, Walczak P, Winnard PT, Jr., Raman V, van Laarhoven HW, Skoglund CM, Bulte JW, van Zijl PC. Artificial reporter gene providing MRI contrast based on proton exchange. Nat Biotechnol 2007;25(2):217-219.

69. McMahon MT, Gilad AA, DeLiso MA, Berman SM, Bulte JW, van Zijl PC. New "multicolor" polypeptide diamagnetic chemical exchange saturation transfer (DIACEST) contrast agents for MRI. Magn Reson Med 2008;60(4):803-812.

70. Chen W, Avison MJ, Bloch G, Shulman RG. Proton NMR observation of glycogen in vivo. Magn Reson Med 1994;31(5):576-579.

71. van Zijl PCM, Jones CK, Ren J, Malloy CR, Sherry AD. MR1 detection of glycogen in vivo by using chemical exchange saturation transfer imaging (glycoCEST). P Natl Acad Sci USA 2007;104(11):4359-4364.

72. Gruetter R, Prolla TA, Shulman RG. 13C NMR visibility of rabbit muscle glycogen in vivo. Magn Reson Med 1991;20(2):327-332.

73. Gore JC, Brown MS, Mizumoto CT, Armitage IM. Influence of glycogen on water proton relaxation times. Magn Reson Med 1986;3(3):463-466.

74. Ling W, Regatte RR, Navon G, Jerschow A. Assessment of glycosaminoglycan concentration in vivo by chemical exchange-dependent saturation transfer (gagCEST). Proc Natl Acad Sci U S A 2008;105(7):2266-2270.

75. Aime S, Calabi L, Biondi L, De Miranda M, Ghelli S, Paleari L, Rebaudengo C, Terreno E. Iopamidol: Exploring the potential use of a well-established x-ray contrast agent for MRI. Magn Reson Med 2005;53(4):830-834.

76. Fullerton GD, Rahal A. Collagen structure: the molecular source of the tendon magic angle effect. J Magn Reson Imaging 2007;25(2):345-361.

77. Burstein D, Bashir A, Gray ML. MRI techniques in early stages of cartilage disease. Invest Radiol 2000;35(10):622-638.

78. Regatte RR, Akella SV, Wheaton AJ, Lech G, Borthakur A, Kneeland JB, Reddy R. 3D-T1rho-relaxation mapping of articular cartilage: in vivo assessment of early degenerative changes in symptomatic osteoarthritic subjects. Acad Radiol 2004;11(7):741-749.

79. Shapiro EM, Borthakur A, Kaufman JH, Leigh JS, Reddy R. Water distribution patterns inside bovine articular cartilage as visualized by 1H magnetic resonance imaging. Osteoarthritis Cartilage 2001;9(6):533-538.

80. Carney SL, Muir H. The structure and function of cartilage proteoglycans. Physiol Rev 1988;68(3):858-910.

81. Gray ML, Burstein D, Kim YJ, Maroudas A. 2007 Elizabeth Winston Lanier Award Winner. Magnetic resonance imaging of cartilage glycosaminoglycan: basic principles, imaging technique, and clinical applications. J Orthop Res 2008;26(3):281-291.

82. Frank EH, Grodzinsky AJ. Cartilage electromechanics--I. Electrokinetic transduction and the effects of electrolyte pH and ionic strength. J Biomech 1987;20(6):615-627.

83. Frank EH, Grodzinsky AJ, Koob TJ, Eyre DR. Streaming potentials: a sensitive index of enzymatic degradation in articular cartilage. J Orthop Res 1987;5(4):497-508.

84. Eisenberg SR, Grodzinsky AJ. Swelling of articular cartilage and other connective tissues: electromechanochemical forces. J Orthop Res 1985;3(2):148-159.

85. Baldassarri M, Goodwin JS, Farley ML, Bierbaum BE, Goldring SR, Goldring MB, Burstein D, Gray ML. Relationship between cartilage stiffness and dGEMRIC index: correlation and prediction. J Orthop Res 2007;25(7):904-912.

86. Dugar A, Farley ML, Wang AL, Goldring MB, Goldring SR, Swaim BH, Bierbaum BE, Burstein D, Gray ML. The effect of paraformaldehyde fixation on the Delayed Gadolinium-Enhanced MRI of Cartilage (dGEMRIC) measurement. J Orthop Res 2008.

87. Nieminen MT, Menezes NM, Williams A, Burstein D. T2 of articular cartilage in the presence of Gd-DTPA2. Magn Reson Med 2004;51(6):1147-1152.

88. Huber M, Trattnig S, Lintner F. Anatomy, biochemistry, and physiology of articular cartilage. Invest Radiol 2000;35(10):573-580.

89. Eckstein F, Sittek H, Gavazzeni A, Schulte E, Milz S, Kiefer B, Reiser M, Putz R. Magnetic resonance chondro-crassometry (MR CCM): a method for accurate determination of articular cartilage thickness? Magn Reson Med 1996;35(1):89-96.

90. Sittek H, Eckstein F, Gavazzeni A, Milz S, Kiefer B, Schulte E, Reiser M. Assessment of normal patellar cartilage volume and thickness using MRI: an analysis of currently available pulse sequences. Skeletal Radiol 1996;25(1):55-62.

91. Xia Y, Moody JB, Alhadlaq H, Hu J. Imaging the physical and morphological properties of a multi-zone young articular cartilage at microscopic resolution. J Magn Reson Imaging 2003;17(3):365-374.

92. Regatte RR, Akella SV, Lonner JH, Kneeland JB, Reddy R. T1rho relaxation mapping in human osteoarthritis (OA) cartilage: comparison of T1rho with T2. J Magn Reson Imaging 2006;23(4):547-553.

93. Regatte RR, Akella SV, Reddy R. Depth-dependent proton magnetization transfer in articular cartilage. J Magn Reson Imaging 2005;22(2):318-323.

94. Menezes NM, Gray ML, Hartke JR, Burstein D. T2 and T1rho MRI in articular cartilage systems. Magn Reson Med 2004;51(3):503-509.

95. Jaramillo D, Connolly SA, Mulkern RV, Shapiro F. Developing epiphysis: MR imaging characteristics and histologic correlation in the newborn lamb. Radiology 1998;207(3):637-645.

96. Jaramillo D, Villegas-Medina OL, Doty DK, Rivas R, Strife K, Dwek JR, Mulkern RV, Shapiro F. Age-related vascular changes in the epiphysis, physis, and metaphysis: normal findings on gadolinium-enhanced MRI of piglets. AJR Am J Roentgenol 2004;182(2):353-360.

97. Rivas R, Shapiro F. Structural stages in the development of the long bones and epiphyses: a study in the New Zealand white rabbit. J Bone Joint Surg Am 2002;84-A(1):85-100.

98. Aronen HJ, Ramadan UA, Peltonen TK, Markkola AT, Tanttu JI, Jaaskelainen J, Hakkinen AM, Sepponen R. 3D spin-lock imaging of human gliomas. Magn Reson Imaging 1999;17(7):1001-1010.

99. Sepponen RE, Pohjonen JA, Sipponen JT, Tanttu JI. A method for T1 rho imaging. J Comput Assist Tomogr 1985;9(6):1007-1011.

100. Witschey WR, 2nd, Borthakur A, Elliott MA, Mellon E, Niyogi S, Wallman DJ, Wang C, Reddy R. Artifacts in T1 rho-weighted imaging: compensation for B(1) and B(0) field imperfections. J Magn Reson 2007;186(1):75-85.

101. Taheri S, Sood R. Spin-lock MRI with amplitude- and phase-modulated adiabatic waveforms: an MR simulation study. Magn Reson Imaging 2006;24(1):51-59.

102. Michaeli S, Sorce DJ, Springer CS, Jr., Ugurbil K, Garwood M. T1rho MRI contrast in the human brain: modulation of the longitudinal rotating frame relaxation shutter-speed during an adiabatic RF pulse. J Magn Reson 2006;181(1):135-147.

103. Borthakur A, Charagundla SR, Wheaton A, Reddy R. T1rho-weighted MRI using a surface coil to transmit spin-lock pulses. J Magn Reson 2004;167(2):306-316.

104. Martirosian P, Rommel E, Schick F, Deimling M. Control of susceptibility-related image contrast by spin-lock techniques. Magnetic Resonance Imaging 2008;26(10):1381-1387.

105. Solomon I. Rotary Spin Echoes. Phys Rev Lett 1959;2(7):301.

106. Zeng H. A composite spin-lock pulse for delta B0 and B1 insensitive T1rho measurements. Proc ISMRM Annual Meeting, Seatte, WA 2006.

107. Borthakur A, Mellon E, Niyogi S, Witschey W, Kneeland JB, Reddy R. Sodium and T1rho MRI for molecular and diagnostic imaging of articular cartilage. NMR Biomed 2006;19(7):781-821.

108. Sled JG, Pike GB. Quantitative imaging of magnetization transfer exchange and relaxation properties in vivo using MRI. Magnet Reson Med 2001;46(5):923-931.

109. Balaban RS, Ceckler TL. Magnetization transfer contrast in magnetic resonance imaging. Magn Reson Q 1992;8(2):116-137.

110. Henkelman RM, Stanisz GJ, Graham SJ. Magnetization transfer in MRI: a review. NMR Biomed 2001;14(2):57-64.

111. Gochberg DF, Gore JC. Quantitative magnetization transfer imaging via selective inversion recovery with short repetition times. Magn Reson Med 2007;57(2):437-441.

112. Sun PZ, van Zijl PC, Zhou J. Optimization of the irradiation power in chemical exchange dependent saturation transfer experiments. J Magn Reson 2005;175(2):193-200.

113. Tynninen O, Aronen HJ, Ruhala M, Paetau A, Von Boguslawski K, Salonen O, Jaaskelainen J, Paavonen T. MRI enhancement and microvascular density in gliomas. Correlation with tumor cell proliferation. Invest Radiol 1999;34(6):427-434.

114. Wheaton AJ, Borthakur A, Corbo M, Charagundla SR, Reddy R. Method for reduced SAR T1rho-weighted MRI. Magn Reson Med 2004;51(6):1096-1102.

115. Pakin SK, Xu J, Schweitzer ME, Regatte RR. Rapid 3D-T1rho mapping of the knee joint at 3.0T with parallel imaging. Magn Reson Med 2006;56(3):563-571.

116. Jin T, Autio J, Obata T, Kim SG. Spin-locking versus chemical exchange saturation transfer MRI for investigating chemical exchange process between water and labile metabolite protons. Magn Reson Med 2010.

117. Zhang H, Xie Y. Dynamics of paramagnetic agents by off-resonance rotating frame technique in the presence of magnetization transfer effect. J Magn Reson 2007;184(2):275-291.

118. Zhang H, Xie Y. Dynamics of paramagnetic agents by off-resonance rotating frame technique. J Magn Reson 2006;183(2):213-227.

119. Zhang H, Xie Y. Efficiency of paramagnetic relaxation enhancement in off-resonance rotating frame. J Magn Reson 2006;181(2):212-222.

120. Zhang H, Xie Y, Ji T. Water diffusion-exchange effect on the paramagnetic relaxation enhancement in off-resonance rotating frame. J Magn Reson 2007;186(2):259-272.

CHAPTER II

$T_{1\rho}$ MAPPING OF PEDIATRIC EPIPHYSEAL AND ARTICULAR CARTILAGE IN THE KNEE

ABSTRACT

Purpose

Adult articular cartilage has been widely studied with spin locking techniques by magnetic resonance imaging. However, no results are available for *in vivo* $T_{1\rho}$ imaging of developing cartilage. This study evaluates the feasibility of measuring $T_{1\rho}$ values in epiphyseal cartilage in children.

Materials and Methods

Ten volunteers of age 6 ± 3 years were recruited to have $T_{1\rho}$ mapping performed on the knee at the conclusion of their clinical study.

$T_{1\rho}$ maps were generated using a spin-lock cluster followed by a fast spin-echo imaging sequence. Regions of interest (ROI) were placed in non-load-bearing (NLB), load-bearing (LB), and articular cartilage.

Results

Student's t-tests were performed to compare means among the ROI. Mean $T_{1\rho}$ for epiphyseal and articular cartilage was 49.8 ± 9 and 76.6 ± 7 ms respectively. LB and NLB $T_{1\rho}$ vales were 47.1 ± 9.5 and 52.5 ± 9 ms respectively. Significant differences were found within subjects among all cartilage types compared ($p < 0.02$).

Conclusion

It is feasible to quantify differences in LB and NLB epiphyseal cartilage, and to differentiate epiphyseal and articular cartilage with SL techniques within a subject. $T_{1\rho}$ holds promise as a non-invasive method of studying normal and abnormal developmental states of cartilage in children.

Key Words: cartilage, $T_{1\rho}$, spin lock, 3T

INTRODUCTION

Magnetic resonance (MR) imaging is a uniquely powerful tool for investigating the structure and composition of the growing skeleton. MR imaging does not use ionizing radiation so it can safely be used to study the growth and development of structures such as epiphyseal and articular cartilage in children. Such studies may provide a greater understanding and early detection of perturbations in normal cartilaginous development that may leave permanent sequelae in the skeletally mature patient.

Cartilage undergoes dramatic changes during the first ten years of life but is more difficult to image than other tissues because it is present only in relatively thin layers, has relatively high density, and features a varied composition. Articular cartilage is composed of a semi-solid matrix of water (65-80%), collagen (15-20%), proteoglycan (~5%), and other proteins (~2%)(1). Proteoglycan (PG) content is of particular interest because of its role in epiphyseal and articular cartilage structure and development. A subset of PGs, glycosaminoglycans (GAGs), are highly negatively charged macromolecules that make up a large percentage of cartilage PG content and contain a high concentration of sulfate groups that strongly bind to water molecules (2). This binding affinity helps to support collagen's triple-helical fiber structure which serves a variety of biomechanical functions *in vivo,* including shock absorption, flexibility, and smoothing of joint motions (3).

Epiphyseal cartilage is found at the ends of long bones between the joint and the primary growth plate in children. The epiphysis is initially completely comprised of cartilage with a high concentration of GAG, but ossifies during development (4,5). By late adolescence, the epiphysis is typically completely ossified. During ossification GAG macromolecules

degrade and the chondrocytes scattered in the epiphysis hypertrophy, reducing the amount of bound water. This transformation gives rise to higher signal on T_2-weighted images (6).

There has been much recent interest in developing new imaging methods to identify the disease state of tissues with large quantities of exchanging protons and to relate them to quantitative relaxation parameters. Proton exchange between water and labile groups in other molecules provides one such potential mechanism that introduces sensitivity for specific chemical components within a mixture. This may be particularly useful for substances such as GAG, which contain a large concentration of chemically exchanging hydroxyl groups. While methods that monitor magnetization transfer such as chemical exchange saturation transfer (CEST) provide direct measurement of exchange(7); other approaches, notably T_2 and $T_{1\rho}$ sequences are also affected by exchange on appropriate time scales and register as large dispersions in signal contrast (8). Measurements of relaxation time constants in the rotating frame ($T_{1\rho}$ and $T_{2\rho}$) using spin-locking techniques have been shown to be sensitive to molecular motions and chemical exchange on the time scale of the locking field (γB_1) (9,10). The advantage of the $T_{1\rho}$ technique lies in the ability to make dispersion measurements in an imaging context in a regime where other approaches, such as CEST or CPMG, may be technically difficult. For example, it is technically much easier to achieve high locking field strength (> 1 kHz) than to use comparable CPMG pulse spacing, making spin locking more appropriate for use in an imaging context. Spin locking techniques typically involve the application of a long, low power B_1 pre-pulse before an imaging sequence to impart $T_{1\rho}$ contrast. The first experiments measuring relaxation in the rotating frame are attributed to Redfield[7], and

Lee and Goldburg (11,12). These types of measurements can, in principle, yield insights into the time scale of molecular motions, the sizes of different pools of protons, chemical and diffusive exchange processes, protein sizes and concentrations, and other attributes of interest (10,13-15). $T_{1\rho}$ contrast has previously been investigated in tissues such as cartilage, brain, breast, and muscle (16-19). However, there is little consensus on the relative contribution of chemical exchange and other changes in tissue composition and their interactions with water on quantitative measures of $T_{1\rho}$.

Articular cartilage has been studied *in vivo* with MRI using a variety of 2D and 3D methods, and articular cartilage degradation in adults has recently been assessed with $T_{1\rho}$-weighted imaging (18,20-23). These studies report that early osteoarthritis (OA) changes are associated with the loss of PG and collagen, although early state molecular degradation is not typically seen on standard MRI using spin-echo and gradient recalled echo imaging sequences. T_2 and $T_{1\rho}$ maps of articular cartilage have been made by several researchers while attempting to correlate proteoglycan degradation in OA to changes in $T_{1\rho}$ values(21,24). A competing technique, Gadolinium-enhanced magnetic resonance imaging of cartilage (dGEMRIC), is quantitatively sensitive to PG loss, but requires the use of an intravenous contrast agent (25). It would therefore be preferable, especially for children, to use an endogenous source of contrast such as the chemical exchange effects of labile protons on GAG. A variety of imaging studies have been performed to measure cartilage structural changes during the maturation process (4,26,27), but to date no applications of spin-lock techniques have been reported in children to quantify these effects *in vivo*. Thus the purpose of this study is to determine the feasibility of $T_{1\rho}$ mapping of pediatric epiphyseal and articular cartilage.

MATERIALS AND METHODS

A total of 13 patient-volunteers were recruited to have $T_{1\rho}$ mapping performed at the conclusion of their clinically indicated MRI studies. Out of this pool of volunteers, ten subjects of age 6 ± 3 years (5 male, 5 female) were included in our study as their epiphyseal and articular cartilage appeared normal based on conventional anatomic MRI sequences that were performed prior to $T_{1\rho}$ mapping.

All study patients underwent safety screening and their guardians provided written informed consent in compliance with the Institutional Review Board. Subjects were imaged using a 3.0T MR scanner with an 8-channel knee coil (Philips Achieva 3T, Philips Healthcare). The structures imaged included the lateral condyle of the knee in a sagittal orientation, and the patella and trochlea in an axial orientation. For each orientation, a single-slice exam of one epiphysis was performed for $T_{1\rho}$ quantification to optimize image quality and speed as some patients were imaged under sedation. For example, though the knee contains three epiphyses (distal femur, proximal tibia, and proximal fibula), $T_{1\rho}$ imaging and quantification was performed only for the distal femur.

First, a clinical 3D T_2-weighted turbo spin-echo (TSE) sequence was used for planning purposes. A position was then identified in either a sagittal or axial orientation to maximize the cross-sectional area of articular and epiphyseal cartilage. For the distal femur, regions of interest (ROI) were placed in non-load-bearing (NLB) and load-bearing (LB) areas of epiphyseal cartilage and also in articular cartilage (Figure 1.a.). For the patella and trochlea, ROI were placed in epiphyseal and articular cartilage (Figure 2.a).

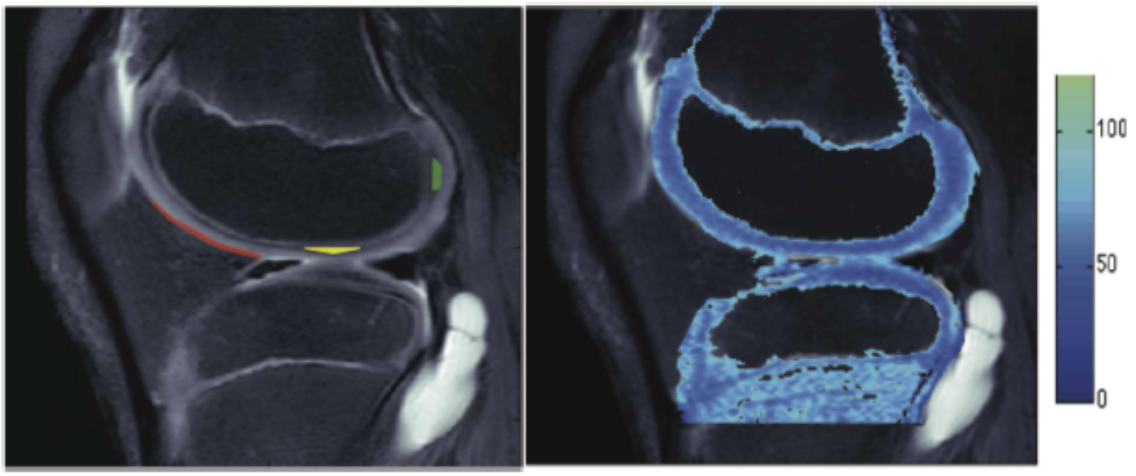

Figure 1: a. A T2-weighted Turbo Spin Echo (TSE) sagittal scan of the knee used to plan ROI for the $T_{1\rho}$ map shown in Fig. 1.b. The red ROI is articular cartilage, the yellow ROI is LB epiphyseal cartilage, and the green ROI is NLB epiphyseal cartilage.

b. $T_{1\rho}$ map of the same subject as shown in Fig. 1.a. A maximum threshold of 120 msec was applied to the $T_{1\rho}$ map, and the soft tissue and patellar regions were removed for clarity. The color scale is given in msec. Note approximately a 25 msec difference in articular and epiphyseal cartilage $T_{1\rho}$ values.

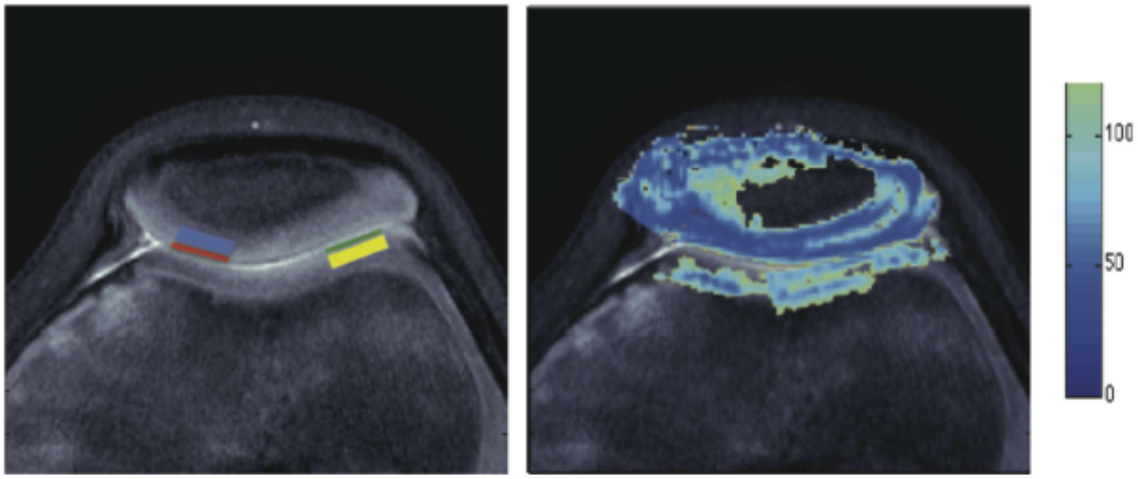

Figure 2.a. T2-weighted Turbo Spin Echo (TSE) axial scan of the trochlea and patella used to plan ROI for the $T_{1\rho}$ map in Figure 2.b. The red ROI is the patellar articular cartilage, the blue ROI is the patellar epiphyseal cartilage, the green ROI is the trochlear articular cartilage, and the yellow ROI is the trochlear

epiphyseal cartilage. Uniform $T_{1\rho}$ maps were more difficult to achieve in this orientation as evidenced by the low signal intensity in the lateral trochea. This region was avoided when placing ROI.

b. $T_{1\rho}$ map of the same subject as shown in Fig. 2.b. A maximum threshold of 120 msec was applied to the $T_{1\rho}$ map, and the soft tissue regions were removed for clarity. The color scale is also given in msec. Note approximately a 25 msec difference in articular and epiphyseal cartilage $T_{1\rho}$ values.

$T_{1\rho}$ contrast was generated using a SL pre-pulse cluster developed by Zeng et al. (28) shown in Figure 3. First, a 500 μs 90-degree hard pulse was applied about the x-axis. This was followed by half of the spin-lock pulse with a SLA of 500Hz along the y-axis. A one millisecond 180 degree hard pulse was then inserted to compensate for B_0 and B_1 inhomogeneities, followed by the second half of the spin-lock pulse with phase reversed (-y). From there, another 90-degree hard pulse returned the $T_{1\rho}$-prepped signal to the longitudinal axis, and the residual transverse magnetization was spoiled. A standard 2D TSE was then used for imaging. TSE parameters included: acquired matrix = 160 x 256, field of view = 100 x 120 mm, slice thickness = 4 mm, echo-train length = 6, TE = 10 ms, TR = 4000 ms, pixel bandwidth = ~155Hz. Spin-lock times of 20, 40, 60, and 80 ms were acquired using the same transmitter and receiver gains among acquisitions.

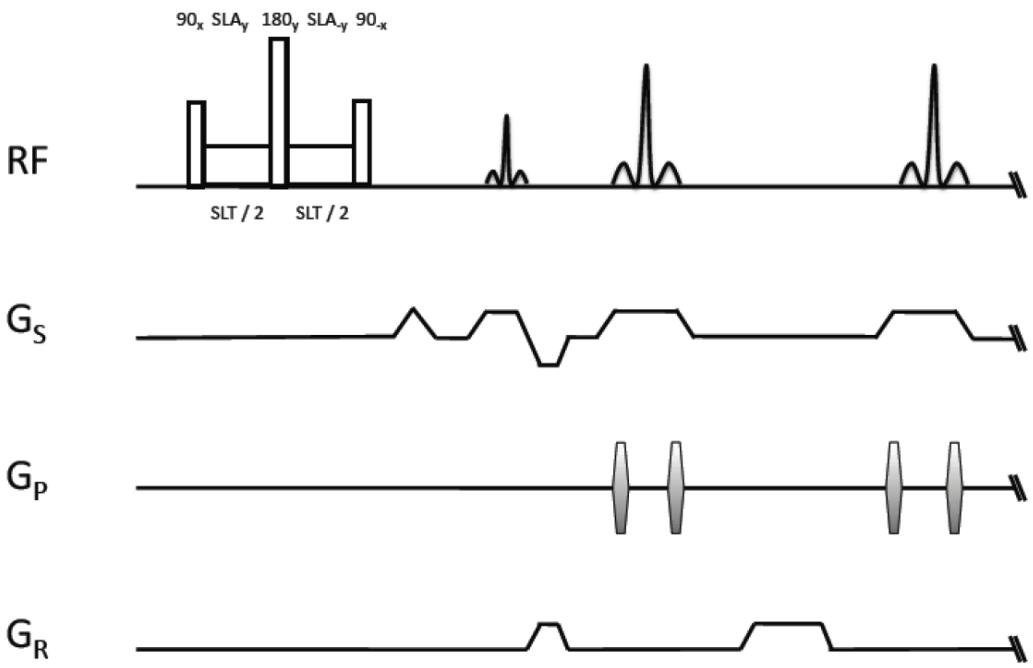

Figure 3: Pulse sequence used to record $T_{1\rho}$-weighted fast spin-echo images.

Each $T_{1\rho}$-weighted scan took approximately one minute and 20 seconds to complete, for approximately a 5-minute scan time to compute a $T_{1\rho}$ map. $T_{1\rho}$ maps were generated by fitting each pixel of the images in the $T_{1\rho}$–weighted scans to a three-parameter mono-exponential decay function in MATLAB (The MathWorks, Inc., Natick, MA).

A one-way analysis of variance (ANOVA) was performed to determine if a statistically significant difference among the ROI means was present. Student's t-tests were then performed to compare the mean $T_{1\rho}$ values among the different ROI. The Bonferroni post-hoc multiple comparisons procedure was used to ensure an overall p-value significance level of less than 0.05. Statistical calculations were also performed in MATLAB.

RESULTS

A representative sagittal planning scan with ROI and a corresponding map of $T_{1\rho}$ values overlaid on the planning image is given in Figure 1.a and 1.b. A 120 msec maximum threshold was applied to the $T_{1\rho}$ map values and the patella and soft tissue regions were removed for clarity. A representative axial planning scan, with overlaid ROI and matching $T_{1\rho}$ map overlay is shown in Figure 2.a and 2.b. The same threshold value of 120 msec was applied to the $T_{1\rho}$ map values in Fig 2.b and soft tissue regions were again removed. Mean values in the lateral condyle of the femur for articular, load-bearing (LB), and non-load-bearing (NLB) epiphyseal cartilage values are shown in Figure 4.a. LB and NLB epiphyseal cartilage values were averaged to give an overall epiphyseal cartilage value for each subject. For the patella and trochlea, mean values from articular and epiphyseal ROI are shown in Figure 4.b.

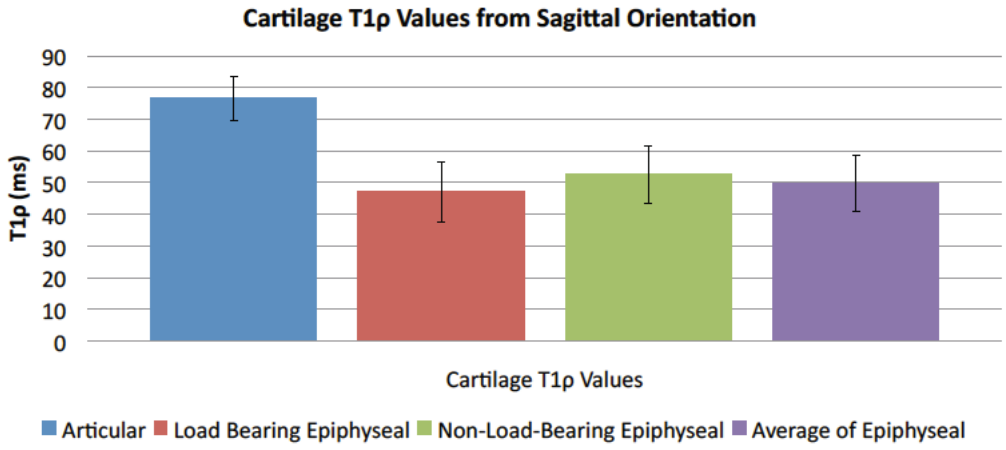

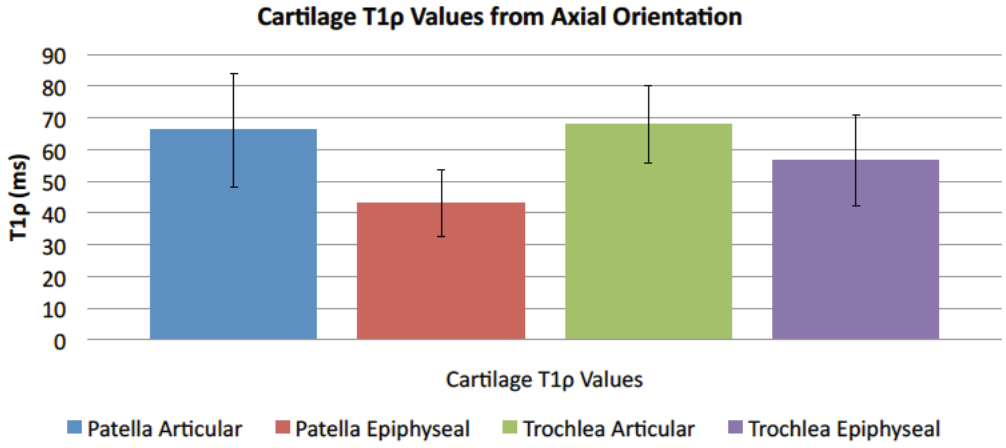

Figure 4: a. Distal Femur Cartilage $T_{1\rho}$ values at 3T (ms ± SD). Articular = 76.6 ± 6.9, Load-Bearing Epiphyseal = 47.1 ± 9.5, Non-Load-Bearing Epiphyseal = 52.5 ± 8.9, Average Epiphyseal = 49.8 ± 9.0.

b. Patella and Trochlear Cartilage $T_{1\rho}$ values at 3T (ms ± SD). Patella Articular = 66.1 ± 17.8, Patella Epiphyseal = 43.0 ± 10.6, Trochlea Articular = 67.9 ± 14.3, Trochlea Epiphyseal = 56.7 ± 12.3.

For each anatomic region, one-way ANOVA was performed across the ROI groups and determined a significant difference between articular and epiphyseal ROI ($p < 0.0001$).

No significant difference between LB and NLB means could be established across subjects ($p = 0.2$). Average $T_{1\rho}$ values for each anatomic region are summarized in Table 1.

Table 1: Average $T_{1\rho}$ values for the lateral condyle, patella, and trochlea in children using a 500Hz SL pulse, measured at 3T. LB = load bearing epiphyseal cartilage, NLB = non-load bearing epiphyseal cartilage.

Anatomical Region		Average ± SD $T_{1\rho}$ value (ms)
Lateral Condyle	Articular	76.6 ± 6.9
	NLB Epiphyseal	52.5 ± 8.9
	LB Epiphyseal	47.1 ± 9.5
	Average Epiphyseal	49.8 ± 9.0
Patella	Articular	66.2 ± 17.8
	Epiphyseal	43.3 ± 10.6
Trochlea	Articular	67.9 ± 14.3
	Epiphyseal	56.7 ± 12.3

Paired Student's t-tests assuming an unequal variance were performed to compare means among the ROI within subjects. For the lateral condyle, significant differences were found between LB epiphyseal and articular, NLB epiphyseal and articular cartilage, and LB and NLB epiphyseal cartilage within subjects. A comparison of the overall epiphyseal cartilage means vs. articular cartilage means also found a significant difference (all p values < 0.02). For the patellar and trochelar regions, a significant difference was found between articular and epiphyseal cartilage ROI ($p = 0.02$). Comparing articular cartilage

values revealed no significant difference in means, as did a comparison between epiphyseal cartilage values.

When comparing $T_{1\rho}$ values with age, no overall trends were noticeable across all ROI and ages. Within each subject, articular values for $T_{1\rho}$ always exceeded epiphyseal cartilage averages. Additionally non-weight-bearing cartilage values were in general greater than weight bearing. However, visual inspection of the ROI plotted against age showed an intriguing bi-phasic trend in $T_{1\rho}$ if the subjects are separated into groups of less than four years of age and greater than four years of age. A linear fit to the young and old articular cartilage values shown in Figure 5 revealed a good fit for the young group ($R^2 = 0.88$), but a less good fit ($R^2 = 0.54$) was obtained from the older group. A linear fit to the young and old epiphyseal cartilage values also displayed a similar trend, with the young epiphyseal cartilage showing better fit ($R^2 = 0.86$) vs. older epiphyseal cartilage ($R^2 = 0.46$).

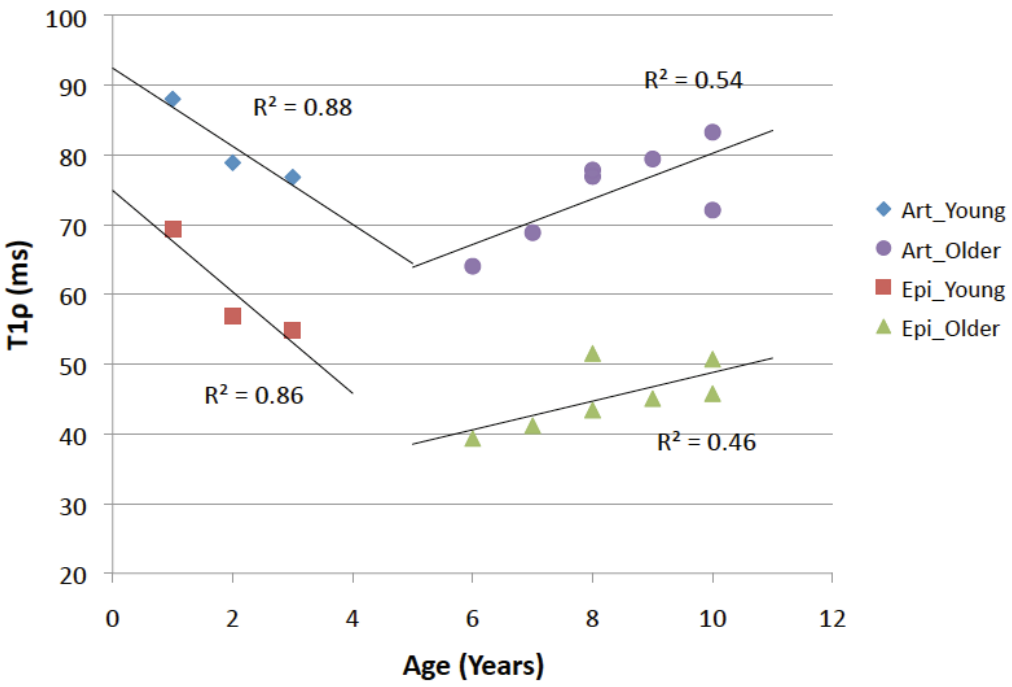

Figure 5: Plot of cartilage $T_{1\rho}$ values vs. age at 3T. Note the modest biphasic trend among the young and old articular cartilage $T_{1\rho}$ values.

DISCUSSION AND CONCLUSIONS

The purpose of this study was to determine the feasibility of measuring $T_{1\rho}$ values in young cartilage and to distinguish between cartilage types in children. The $T_{1\rho}$ measurement technique described here is a feasible method for differentiating epiphyseal and articular cartilage within a subject. Epiphyseal cartilage composition has previously been compared with articular cartilage in T_2-weighted images (26). This study establishes that these differences are also visible and are quantitatively different based on $T_{1\rho}$-weighted images.

Extensive laboratory and clinical research has been performed attempting to validate the utility of $T_{1\rho}$ in assessing articular cartilage and the study of osteoarthritis in adults

(18,20,24,29). To our knowledge, this is the first study that attempts *in vivo* $T_{1\rho}$ imaging of epiphyseal cartilage. Epiphyseal cartilage is an important precursor to epiphyseal ossification; perturbations in its normal development may have profound effects on joint function and may lead to early osteoarthritis. Epiphyseal cartilage composition is uniquely different from articular cartilage in that it has a greater concentration of GAG, is more loosely structured, is infiltrated by vascular channels, and is present in far greater quantities than articular cartilage depending on skeletal maturation (4,5). Cartilage cell hypertrophy and vacuolization occurs during normal epiphyseal skeletal maturation and reflects the dynamic and unique nature of epiphyseal cartilage compared with articular cartilage whose morphology is more static. The limited resolution of the scans and wide range of ages studied precluded systematic evaluation of epiphyseal zonal variation. A larger study with a higher image resolution may be sensitive to these features, and therefore the $T_{1\rho}$ pulse sequence may need to be tailored accordingly to maximize sensitivity to the features of this cartilage type. Despite the small study size and heterogeneous age of patients, epiphyseal cartilage $T_{1\rho}$ values were relatively similar across age ranges.

Artifacts related to B_1 and B_0 inhomogeneity are commonly seen in $T_{1\rho}$-weighted imaging techniques especially at low spin-lock amplitudes (30). The use of a self-compensating SL pulse in this study mitigated these effects so that banding artifacts were relegated to the edges of the field of view. However, self-compensating pulses do not perfectly counteract B_1 and B_0 inhomogeneity as the spins may not be perfectly refocused by the 180-degree pulse or rewound by the phase inversion. Thus B_1 and B_0

inhomogeneity could alter the effective locking field applied across the sample ROI and thus affect the measured $T_{1\rho}$ values.

Alternative methods of quantifying articular cartilage quality by MRI have been studied, including T_2 mapping and dGEMRIC (25,31,32). These methods may be useful for evaluating articular cartilage, but may have limited utility in the evaluation of epiphyseal cartilage. Epiphyseal cartilage uniquely has prominent vascular channels, a property not seen in articular cartilage (4). These channels may falsely indicate a low level of glycosaminoglycans using the dGEMRIC technique with the intravenous administration of Gadolinium, however this effects has yet to be quantitatively established. Quantitative T_2 and measurements will also be affected by the presence of water channels, where changes in water content may be difficult to distinguish from chemical exchange effects from changes in the concentration of GAG. For these reasons, optimizing $T_{1\rho}$ measurement techniques to the study of chemical exchange effects in epiphyseal cartilage may be valuable as a method to monitor variations in tissue composition. At high fields the increased separation of resonance frequencies between water and other chemical species such as hydroxyls on GAG gives rise to greater contributions to $T_{1\rho}$ decay from chemical exchange. These exchange processes are of interest not only for their effects on $T_{1\rho}$ but also on T_2 and as modulators of saturation transfer contrast (CEST) (15,33). There have been few studies undertaken which attempt to quantify these processes or derive parameters that describe them in biological samples, and these findings represent an important first step towards quantification of these processes *in vivo*.

Significant differences in $T_{1\rho}$ values are reported here in load- and non-load-bearing epiphyseal cartilage in the knee. Load-bearing epiphyseal cartilage has relatively lower $T_{1\rho}$ presumably related to relative epiphyseal cartilage desiccation compared with non-load-bearing epiphyseal cartilage (34). This suggests that $T_{1\rho}$ values are affected by free water content and/or by glycosaminoglycan composition changes due to variability between load and non-load bearing sites. $T_{1\rho}$ dispersion measurements, where the measured value of $T_{1\rho}$ varies with locking field, may be required to distinguish between these effects. Appropriate model fitting of $T_{1\rho}$ dispersion curves may be used to distinguish the effects of variations in water content, GAG concentration, pH, or disease state (8,24). However, these quantitative methods are not widely used and have not yet been applied to epiphyseal cartilage *in vivo*.

Presenting normative epiphyseal cartilage $T_{1\rho}$ values based on the stage of epiphyseal cartilage development will be important for comparison to perturbations in $T_{1\rho}$ values induced by pathology. Our findings differed from adult studies of $T_{1\rho}$ values in articular cartilage. The pediatric articular cartilage $T_{1\rho}$ values reported here are somewhat longer than those of healthy adult articular cartilage recently reported as 62 ± 5 ms at 4T (35) and 46 ± 3 ms at 3T (22). However $T_{1\rho}$ relaxation values in developing and mature articular cartilage may not be directly comparable. Numerous studies on developing cartilage illustrate the role of chondrocyte density, vascular canals, and epiphyseal vessels on young cartilage hydration (5,36,37). This is in contrast to mature cartilage, which is typically avascular, and thus subject only to synovial hydration and thus may impart different mechanistic effects on $T_{1\rho}$ and T_2. The large variance in articular cartilage $T_{1\rho}$ values is most likely related to the wide age range in developmental terms

that also is likely reflected in changes in tissue structure and hydration status (5,26). Trends in these tissue changes may be reflected in Figure 5 and is worthy of further study. Additionally, partial volume effects from non-cartilage tissue or epiphyseal cartilage being included in the ROI may have affected the reported $T_{1\rho}$ values. Free water has a long $T_{1\rho}$ value and any contamination of the articular ROI from adjacent joint fluid would lengthen the reported value. Finally, epiphyseal cartilage is also different from articular cartilage in terms of structure and of water content and its inclusion in an ROI would have an effect on the reported values.

In conclusion, $T_{1\rho}$ is a feasible method for quantifying differences in load- and non-load-bearing epiphyseal cartilage, and for differentiating epiphyseal and articular cartilage. $T_{1\rho}$ holds promise as a non-invasive method of studying normal and abnormal developmental states of epiphyseal cartilage.

REFERENCES

1. Shapiro EM, Borthakur A, Kaufman JH, Leigh JS, Reddy R. Water distribution patterns inside bovine articular cartilage as visualized by 1H magnetic resonance imaging. Osteoarthritis Cartilage 2001;9(6):533-538.

2. Carney SL, Muir H. The structure and function of cartilage proteoglycans. Physiol Rev 1988;68(3):858-910.

3. Huber M, Trattnig S, Lintner F. Anatomy, biochemistry, and physiology of articular cartilage. Invest Radiol 2000;35(10):573-580.

4. Jaramillo D, Connolly SA, Mulkern RV, Shapiro F. Developing epiphysis: MR imaging characteristics and histologic correlation in the newborn lamb. Radiology 1998;207(3):637-645.

5. Jaramillo D, Villegas-Medina OL, Doty DK, et al. Age-related vascular changes in the epiphysis, physis, and metaphysis: normal findings on gadolinium-enhanced MRI of piglets. AJR Am J Roentgenol 2004;182(2):353-360.

6. Rivas R, Shapiro F. Structural stages in the development of the long bones and epiphyses: a study in the New Zealand white rabbit. J Bone Joint Surg Am 2002;84-A(1):85-100.

7. Ling W, Regatte RR, Navon G, Jerschow A. Assessment of glycosaminoglycan concentration in vivo by chemical exchange-dependent saturation transfer (gagCEST). Proc Natl Acad Sci U S A 2008;105(7):2266-2270.

8. Duvvuri U, Goldberg AD, Kranz JK, et al. Water magnetic relaxation dispersion in biological systems: the contribution of proton exchange and implications for the noninvasive detection of cartilage degradation. Proc Natl Acad Sci U S A 2001;98(22):12479-12484.

9. Hills BP. The Proton-Exchange Cross-Relaxation Model of Water Relaxation in Biopolymer Systems. Mol Phys 1992;76(3):489-508.

10. Hills BP. The Proton-Exchange Cross-Relaxation Model of Water Relaxation in Biopolymer Systems .2. The Sol and Gel States of Gelatin. Mol Phys 1992;76(3):509-523.

11. Redfield AG. Nuclear Magnetic Resonance Saturation and Rotary Saturation in Solids. Physical Review 1955;98(6):1787.

12. Lee M, Goldburg WI. Nuclear-Magnetic-Resonance Line Narrowing by a Rotating Rf Field. Physical Review 1965;140(4A):1261–1271.

13. Henkelman RM, Huang X, Xiang QS, Stanisz GJ, Swanson SD, Bronskill MJ. Quantitative interpretation of magnetization transfer. Magn Reson Med 1993;29(6):759-766.

14. Koenig SH, Brown RD, 3rd, Ugolini R. A unified view of relaxation in protein solutions and tissue, including hydration and magnetization transfer. Magn Reson Med 1993;29(1):77-83.

15. Gore JC, Brown MS, Zhong J, Mueller KF, Good W. NMR relaxation of water in hydrogel polymers: a model for tissue. Magn Reson Med 1989;9(3):325-332.

16. Santyr GE, Henkelman RM, Bronskill MJ. Spin locking for magnetic resonance imaging with application to human breast. Magn Reson Med 1989;12(1):25-37.

17. Aronen HJ, Ramadan UA, Peltonen TK, et al. 3D spin-lock imaging of human gliomas. Magn Reson Imaging 1999;17(7):1001-1010.

18. Regatte RR, Akella SV, Wheaton AJ, et al. 3D-T1rho-relaxation mapping of articular cartilage: in vivo assessment of early degenerative changes in symptomatic osteoarthritic subjects. Acad Radiol 2004;11(7):741-749.

19. Virta A, Komu M, Lundbom N, Kormano M. T1 rho MR imaging characteristics of human anterior tibial and gastrocnemius muscles. Acad Radiol 1998;5(2):104-110.

20. Akella SV, Regatte RR, Gougoutas AJ, et al. Proteoglycan-induced changes in T1rho-relaxation of articular cartilage at 4T. Magn Reson Med 2001;46(3):419-423.

21. Menezes NM, Gray ML, Hartke JR, Burstein D. T2 and T1rho MRI in articular cartilage systems. Magn Reson Med 2004;51(3):503-509.

22. Li X, Benjamin Ma C, Link TM, et al. In vivo T(1rho) and T(2) mapping of articular cartilage in osteoarthritis of the knee using 3 T MRI. Osteoarthritis Cartilage 2007;15(7):789-797.

23. Souza RB, Stehling C, Wyman BT, et al. The effects of acute loading on T1rho and T2 relaxation times of tibiofemoral articular cartilage. Osteoarthritis Cartilage 2010;18(12):1557-1563.

24. Regatte RR, Akella SV, Borthakur A, Reddy R. Proton spin-lock ratio imaging for quantitation of glycosaminoglycans in articular cartilage. J Magn Reson Imaging 2003;17(1):114-121.

25. Gray ML, Burstein D, Kim YJ, Maroudas A. 2007 Elizabeth Winston Lanier Award Winner. Magnetic resonance imaging of cartilage glycosaminoglycan: basic principles, imaging technique, and clinical applications. J Orthop Res 2008;26(3):281-291.

26. Laor T, Jaramillo D. MR imaging insights into skeletal maturation: what is normal? Radiology 2009;250(1):28-38.

27. Xia Y, Moody JB, Alhadlaq H, Hu J. Imaging the physical and morphological properties of a multi-zone young articular cartilage at microscopic resolution. J Magn Reson Imaging 2003;17(3):365-374.

28. Zeng H. A composite spin-lock pulse for delta B0 and B1 insensitive T1rho measurements. Proceedings of the 14th Annual Meeting of ISMRM, Seattle, WA, USA, 2006 (Abstract 2356) 2006.

29. Burstein D, Bashir A, Gray ML. MRI techniques in early stages of cartilage disease. Invest Radiol 2000;35(10):622-638.

30. Witschey WR, 2nd, Borthakur A, Elliott MA, et al. Artifacts in T1 rho-weighted imaging: compensation for B(1) and B(0) field imperfections. J Magn Reson 2007;186(1):75-85.

31. Trattnig S, Marlovits S, Gebetsroither S, et al. Three-dimensional delayed gadolinium-enhanced MRI of cartilage (dGEMRIC) for in vivo evaluation of reparative cartilage after matrix-associated autologous chondrocyte transplantation at 3.0T: Preliminary results. J Magn Reson Imaging 2007;26(4):974-982.

32. McKenzie CA, Williams A, Prasad PV, Burstein D. Three-dimensional delayed gadolinium-enhanced MRI of cartilage (dGEMRIC) at 1.5T and 3.0T. J Magn Reson Imaging 2006;24(4):928-933.

33. Zhou JY, Payen JF, Wilson DA, Traystman RJ, van Zijl PCM. Using the amide proton signals of intracellular proteins and peptides to detect pH effects in MRI. Nat Med 2003;9(8):1085-1090.

34. Jaramillo D, Connolly SA, Vajapeyam S, et al. Normal and ischemic epiphysis of the femur: diffusion MR imaging study in piglets. Radiology 2003;227(3):825-832.

35. Regatte RR, Akella SV, Lonner JH, Kneeland JB, Reddy R. T1rho relaxation mapping in human osteoarthritis (OA) cartilage: comparison of T1rho with T2. J Magn Reson Imaging 2006;23(4):547-553.

36. Menezes NM, Olear EA, Li X, et al. Gadolinium-enhanced MR images of the growing piglet skeleton: ionic versus nonionic contrast agent. Radiology 2006;239(2):406-414.

37. Menezes NM, Connolly SA, Shapiro F, et al. Early ischemia in growing piglet skeleton: MR diffusion and perfusion imaging. Radiology 2007;242(1):129-136.

CHAPTER III

CONTRIBUTIONS OF CHEMICAL EXCHANGE TO $T_{1\rho}$ DISPERSION IN A TISSUE MODEL

ABSTRACT

Variations in $T_{1\rho}$ with locking-field strength ($T_{1\rho}$ dispersion) may be used to estimate proton exchange rates. We developed a novel approach utilizing the second derivative of the dispersion curve to measure exchange in a model system of cross-linked polyacrylamide gels. These gels were varied in relative composition of co-monomers, increasing stiffness, and in pH, modifying exchange rates.

MR images were recorded with a spin-locking sequence as described by Sepponen et al. These measurements were fit to a mono-exponential decay function yielding values for $T_{1\rho}$ at each locking-field measured. These values were then fit to a model by Chopra et al. for estimating exchange rates.

For low stiffness gels, the calculated exchange values increased by a factor of 4 as pH increased, consistent with chemical exchange being the dominant contributor to $T_{1\rho}$ dispersion. Interestingly, calculated chemical exchange rates also increased with stiffness, likely due to modified side-chain exchange kinetics as the composition varied.

This paper demonstrates a new method to assess the structural and chemical effects on $T_{1\rho}$ relaxation dispersion with a suitable model. These phenomena may be exploited in an imaging context to emphasize the presence of nuclei of specific exchange rates, rather than chemical shifts.

INTRODUCTION

A more complete understanding of proton relaxation processes in heterogeneous tissues would likely assist the interpretation of magnetic resonance images in both clinical and pre-clinical applications, and potentially provide the basis for improved methods of tissue characterization. Quantitative information about proton relaxation dynamics in tissues may be obtained by a variety of magnetic resonance techniques, which provide insights into the manner in which water protons interact with macromolecules. These interactions affect relaxation times and image contrast, and quantitative measurements can in principle yield insights into the time scale of molecular motions, the sizes of different pools of protons, chemical and diffusive exchange processes, protein sizes and concentrations, and other attributes (1-5).

Measurements of relaxation rates in the rotating frame ($R_{1\rho}$ and $R_{2\rho}$) using spin-locking techniques have been shown to be sensitive to molecular motions and interactions on the time scale of the locking field. The variation or dispersion of such measurements with locking-field strength provides information on relatively slow molecular motions and previous studies have shown that the variations in $R_{1\rho}$ with locking field in proteins and tissues may also reflect chemical exchange on an appropriate time-scale (4,6). Cross-

relaxation in the rotating frame may allow exchanging protons to be affected by non-exchanging protons in macromolecules via through space dipolar coupling, when dispersion could reflect motions on the times scale of γB_1. Such effects are reduced when the line-width of the macromolecular protons is much greater than the locking frequency, as is typically the case in tissues, and may be eliminated by locking at the magic angle (4). However, at high fields the increased separation of resonance frequencies between water and other chemical species such as amides gives rise to greater contributions from chemical exchange. These exchange processes are of interest not only for their effects on $R_{1\rho}$ but also on R_2 and as modulators of saturation transfer contrast (CEST) (5,7). There have been few studies undertaken which attempt to quantify these processes or derive parameters that describe them in biological samples. However, appropriate experimental $R_{1\rho}$ data may be analyzed and used to estimate the rate of chemical exchange and other properties of a system in a manner analogous to the measurement of Carr-Purcell-Meiboom-Gill (CPMG) dispersion (8). In CPMG multi-echo measurements, as the pulse rate is increased, dephasing caused by chemical exchange or other process such as diffusion (9) between sites of different resonant frequencies is more effectively refocused, resulting in an increase in measured T_2 ($1/R_2$). Similarly, with spin-locking experiments, only nuclei exchanging slowly with respect to γB_1 will be "locked" and thus not experience dephasing effects. However, it is technically much easier to achieve high locking field strength (> 1 kHz) than to use comparable CPMG pulse spacing, making spin locking more appropriate for use in an imaging context.

Spin-lock contrast ($T_{1\rho}$-weighting) may be imparted to an image by the addition of a spin-lock (SL) "cluster" of pulses before a standard imaging sequence (10,11). A typical cluster consists of a 90-degree pulse that nutates the longitudinal magnetization vector into the transverse plane, followed by a long, pseudo-continuous wave (*cw*) pulse that locks magnetization to the applied B_1 field. Longitudinal magnetization decays along the applied field in the rotating frame with time constant $T_{1\rho}$. After the prescribed spin-lock time (TSL) has elapsed, another 90-degree pulse returns the magnetization vector to alignment to the Z-axis (B_0). The residual transverse magnetization is then spoiled, and an imaging sequence may then be applied to read out the $T_{1\rho}$-weighted magnetization. By measuring for different times of application of the lock $T_{1\rho}$ can be calculated, and by measuring $T_{1\rho}$ at different spin-lock amplitudes, the dispersion of $T_{1\rho}$ with frequency may be obtained (4).

Although the contributions of chemical exchange to relaxation in proteins and sugars have been well studied, there is no consensus on their contribution to the origins of $T_{1\rho}$ dispersion in more complex samples. In modeling exchange effects, there has been little theoretical discussion or experimental evidence of the values of critical model parameters. While chemical exchange may dominate relaxation effects in dilute protein or sugar solutions, it may be quantitatively different in organized, viscous, or dense tissue structures (4). Here we describe a set of measurements on a simple model system designed to demonstrate how quantitative parameters such as chemical exchange rates can be derived from appropriate sets of measurements in the rotating reference frame. We have selected a system of cross linked polyacrylamide gels that can be manipulated to

modify the contributions of chemical exchange and magnetization transfer between amide groups and water on rotating frame relaxation. Using this system, $T_{1\rho}$ dispersion measurements are fit to a theoretical two-pool model of proton exchange to extract chemical exchange rates. We demonstrate the effects of modified chemical exchange rate and polymer cross-link density on rotating frame relaxation rates and illustrate several interesting features of relaxation in the rotating frame that may be useful for understanding proton exchange dynamics in tissues. In addition, we propose a simplified method to estimate a chemical exchange rate that does not rely upon on extensive model fitting and parameter estimation. The advantage of this method lies in the ability to make dispersion measurements in an imaging context under experimental conditions that otherwise may be technically difficult and that has not been previously reported. This method will be briefly evaluated for its potential to quantify the effects of macromolecular organization, composition and pH on exchange contributions to $T_{1\rho}$ with a reduced dataset.

THEORY

$R_{1\rho}$ relaxation in a one-pool model

In a simple one-pool model as described by Hills (9), the rotating frame relaxation rate is governed by the randomly fluctuating local magnetic fields of dipolar interactions among protons. If the time scale of fluctuations is given by correlation time τ_c, $R_{1\rho}$ (= $1/T_{1\rho}$) can be described by:

$$R_{1\rho,dip} = 0.2A\left[3J(\omega_1,\tau_c) + 5J(\omega_0,\tau_c) + 2J(4\omega_0,\tau_c)\right] \qquad [1]$$

where ω_0 is the Larmor frequency, $\omega_1 = \gamma B_1$ is the applied RF field frequency, J describes the spectral density function, $J(n\omega, \tau_c) = \tau_c / (1+n\omega^2\tau_c^2)$, and

$$A = \left(\mu_0 / 4\pi\right)^2 * \left(h / 2\pi\right)^2 * \gamma^4 I\left(I+1\right) / r^6$$

where μ_0 is the permeability of space, γ the gyromagnetic ratio, h is Plank's constant, I is the spin number (1/2) and r is the inter-nuclear distance.

As ω_1 approaches ω_0, $R_{1\rho}$ approaches R_1; as ω_1 approaches 0, $R_{1\rho}$ approaches R_2. $R_{1\rho}$ thus displays frequency dispersion between a maximum value of R_2 and a minimum value of R_1. When $(\omega_1\tau_c)^2 << 1$ and $\omega_1 << \omega_0$,

$$R_{1\rho} = R_1 \cos^2\theta + R_2 \sin^2\theta \qquad [2]$$

where θ is the tilt angle of the effective locking field ($\tan\theta = \omega_1/\Delta$, and Δ = offset from resonance).

$R_{1\rho}$ relaxation in a two-pool model

Eq. 1 is inadequate for describing more complex substances such as polymers and tissues where different proton pools exist and interact. Often the behaviors of polymerized gels and tissues can be approximately described in terms of a two-pool system in which the first pool is a liquid pool of free water (noted as pool "f") and a second pool (noted as

pool "b") that includes non-exchanging protons in the polymer. Clearly more elaborate multi-pool models can be developed, such as the inclusion of an intermediate pool or hydration layer with intermediate characteristics but similar chemical shift. In addition, chemical exchange between water and labile protons in the solute may occur at specific sites such as hydroxyl ($^{-}$OH) and amine (NH^{+}) groups. These solutes resonate at a different frequency from water and thus contribute an additional dephasing term to rotating frame relaxation. For practical locking field strengths on or near resonance

$$R_{1\rho} = R_1 \cos^2\theta + \left(R_2^0 + p_f p_b \Delta\omega_b^2 \frac{r_b}{r_b^2 + \omega_1^2} \right) \sin^2\theta \qquad [3]$$

where p_f and p_b are the relative pool sizes (f = free, b = bound and exchanging proton pool) where $p_f + p_b = 1$, $\Delta\omega_b$ is the frequency difference between the two pools, r_b is the exchange rate, and R_2^0 is the transverse relaxation rate without exchange.

Chopra et al. (12) considered the more general case in which exchanging nuclei experience different relaxation rates as well as chemical shifts when moving between phases, which is more appropriate for biopolymers which exhibit strong dipolar relaxation effects. Chopra et al. modified the Bloch equations and showed how, under specific conditions, an experiment measuring $R_{1\rho}$ at different locking field strengths (γB_1) may be used to determine solvent exchange rate. Over the limited range of locking frequencies usually available in MR imaging systems, there are negligible variations in

the dipolar contributions to longitudinal relaxation, so Chopra's equation may adequately describe rotating frame relaxation in a two-pool system as given in Eq. 4.

$$R_{1\rho} = R_{2f} + p_b r_b \left(R_{2b} \left(R_{2b} + r_b \right)^{-1} \right) \left\{ \frac{\left(R_{1b} + r_b \right) \left(R_{2b} + r_b + \frac{\Delta\omega_b^2}{R_{2b}} \right) + \omega_1^2}{\left(R_{1b} + r_b \right) \left(R_{2b} + r_b + \frac{\Delta\omega_b^2}{R_{2b} + r_b} \right) + \omega_1^2} \right\} \qquad [4]$$

In Eq. 4, R_{2f} is the relaxation rate of free water, p_b is the ratio of exchangeable sites, r_b is the exchange rate from the bound to free water pools, R_{1b} and R_{2b} are the relaxation rates of the bound sites, ω_1 is the spin lock amplitude, and the chemical shift is given as $\Delta\omega_b$.

By substituting expressions for the limits of weak [$R_{1\rho}^0 = R_2$] and strong [$R_{1\rho}^\infty$] locking fields into Eq. 4, the expression for the observed $R_{1\rho}$ reduces to:

$$R_{1\rho} = \left\{ \frac{R_2 + \frac{\left(R_{1\rho}^\infty * \omega_1^2 \right)}{S_\rho^2}}{1 + \frac{\omega_1^2}{S_\rho^2}} \right\} \qquad [5]$$

where $S_\rho^2 = (R_{1b} + r_b) / (R_{2b} + r_b) * \{ (R_{2b} + r_b)^2 + \Delta\omega_b^2 \}$. A non-linear least-squares fit of the variation of $R_{1\rho}$ with ω_1 to Eq. 5 may be used to obtain best fits of R_2, $R_{1\rho}^\infty$, and S_ρ^2.

Thus, a study of $R_{1\rho}$ vs. ω_1 may be used to estimate exchange rates. This approach has been used previously in an effort to quantify proteoglycans in bovine articular cartilage (13).

We propose a simplification of this method that yields similar results under certain experimental conditions, yet requires less data and fewer assumptions regarding exchanging pool relaxation parameters. If the analytic expression in Eq. 5 is twice differentiated with respect to ω_1, the resulting equation is:

$$\frac{d^2 R_{1\rho}(\omega_1)}{d\omega_1^2} = 2S_\rho^2(R_{1\rho}^\infty - R_2)(S_\rho^2 - 3\omega_1^2)(S_\rho^2 + \omega_1^2)^{-3} \qquad [6]$$

This expression is equal to zero at the inflection point of Eq. 5 and corresponds to the minimum of the first derivative and the following condition:

$$0 = S_\rho^2 - 3\omega_1^2 \qquad [7]$$

If S_ρ is simplified as suggested by Chopra et al. with the reasonable assumptions that ($r_b >> R_{1b}$) and ($r_b > R_{2b}$) given narrow lines in exchange, S_ρ may be simplified to:

$$S_\rho^2 = r_b^2 + \Delta\omega_b^2 \qquad [8]$$

If Eq. 8 is substituted into Eq. 7, the resulting expression may be rearranged to:

$$r_b = \sqrt{3\omega_1^2 - \Delta\omega_b^2} \qquad [9]$$

Thus an exchange rate estimate may be simply made with knowledge of the chemical shift of the exchanging species and the rate of variation of $R_{1\rho}$ with ω_1.

Procedurally, for a two-pool system, if the second derivative is calculated after finding each successive $T_{1\rho}$ value in a dispersion curve, the experiment may be stopped when the value of the second derivative crosses zero going from a negative to a positive value. This corresponds to the inflection point of the dispersion curve where, for a continuous function, the shape changes from concave downward to concave upwards. Then, the locking-field frequency where this event occurs and the chemical shift derived from prior knowledge, ^{1}H spectra, or CEST data can be substituted into Eq. 9 to estimate the exchange rate. This obviates the need for fitting an entire dispersion data set, and allows for estimating exchange rates in a number of useful situations. We developed a computer simulation and performed experiments to evaluate the conditions where this approach may be adapted.

METHODS

Rotating-Frame Relaxation Simulations

In order to test this model and assess the robustness of fitting experimental data, $R_{1\rho}$ relaxation measurements from a simple two-pool system were simulated using modified Bloch equations in a manner described by Hills (14). Zero-mean, Gaussian white noise

was added to the simulated relaxation data, and the noisy data were subsequently fit to Eq. 5 using a Levenberg-Marquardt based non-linear least squares fitting algorithm implemented in MATLAB (R2008a, MATLAB, Natick, MA). Exchange rates (r_b) of 500 Hz to 20 kHz were simulated for a two-pool system with these characteristics: $T_{1f} = T_{2f} =$ 3 sec, $T_{1b} = T_{2b} = 10$ msec, $p_f = 0.99$, $p_b = 0.01$, $\Delta\omega_b = 2$ ppm, $\omega_0 = 2\pi*400$ MHz. The locking field (ω_1) was simulated over a range of amplitudes easily achievable experimentally, from $2\pi*$[250 Hz to 8 kHz].

Experimental Studies

Magnetic Resonance Imaging (MRI) studies were performed on a series of cross-linked polyacrylamide gels composed of acrylamide (AC) and N,N'-methylene-bis-acrylamide (BIS). These were chosen because they contain amides that are believed to be conduits for relaxation, and because their rigidity and pH can be varied without changing important elements of the composition. We have previously also studied relaxation in such gels by other methods (15). The structures of monomer acrylamide (1A), cross-linking agent BIS (1B), and PAG (1C, 1D) are illustrated in Fig. 1.

The cross-linking agent BIS is essentially two acrylamide molecules joined via a methylene group, and forms bridges between acrylamide chains in the polymer. A common feature to the acrylamide and BIS monomers are the amide groups, which are highlighted in bold in Figure 1. This structural group is common to many amino acids, and contributes to base-catalyzed exchange due to the oxygen's proximity to the NH

group. These oxygen groups withdraw electrons from the neighboring NH group, thus increasing local acidity, and catalyzing exchange in the presence of base (16).

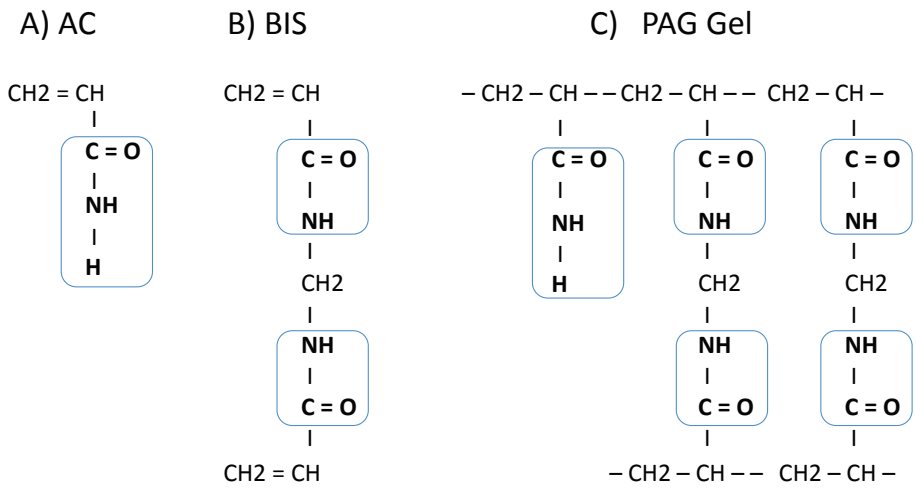

Figure 1: a) Acrylamide monomer (AC), b) N,N'=methylene-bis-acrylamide monomer (BIS). c) Cross-linked co-monomers representing a typical structural element in cross-linked polyacrylamide gel. The amide groups (CONH-R) are outlined.

Gel Phantom Preparation

Acrylamide and N,N'-methylene-bis-acrylamide co-monomers were dissolved in deionized Milipore water (Milipore, USA) at 60 °C such that the total weight fraction of monomer in solution was held at 5%. The fractional composition of BIS monomer was varied from 2.5 to 97.5% (i.e. from 97.5% acrylamide, 2.5% BIS to 97.5% BIS, 2.5% acrylamide) in 6 increments of ~20%. Ammonium persulfate, a free radical initiator was then added (0.05% weight fraction). To catalyze the polymerization, 0.05 mL of N,N,N',N'-tetramethylethyenediamin (TEMED) was added per 100 ml of monomer

solution. Gelation occurred within 5-10 min. The gels were then incubated at 25 deg C for 2 days to allow for complete polymerization. Other details of the gel preparation have been reported previously (15).

The 30 gel samples were prepared at neutral pH in 0.6 mL plastic microtubes and then soaked for several days in buffers of known pH (Hydrion buffer, Sigma-Aldrich). The gels were titrated with buffers over a pH range of 2-11 in 5 increments. The pH of each buffer was monitored and shown not to change with soaking. Excess buffer was removed and the weight was found to stay consistent within 5% of the initial value.

MRI Measurements

Magnetic resonance experiments to measure $T_{1\rho}$ dispersion were performed in a horizontal 400 MHz magnet (Magnex Scientific Lrd, Abingdon, UK) interfaced to a Varian Inova imaging system (Varian, Palo Alto, CA, USA). A 10 mm loop-gap coil (Doty Scientific, USA) was used to transmit and receive RF signals. The pulse sequence used was described by Sepponen et al. (10) to obtain $T_{1\rho}$ weighted images (See Fig. 2). The SLT was arrayed in ten logarithmically spaced intervals from 20 ms to 1 second. The SLA was also logarithmically arrayed from 2π*[250 Hz to 8 kHz], (5.87 μT to 187.88 μT) in 10 intervals. Temperature was monitored by thermocouple connected to an animal physiologic monitoring system (SA Instruments, Stony Brook, NY). All measurements were maintained at 21 °C.

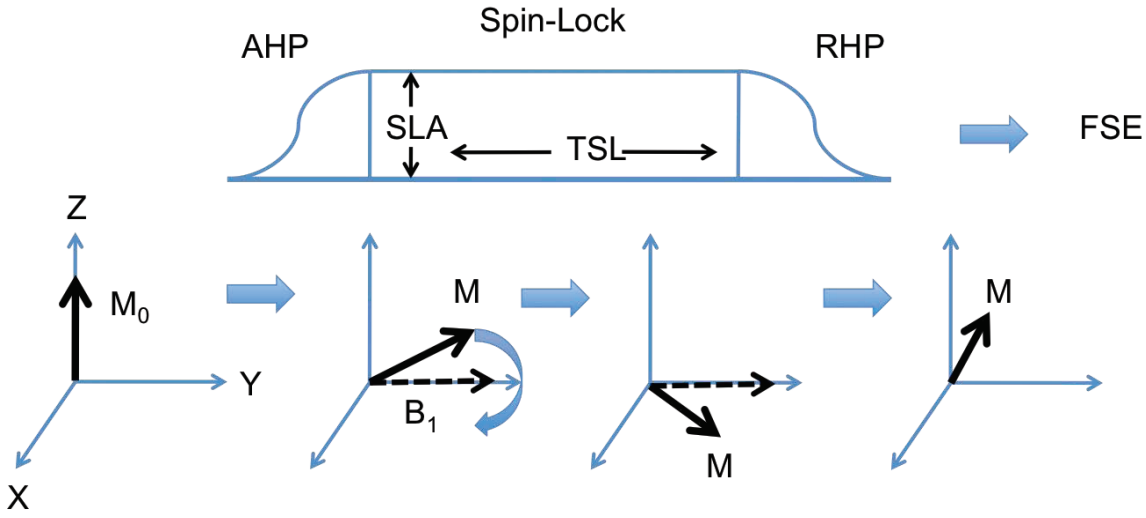

Figure 2: Spin lock cluster before fast spin-echo (FSE) sequence as described by Sepponen et al. AHP represents a 90-degree adiabatic half-passage excitation pulse. SLA and TSL are the spin lock amplitude and spin lock time respectively. RHP represents a reverse adiabatic 90-degree pulse that returns $T_{1\rho}$-prepped magnetization to the Z-axis. Residual transverse magnetization is spoiled prior to image acquisition.

The SL cluster was added before a standard fast spin echo (FSE) imaging sequence. The imaging parameters were: field of view (FOV) = 10 mm^2, matrix = 64x32, slice thickness = 3 mm, echo train length (ETL) = 16 with centric phase encoding, TR = 4 sec, and NEX = 1.

A region of interest (ROI) was placed in the center of each sample image and propagated to all the images in the arrayed dispersion data set in MATLAB. $T_{1\rho}$ values were calculated with a three-parameter, least-squares fit to a monoexponential decay function for each SLA using the Levenberg-Marquardt algorithm (17). The dispersion data were

then fit to the Chopra two-site fast exchange model [Eq. 5] yielding values of R_2, $R_{1\rho}^{\infty}$, and r_b. In addition, the data points were used to estimate numerically the second derivative of the dispersion curve, and the zero crossing frequency was used along with the measured chemical shift to estimate r_b with Eq. 9.

RESULTS

Simulation Results

The results of progressively adding noise to simulated $R_{1\rho}$ dispersion data revealed the minimum SNR values that would produce stable fits of data to the Chopra model. The fits of the simulated $R_{1\rho}$ dispersion data with a SNR greater than 20:1 to Eq. 5 yielded r_b values accurate to within 5% of the input values over exchange rates from 2 kHz to 10 kHz. As the simulated exchange rate dropped below 1 kHz to the lowest simulated rate of 500 Hz, the fitting became more unreliable, accurate to within 11% of the simulated r_b value. As the simulated r_b approaches 20 kHz, the fit became less accurate with the calculated error rate growing to 4% of the simulated value. These data provided guidance for minimum imaging SNR, which was held greater than 80:1 for the first image of the $R_{1\rho}$ relaxation sequence and truncated when SNR decayed below 10:1 to avoid noise bias in the fitting procedure (18).

Taking the second derivative of the simulated $R_{1\rho}$ dispersion data provided the frequency of the inflection point of the curve. This frequency was then inserted into Eq. 9 and the results compared to the results of the Chopra fitting. The results are nearly identical as long as the condition $r_b >> R_{2b}$ holds. If the inflection point falls too low, the model

subtraction in Eq. 9 fails. This effect is shown in Fig. 3 over a range of chemical shifts where for exchange rates from 100 Hz to 2.5 kHz, and R_{2b} = 125 Hz, the second derivative estimate falls below the simulated exchange rate. As the simulated exchange rate increases, the estimate from the second derivative approaches the simulated rate asymptotically.

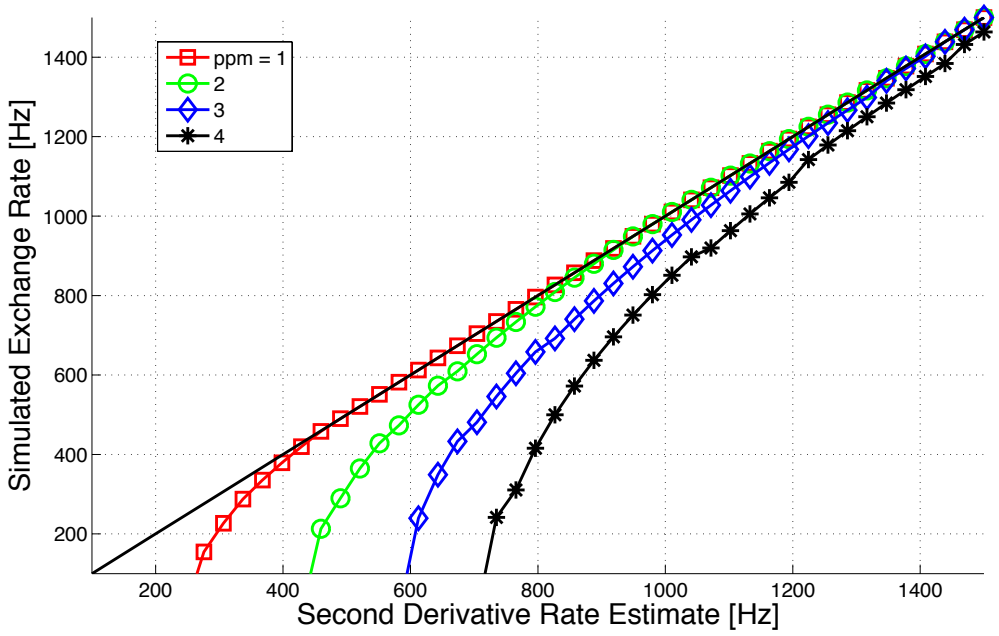

Figure 3: Simulated exchange rates from the Bloch equations plotted vs. the estimated rates from the second derivative method and Eq. 9. The results are nearly identical as long as the condition $r_b >> R_{2b}$ holds. As the simulated exchange rate increases the estimate from the second derivative approaches the simulated rate asymptotically.

As there is no fitting for the second derivative method, adding noise to the simulated signal affected the results in a different manner. The second derivative exchange rate estimates are stable as long as the conditions stated in the previous section are met and

the measured $R_{1\rho}$ values do not fluctuate up and down causing additional zero crossings in the second derivative. This occurred in simulation when the SNR dropped below 10.

Figure 4.a shows measured $R_{1\rho}$ vs. %BIS across different pH values at low SLA (250 Hz). $R_{1\rho}$ increases with BIS concentration and with pH above 7. Figure 4.b shows the measured $R_{1\rho}$ relaxation rates at high SLA (4 kHz). The $R_{1\rho}$ values also increased as BIS replaces AC as a percentage of total monomer concentration at high SLA. Above 40% BIS there appears to be a rapid increase in $R_{1\rho}$ as opposed to the values below 40% BIS concentration. $R_{1\rho}$ values also increase with pH at high SLA.

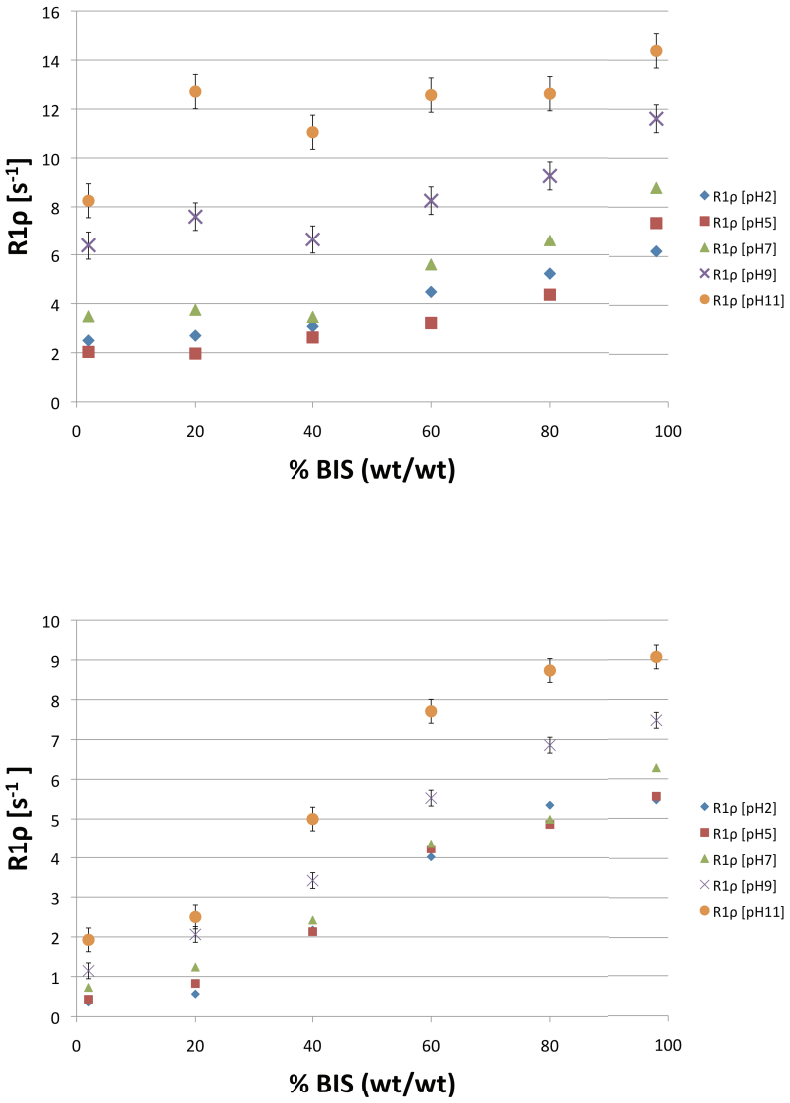

Figure 4: a. $R_{1\rho}$ vs. BIS at low SLA. b. $R_{1\rho}$ vs. BIS at high SLA. $R_{1\rho}$ values increase rapidly above neutral pH. Note that $R_{1\rho}$ values increase with % BIS which is consistent with increasing gel rigidity.

Figure 5 illustrates a typical set of $R_{1\rho}$ dispersion curves at a fixed low %BIS concentration across a range of pH values. These curves illustrate the effect of increasing SLA on measured $R_{1\rho}$. In general $R_{1\rho}$ approaches a maximum value at the minimum

measured SLA. $R_{1\rho}$ approaches a minimum at the maximum measured SLA. As pH rises from 2 to 11, the measured $R_{1\rho}$ shows a marked increase in values above pH 7.

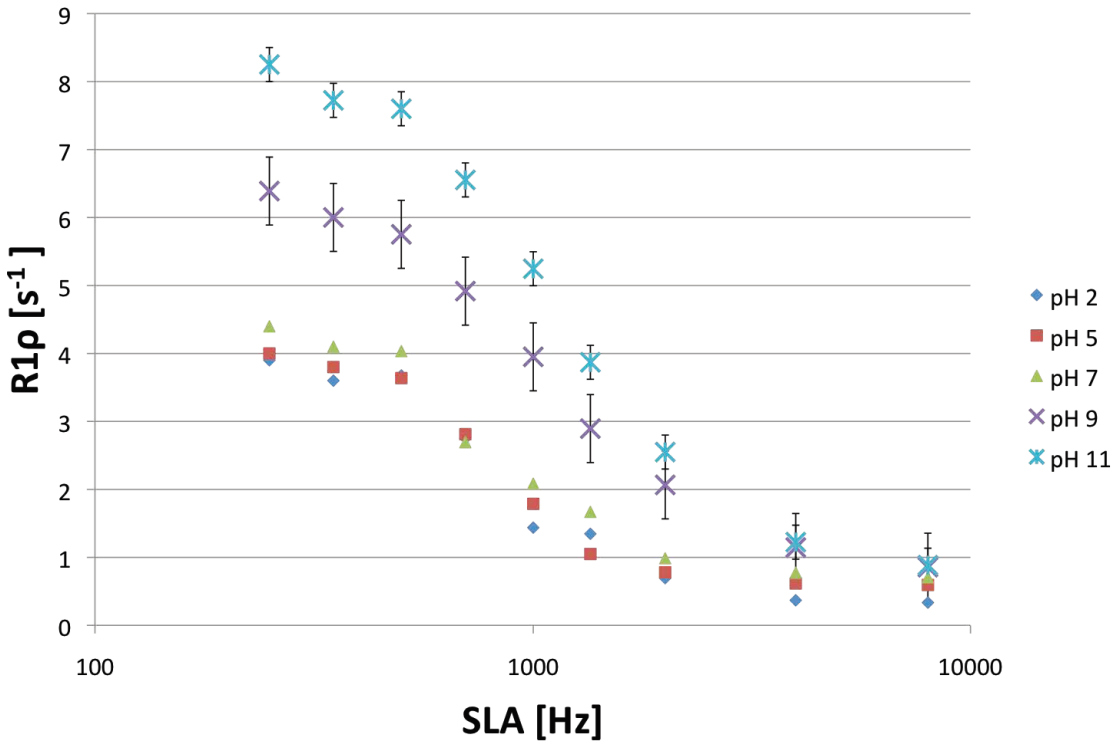

Figure 5: $R_{1\rho}$ vs. SLA at low % BIS. These characteristic dispersion curves were fit to the Chopra model in Eq. 5. The error bars represent one standard deviation.

Fitting to Chopra Model

Figure 6 shows typical $R_{1\rho}$ dispersion curves and corresponding best fit to the Chopra model in Eq. 5 for both low and high % BIS samples at high pH. The solid stars represent the measured $R_{1\rho}$ and corresponding standard deviation confidence interval from the

fitting algorithm. The solid line represents the best fit of the data to the model, and the dashed line represents the second derivative.

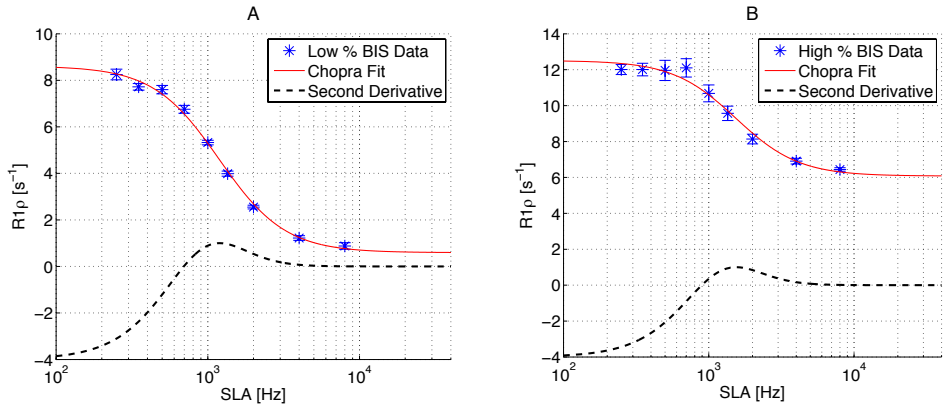

Figure 6: Fit of $R_{1\rho}$ data to Chopra model (solid red line, Eq. 5) for both low %BIS (6.a) and high % BIS (6.b) along with second derivative (dashed line). Note that the dispersion curve is shifted to higher frequency in Fig. 6.b. The error bars represent one standard deviation.

Fitting the experimental data to the Chopra model yields values for R_2, $R_{1\rho}^{\infty}$, and exchange rate (r_b). Assumed parameters for the fitting were taken from literature values and include T_{2b} = 8 msec, T_{1b} = 1 sec (15,19), and a chemical shift ($\Delta\omega_b$) of 3 ppm, confirmed via CEST spectrum (20) (Data not shown). In general the values of r_b were robust and not significantly sensitive with respect to the assumed B pool relaxation values, consistent with simulations by both Hills and Woessner (19,21). For example, the 2.5% BIS samples had r_b values estimated within ±10% of the reported value for R_{2b} values between 10 ms and 10 μs.

Figure 7a shows a trend in the calculated chemical exchange rate vs. pH for 2.5 % BIS tubes. The Chopra fitting and the second derivative methods are shown. For the lower pH values, the zero crossing frequency fell below the threshold to yield a positive number from Eq. 9 and so those values are given as zero. This is consistent with Figure 5, which shows the inflection point moving from just over 500 Hz for the lower pH values to just over 700 Hz at higher pH values. It is clear that as the pH increases the calculated r_b value increases by a factor of 4. Figure 7b shows the measured chemical exchange rate at 98% BIS across a range of pH values. This figure also shows an increase in calculated r_b by a factor of 4, but at rate approximately an order of magnitude greater than at the low % BIS. Figure 8 shows trends in measured chemical exchange rate vs. % BIS at a fixed pH value. Calculated chemical exchange rates increased with % BIS. The second derivative method calculated exchange rates also reflect this trend. The first few values in 8.a. are reported as zero as the zero crossing frequency fell below the threshold for a positive result from Eq. 9.

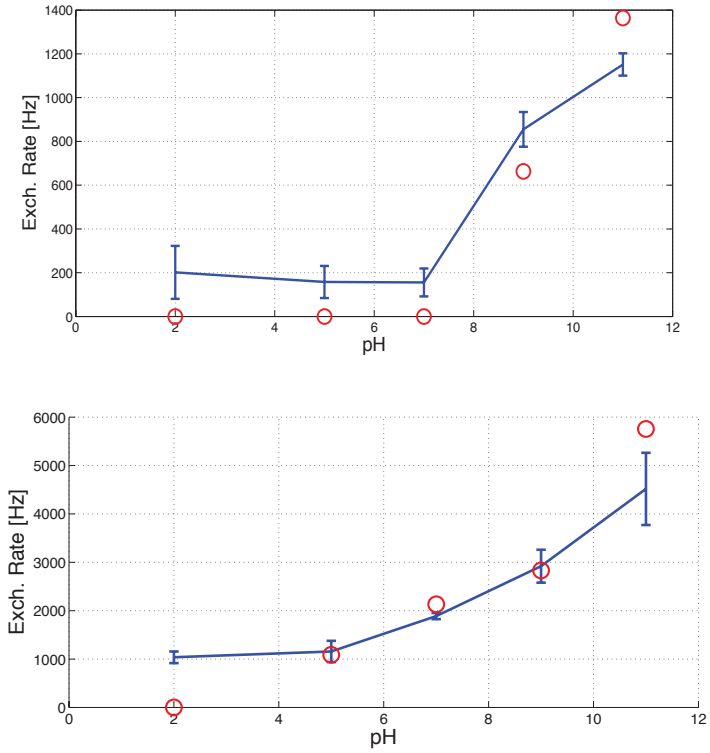

Figure 7: a. Shows mean exchange rate (r_b) as a function of pH at low (2.5%) BIS. 7.b. Mean exchange rate vs. pH at high (98%) BIS. The blue lines correspond to the Chopra fit (Eq. 5) with 1 SD error bars. The red circles are the second derivative method (Eq. 9). The second derivative estimate is given as zero if the inflection point fell below the rate necessary for a positive result. Note the calculated exchange rates increase by approximately an order of magnitude from low to high % BIS.

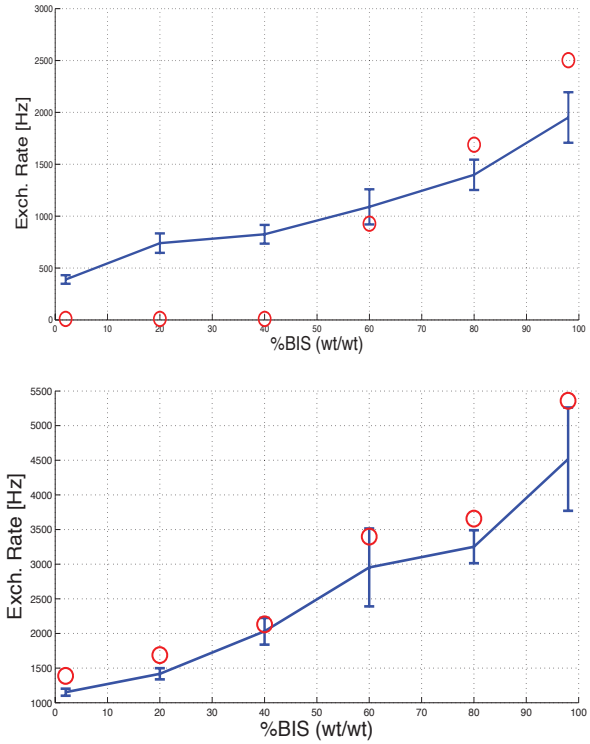

Figure 8: a. Calculated exchange rate (r_b) vs. %BIS at pH 7. 8.b. Calculated exchange rate vs. %BIS at pH 11. The blue lines correspond to the Chopra fit (Eq. 5) with 1 SD error bars. The red circles are the second derivative method. The second derivative estimate is given as zero if the inflection point fell below the rate necessary for a positive result from Eq. 9. Note that the overall exchange rates are much higher at each %BIS value at high pH.

DISCUSSION AND CONLCUSIONS

The increase of measured $R_{1\rho}$ values with pH is consistent with the hypothesis that chemical exchange can be a dominant contributor to rotating frame dispersion. The most likely sites for chemical exchange in this model system are the amide protons in the polymer chain. Previous reports have shown that amide proton exchange is

predominantly a base-catalyzed reaction over the range of pH values measured, and that exchange rates decrease sharply in high pH environments (7,22). The intrinsic exchange rate at neutral pH is approximately T_{ex} = 10 sec, while at pH 9 this drops to 10^{-5} sec. Therefore it is likely that the increase in $R_{1\rho}$ seen at high pH is related to an increase in exchange rates between water and amide protons on the PAG polymer chain. The increase in $R_{1\rho}$ values with pH as is shown in Figure 4a and 4b support this hypothesis, as the measured relaxation rates increase markedly above neutral pH. It is thought that the increased base-catalyzed exchange rate at high pH acts as a conduit to allow protons in free water to exchange with the protons on the macromolecule (23).

$R_{1\rho}$ was also observed to rise with % BIS. The increased rigidity of the gels as BIS replaces AC likely serves to increase the size of the B pool and the possibilities of spin diffusion (3,4). Previous MT experiments by Kennan et al. (15) support this view and they reported a linear increase in the value of the measured macromolecular pool size with increased % BIS. Their observed T_2 shortening was attributed to rigid structures formed during the cross-linking reaction. Their effects on calculated exchange rates are discussed later.

Exchange Dependence on Polymer Side Chains

The increase of exchange rates with %BIS shown in Figure 8 is also consistent with the view that the predominant factor mediating $T_{1\rho}$ dispersion in this tissue model is amide proton exchange. Figure 8a at pH 7, shows a near linear increase (R^2 = 0.95) of exchange rate from 2.5% BIS to 97.5% BIS. Figure 8b shows the same experiment at pH 11, where

a similar linear dependence is shown (R^2 = 0.96). This result was somewhat unexpected as the total weight fraction of monomer was kept constant at 5% (wt/wt). It was thought that the exchange rate would remain constant and that $R_{1\rho}$ would show a slight decrease due to the small difference between the numbers of exchanging protons per mass as BIS replaces AC. However, a plausible explanation may be found in the work of Molday and Bai (16,24), who showed that the addition of side chains to simple peptides such as N-methylacetamide resulted in greatly increased exchange rates, due to increased local acidity, thus making the NH group susceptible to exchange with OH^- catalyst. A similar effect may account for the increase in calculated exchange rates as BIS replaces AC in the PAG samples due to the increasing chain length modifying the local acidity of NH groups. It is typically not possible to precisely extract proton pool sizes from $T_{1\rho}$ dispersion measurements. Hills et al. and others (19,25) have demonstrated that these dispersion curves may be adequately fit with a significant range of values with the mean exchange rate being the most robustly fitted parameter. Thus, no attempt was made to estimate pool size changes in these gels from Eq 4.

With a linear fit to the data in Figure 8b, the mean exchange rates for pure AC and BIS are estimated as 300 Hz and 1800 Hz respectively at pH 7 and 21 deg C. These rates compare favorably to those of Bai and Molday at pH 7 and 25 deg C for primary amides (such as AC) and N-methylacetamide, which differs only slightly from BIS. These results are also supported by the work of Kennan et al. and Gochberg et al (15,26), who showed similar side-chain and pH dependence in BIS and AC gels in magnetization transfer experiments.

It is important to note that the calculated exchange rate estimates are apparent average rates and may reflect the combined effects of chemical exchange, diffusion or other processes in the phantom. However, the contribution of chemical exchange to the overall rate $R_{1\rho}$ may be estimated. As an example, for the 2% BIS gel the calculated exchange rate was near 150 Hz from pH 2 through 7 where amide chemical exchange is slow. However, in basic solutions the calculated rate increased greatly to near 1200 Hz as shown in Fig. 7.a. By inputting pool sizes from the molecular composition of the 2% BIS gel (calculations not shown) and appropriate relaxation terms for the two proton pools into the Bloch equation simulation (P_a = 0.99, P_b = 0.01, T_{1a} = T_{2a} = 3 sec, T_{2a} = 1 sec, T_{2b} = 8 msec, r_b = 150 Hz, $\Delta\omega_b$ = 3.0 ppm), $R_{1\rho}$ is predicted to be near 2.0 s^{-1} for an exchange rate of 150 Hz. The fitted $R_{1\rho}$ value from Figure 5 is near 4.0 s^{-1} at pH 7 where the calculated exchange value is 150 Hz. As the simulated exchange rate nears 1200 Hz, the predicted $R_{1\rho}$ approaches 9.0 s^{-1}, which nearly matches the Figure 5 value of s^{-1} Hz for pH 11. Thus, for the acrylamide system studied here at 9.4T, exchange-mediated relaxation may correspond to near 50% of the observed $R_{1\rho}$ value at neutral pH and below. At high pH, exchange accounts for approximately the entire observed relaxation rate. This finding is consistent with Duvvuri who estimated a 66% contribution of proton exchange to dispersion in model cartilage systems (6).

pH Dependence

Both low and high %BIS samples in Figure 7 show increases in calculated exchange rate by a factor of 4 over the range of pH values studied. This change is not equivalent to the

intrinsic lifetime of amide protons on the PAG, since the intrinsic rates would have changed by a factor of over 10^6 over the same pH range. This difference may be attributed to a number of issues that will be addressed separately below.

The pH dependence of exchange at NH sites on the BIS and AC polymer chains cannot be adequately described by simple acid or base-catalyzed chemical exchange as shown in Eq. 10. Following the work of Liepinsh and Otting (23), the observed chemical exchange rate may be estimated by:

$$k_{obs} = k_a\left[\mathrm{H}^+\right] + k_b\left[{}^-\mathrm{OH}\right] + \sum k_{ci}\left[catalyst\right]^{di} \qquad [10]$$

where k_{obs} is the observed chemical exchange rate as a function of the exchange rate constants k_a, k_b, and k_{ci} due to catalysis by H^+, ^-OH or other catalyst such as water. The term *di* is typically 1 or 2 depending on the exchange mechanism.

For base-catalyzed exchange, logarithmic pH-dependence is typically observed over a wide range of pH values in amide proton exchange. This behavior is typically observed in monomers in solution (7). Such an analysis cannot account for the more linear pH dependent proton exchange results shown in Fig. 7. Similar dependences on pH have been reported previously in other PAG and gel systems (15,26,27). Monomers of AC and BIS in aqueous solution could not be tested over the same pH range due to solute precipitation.

Possible explanations for the non-logarithmic dependence of pH include at least four factors: differences in the number of exchanging sites on the macromolecule, the existence of a distribution of pK values on the polymer chain, conformational changes induced by extreme pH, and heterogeneity in the gel structure inherent in the PAG cross-linking reaction. First, there may be a distribution in the degree of protonation among the exchanging sites on the macromolecule. Then, the value of k_{obs} would no longer be adequately represented by Eq. 10 and must be modeled using n-site chemical exchange models (28). This concept may then be extended to the possibility of a distribution of pK values among the exchanging sites, thus complicating analysis by traditional chemical methods and resulting in a non-logarithmic dependence of exchange rate on pH. The third issue pertains to the spatial distribution of pH in the gel, whereby the local environment of the PAG may be heterogeneous in terms of its structural and electrical properties. Cross-linking the samples prior to pH manipulation mitigated this effect on gel preparation. However, the degree to which subsequent changes were induced in the gel is unknown. The fourth issue may be related to structural changes within the gel as BIS replaces AC in the more rigid gels (above 30% BIS). These changes were easily observed in the more rigid gels as they became opaque and scattered light. Gelfi et al. (29) have previously reported this phenomenon, and they describe small beadlike structures formed of hydrophobic BIS cross-linking with itself as AC becomes scarce. These hydrophobic regions contribute an unknown set of perturbations to the local electrical environment of the polymer, often grouped together as polyelectrolyte effects (30). These hydrophobic regions may have an effect on the amount of bound water on the macromolecule and have an unknown subsequent effect on the protonation of exchanging sites.

Fitting Methods Compared

The Chopra and second derivative methods give similar results as long as the appropriate conditions are met ($r_b >> R_{2b}$). This restriction suggests the second derivative technique is best used under intermediate to fast exchange conditions at small chemical shift as shown in Fig. 3. The proposed technique may prove especially useful for clinical imaging systems in which the available B_1 amplitudes can exceed R_{2b} and $\Delta\omega_b$ several fold, but where maximum B_1 is ultimately limited by specific absorption rate requirements. This method carries the obvious advantage of requiring less data and no model fitting, thus removing the need to estimate pool sizes or relaxation parameters. However, the potential SNR requirements of ~80:1 identified in the simulations may extend imaging time beyond clinically acceptable lengths. Further optimization for clinical scanners may be required. Although, prior knowledge of the exchanging species must first be determined, maps of ω_1^2 will be linearly proportional to r_b^2 with offset $\Delta\omega_b$, so these may be useful for portraying distributions of relative exchange rates. Therefore, an additional advantage of this technique may exist in providing unique contrast from exogenous contrast agents with numerous chemically exchanging groups at known exchange rates (31). These agents may alter the average observed exchange rate and shift the $T_{1\rho}$ dispersion curve obtained in a tissue of interest towards that of the contrast agent alone. This may allow for a rate-dependent SL imaging method as compared to a chemical shift-dependent method with CEST imaging.

It is worth considering that the B_1 powers used were not explicitly tailored to the resulting rate estimates. There may be some dependence on the spacing of locking field

frequencies that may need to be optimized in an iterative fashion. This would provide improved spacing of data points around each inflection point. Due to the large number of samples and wide range of calculated rates, iterative adjustment of locking field was not attempted for these experiments. It may also be useful to employ some simple smoothing or windowing algorithm to the $R_{1\rho}$ dispersion values to reduce the effects of small fluctuations in measured rates. Alternatively, the data may be fit to Eq. 5 to estimate the inflection point, R_2, and $R_{1\rho}^{\infty}$. The second derivative of the fit data may then be taken, thus providing a smooth curve for interpretation. This represents an intermediate method, requiring some data to be fit, but it makes no assumptions regarding the characteristics of the exchanging species.

Conclusions

The advantage of the $T_{1\rho}$ technique lies in the ability to make dispersion measurements in an imaging context in a regime where other approaches may be technically difficult. This allows for ready translation to *in vivo* imaging, with the range of achievable locking fields being the primary limitation. The upper limit is given by the stable pseudo-*cw*-power achievable by the RF amplifier and specific absorption rate considerations. This is typically in the 20 kHz range on small animal systems and 2 kHz for human imagers. The newly proposed second derivative estimation method may address some of these limitations, specifically for low available B_1, low field strength, and moderate to high exchange rates often encountered clinically. With most biological exchange processes in the kHz range (4,6,32), $T_{1\rho}$ dispersion holds much promise for characterizing these processes in a variety of *in vivo* and *ex vivo* experiments.

Here we have demonstrated that there are a variety of structural and chemical effects on $T_{1\rho}$ relaxation dispersion and that these effects may be characterized and fit with suitable models of chemical exchange. Relaxation measurements and fit to a dispersion model of chemical exchange in a simple polymer system avoids many of the complexities of heterogeneous tissue systems and allows for a more clear understanding of the effects of chemical exchange on rotating frame relaxation. The technique is sensitive to perturbations in measured chemical exchange rate and in composition of polymer. The observed relaxation data and fits for chemical exchange parameters are consistent with known relaxation models and literature values, and therefore this technique holds promise for refinement and application to more complex tissues.

ACKNOWLEDGEMENTS

NIH EB000214

REFERENCES

1. Henkelman RM, Huang X, Xiang QS, Stanisz GJ, Swanson SD, Bronskill MJ. Quantitative interpretation of magnetization transfer. Magn Reson Med 1993;29(6):759-766.
2. Koenig SH, Brown RD, 3rd, Ugolini R. A unified view of relaxation in protein solutions and tissue, including hydration and magnetization transfer. Magn Reson Med 1993;29(1):77-83.
3. Hills BP. The Proton-Exchange Cross-Relaxation Model of Water Relaxation in Biopolymer Systems. Mol Phys 1992;76(3):489-508.
4. Hills BP. The Proton-Exchange Cross-Relaxation Model of Water Relaxation in Biopolymer Systems .2. The Sol and Gel States of Gelatin. Mol Phys 1992;76(3):509-523.
5. Gore JC, Brown MS, Zhong J, Mueller KF, Good W. NMR relaxation of water in hydrogel polymers: a model for tissue. Magn Reson Med 1989;9(3):325-332.
6. Duvvuri U, Goldberg AD, Kranz JK, Hoang L, Reddy R, Wehrli FW, Wand AJ, Englander SW, Leigh JS. Water magnetic relaxation dispersion in biological systems: the contribution of proton exchange and implications for the noninvasive detection of cartilage degradation. Proc Natl Acad Sci U S A 2001;98(22):12479-12484.
7. Zhou JY, Payen JF, Wilson DA, Traystman RJ, van Zijl PCM. Using the amide proton signals of intracellular proteins and peptides to detect pH effects in MRI. Nat Med 2003;9(8):1085-1090.

8. Santyr GE, Henkelman RM, Bronskill MJ. Variation in Measured Transverse Relaxation in Tissue Resulting from Spin Locking with the Cpmg Sequence. J Magn Reson 1988;79(1):28-44.

9. Hills B. Magnetic resonance imaging in food science. New York: Wiley; 1998. ix, 342 p. p.

10. Sepponen RE, Pohjonen JA, Sipponen JT, Tanttu JI. A method for T1 rho imaging. J Comput Assist Tomogr 1985;9(6):1007-1011.

11. Witschey WR, 2nd, Borthakur A, Elliott MA, Mellon E, Niyogi S, Wallman DJ, Wang C, Reddy R. Artifacts in T1 rho-weighted imaging: compensation for B(1) and B(0) field imperfections. J Magn Reson 2007;186(1):75-85.

12. Chopra S, Mcclung RED, Jordan RB. Rotating-Frame Relaxation Rates of Solvent Molecules in Solutions of Paramagnetic-Ions Undergoing Solvent Exchange. J Magn Reson 1984;59(3):361-372.

13. Regatte RR, Akella SV, Borthakur A, Reddy R. Proton spin-lock ratio imaging for quantitation of glycosaminoglycans in articular cartilage. J Magn Reson Imaging 2003;17(1):114-121.

14. Hills BP. Water proton relaxation in dilute and unsaturated suspensions of non-porous particles. Magn Reson Imaging 1994;12(2):183-190.

15. Kennan RP, Richardson KA, Zhong JH, Maryanski MJ, Gore JC. The effects of cross-link density and chemical exchange on magnetization transfer in polyacrylamide gels. J Magn Reson Ser B 1996;110(3):267-277.

16. Bai YW, Milne JS, Mayne L, Englander SW. Primary Structure Effects on Peptide Group Hydrogen-Exchange. Proteins 1993;17(1):75-86.

17. Marquardt DW. An Algorithm for Least-Squares Estimation of Nonlinear Parameters. SIAM Journal on Applied Mathematics 1963;11(2):431-441.

18. Does MD, Gore JC. Complications of nonlinear echo time spacing for measurement of T (2). NMR Biomed 2000;13(1):1-7.

19. Hills BP, Takacs SF, Belton PS. The Effects of Proteins on the Proton Nmr Transverse Relaxation-Times of Water .1. Native Bovine Serum-Albumin. Mol Phys 1989;67(4):903-918.

20. Ward KM, Aletras AH, Balaban RS. A new class of contrast agents for MRI based on proton chemical exchange dependent saturation transfer (CEST). J Magn Reson 2000;143(1):79-87.

21. Woessner DE, Zhang S, Merritt ME, Sherry AD. Numerical solution of the Bloch equations provides insights into the optimum design of PARACEST agents for MRI. Magn Reson Med 2005;53(4):790-799.

22. Wüthrich K. NMR of proteins and nucleic acids. New York: Wiley; 1986. xv, 292 p.

23. Liepinsh E, Otting G. Proton exchange rates from amino acid side chains - Implications for image contrast. Magnet Reson Med 1996;35(1):30-42.

24. Molday RS, Englander SW, Kallen RG. Primary structure effects on peptide group hydrogen exchange. Biochemistry-Us 1972;11(2):150-158.

25. Chen EL, Kim RJ. Magnetic Resonance Water Proton Relaxation in Protein Solutions and Tissue: T-1p Dispersion Characterization. Plos One 2010;5(1):-.

26. Gochberg DF, Kennan RP, Maryanski MJ, Gore JC. The role of specific side groups and pH in magnetization transfer in polymers. J Magn Reson 1998;131(2):191-198.

27. Ceckler TL, Wolff SD, Yip V, Simon SA, Balaban RS. Dynamic and Chemical Factors Affecting Water Proton Relaxation by Macromolecules. J Magn Reson 1992;98(3):637-645.

28. Trott O, Palmer AG. Theoretical study of R-1p rotating-frame and R-2 free-precession relaxation in the presence of n-site chemical exchange. J Magn Reson 2004;170(1):104-112.

29. Gelfi C, Righetti PG. Polymerization kinetics of polyacrylamide gels I. Effect of different cross-linkers. Electrophoresis 1981;2(4):213-219.

30. Philippova OE, Hourdet D, Audebert R, Khokhlov AR. pH-Responsive Gels of Hydrophobically Modified Poly(acrylic acid). Macromolecules 1997;30(26):8278-8285.

31. Aime S, Calabi L, Biondi L, De Miranda M, Ghelli S, Paleari L, Rebaudengo C, Terreno E. Iopamidol: Exploring the potential use of a well-established x-ray contrast agent for MRI. Magn Reson Med 2005;53(4):830-834.

32. Virta A, Komu M, Kormano M. T-1 rho of protein solutions at very low fields: Dependence on molecular weight, concentration, and structure. Magnet Reson Med 1997;37(1):53-57.

CHAPTER IV

EXCHANGE-MEDIATED CONTRAST AGENTS FOR SPIN-LOCK IMAGING

ABSTRACT

Measurements of relaxation rates in the rotating frame with spin-locking (SL) techniques are sensitive to substances with exchanging protons with appropriate chemical shifts. We develop a novel approach to exchange rate selective imaging based on measured $T_{1\rho}$ dispersion with applied locking field strength, and demonstrate the method on samples containing the X-ray contrast agent Iohexol (IO) with and without cross-linked bovine serum albumin (BSA). $T_{1\rho}$ dispersion of water in the phantoms was measured with a Varian 9.4T magnet by an on-resonance SL pulse with fast spin-echo readout, and the results used to estimate exchange rates. The IO phantom alone gave a fitted exchange rate of ~1 kHz, BSA alone was ~11 kHz, and in combination gave rates in between. By using these estimated rates, we demonstrate how a novel SL imaging method may be used to enhance contrast due to the presence of a contrast agent whose protons have specific exchange rates.

Key Words: iohexol, $T_{1\rho}$, spin lock, chemical exchange

INTRODUCTION

There has been much recent interest in developing new chemical exchange saturation transfer contrast (CEST) agents that take advantage of the specific MR properties of tissues or substances with large concentrations of exchanging protons with appropriate chemical shifts. The dynamics of protons in exchange with amide (RC(O)NR'R), which will be abbreviated here by its functional site (NH^+) for brevity, or hydroxyl (^-OH) sites on polymers, peptides, or sugars, have been explored for generating novel endogenous sources of contrast (1-4). Alternately, for exogenous contrast agents, paramagnetic metals such as europium may be used to shift proton precession frequencies to selectively increase exchange effects in conjunction with saturation contrast experiments (paraCEST) (5,6). Radiographic contrast agents such as Iohexol **(**Omnipaque®, GE Healthcare) or Iopamidol (Isovue®, Bracco) contain numerous NH^+ and ^-OH functional groups and so have also been explored recently as promising CEST contrast agents (7,8).

An alternate method of exploring chemical exchange-based contrast uses spin-locking techniques. Measurements of relaxation rates in the rotating frame ($R_{1\rho}$ and $R_{2\rho}$) with spin-locking (SL) techniques have been shown to be sensitive to molecular motions and exchange processes on the time scale of the locking field ($\omega_1 = \gamma B_1$) (9,10). Observed variations in $T_{1\rho}$ with locking-field strength ($T_{1\rho}$ dispersion) provide information on molecular motions and chemical exchange on intermediate to fast time-scales (11). At high fields the increased separation of resonance frequencies between water and other chemical species such as amides can give rise to relatively greater contributions from

chemical exchange. These variations can be exploited to distinguish differences in tissue composition, pH, or other chemical properties. These exchange processes are of interest not only for their effects on $R_{1\rho}$ but also on R_2 and as modulators of saturation transfer contrast (12,13).

Here we demonstrate that $T_{1\rho}$ dispersion may be used in conjunction with a novel image subtraction method to emphasize the presence of nuclei characterized by specific exchange rates (rather than chemical shifts) and thereby can be used to generate novel image contrast. $T_{1\rho}$ dispersion techniques may complement or provide a number of advantages over traditional saturation transfer techniques. These advantages include the elimination of saturation effects near the water resonance for protons with small chemical shifts and also for the exploration of tissues or agents with non-symmetric CEST spectra such as those with significant lipid content. These two effects may complicate the off-resonance spectral subtraction technique used in CEST imaging (2,14,15). Spin locking techniques may carry an advantage in sensitivity to exchanging sites with either rapid exchange or small chemical shift such as from $^{-}$OH groups (typically 0.8-1.8 ppm, and k_{ex} > 1 kHz) where rapid exchange broadening limits CEST enhancement (16,17).

Here we show how a commonly used X-ray contrast agent can be used as an exchange-based exogenous agent to generate novel image contrast. Iohexol (CAS Num: 66108-95-0) is a member of a family of iodine-based CT contrast agents used clinically in a variety of angiographic and neurologic screening protocols. Iohexol carries two available NH^{+} and six $^{-}$OH functional groups that impart it with suitable MR properties for use as an

exchange-based contrast agent. Note that the structure of Iohexol is different from Iopamidol. Iopamidol has three available NH^+ and five ^-OH sites (See Figure 1). We demonstrate how appropriate spin-locking techniques can be used to produce novel contrast in the presence of Iohexol.

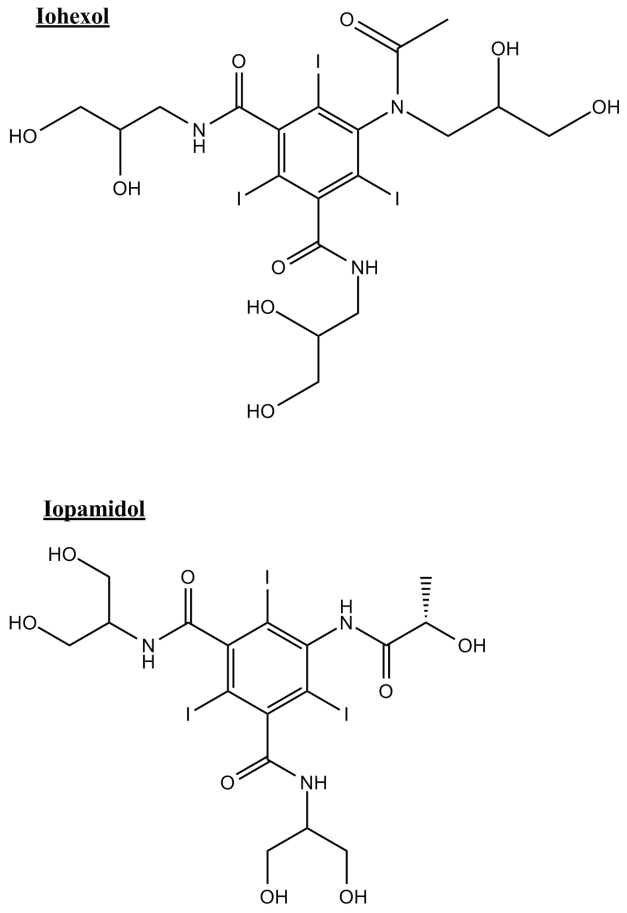

Figure 1. 1.a. Structure of Iohexol. 1.b. Structure of Iopamidol. Note the differences in available NH^+ and $^-$ OH sites.

METHODS

Samples of cross-linked 10% bovine serum albumin (BSA) were created in 0.6 mL plastic tubes by the addition of 1% glutaraldehyde with and without Iohexol (IO) in 32 mM concentrations. Additional tubes of 16 mM IO were created with D_2O replacing the stock solution's tris(hydroxymethyl)aminomethane (TRIS) buffer in three increments. Finally, tubes of 16 mM IO were modified by the addition of hydrochloric acid to create phantoms with pH ranging from 5.5 to 7.4.

NMR Experiments

All NMR experiments were performed on a Varian 9.4T magnet (Varian Medical Systems, Palo Alto, CA) with a 10-mm loop-gap coil. Temperature was monitored by thermocouple connected to an animal physiologic monitoring system (SA Instruments, Stony Brook, NY) and was maintained at 37° C.

To identify the chemical shifts of exchanging protons, ^1H spectra of partially deuterated samples were acquired with the following parameters: a 50 μs 90-degree pulse, 12k complex points, TR = 12 sec, NEX = 16.

$T_{1\rho}$ dispersion was measured with a spin-locking sequence consisting of an adiabatic 90-degree pulse, followed by an on-resonance spin-locking (SL) pulse for half of the spin lock time (SLT). Then a 180-degree refocusing pulse is inserted, followed by the other half of the SL pulse with phase reversal (18). The SL pulse was varied in 10 time

increments (SLT) between 20 ms and one sec and also in amplitude (SLA) in 12 increments between 2π*[250 Hz and 10 kHz]. TR was set at 5 times the T_1 of the Iohexol solution.

Imaging Experiments

Imaging experiments were performed with a 38 mm birdcage coil at 9.4T. $T_{1\rho}$ weighted images were recorded with a modified ΔB_0 and ΔB_1 insensitive SL pulse as described by Witschey et al. followed by a fast spin-echo acquisition (18). The spin-lock pre-pulse also utilizes an adiabatic 90-degree excitation, followed by on-resonance spin lock at a power of SLA for one half of the SLT. This is followed by a 180-degree refocusing pulse and the second half of the SL pulse with phase reversed. A reverse adiabatic 90-degree pulse returns the $T_{1\rho}$-prepped signal to the Z-axis and then residual transverse magnetization is spoiled. Ten SLTs were acquired as before at twelve SLAs between 2π*[250 and 10 kHz]. Other parameters included: FOV = 25 x 25 x 1 mm, matrix = 64 x 128 x 1, TR = 4 sec, TE = 10 ms, Echo Train Length = 8.

Theory and Data Analysis

$T_{1\rho}$ values were calculated by fitting the signal variation with SLT to a three-parameter mono-exponential decay function in MATLAB (The MathWorks, Inc., Natick, MA). Then the $T_{1\rho}$ dispersion data with locking field (ω_1) were fit to a three-parameter model described by Hills and Chopra et al. (shown in Eq. 1) to provide an estimate of exchange rate (k_{ex}), R_2, and $R_{1\rho}^{\infty} \approx R_1$ in MATLAB (9,10,19).

$$R_{1\rho} = \left\{ \frac{R_2 + \frac{\left(R_{1\rho}^{\infty} * \omega_1^2\right)}{S_\rho^2}}{1 + \frac{\omega_1^2}{S_\rho^2}} \right\} \qquad [1]$$

Chopra et al. considered the general case of rotating-frame relaxation in which exchanging nuclei experience different relaxation rates as well as chemical shifts when moving between phases. Chopra et al. modified the Bloch equations and showed how, under specific conditions, an experiment measuring $R_{1\rho}$ at different locking field strengths (ω_1) may be used to determine solvent exchange rate. A non-linear least-squares fit of the variation of $R_{1\rho}$ with ω_1 to Eq. 1 may be used to obtain best fits of R_2, $R_{1\rho}^{\infty}$, and S_ρ^2, where $S_\rho^2 = \sim k_{ex}^2$ given the following simplifications. It was assumed that the exchange is dominated by one exchanging site, operates in the fast-exchange limit ($k_{ex}/\Delta\omega_b > 1$), and that the exchange rate exceeds the exchanging site relaxation parameters R_1 and R_2. Metabolite R_1 and R_2 values are typically on the order of 1 s^{-1} and 10 s^{-1} respectively for aqueous solutions (20,21). These assumptions were deemed reasonable in light of previous reports giving amide exchange rates of 2560 Hz at 7T in a similar molecule (7), and that hydroxyl exchange rates often meet the requirements for fast-exchange (16). These assumptions are consistent with simulations and model fittings by both Hills and Woessner (6,22). Thus, a study of $R_{1\rho}$ vs. ω_1 may be used to estimate exchange rates. This approach has been previously used to estimate exchange rates in cartilage systems and also in acrylamide gels (23,24).

Two image subtraction methods were used to derive contrast based upon the features of $R_{1\rho}$ dispersion profiles that are a function of a species' mean exchange rate. A plot of $R_{1\rho}$ dispersion ($R_{1\rho}$ vs. applied locking field (ω_1)) will feature an inflection point near the mean exchange rate (10). The first approach, taken by Kogen et al. (25) and shown in Eq. 2, acts as a low-pass exchange rate filter, and emphasizes contrast from species whose mean exchange rate falls between ω_1(low) and the maximum selected locking field in Eq. 2, ω_1(high). This is because a species with exchange in this regime will also have maximum dispersion in this region, thus producing a larger difference between signal acquired at ω_1(high) and ω_1(low), to enter into Eq. 2. This method is also dependent on the magnitude of $R_{1\rho}$ dispersion observed in a species, and hence is also strongly affected by variations in R_2 and $R_{1\rho}^{\infty}$.

$$\%CE\left(\omega_1(ex),SLT\right)=\frac{S_0\left(\omega_1(high),SLT\right)-S_0\left(\omega_1(low),SLT\right)}{S_0\left(\omega_1(high),SLT\right)}*100\% \qquad [2]$$

where S is the signal in each pixel, ω_1(high) is the high frequency locking field, ω_1(low) is the low frequency locking field, and SLT is the spin lock time.

We propose an extension of this concept to reduce the effects of the magnitude of $T_{1\rho}$ dispersion on image contrast, which is a function of R_2- $R_{1\rho}^{\infty}$. Instead we wish to emphasize contrast based primarily upon an exchange rate of interest. Equation 3 modifies Eq. 2 with the addition of another locking-field measurement at a specific

exchange rate, ω_1(ex), and now uses ω_1(high) and ω_1(low) to refer to ω_1 values much greater and much less than the expected exchange rate respectively.

$$CE(\omega_1(ex),SLT) = 4 * \frac{\left(S_0(\omega_1(high),SLT) - S_0(\omega_1(ex),SLT)\right) * \left(S_0(\omega_1(ex),SLT) - S_0(\omega_1(low),SLT)\right)}{\left(S_0(\omega_1(high),SLT) - S_0(\omega_1(low),SLT)\right)^2} \quad [3]$$

For the imaging experiments performed here, ω_1(high) is set to the maximum SLA acquired and ω_1(low) is set to the minimum SLA. The term in the numerator gives a maximum value when the locking field ω_1(ex) is set equal to the mean exchange rate (k_{ex}). The terms in the denominator scale the numerator by the magnitude of the $T_{1\rho}$ dispersion ($R_2 - R_{1\rho}^{\infty}$), thus minimizing the effect of a large dispersion on the resulting image. As the maximum value obtained from the ratio is ¼ when the exchange rate equals ω_1(ex) and zero when the exchange rate is far from ω_1(ex), thus a normalization factor of 4 was also used. A 5% threshold mask was applied before subtraction to reduce the effects of background noise.

RESULTS

The proton spectra acquired to estimate the frequency of exchanging species revealed a peak near 0.6 ppm that is attributed to $^{-}$OH protons on the Iohexol molecule. A small NH^{+} peak near 4.2 ppm is initially visible on the ^{1}H spectrum of the 16 mM solution but not after deuteration.

$R_{1\rho}$ dispersion data with locking field and with varied pH were acquired to verify the presence of chemical exchange. Figure 2 shows $R_{1\rho}$ dispersion as a function of applied locking field (γB_1) for the 16 mM IO phantoms. After pH modification the $T_{1\rho}$ value at the lowest locking field, where $R_{1\rho} \approx R_2$, showed a small increase with pH. Proton exchange rates were fitted as 750, 810, 1260 Hz for the 5.5, 6.5, and 7.4 pH phantoms respectively.

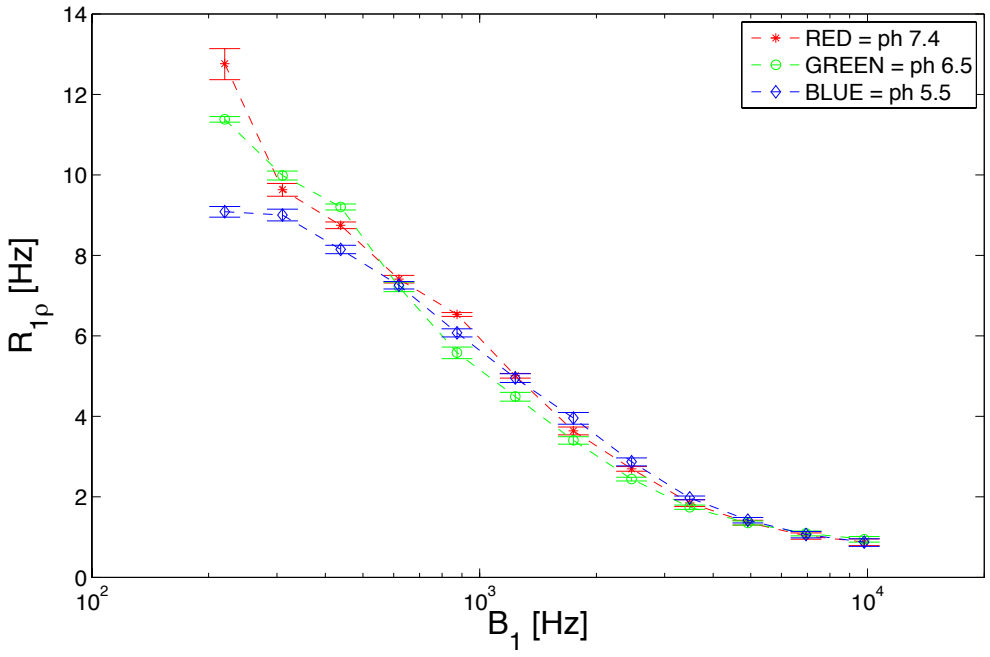

Figure 2. $R_{1\rho}$ (1/ $T_{1\rho}$) dispersion variation with pH for the 16 mM IO phantom to verify the presence of an exchanging species. Note only a slight difference in profile with the largest difference in $R_{1\rho}$ occurring at the lowest acquired power of B_1 = 250 Hz.

Figure 3.a shows $T_{1\rho}$ dispersion profiles for the 32 mM IO with and without BSA and buffer solutions. Calculated values of R_2, $R_{1\rho}^{\infty} \approx R_1$ and exchange rate from the Chopra

fitting of these dispersion curves are given in Table 1. The 10% cross-linked BSA alone is characterized by a very flat profile with $R_{1\rho}$ ($1/T_{1\rho}$) vales ranging from 8.6 s^{-1} at a locking field of 225 Hz to near 6 s^{-1} at 10 kHz with little contributions from apparent exchange over this range. The IO alone showed a large dispersion from a value of 23.6 s^{-1} at a locking field of 250 Hz to 1.6 s^{-1} at 10 kHz. The calculated exchange rate for the 32 mM IO phantom is 1128 Hz. For the combined BSA and IO substance, $T_{1\rho}$ dispersion was much more marked than for BSA alone. However, the dispersion curve is not a simple sum of these components, and the inflection point moves to higher frequencies than for IO alone (Fig. 3.a). The mean exchange rate for the 32 mM IO plus 10% BSA phantom occurs near 2860 Hz. Note that the contrast is also dependent on the large dispersion between $R_{1\rho}^{0}$ and $R_{1\rho}^{\infty}$ as shown in Figure 3.a. and Table 1, giving a large potential enhancement to the IO and the IO plus BSA phantoms at locking field frequencies less than ~5 kHz.

Table 1: Fitted parameters from the Chopra expression for chemical exchange mediated rotating frame relaxation [Eq. 1].

	R_2 [s^{-1}]	$R_{1\rho}^{\infty}$ [s^{-1}]	Exchange Rate [Hz]
10 % BSA	8.6	2.8	11350
Buffer	1.1	0.8	2920
BSA + IO	20.8	7.9	2860
32 mM IO	23.6	1.6	1128

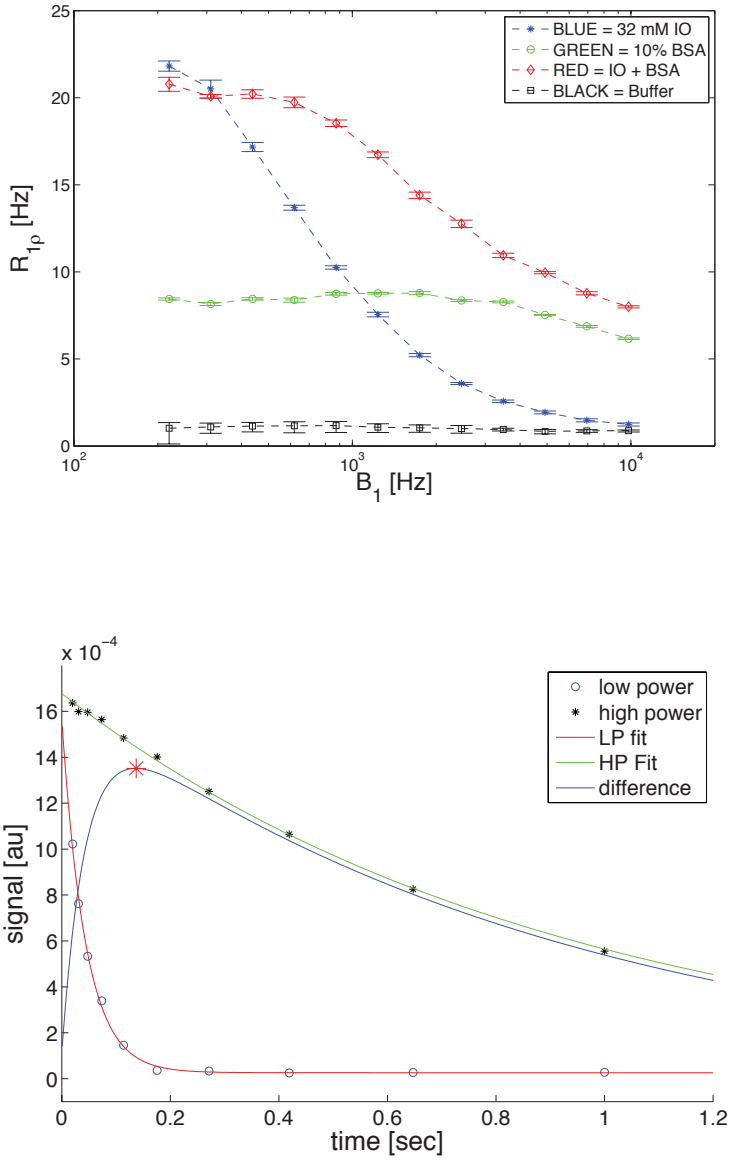

Figure A, and the combined IO + BSA substance, with the buffer solution for reference.

3.a. 32 mM IO (blue stars), BSA (green circles), IO+BSA (red diamonds), and buffer (black squares) phantoms. Note that the $R_{1\rho}$ dispersion for the IO + BSA phantom was much more marked and occurs at a lower frequency than for BSA alone.

3.b. Time course of signal decay for 32 mM IO phantom at low (250 Hz) and high power (1 kHz). The point of maximum contrast occurs at 137 msec.

$T_{1\rho}$ signal decay of the IO phantom at low locking field (SLA = 250 Hz) and at the mean exchange rate of 1128 Hz (SLA = ~1 kHz) was plotted in Figure 3.b to evaluate the magnitude of the signal difference between the two decay rates. The exchange dependent signal difference between low locking field and the locking field nearest the calculated exchange rate is also shown in Figure 3.b. The maximum signal difference between the signal at low and high locking fields occurs at SLT ≈ 137 msec.

Figure 4 uses Eq. 2 to enhance contrast based on exchange rate and the magnitude of $R_{1\rho}$ dispersion in the IO and BSA phantoms. Figure 4.a. shows a "T_2-weighted" image to demonstrate the initial similarity of the 32 mM Iohexol, 10% BSA, and combined IO and BSA phantoms at SLT = 20 msec and SLA = 250 Hz. Figure 4.b. shows a difference image representing the numerator of Eq. 2 at the closest measured locking field to the calculated exchange rate of the combined IO and BSA phantom (SLA (2800 Hz) – SLA (250 Hz)). This high power value was chosen to enhance sensitivity to the exchange rate of the IO + BSA phantom where k_{ex} = ~2860 Hz. The maximum signal difference between the low and high locking fields occurs at 173 msec, and so the closest measured SLT of 176 msec was used for the subtraction image. A large contrast difference between the BSA phantoms with and without the presence of IO was observed. Additionally, the IO phantom was significantly enhanced. Figure 4.c. uses the subtraction technique from Eq. 2 to generate a percent contrast image. Phantoms with IO show a large contrast

enhancement. Using this exchange selective approach, contrast in the BSA was increased by 70-80% due to the presence of Iohexol in the phantom, while BSA alone has almost no enhancement.

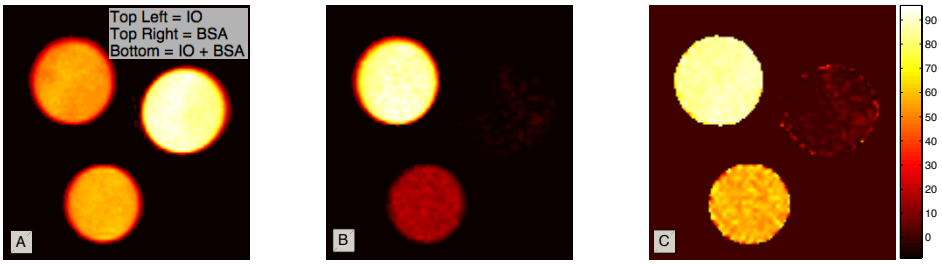

Figure 4. Demonstrates the use of Eq. 2 to generate contrast based on the magnitude of dispersion and chemical exchange rate for phantoms of the X-ray contrast agent Iohexol (32 mM), BSA (10 % wt/wt), and a combined IO + BSA mixture.

4.a. Low power (SLA = 250 Hz), short duration (SLT = 20 msec) image of all three phantoms: Top Left = IO alone, Top Right = BSA alone, Bottom = Both.

4.b. An image representing the numerator of Eq. 2, with the subtraction of a low power (250 Hz) image from a higher power image (2800 kHz) at 176 msec. The high power value was chosen to enhance sensitivity to the exchange rate of the IO + BSA phantom. Note the large contrast difference between the BSA phantoms with and without the presence of IO. The spin-locking pulse acts as an exchange-rate filter, enhancing contrast from the phantoms with exchange rates slower than the high-power locking field and with large dispersions.

4.c. A normalized percent contrast enhancement image from Eq. 2. Phantoms with IO show a large contrast enhancement. Note that the BSA+IO phantom shows an enhancement of 70-80% due to the presence of IO, while BSA alone has almost no enhancement.

In order to reduce the effect of the magnitude of $R_{1\rho}$ dispersion on the subtraction technique from Eq. 2, the same data from Figure 4 were used with Eq. 3 to generate Figure 5. For consistency, the same locking field time (SLT) of 156 msec was used for all image subtractions with only the ω_1 value being varied. This time point is an empirically derived choice for all phantoms, and is nearly twice the average $T_{1\rho}$ of all the species, and allows sufficient time for spin-lock contrast to develop, but is not so long as to allow all species' signal to deteriorate into noise. The SLT may also be varied to provide an optimal value when comparing any two substances of interest. Figure 5.a. shows the results of choosing ω_1(ex) at the nearest acquired SLA (~2π*1 kHz) to the mean exchange rate of the IO phantom (1186 Hz). Note that the signal from the IO only phantom dominates the image contrast. Figure 5.b. used a ω_1(ex) of ~2π*2800 Hz. Here the contrast from the IO+BSA contrast is maximized. Figure 5.c. shows the results of choosing ω_1(ex) to be (~2π*7800 Hz), which was the highest available SLA to use for the technique. Even though the estimated mean BSA exchange rate is near 11 kHz, sufficient separation of frequencies allows for the BSA phantom to show good selective contrast.

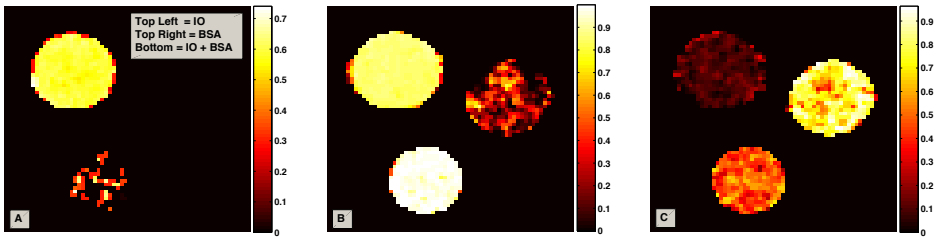

Figure 5. Demonstrates a novel exchange rate based contrast enhancement method using Eq. 3. The same image data from Figure 4, which used Eq. 2, were used to generate Figure 5. Image values near one represent a good match between the selected ω_1(ex) and the average exchange rate. Values for ω_1(high) and

ω_1(low) were fixed at the maximum and minimum acquired SLA. Top Left = IO alone, Top Right = BSA alone, Bottom = Both.

5.a. ω_1(ex) = ~1 kHz, SLT = 156 msec.

5.b. ω_1(ex) = ~2800 Hz, SLT =156 msec.

5.c. ω_1(ex) = ~7800 Hz, SLT = 156 msec.

Note that by choosing an exchange rate near the mean exchange rate of the phantom of interest, the contrast can be modified to emphasize the presence of a substance with an exchange rate near the selected ω_1(ex) value.

DISCUSSION AND CONCLUSION

The novel technique based on Eq. 3 and demonstrated in Fig. 5 illustrates that images can be made with spin-locking methods whose contrast reflects the presence of exchanging protons with specific exchange rates. Prior methods used spin-locking pulses as an exchange rate filter, enhancing signal from exchange rates below the selected locking field and with large $R_{1\rho}$ ($1/T_{1\rho}$) dispersions. However, these methods produce contrast that depends on the magnitude of the dispersion ($R_{1\rho}^{0} - R_{1\rho}^{\infty}$) with locking field, and therefore they are not specific to exchange rate. For Iohexol, a large $R_{1\rho}$ dispersion is observed around 1 kHz that is due to chemical exchange at one or more of the $^{-}$OH or NH^{+} sites on the Iohexol molecule with the surrounding water. The exchange seen in BSA alone occurs at much higher rates and results in a much flatter dispersion profile, while the combined materials show intermediate exchange rates. By appropriate selection

of the spin lock field amplitudes, maximal contrast can be derived from nuclei whose dispersion (exchange rate) occurs at the locking frequency.

Multiple exchanging peaks were identified from the proton spectrum and were reduced when D_2O replaced H_2O. This verifies that the NH^+ at 4.2 ppm and ^-OH protons on the Iohexol molecule near 0.6 ppm are in exchange with the solvent. Note that the exact peak locations are not critical for obtaining our exchange estimates and that rapid proton exchange may have shifted the observed peak locations. The ^-OH and NH^+ peak assignments were made by comparison of the acquired spectrum to other published high-resolution ^1H spectra (8,26).

The Iohexol samples in Figure 2 show small increases in calculated exchange rate over the range of pH values studied. It is important to note that the calculated exchange rate estimates are apparent average rates and may reflect the combined effects of molecular motions and chemical exchange of several exchanging species in the phantom. No attempt has been made to separate the relative contributions of ^-OH vs. NH^+ (11). These species resonate with different relative chemical shifts and have been shown to exchange with water at different rates (2,16,27). At low exchange rates, the $T_{1\rho}$ dispersion profile scales to higher frequency as the chemical shift of a species increases (19). This may contribute an error in the estimated exchange rates due to the assumptions listed in the methods section. However at the relatively rapid exchange rates reported here, especially for hydroxyl exchange, the effect on the estimates should be small. There is also a potentially important effect of the TRIS buffer solution where the primary amine (R-

NH_2) may contribute to the overall $T_{1\rho}$ dispersion profile (16). For this reason the buffer solution was explicitly included in Fig. 3.a. to demonstrate that its effect was also small.

BSA was chosen as a tissue phantom due to its well-studied proton relaxation properties and the ability to modulate the number of exchanging amide groups via glutaraldehyde (GA) cross-linking. The amount of GA used determines the approximate degree to which the protein matrix is cross-linked. For a 1% GA solution, the resulting gel should be nearly 100% linked (28), leaving only a few exchanging groups to conflict with Iohexol proton exchange.

Figure 3.a. shows the dramatic effect of the presence of the X-ray contrast agent Iohexol on the BSA tissue phantom. The addition of IO to the BSA phantom greatly alters its $R_{1\rho}$ dispersion profile, where at low SLA the combined phantom has an $R_{1\rho}$ near that of IO alone (~ 22 s^{-1}). This shift to much higher $R_{1\rho}$ value at low locking field may be best thought of as a change in R_2. At high frequency the measured $R_{1\rho}$ approaches that of BSA alone (~ 3 s^{-1}). The observed mean chemical exchange rate moves to lower frequencies by the addition of IO to BSA. This shift to lower frequencies is due to a corresponding shift in the average exchange rates, and it allows for contrast to be selected via locking field (within the limits of the imaging system) and it demonstrates a unique way to selectively modulate contrast based upon species exchanging at specific rates.

The potential contrast demonstrated as a large exchange-mediated $R_{1\rho}$ dispersion in Figure 3 is consistent with other authors who report similar effects in image contrast with

CEST techniques on Iopamidol (7,8). This technique may be improved by an optimized sampling scheme where sampling points in time and in locking field are more closely spaced around appropriate inflection points (29). For example, as shown in Fig. 3.b., the nearest time point to the point of maximal contrast is several tens of msec away.

We have presented two different approaches to use $R_{1\rho}$ dispersion contrast. Either $R_{1\rho}$ subtraction technique may be used to emphasize the presence of IO in the BSA phantom by appropriate selection of locking fields. For the method demonstrated in Eq. 2, the high SLA rate acts as an exchange rate filter, emphasizing contrast from species with large $R_{1\rho}$ dispersions at rates slower than the selected maximum locking field. This phenomenon is demonstrated in Figure 4 where selective contrast enhancement of between 70 and 80% was achieved in the IO + BSA phantom due to the presence of the Iohexol. As the BSA phantom alone has much higher apparent exchange rates, the $T_{1\rho}$-weighted signal at low (250 Hz) and high (2800 Hz) SLA is essentially the same and the BSA phantom drops out of the subtraction image. However, the phantom of Iohexol alone was also greatly enhanced as it has a large $R_{1\rho}$ dispersion at frequencies lower than the selected maximum locking field. This is contrasted to Figure 5, which uses the subtraction technique outlined in Eq. 3. Here the effect of the large $T_{1\rho}$ dispersion shown in the IO phantom may be reduced by selectively choosing the locking field nearest to the exchange rate of the species of interest as illustrated in Fig. 5.b. and 5.c. This technique may therefore be thought of as exchange rate selective. This technique may be useful in distinguishing two substances with similar R_2 values but differing mean exchange rates.

The most significant drawback of either subtraction technique is the large SNR degradation suffered during image subtraction. The method outlined in Eq. 3 suffers a greater time- and ω_1-dependent degradation of image contrast as compared to the method outlined in Eq. 2 due to division by a squared signal difference. Therefore as mentioned in the methods section, a 5% threshold mask was applied to the images in Figure 5 before subtraction to reduce the effects of background noise. This measure was not necessary for the method outlined in Eq. 2, as the normalized subtraction still produced acceptable images.

For the Iohexol system studied here, the simultaneous contributions of ^{-}OH vs. NH^{+} to overall image contrast and $T_{1\rho}$ dispersion in spin-locking experiments highlights a potential weakness of the SL technique in comparison to CEST imaging. The CEST technique carries a few advantages in terms of power deposition and in spectral selectivity. Both CEST and SL techniques generate contrast with long saturation pulses, but the CEST saturation pulse is typically low-power and well off-resonance with respect to water. This allows for easier translation to *in vivo* and clinical imaging with respect to specific absorption rate (SAR) restrictions. CEST has been used clinically in a number of applications, and an excellent review of the technique has recently been published (30). Additionally, the spectral selectivity of CEST allows for the saturation of an exchanging species of choice, thus minimizing effects from other exchanging species. For example, previous studies of X-ray contrast agents typically use the amide peak, which is well separated from water, to generate image contrast (7). However, for spin locking, the contribution of exchanging ^{-}OH groups may exceed the contribution of NH^{+} groups

especially as typical hydroxyl exchange rates are generally an order of magnitude greater than amide exchange rates (2,8). Due to the small chemical shift of hydroxyl peaks, these are rarely used for quantitative CEST imaging due to conflation with the water peak. In addition, for rapidly exchanging species, CEST techniques are adversely affected by line broadening, while SL techniques may still be used to generate useful image contrast (17). Spin-locking techniques may be sensitive more to the rate of exchange than to the chemical shift, and thus the contribution of the slowly exchanging species to $T_{1\rho}$ contrast is often ignored (31), which makes $T_{1\rho}$ contrast complementary to the CEST sensitivity to slow amide exchange.

As demonstrated here, large exchange rate differences may be exploited to generate novel contrast. Spin-locking techniques have seen less adoption than CEST, presumably due to the multiple on- and off-resonance effects to which it is sensitive. The majority of applications reported to date have been in musculoskeletal imaging where changes in sugars such as chondroitin sulfate have been implicated in disease processes (32). A new method to separate the multiple contributions to $T_{1\rho}$ may be the so-called "CESTrho" technique that combines off resonance CEST saturation of one spin population with subsequent on-resonance spin locking (33). However, the use of two long saturation pulses poses considerable problems for use *in vivo* due to SAR restrictions. Further study is required to illuminate the relative benefits and applications for each technique.

A strength of the $T_{1\rho}$ technique is the ability to make dispersion measurements in an imaging context to reveal contrast at specific exchange rates. This is opposed to T_2

dispersion observed in the Carr-Purcell-Meiboom-Gill sequence, where the ability to string together 180 degree pulses is limited to a relatively low frequency. Spin-locking allows for ready translation to *in vivo* imaging, with the range of achievable locking fields being the primary limitation (9,10). Typically the lower limit of measurable exchange rates is given by the heterogeneity in the B_1 or B_0 fields generated in the tissue of interest. The upper limit is given by the stable *cw*-power achievable by the RF amplifier and specific absorption rate considerations. These rates are typically in the 20 kHz range on small animal systems and 2 kHz for human imagers. With most biological exchange processes in the kHz range (2,10,11,16,34), $T_{1\rho}$ dispersion holds much promise for characterizing these processes in a variety of *in vivo* and *ex vivo* experiments.

In conclusion, spin locking may be used to enhance contrast in tissues due to the presence of an intrinsic or exogenous agent whose protons have specific exchange rates. For Iohexol, $R_{1\rho}$ dispersion around 1 kHz is due to chemical exchange at one or more of the $^-$OH and NH^+ sites on the Iohexol molecule with the surrounding water. The exchange seen in BSA alone occurs at higher rates, while the combined materials show intermediate exchange rates. By appropriate selection of the spin lock fields, maximal contrast can be derived from nuclei whose dispersion (exchange rate) occurs at the locking frequency.

ACKNOWLEDGEMENTS

NCRR 1S10 RR17799

NIH R01 EB000214

REFERENCES

1. Ling W, Regatte RR, Navon G, Jerschow A. Assessment of glycosaminoglycan concentration in vivo by chemical exchange-dependent saturation transfer (gagCEST). Proc Natl Acad Sci U S A 2008;105(7):2266-2270.
2. Ward KM, Aletras AH, Balaban RS. A new class of contrast agents for MRI based on proton chemical exchange dependent saturation transfer (CEST). J Magn Reson 2000;143(1):79-87.
3. van Zijl PCM, Jones CK, Ren J, Malloy CR, Sherry AD. MR1 detection of glycogen in vivo by using chemical exchange saturation transfer imaging (glycoCEST). P Natl Acad Sci USA 2007;104(11):4359-4364.
4. McMahon MT, Gilad AA, DeLiso MA, Berman SM, Bulte JW, van Zijl PC. New "multicolor" polypeptide diamagnetic chemical exchange saturation transfer (DIACEST) contrast agents for MRI. Magn Reson Med 2008;60(4):803-812.
5. Zhang S, Merritt M, Woessner DE, Lenkinski RE, Sherry AD. PARACEST agents: modulating MRI contrast via water proton exchange. Acc Chem Res 2003;36(10):783-790.
6. Woessner DE, Zhang S, Merritt ME, Sherry AD. Numerical solution of the Bloch equations provides insights into the optimum design of PARACEST agents for MRI. Magn Reson Med 2005;53(4):790-799.
7. Aime S, Calabi L, Biondi L, De Miranda M, Ghelli S, Paleari L, Rebaudengo C, Terreno E. Iopamidol: Exploring the potential use of a well-established x-ray contrast agent for MRI. Magn Reson Med 2005;53(4):830-834.

8. Longo DL, Dastrù W, Digilio G, Keupp J, Langereis S, Lanzardo S, Prestigio S, Steinbach O, Terreno E, Uggeri F, Aime S. Iopamidol as a responsive MRI-chemical exchange saturation transfer contrast agent for pH mapping of kidneys: In vivo studies in mice at 7 T. Magnet Reson Med 2011;65(1):202-211.

9. Hills BP. The Proton-Exchange Cross-Relaxation Model of Water Relaxation in Biopolymer Systems. Mol Phys 1992;76(3):489-508.

10. Hills BP. The Proton-Exchange Cross-Relaxation Model of Water Relaxation in Biopolymer Systems .2. The Sol and Gel States of Gelatin. Mol Phys 1992;76(3):509-523.

11. Duvvuri U, Goldberg AD, Kranz JK, Hoang L, Reddy R, Wehrli FW, Wand AJ, Englander SW, Leigh JS. Water magnetic relaxation dispersion in biological systems: the contribution of proton exchange and implications for the noninvasive detection of cartilage degradation. Proc Natl Acad Sci U S A 2001;98(22):12479-12484.

12. Gore JC, Brown MS, Zhong J, Mueller KF, Good W. NMR relaxation of water in hydrogel polymers: a model for tissue. Magn Reson Med 1989;9(3):325-332.

13. Zhou JY, Payen JF, Wilson DA, Traystman RJ, van Zijl PCM. Using the amide proton signals of intracellular proteins and peptides to detect pH effects in MRI. Nat Med 2003;9(8):1085-1090.

14. Overhauser AW. Polarization of Nuclei in Metals. Physical Review 1953;92(2):411.

15. Sun PZ, Zhou J, Sun W, Huang J, van Zijl PC. Suppression of lipid artifacts in amide proton transfer imaging. Magn Reson Med 2005;54(1):222-225.

16. Liepinsh E, Otting G. Proton exchange rates from amino acid side chains - Implications for image contrast. Magnet Reson Med 1996;35(1):30-42.

17. Zhou JY, van Zijl PCM. Chemical exchange saturation transfer imaging and spectroscopy. Prog Nucl Mag Res Sp 2006;48(2-3):109-136.

18. Witschey WR, Borthakur A, Elliott MA, Mellon E, Niyogi S, Wang C, Reddy R. Compensation for spin-lock artifacts using an off-resonance rotary echo in T1rhooff-weighted imaging. Magn Reson Med 2007;57(1):2-7.

19. Chopra S, Mcclung RED, Jordan RB. Rotating-Frame Relaxation Rates of Solvent Molecules in Solutions of Paramagnetic-Ions Undergoing Solvent Exchange. J Magn Reson 1984;59(3):361-372.

20. Hills B. Magnetic resonance imaging in food science. New York: Wiley; 1998.

21. Woessner DE. Brownian motion and its effects in NMR chemical exchange and relaxation in liquids. Concept Magnetic Res 1996;8(6):397-421.

22. Hills BP, Takacs SF, Belton PS. The Effects of Proteins on the Proton Nmr Transverse Relaxation-Times of Water .1. Native Bovine Serum-Albumin. Mol Phys 1989;67(4):903-918.

23. Regatte RR, Akella SV, Borthakur A, Reddy R. Proton spin-lock ratio imaging for quantitation of glycosaminoglycans in articular cartilage. J Magn Reson Imaging 2003;17(1):114-121.

24. Cobb JG, Xie J, Gore JC. Contributions of chemical exchange to T1ρ dispersion in a tissue model. Magnet Reson Med 2011:[Epub ahead of release].

25. Kogen F. Comparison of chemical exchange saturation transfer (CEST) and T1ρ MRI for measurement of proton chemical exchange between metabolites and water at 7T. Proc ISMRM 2010;3003(6499).

26. Ijare OB, Bezabeh T, Albiin N, Arnelo U, Bergquist A, Lindberg B, Smith IC. Absence of glycochenodeoxycholic acid (GCDCA) in human bile is an indication of cholestasis: a 1H MRS study. NMR Biomed 2009;22(5):471-479.

27. Haris M, Cai K, Singh A, Hariharan H, Reddy R. In vivo mapping of brain myo-inositol. Neuroimage 2011;54(3):2079-2085.

28. Chen EL, Kim RJ. Magnetic Resonance Water Proton Relaxation in Protein Solutions and Tissue: T-1p Dispersion Characterization. Plos One 2010;5(1).

29. Skinner MG, Kolind SH, MacKay AL. The effect of varying echo spacing within a multiecho acquisition: better characterization of long T2 components. Magn Reson Imaging 2007;25(6):840-847.

30. van Zijl PCM, Yadav NN. Chemical exchange saturation transfer (CEST): What is in a name and what isn't? Magnet Reson Med 2011;65(4):927-948.

31. Jin T, Autio J, Obata T, Kim S-G. Spin-locking versus chemical exchange saturation transfer MRI for investigating chemical exchange process between water and labile metabolite protons. Magnet Reson Med 2011;65(5):1448-1460.

32. Akella SV, Regatte RR, Gougoutas AJ, Borthakur A, Shapiro EM, Kneeland JB, Leigh JS, Reddy R. Proteoglycan-induced changes in T1rho-relaxation of articular cartilage at 4T. Magn Reson Med 2001;46(3):419-423.

33. Kogan F. CESTrho: A New Method for Studying Chemical Exchange at Intermediate Exchange Rates. Proceedings of the 19th Annual Meeting of ISMRM, Montreal, QC, CA, 2011 (Abstract 706).

34. Virta A, Komu M, Kormano M. T-1 rho of protein solutions at very low fields: Dependence on molecular weight, concentration, and structure. Magnet Reson Med 1997;37(1):53-57.

CHAPTER V

EXCHANGE-MEDIATED CONTRAST MECHANISMS FOR CEST AND SPIN-LOCK IMAGING PART I: THEORY AND SIMULATIONS

ABSTRACT

Magnetic resonance imaging (MRI) of biological media based on chemical exchange saturation transfer (CEST) and rotating frame ($R_{1\rho}$) dispersion measurements with spin-locking (SL) techniques both demonstrate that endogenous contrast depends on chemical exchange processes. Each approach is influenced by different properties of the medium and parameters of the contributing exchange process. In this first of two papers, simulations are performed on two model biologic systems to illustrate the factors that influence contrast measureable by each technique and to determine what information may be obtained from each technique under appropriate conditions. In Part II, we validate these predictions and demonstrate how chemical exchange modifies contrast in MRI studies of biologic systems of interest.

Simulations of rotating frame dispersion and CEST contrast were performed on two model systems. Poly-L-lysine, a simple polypeptide of known relaxation parameters, was chosen as a model of amide (NH^+) exchange. Dextran, a simple poly-glucose molecule,

was selected as a model of hydroxyl ($^{-}$OH) exchange. These were chosen because of the simplicity of their CEST z-spectra and their moderate exchange rates (< 1 kHz).

The simulations reveal that for systems in which appropriate exchange occurs, both CEST and $R_{1\rho}$ measurements depend on similar exchange parameters but they manifest themselves differently in their effects on MRI contrast. CEST contrast may be larger in the slow and intermediate exchange regimes for protons with large resonant frequency offsets (> 2ppm). On the other hand, the SL technique produces larger contrast enhancement when resonant frequency offsets are small (< 2 ppm) and exchange is in the intermediate to fast regime. Both techniques benefit from increasing main field (B_0), and each provides a useful approach to producing images that emphasize protons undergoing chemical exchange under specific experimental conditions.

Key words: CEST, spin lock, $R_{1\rho}$, chemical exchange

INTRODUCTION

There is continuing interest in developing and exploiting novel mechanisms that affect proton contrast in MRI, and in the use of both endogenous and exogenous sources of contrast. Proton exchange between water and labile groups in other molecules provides one such potential mechanism that is sensitive to specific chemical components within a mixture. While methods that manipulate magnetization transfer such as chemical exchange saturation transfer (CEST) depend directly on exchange, other approaches, notably sequences that measure T_2 or $T_{1\rho}$ are also affected by exchange on appropriate

time scales. The dynamics of protons in exchange with amide (RC(O)NR'R, abbreviated here as NH^{+}) and hydroxyl (^{-}OH) sites on polymers, peptides, or sugars, have been recently exploited to generate novel endogenous contrast in CEST imaging (1-3). The protons within a sample are separated into two pools, one of free water, and the other of exchangeable protons, as shown in Figure 1. Each pool is characterized by its own relaxation rates and chemical shift, but communicate via chemical exchange. Alternately, for exogenous contrast agents, paramagnetic metals such as europium have been used to shift proton precession frequencies to selectively increase exchange effects (paraCEST) (4,5), while common x-ray contrast agents such as Iohexol **(**Omnipaque®, GE Healthcare) or Iopamidol (Isovue®, Bracco), which contain numerous amide and hydroxyl groups, have also been shown to produce significant CEST effects (6,7). Tissue constituents such as glycogen (glycoCEST) and gycosaminoglycan (gagCEST) have also been used to generate endogenous contrast specific tissues (8,9).

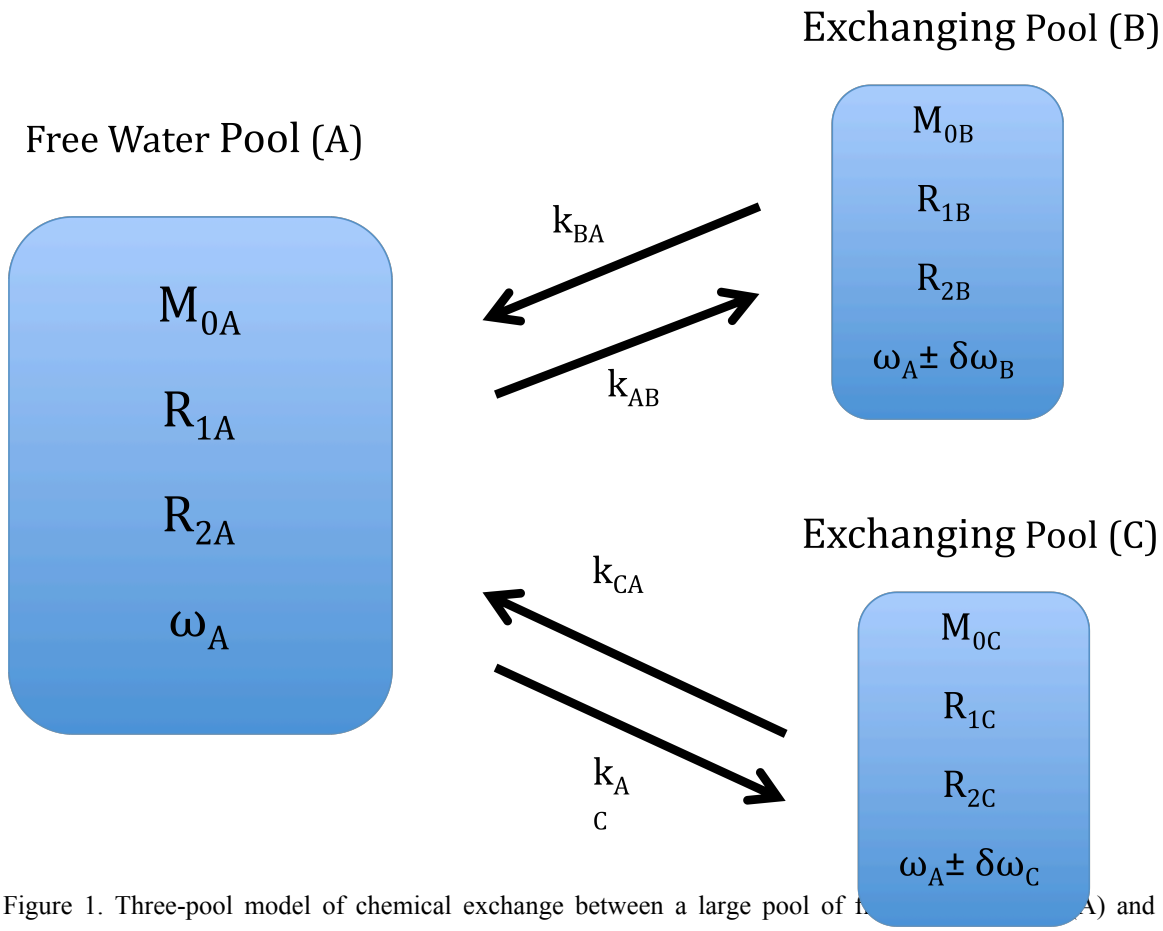

Figure 1. Three-pool model of chemical exchange between a large pool of f A) and smaller pools of exchangeable protons B and C. The rate k_{ba} represents the exchange rate from free water to the exchangeable proton site, and k_{ab} is the reverse rate. M_0, R_1, and R_2 are the assumed independent parameters for each site and are distinguished by an appropriate subscript. There is no presumed communication between pools B and C, and a two-pool model is achieved by simply removing one of the exchanging pools.

CEST methods induce radio frequency (RF) saturation of an exchanging species, which is then transferred to water, reducing the water MR signal as shown in Figure 2. The change in water signal and image contrast depends on the exchange rate and the concentrations of the exchanging species. The saturating energy must be applied at the

resonant frequency of the labile proton, but the signal change does not, in the ideal case of perfectly selective RF saturation, explicitly depend on the magnitude of the chemical shift.

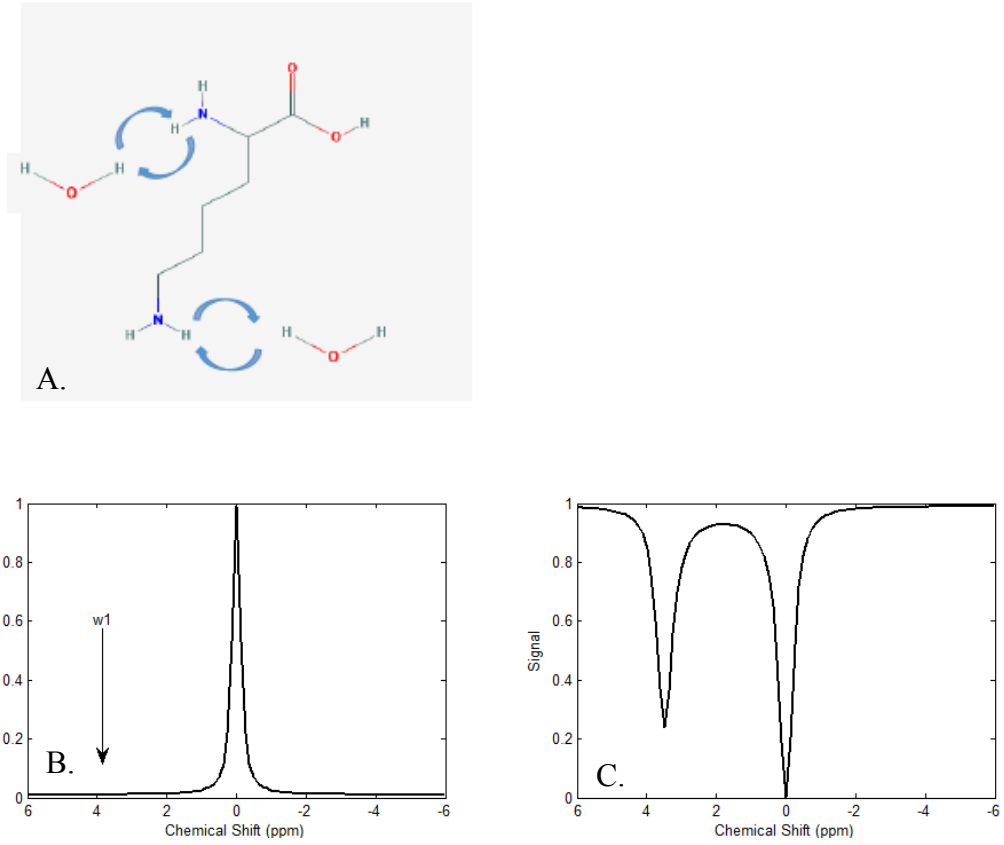

Figure 2. An illustration of the chemical exchange saturation transfer (CEST) technique to probe chemical exchange effects.

2.a. Chemical exchange mechanism between the free water and metabolite pool for lysine

2.b. Simulated proton spectrum demonstrating the CEST technique with off-resonance RF irradiation at some frequency offset (δω).

2.c. Simulated CEST z-spectrum showing the location of a metabolite near δω = 3.5 ppm from water.

To obtain CEST contrast, typically an RF pulse is applied at an offset frequency (typically several ppm, $\delta\omega$) as referenced to the water peak (ω_0 = 0 ppm), and after saturated protons exchange with the water the reduced signal is then acquired. The off-resonance irradiation pulse may then be swept across a range of frequencies surrounding the water peak forming a "z-spectrum" of the resulting signal intensity at each obtained frequency step. If this spectrum is then normalized to a non-saturated image acquired on-resonance (M_0), the magnetization transfer ratio (MTR) is generated as shown in Eq. 1. Peaks in this z-spectrum identify resonance frequency offsets of specific exchanging species. However, the applied pulse may also alter the water signal because of direct saturation or non-specific magnetization transfer (10) with other broad resonances, and so generally two images are acquired for CEST imaging. Each image is acquired at the opposite frequency offset (± ppm of metabolite resonance of interest). The difference in the normalized saturation contrast on opposite sides of the water peak is referred to as the magnetization transfer ratio asymmetry (MTR_{asym}) as shown in Eq. 2, where $\delta\omega$ is the resonant frequency offset, and ω_0 is the reference water frequency.

$$MTR = 1 - \frac{S(\delta)}{S(0)} \qquad [1]$$

$$MTR_{asym} = \frac{S(-\delta) - S(+\delta)}{S(0)} \qquad [2]$$

The design performance and applications of CEST methods have been recently reviewed (2,11). An alternate method for introducing chemical exchange-based contrast uses spin-locking (SL) techniques as depicted in Figure 3.

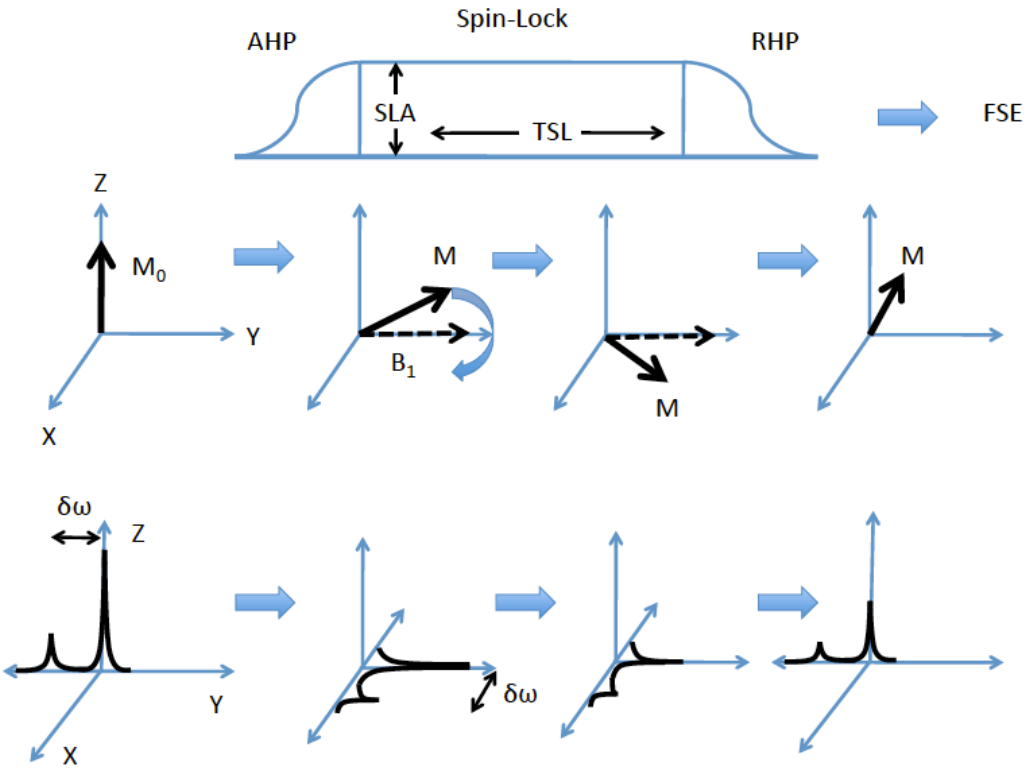

Figure 3. An illustration of the Spin locking (SL) technique to probe chemical exchange effects.

3.a. SL pulse sequence used to impart spin-lock contrast before an imaging sequence.

3.b. Magnetization vector (M_0) is nutated into the transverse plan where it is locked by the applied B_1 field.

3.c. Dephasing due to chemical exchange during the applied locking field is more effectively refocused with an increasingly large applied B_1 field, resulting in $T_{1\rho}$ dispersion, which may be fit to an appropriate model to estimate exchange rates.

Several published methods exist to generate SL contrast (12,13); generally, as shown in Fig. 3.a, a 90-degree adiabatic half-passage (AHP) pulse nutates longitudinal magnetization to the transverse plane, followed by a hard spin-locking pulse with amplitude (SLA) and duration (SLT) along the y-axis. From there, another 90-degree reverse half-passage (RHP) pulse returns magnetization to the longitudinal axis, and the residual transverse component is spoiled as shown in Fig. 3.b. An imaging sequence may then be used to read the $T_{1\rho}$-weighted signal. Measurements of relaxation rates in the rotating frame ($R_{1\rho}$ and $R_{2\rho}$) with such techniques have been shown to be sensitive to molecular motions and interactions on the time scale of the locking field (14,15). Observed variations in $T_{1\rho}$ with locking-field strength ($T_{1\rho}$ dispersion) can provide information on specific types of molecular motions and interactions including chemical and diffusive exchange in tissues (16,17). Cross-relaxation in the rotating frame may allow exchanging protons to be affected by non-exchanging protons in macromolecules via through-space dipolar coupling. Here again, dispersion will reflect motions on the times scale of γB_1. Such effects are reduced when the line-width of the macromolecular protons is much greater than the locking frequency, as is typically the case in tissues, and may be eliminated by locking at the magic angle (15). In tissues, the relaxation rate and image contrast depend almost exclusively on the chemical shift and exchange rates, as well as the locking field of choice. At high main fields, the increased separation of

resonance frequencies between water and other chemical species that are not in extremely fast exchange such as amides or hydroxyls gives rise to greater contributions from chemical exchange as depicted in Fig. 3.c. These variations may provide a useful feature to distinguish differences in tissue composition, pH, or other chemical properties.

CEST and SL techniques are both sensitive to chemical exchange effects. However, differences in experimental technique confer different constraints and sensitivities upon the two methods. The two primary constraints are the chemical shift difference between water and metabolite ($\delta\omega$) and the chemical exchange rate of protons from the metabolite to free water (k_{ba}) (1,18). CEST is sensitive to relatively slow chemical exchange interactions because the chemical shift of the exchanging species must typically be greater than the exchange rate (k_{ba}), i.e. ($\delta\omega/k_{ba} > 1$). Measureable CEST contrast has previously been demonstrated in millimolar concentrations of poly-L-lysine (PLK), which contain exchanging protons in this regime ($k_{ba} \cong 100$ Hz) at NH^+ (~3.5 ppm) sites on the polypeptide (19). Comparable studies with spin-locking techniques show little contrast enhancement in this regime (20). This sensitivity changes as k_{ba} increases relative to $\delta\omega$ into the "intermediate" exchange regime where $\delta\omega/k_{ba} \cong 1$ and line broadening begins to attenuate the ability to select solely for the metabolite peak in CEST with a RF pulse without simultaneously saturating the water peak (1,8). However, with increased exchange rates, the contribution of chemical exchange to transverse relaxation creates an increased difference between R_1 and R_2 rates. Contrast may then be selectively modulated between these two limits using spin-locking techniques. This has been previously demonstrated with large contrast enhancements from millimolar solutions of

simple sugars and polypeptides (16,20). As the exchanging species' exchange rate increases into the fast-exchange regime ($\delta\omega/k_{ba} < 1$) line broadening causes the two peaks to coalesce and the CEST technique becomes untenable as suggested by Ward and Zhou (1,21). However, in this regime, spin-locking techniques may still be used to generate contrast from the rapidly exchanging species until the rates become so large that the necessary locking field, γB_1, becomes impractical.

It would be useful to further explore the role of exchange processes in solutions of biologically relevant macromolecules with one or more types of exchanging sites such as polypeptides and sugars in order to better understand the factors that modulate exchange-based image contrast and the limits of each technique's sensitivity. To these ends we have studied various samples in order to show how $T_{1\rho}$ dispersion and CEST contrast due to chemical exchange may be used to emphasize the presence of nuclei characterized by specific exchange rates or chemical shifts, and thus used to generate novel image contrast. The results are reported in two parts. In Part I, a theoretical framework and computer simulations are developed to demonstrate the role of exchanging species and to quantify the contributions of exchange to spin-lock and CEST contrast. This framework is then used in Part II to interpret experimental measurements on model systems designed to illustrate how rotating frame dispersion and CEST may be used to derive contrast from specifically targeted chemically exchanging groups.

THEORY

We developed computer simulations and performed experiments to quantify the contributions of exchange to measurements made by spin locking and CEST techniques. We evaluated the influence of specific factors such as exchange rates and chemical shifts for the simple two-pool model shown in Figure 1. Each pool is characterized by its own relaxation rates, chemical shift, and relative size, and communicates via chemical exchange with the rates k_{ba} and k_{ab}. The effect of chemical exchange on $R_{1\rho}$ and CEST contrast may be described using the Bloch equations modified with exchange terms for each species (22,23). For the simulations below, two pools are used to represent a single proton exchange process. For substances such as poly-L-threonine (PLT) that contain two exchanging species, ^{-}OH and NH^{+}, at least three pools are necessary, and the formalism required is included below. The two- and three-pool models of the Bloch equations modified for exchange may be solved by a variety of numerical methods (5,15). These simulation data may be used with Eqs. 1 and 2 to estimate the contributions of chemical exchange to CEST image contrast.

Quantitative estimates of the contribution of chemical exchange to $R_{1\rho}$ dispersion contrast may also be made in an analogous manner. Kogen et al. (24) suggested a metric, shown in Eq. 3, that emphasizes contrast from species whose mean exchange rate falls below the maximum selected locking field, ω_1(high), which incorporates the concept that $R_{1\rho}$ can act as a low-pass filter on exchange rates. This metric emphasizes contrast from species whose exchange rate is less than the maximum locking field, and also is a function of how much $R_{1\rho}$ varies between ω_1(high) and ω_1(low) locking fields, or (R_2- $R_{1\rho}^{\infty}$).

$$\%CE\left(\omega_1(ex),SLT\right)=\frac{S_0\left(\omega_1(high),SLT\right)-S_0\left(\omega_1(low),SLT\right)}{S_0\left(\omega_1(high),SLT\right)}*100\% \qquad [3]$$

In this equation percent contrast enhancement (%CE) is given for signal in a voxel (S_0), and is a function of locking field, ω_1, and spin lock time (SLT). The term ω_1(high) is the locking field at high power where $R_{1\rho} \simeq R_1$, and ω_1(low) is the locking field at low power where $R_{1\rho} \cong R_2$. Thus, this expression depends on the magnitude of $T_{1\rho}$ dispersion, which may contain components attributed to chemical exchange, diffusion or other processes. We propose an extension of Eq. 3 that normalizes the effects of the magnitude of $T_{1\rho}$ dispersion to emphasize contrast based primarily upon a specific exchange rate of interest. Equation 4 incorporates an experimentally-chosen locking-field measurement, ω_1(ex).

$$CE\left(\omega_1(ex),SLT\right)=4*\frac{\left(S_0\left(\omega_1(high),SLT\right)-S_0\left(\omega_1(ex),SLT\right)\right)*\left(S_0\left(\omega_1(ex),SLT\right)-S_0\left(\omega_1(low),SLT\right)\right)}{\left(S_0\left(\omega_1(high),SLT\right)-S_0\left(\omega_1(low),SLT\right)\right)^2} \qquad [4]$$

The numerator gives a maximum value when the term ω_1(ex) is set equal to the mean of R_1 and R_2. This value is primarily a function of exchange rate (k_{ba}) and chemical shift ($\delta\omega$). The terms in the denominator scale the numerator by the magnitude of the $T_{1\rho}$ dispersion (R_2-R_1), thus reducing the effects of a large dispersion on the resulting ratio. A factor of 4 normalizes the contrast enhancement (CE) ratio such that it equals one when the exchange rate equals ω_1(ex) and zero when the exchange rate is very far from ω_1(ex).

CEST and Spin-Locking Simulations

Simulations were performed for selected substances using reference values for each substance and then varying parameters of interest, including chemical exchange rate, chemical shift, concentration, or main field strength, using modified Bloch equations in a manner described by Hills et al. with minor corrections for consistency of notation (25).

$$\dot{\mathrm{M}} = A \bullet \mathrm{M} + \mathrm{M}', \qquad [5]$$

where

$$M = \begin{bmatrix} M_a \\ M_b \\ M_c \end{bmatrix} \text{ and } M_i = \begin{bmatrix} M_x^i \\ M_y^i \\ M_z^i \end{bmatrix}, \text{ i = a,b,c}$$

and A is the 9 x 9 matrix

$$A = \begin{bmatrix} a & \prod(k_b + \kappa_b) & \prod \kappa'_{-c} \\ \prod(k_a + \kappa_a) & b & \prod \kappa_{-c} \\ \prod \kappa'_c & \prod \kappa_c & c \end{bmatrix} \qquad [6]$$

where Π is the 3 x 3 identity matrix and

$$a = \begin{bmatrix} -(R_{2a} + k_a + \kappa_a + \kappa'_c) & (\omega - \omega_a) & \omega_1 \\ -(\omega - \omega_a) & -(R_{2a} + k_a + \kappa_a + \kappa'_c) & 0 \\ -\omega_1 & 0 & -(R_{1a} + k_a + \kappa_a + \kappa'_c) \end{bmatrix} \qquad [7]$$

$$b = \begin{bmatrix} -\left(R_{2b} + k_b + \kappa_b + \kappa'_b\right) & \left(\omega - \omega_b\right) & \omega_1 \\ -\left(\omega - \omega_b\right) & -\left(R_{2b} + k_b + \kappa_b + \kappa'_b\right) & 0 \\ -\omega_1 & 0 & -\left(R_{1b} + k_b + \kappa_b + \kappa'_b\right) \end{bmatrix} \quad [8]$$

$$c = \begin{bmatrix} -\left(R_{2c} + \kappa'_{-c} + \kappa_{-c}\right) & \left(\omega - \omega_c\right) & \omega_1 \\ -\left(\omega - \omega_c\right) & -\left(R_{2c} + \kappa'_{-c} + \kappa_{-c}\right) & 0 \\ -\omega_1 & 0 & -\left(R_{1a} + \kappa'_{-c} + \kappa_{-c}\right) \end{bmatrix} \quad [9]$$

This notation corresponds to a three-pool system of free water (A) and two exchangeable proton pools (B and C). The rate terms of k and κ are used to modulate exchange among pools. M is the equilibrium vector:

$$\mathbf{M'} = \begin{bmatrix} M_a^0 R_{1a} \\ M_b^0 R_{1b} \\ M_c^0 R_{1c} \end{bmatrix} \text{where } \mathbf{M}_i^0 = \begin{bmatrix} 0 \\ 0 \\ M_z^{i0} \end{bmatrix} \text{ i = a,b,c} \quad [10]$$

Resonance frequency offsets may be explicitly accounted for with the following expressions:

$$\omega - \omega_a = \omega_z + \left(1 - P_a\right)\delta\omega + P_c\delta\Omega \ , \quad [11]$$

$$\omega - \omega_b = \omega_z + P_a\delta\omega + P_c\delta\Omega \, , \quad [12]$$

$$\omega - \omega_c = \omega_z - P_a\delta\omega - \left(P_a + P_b\right)\delta\Omega \, , \quad [13]$$

where $\delta\omega = (\omega_b-\omega_a)$, $\delta\Omega = (\omega_c-\omega_b)$, and the rf offset $\omega_z = (\omega-\omega_{avg})$, where ω_{avg} is the weighted average of the resonance frequency of all three pools. Mass balance still holds in the rotating frame, so the flux equalities of $P_a k_a = P_b k_b$, $P_a \kappa_a = P_b \kappa_b$, $P_c \kappa'_{-c} = P_a \kappa'_c$ and $P_b \kappa_c = P_c \kappa_{-c}$ remain valid. Simulations for two-pool models are performed by simply removing pool "C."

METHODS

Computer Simulations

Chemical exchange effects in a simple two-pool system were simulated using parameters appropriate for poly-L-lysine (PLK) and dextran (DXT) as a representative polypeptide and sugar. These were selected due to the simplicity of their CEST z-spectra and moderate exchange rates (both are typically < 1 kHz). Simulation parameters for the substances were adapted from literature values and experimentally measured CEST z-spectra. PLK was modeled with the following parameters: T_{1a} = 3 sec T_{2a} = 2 sec, T_{1b} = 1 sec, T_{2b} = 30 msec, p_a = 0.99, p_b = 0.01, $\Delta\omega_b$ = 3.5 ppm, k_b = 140 Hz (2,26). DXT was modeled with the following parameters: T_{1a} = 3 sec T_{2a} = 2 sec, T_{1b} = 1 sec, T_{2b} = 30 msec, p_a = 0.99, p_b = 0.01, $\Delta\omega_b$ = 1.2 ppm, k_b = 1 kHz (1,27). For spin-locking simulations, the locking field (ω_1) was varied over a range of amplitudes easily achievable experimentally, from 2π*(150 Hz to 10 kHz). A maximum simulated γB_1 of 10 kHz was chosen because stronger locking fields may be difficult to achieve even on pre-clinical systems. For CEST simulations, the frequency offset was arrayed from -10 to +10 ppm and used an RF amplitude of 1 μT of duration 8 sec. Note that for simplicity of

comparison across a varied parameter, the RF amplitude was not continuously optimized for each perturbation to the model as suggested by Sun et al. (26).

The effect of moving to increasingly higher main field (B_0) was evaluated by varying ω_0 from 2π*(23 to 400) MHz. The effects of increasing chemical exchange rate were modeled by arraying k_b from (0.1 to 50) kHz. The effects of metabolite concentration or, analogously, the number of exchanging sites were modeled by varying p_b from (0.001 to 0.05). The effects of chemical shift were explored by comparing a typical hydroxyl chemical shift of 1.2 ppm at k_b = 1 kHz to a typical amide shift and rate ($\Delta\omega_b$ = 3.5 ppm and k_b = 140 Hz).

A three-pool model was also evaluated to illustrate the effects of multiple exchanging sites at differing chemical exchange rates for substances such as PLT or CS that carry both NH^+ and ^-OH groups. Two exchanging pools at two different offset frequencies from water were modeled in equal concentrations at two different rates per site. The following parameters were used for this simulation: P_a = 0.98, P_b = 0.01, P_c = 0.01, $\Delta\omega_b$ = 3.5 ppm, $\Delta\omega_c$ = 1.2 ppm, k_b = 140 Hz and 1 kHz, K_b = 140 Hz and 1 kHz.

RESULTS

The simulations were designed to illustrate the effects of several common experimental and system variations on the MR signal. Figure 4 illustrates the effect of moving to higher field on $R_{1\rho}$ ($1/T_{1\rho}$) dispersion, assuming other relaxation rates (R_1, R_2) remain

fixed. Note the difference in simulated dispersion between the model amide (NH^+) and hydroxyl (^-OH) system in Fig 4.a and 4.b respectively. The sugar (^-OH exchange) model system increases from a value of 1 s^{-1} to 9 s^{-1} whereas the peptide model (NH^+ exchange) increases only from 1 s^{-1} to less than 2 s^{-1} as main field increases, given typical chemical shifts and exchange rates. Figure 4.c and 4.d show the results of applying Eq. 4 to the dispersion data in 4.a and 4.b. The frequency of maximum contrast scales with B_0 as the chemical shift increases for each species.

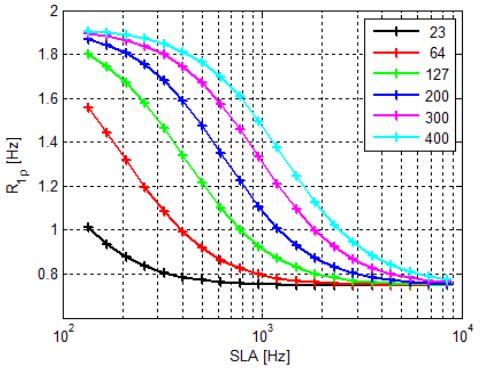

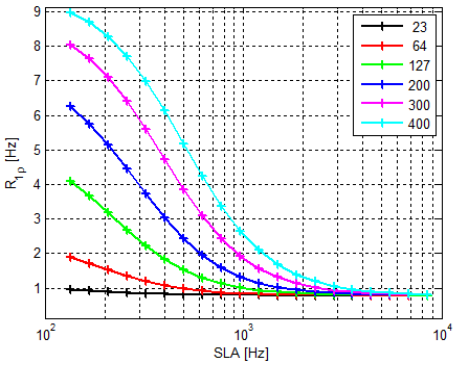

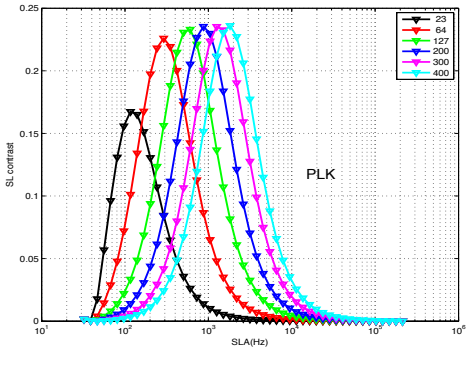

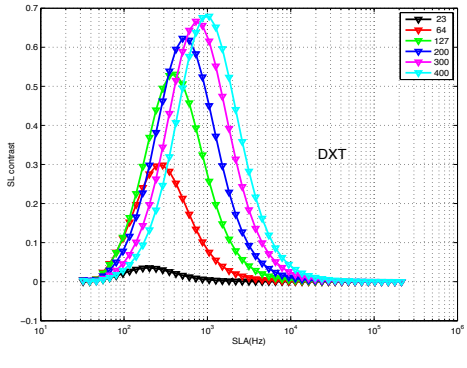

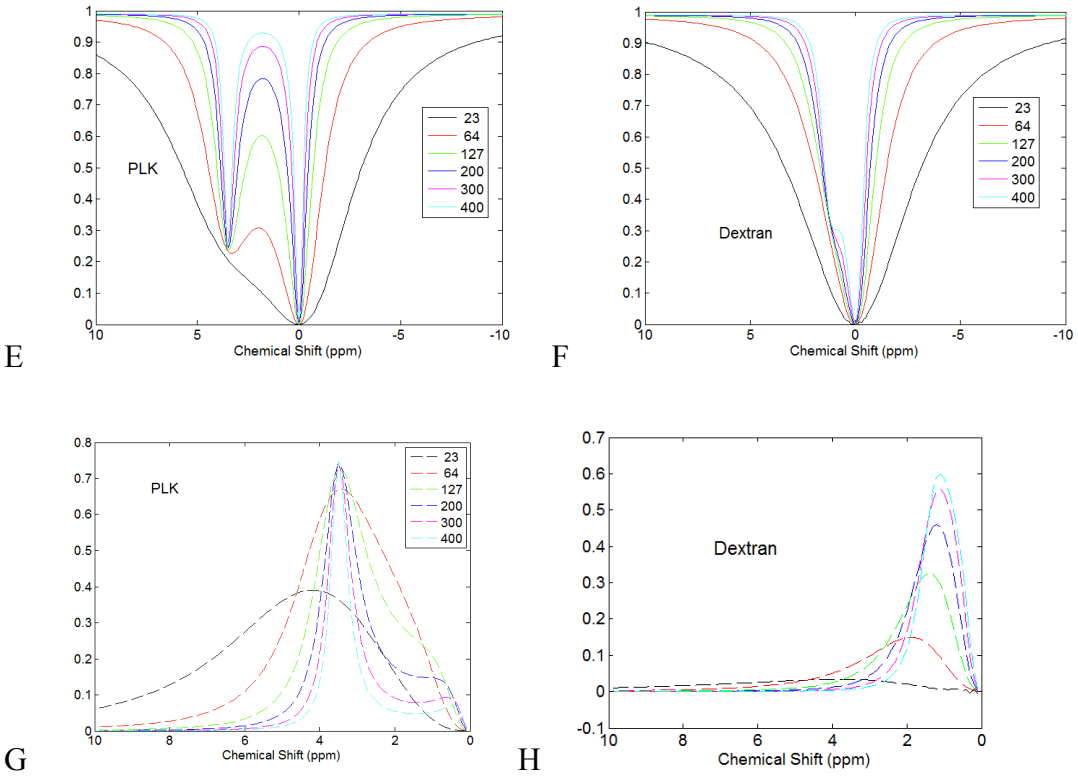

Figure 4. Simulated effect of moving to higher main field on chemical exchange mediated $R_{1\rho}$ dispersion for a two-pool model of peptides (PLK model on left) or sugars (DXT model on right). (T_{1a} = 3 sec T_{2a} = 2 sec, T_{1b} = 1 sec, T_{2b} = 30 msec, p_a = 0.99, p_b = 0.01, $\Delta\omega_b$ = 3.5 ppm or 1.2 ppm, k_{ba} = 140 Hz or 1 kHz)

4.a. Peptide model $R_{1\rho}$ dispersion with applied locking field (B_1) with increasing main field (B_0).

4.b. Sugar model $R_{1\rho}$ dispersion. Note the greater contribution of exchange to $R_{1\rho}$ dispersion in the sugar model due to the higher exchange rate.

4.c & d. SL contrast enhancement using Eq. 4. Note that with this method, contrast enhancement scales with main field.

4.e & f. CEST z-spectra for PLK model (left) and DXT model (right). CEST sensitivity also scales with main field, best shown in 4.f where sensitivity peaks above 127 MHz.

4.g & h. CEST MTR_{asym} for the PLK and DXT model, respectively. CEST is less sensitive to the DXT model due to the smaller chemical shift and higher exchange rates. This is shown in 4.h as the MTR_{asym} profile is low and broad below 300 MHz.

The CEST simulations in Figure 4.e shows the dramatic effect of moving from a main frequency of 23 to 400 MHz on the separation of the water and metabolite peak of the polypeptide. The MTR asymmetry plots for the peptide model in 4.g are very similar above 64 MHz with a MTR_{asym} value near 0.75. Figure 4.f demonstrates how the small chemical shift and rapid chemical exchange rate of the sugar results in a broad coalesced water peak below 200 MHz. Above 200 MHz, the $^{-}$OH shoulder becomes more pronounced, leading to a more distinct MTR asymmetry as shown in Figure 4.h. The MTR_{asym} peak approaches the simulated chemical shift of 0.6 ppm only as the main field increases above 2T, indicating less sensitivity to $^{-}$OH exchange.

Figure 5 demonstrates the effect of increasing chemical exchange rates within each model system at a main field strength of 400 MHz. Figures 5.a shows a small initial $R_{1\rho}$ value at the lowest simulated SLA (150 Hz) of ~ 2 s^{-1} when the exchange rate is low at 100 Hz, that increases to nearly 45 s^{-1} at 10 kHz exchange rate for the polypeptide model. Above 10 kHz, $R_{1\rho}$ becomes insensitive to ω_1 and the resulting $R_{1\rho}$ drops to ~16 s^{-1}. Note that due to the larger chemical shift ($\delta\omega_b$), the polypeptide model shows a much larger dispersion at equivalent rates when compared to the sugar model. The hydroxyl exchange mediated $R_{1\rho}$ dispersion in figure 5.b ranges from a low value of ~1.8 s^{-1} at the lowest measured SLA and exchange rate to ~14 s^{-1} at 5 kHz exchange rate. Above 5 kHz, the

sugar model's simulated $R_{1\rho}$ dispersion also becomes insensitive to ω_1 and the resulting $R_{1\rho}$ drops to ~9 s^{-1}. Figure 5.c and 5.d show the results of applying Eq. 4 to simulated data from Fig 5.a and 5.b. Contrast enhancement from Eq. 4 is maximized when $\omega_1(ex)$ is chosen to be around the mean of the R_2-R_1 value in the $R_{1\rho}$ dispersion curve which is near the sum of the chemical exchange rate and chemical shift. The point of maximum contrast increases with the chemical exchange rate and is shown in Figure 5.c and 5.d.

Figures 5.e through 5.h show the simulated CEST z-spectra and MTR asymmetry for the model polypeptide and sugar with increasing exchange rates. For the polypeptide in 5.e, as the exchange rate increases from the slow ($\delta\omega/k_{ba} > 1$) to the intermediate ($\delta\omega/k_{ba} \cong 1$) exchange regimes, the two peaks coalesce and result in a much reduced MTR asymmetry as shown in 5.g. By the time the exchange rate = 10 kHz, the MTR asymmetry is reduced fourfold. When the chemical shift is reduced from 3.5 to 1.2 ppm (polypeptide vs sugar) and the exchange rate increases, this drop occurs at even lower rates as shown in 5.g and 5.h.

A 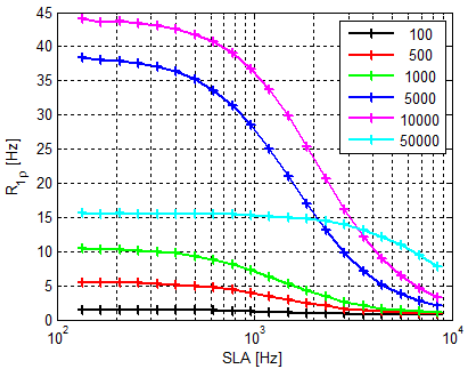

B 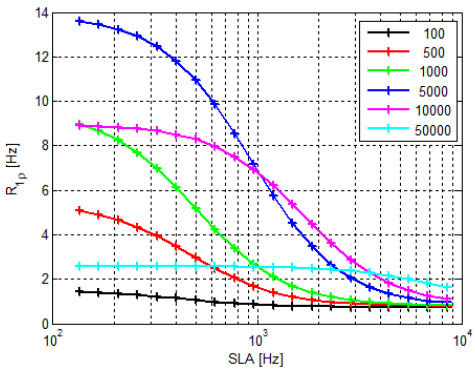

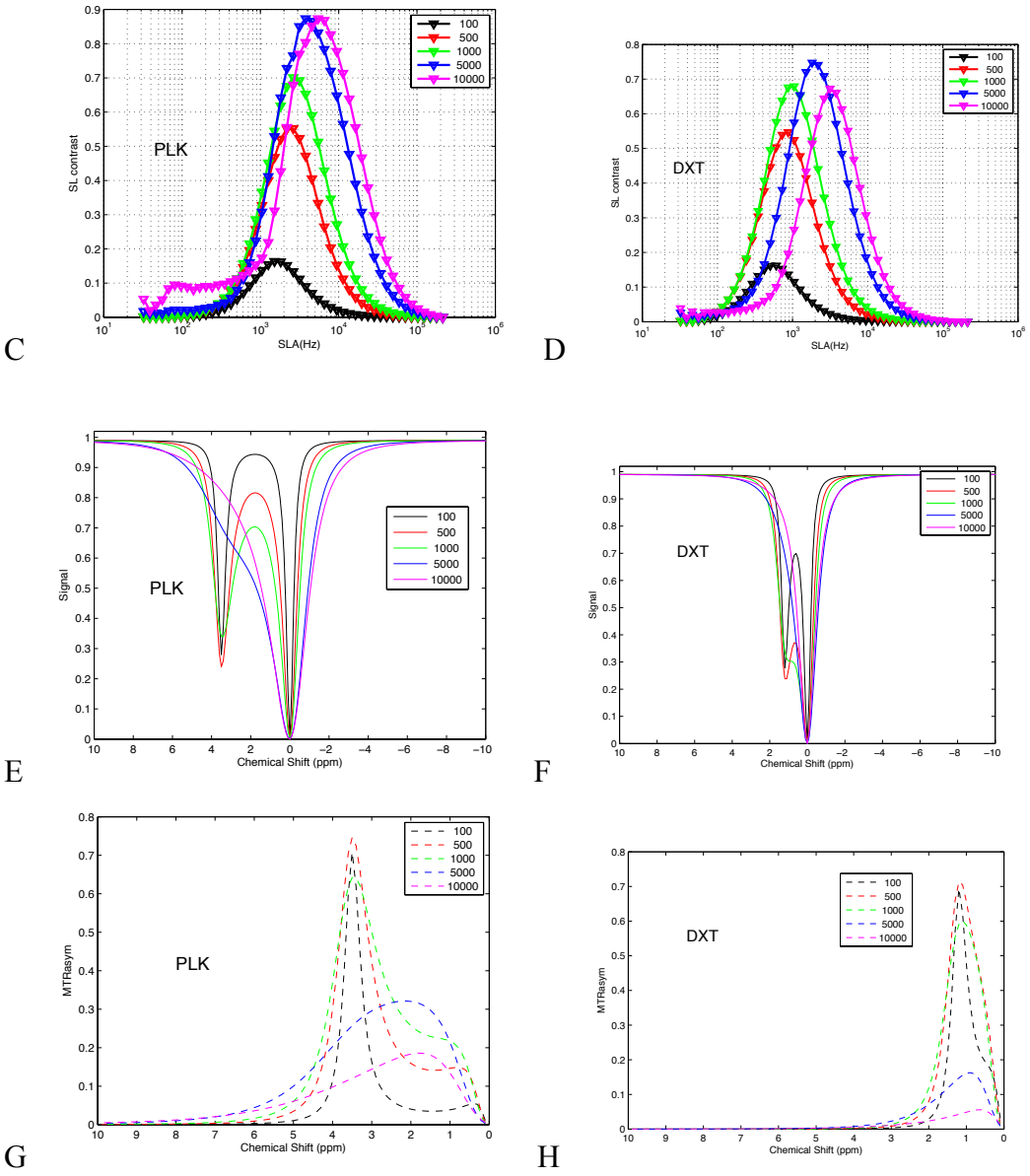

Figure 5. Simulated effect of changes in chemical exchange rate (k_{ba}) on $R_{1\rho}$ dispersion and CEST contrast in a two-pool model. (T_{1a} = 3 sec T_{2a} = 2 sec, T_{1b} = 1 sec, T_{2b} = 30 msec, p_a = 0.99, p_b = 0.01, $\Delta\omega_b$ = 3.5 ppm or 1.2 ppm, $\omega_0 = 2\pi$*400 MHz)

5.a. Peptide model $R_{1\rho}$ dispersion with increasing exchange rate. Note the greater contribution of exchange to $R_{1\rho}$ dispersion at high exchange rates for the peptide model as compared to the sugar model in 5.b.

5.b. Sugar model $R_{1\rho}$ dispersion with increasing exchange rate.

5.c & 5.d. Contrast enhancement with Eq. 4 with the value of $\omega_1(ex)$ chosen to be equal to the midpoint of the $R_{1\rho}$ dispersion curve, which is approximately equal to the sum of the chemical shift and exchange rates (in Hz). This method shows maximum contrast increasing with exchange rate. The DXT model in 5.d shows more separation between simulated rates than the PLK model.

5.e & f. CEST z-spectra for the PLK (left) and DXT model (right). Note how CEST contrast sensitivity decreases rapidly as line broadening causes the metabolite peak to coalesce into the water peak above 10 kHz exchange rates.

5.g & h. CEST MTR_{asym} for the PLK and DXT models, respectively. Note that as the chemical shift is smaller for the DXT model, line broadening occurs at lower frequency. This causes CEST contrast enhancement to be greatly reduced for exchange rates > 1 kHz.

The effect of increasing the concentration of the exchanging pool on $R_{1\rho}$ is shown in Figure 6. The $R_{1\rho}$ values increase monotonically with the concentration as seen in 6.a and 6.b. Although there is little $R_{1\rho}$ dispersion at low concentrations (< 0.01) for the slow exchange rate of 140 Hz in PLK, there is greater dispersion in DXT due to the higher exchange rate (1 kHz), despite the relatively smaller chemical shift (1.2 vs. 3.5 ppm). By inserting the dispersion data into Eq. 4, contrast enhancement plots were generated, and these demonstrate an increase with concentration as shown in Fig. 6.c and 6.d.

The effect of varying labile proton concentration on CEST contrast is simulated in Figures 6.e for the polypeptide and 6.f for the sugar model, respectively. The magnitude of the CEST contrast here depends little on the amount of solute present under the chosen conditions of irradiation. There is a slight conflation of the peaks shown in Fig. 6.e and 6.f at the $P_b = 0.05$ concentration that affects the MTR asymmetry shown in 6.g and 6.h,

giving the appearance of an additional exchanging species near 0.8 ppm most likely due to non-optimal power selection. A difference in MTR_{asym} of only 0.1 is observed between low and high concentrations in the polypeptide shown in Fig. 6.g. For the sugar in Fig. 6.h, slightly less sensitivity was shown with a MTR_{asym} value averaging near 0.6 and with slightly shifted peaks (ppm) with increasing concentration.

A

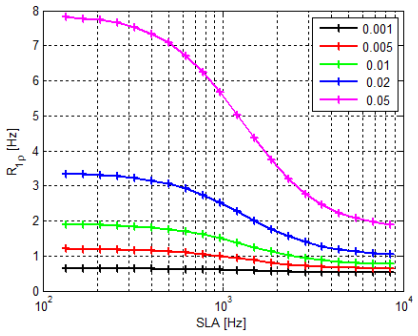

B

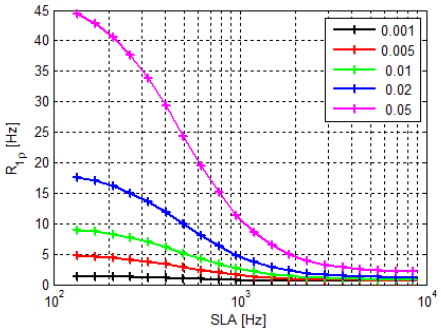

C

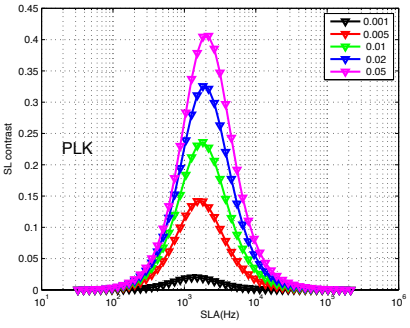

D

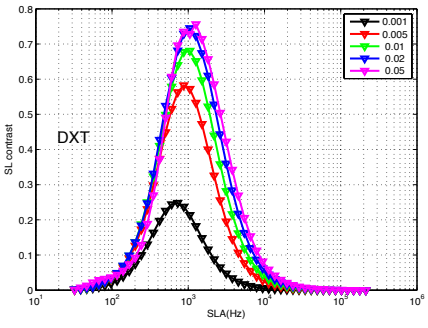

E

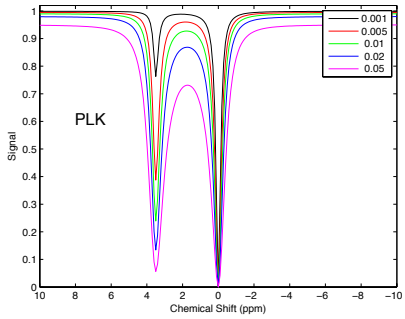

F

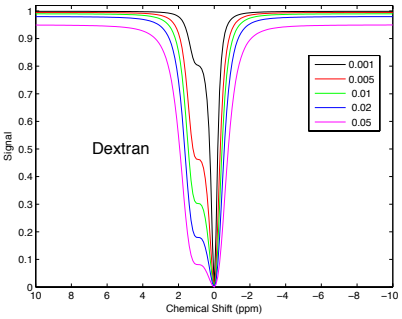

G 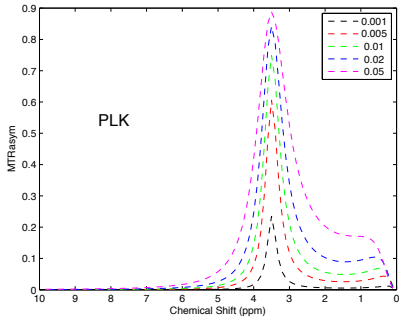

H 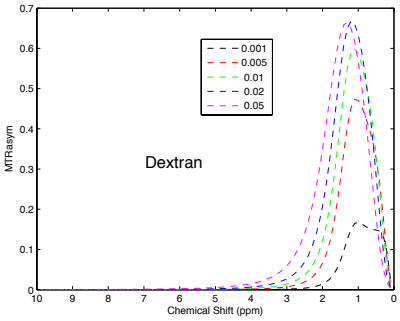

Figure 6. Simulated effect of increasing concentration of metabolite pool on $R_{1\rho}$ dispersion and CEST in a two-pool model. (T_{1a} = 3 sec T_{2a} = 2 sec, T_{1b} = 1 sec, T_{2b} = 30 msec, $\Delta\omega_b$ = 3.5 ppm or 1.2 ppm, k_{ba} = 140 Hz or 1 kHz, $\omega_0 = 2\pi$*400 MHz)

6.a. $R_{1\rho}$ dispersion for the peptide model (PLK). Note how dispersion is very small at low metabolite ($p_b < 0.01$) concentrations and the low simulated exchange rate (140 Hz).

6.b. $R_{1\rho}$ dispersion for the sugar model (DXT). Note the greater contribution of exchange to $R_{1\rho}$ dispersion in this model, attributed to the higher exchange rate (1 kHz), as compared to the peptide model in 6.a.

6.c & 6.d. SL contrast enhancement using Eq. 4 for both models. The potential contrast scales with the B-pool concentration in contrast with CEST method shown in 6.f and 6.h.

6.e & f. CEST z-spectra for the PLK model (left) and DXT model (right). Note how CEST contrast is relatively insensitive to pool size, and large contrast enhancement is available at low concentrations and at low exchange rates.

6.g & h. CEST MTR_{asym} for the PLK and DXT model, respectively.

Figure 7 highlights the relative contributions of two different chemically exchanging species on $R_{1\rho}$ dispersion. $R_{1\rho}$ dispersion curves simulated from the individual

contributions of NH^+ and ^-OH species at typical exchange rates are plotted in Figure 7.a. If the rates are reversed so that the NH^+ rate now is much faster than the ^-OH exchange rate, the contribution to $R_{1\rho}$ of the larger chemical shift species now dominates the dispersion curve. Fig. 7.b shows the combined contributions of NH+ and -OH groups at typical rates to $R_{1\rho}$ dispersion using a 3-pool model simulation. The simulation suggests that ^-OH exchange may dominate $R_{1\rho}$ dispersion at typical rates and chemical shifts. Eq. 4 was used to generate the plot in Figure 7.c and shows that contrast is dominated by ^-OH exchange and that the two rates are too close to be separated. Figure 7.d and 7.e show the simulated CEST z-spectrum and MTR_{asym} for the three-pool model system. The contribution of NH^+ and ^-OH exchange to the z-spectrum are plotted separately and in combination for each figure. The separate sugar and polypeptide exchanging peaks are clearly identified and show only a mild conflation near 2.2 ppm on the MTR_{asym} figure.

A

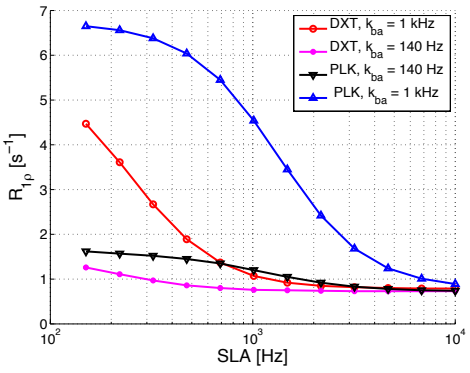

B

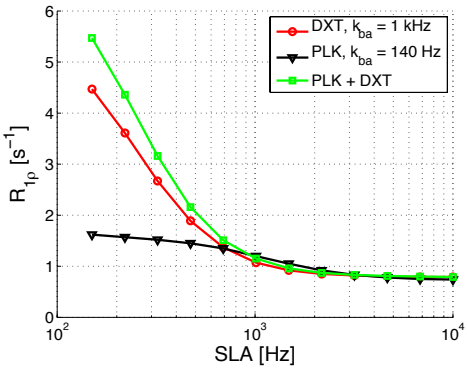

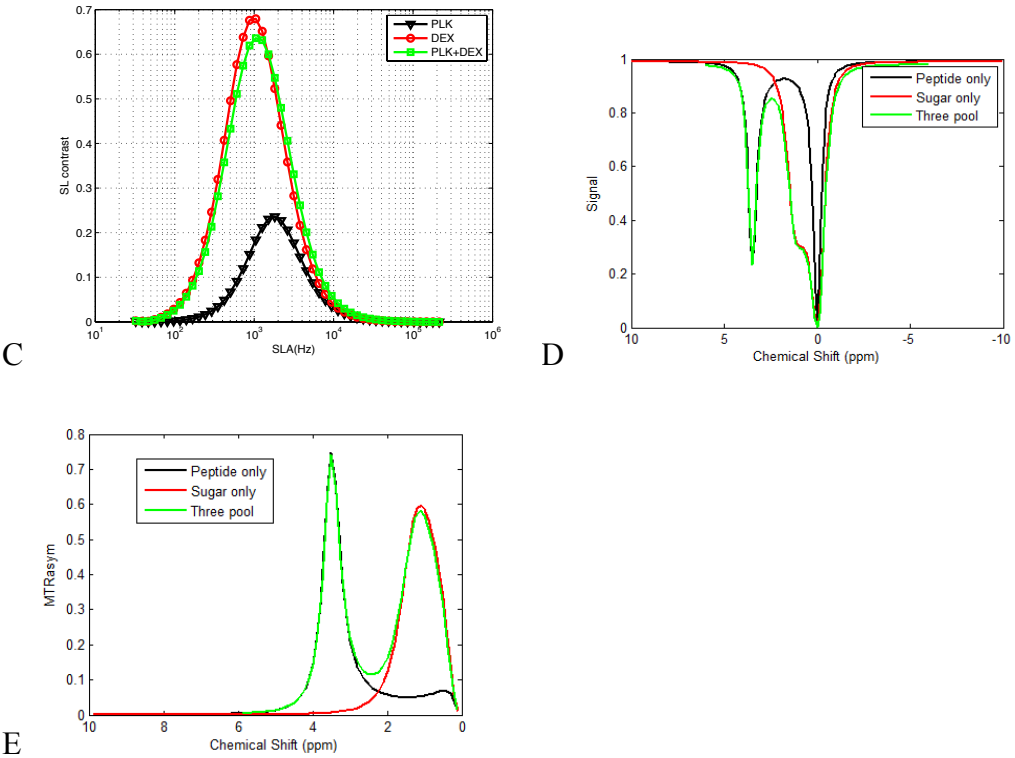

Figure 7. Demonstration of a three-pool model of proton relaxation on $R_{1\rho}$ dispersion and CEST contrast (as shown in Figure 1). This figure gives the simulated effects of multiple exchanging species and demonstrates the relative effects of slowly exchanging NH^+ groups vs. typically faster ^-OH groups at typical chemical shifts and exchange rates under physiologic conditions.

7.a. Contributions of exchange to $R_{1\rho}$ dispersion from ^-OH and NH^+ sites at typical (1 kHz and 140 Hz, respectively) and atypical rates (rates reversed). Note that exchange rate dominates the contribution to $R_{1\rho}$ dispersion irrespective of chemical shift.

7.b. The individual and combined predicted contribution of exchange at different sites to $R_{1\rho}$ dispersion at typical rates. This demonstrates that for a substance with an equal amount of peptide and sugar, the sugar dispersion contribution may dominate the overall $R_{1\rho}$ dispersion curve.

7.c. Contrast enhancement using Eq. 4. Note that potential contrast enhancement is dominated by DXT.

7.d & e. CEST z-spectrum and MTR_{asym} for combined 3-pool model. Note how, unlike $R_{1\rho}$ dispersion, the effects of each species may be separated by chemical shift.

DISCUSSION

The simulation results illustrate several unique features of both the spin locking and CEST techniques. The simulation results confirm that both CEST and SL techniques are sensitive to chemical exchange effects. Additionally, the characteristic limitations of the two techniques are such that each can provide complementary information about chemical exchange-based contrast. The chemical shift and exchange rate are the most important factors to consider when designing pulse sequences that are optimally sensitive to a particular exchanging system. Their relative frequencies determine the precise behavior of both SL and CEST contrast for the two model systems studied.

Imaging is being performed at ever-greater magnetic field strengths both clinically and in pre-clinical research, and the field strength at which a chemical exchange-based experiment is performed is of great importance, but field affects each method differently. At higher fields both CEST and SL imaging can provide images sensitive to specific exchange mechanisms as demonstrated in Figures 4 though 7. Values of $R_{1\rho}$ depend explicitly on B_0 because spin locking is sensitive to the time scales of the local fields that promote relaxation and in an exchanging system these depend on the frequency separation of the exchanging species and the lifetimes spent in each location. Increasing B_0 in SL experiments results in larger magnitude of dispersive effects that make the

effects of exchange rate less important. Conversely, when the saturating RF pulse in CEST has an ideal narrow-band frequency content, the CEST signal change does not depend explicitly on the chemical shift. Increasing B_0 clarifies where the exchanging peak is but not the magnitude of the shift. The effects are seen only indirectly as the resulting z-spectrum suffers from the effects of pulse bandwidth and direct saturation that must be optimized experimentally.

The effect of increasing B_0 from the low clinical range of 23 MHz (0.5 T) to the upper pre-clinical range of 400 MHz (9.4T) shows that for both the NH^+ (3.5 ppm) and ^-OH (1.2 ppm) model systems, an increase in $R_{1\rho}$ is expected. This is shown in Fig. 4.a for poly-L-lysine (PLK) and 4.b for dextran (DXT) with an increase in dispersion of nearly 2 and 9 times, respectively. This phenomenon is attributed to increased dephasing of spins as the water protons exchange back and forth between the species at a larger resonant frequency difference ($\delta\omega_b$). Applying Eq. 4 to the dispersion data, as shown in Fig. 4.c and 4.d, shows this effect more clearly as the point of maximum contrast scales with chemical shift. The variation of CEST response with B_0 largely reflects the effects of direct saturation of the water as mentioned above. The z-spectrum plots have improved peak separation due to reduced saturation effects with increasing main field, shown in 4.e and 4.f. The MTR_{asym} shown in Figure 4.g and 4.h also reflect this trend with a twofold increase in MTR for the polypeptide and a nearly 10x increase for the sugar. These observations are consistent with the findings of Ling et al. who showed an ever more distinct ^-OH peak with increasing main field (9). It is important to note that the modeled T_1 and T_2 values for each species were kept constant, consistent with literature values

measured at 200 MHz, throughout the range of simulated range of B_0. Even if these values were scaled appropriately with B_0, chemical exchange would dominate the simulated relaxation as demonstrated in similar simulations by Hills (28). Also note that the RF saturation power was not continuously optimized for each B_0 value and resonance frequency offset, as performed by Sun et al. (26).

Each technique shows unique chemical exchange contrast that is dependent on the exchange regime in which the experiment is performed. It is useful to identify exchange regimes where each technique has highest sensitivity. The effects of increasing chemical exchange rates on SL and CEST contrast with species of two different chemical shifts are shown in Figures 5. For instance, when comparing Figure 5.a and 5.e, CEST displays greater potential contrast sensitivity for the polypeptide in the slow exchange regime (where $\delta\omega/k_{ba} >> 1$) than the comparable $R_{1\rho}$ dispersion plot. In Fig. 5.a, at these rates and chemical shift, potential contrast enhancement from an image subtraction technique such as Eqs. 3 or 4 is very small as shown in Fig. 5.c. Sensitivity primarily to exchange rate may be described using Eq. 4 as shown in Figure 5.c and 5.d, which show that very little contrast enhancement may be expected from this method at slow exchange rates. Eq. 4 is maximized when $\omega_1(ex)$ is chosen to be the mid-point of the $R_{1\rho}$ dispersion curve, which depends on the chemical exchange rate and shift (expressed in Hz for Fig 5). Analytical derivations of this equality may be found in the work of Chopra et al. and Trott and Palmer (18,29). Thus, the smaller chemical shift of the dextran substance results in less overlap between the contrast curves. This implies that more distinct

contrast may be obtained from substances with smaller chemical shifts if exchange rates are sufficiently separated and sufficient B_1 power is available.

Note that the CEST z-spectrum in 5.e shows a large, distinct peak at 3.5 ppm at rates < 1 kHz. This is consistent with other authors' simulations and experimental findings on PLK which has an experimentally reported chemical shift of ~3.5 ppm and an exchange rate near 140 Hz (2,8,26). Figure 5.e shows the effect of exchange rate on CEST spectra and the impact of the smaller chemical shift from hydroxyl groups. Here, CEST contrast becomes negligible above a 1 kHz exchange rate as the system is pushed into the intermediate and fast regimes. This is contrasted by the SL technique shown in Fig. 5.b, which produces significant $R_{1\rho}$ dispersion at intermediate and fast rates. This regime is typical of hydroxyl exchange in sugars that is simulated here by the dextran model with a chemical shift of 1.2 ppm and exchange rates in the kHz range (17,30). These shifts and rates generate $R_{1\rho}$ dispersion curves consistent with simulations by Hills and Trott and Palmer, and with experiments by Jin et al. among others (15,20,29).

When exchange is very fast compared to the chemical shift ($\delta\omega/k_{ba} < 1$), line broadening adversely affects the CEST experiment's ability to produce difference images as the exchanging peak coalesces with the water resonance. For example, at rates greater than 1 kHz, the $^{-}$OH peak broadens into the water peak and the corresponding MTR asymmetry shown in 5.h reduces to near zero. Thus, an increase in k_{ba} reduces contrast in CEST, but for SL techniques, fast exchange between the water and metabolite site promotes rapid signal dephasing that may be recovered with the locking field (B_1) as shown in Figures

5.a and 5.b. The larger this dephasing effect is, the greater the contrast enhancement that may be obtained as per Eq. 3. However, at extremely high rates (> 10 kHz) $R_{1\rho}$ dispersion loses sensitivity to ω_1 and $R_{1\rho}$ begins to drop as shown in Fig. 5.a and 5.b. This may be explained by referring to Eq. 14, an analytic expression of $R_{1\rho}$ dispersion, which is a simplification of the Bloch equations given certain assumptions (18,31). The expression derived by Chopra et al. may be simplified under the reasonable conditions of $R_{1b}<R_{2b}<r_b$ as:

$$R_{1\rho,\mathrm{obs}} \cong R_{2,A} + P_B R_{2B}\left[1 + \frac{\frac{r_B}{R_{2B}} * \Delta\omega_B^2}{r_B^2 + \Delta\omega_B^2 + \omega_1^2}\right] \quad [14]$$

where P_b is the size of the B pool, $\Delta\omega_b$ is the chemical shift, r_b is the exchange rate from pool B to A, and ω_1 is the locking field amplitude.

As r_b becomes extremely high, the second term in brackets approaches zero and $R_{1\rho,\mathrm{obs}}$ decreases and becomes exchange insensitive. However, these rates are typically outside the range of physiologic relevance (32). At extremely slow rates, SL contrast may be primarily determined by chemical shift as shown in Figure 5.a, where the midpoint of the dispersion curve is near the chemical shift frequency.

In addition to exchange rate and chemical shift, the effect of pool size variation was modeled. The two techniques demonstrated different sensitivity to variance in this parameter under the conditions examined. CEST contrast does not scale in proportion to concentration, unlike SL. Figures 6.a and 6.b show a linear dependence on concentration

for SL at low locking fields for both the polypeptide and sugar models respectively. This dependence becomes non-linear when analyzed with Eq. 4 as shown in Figures 6.c and 6.d. The potential CEST contrast shown in Figure 6.e for the peptide model and 6.f for the sugar model is relatively unchanged for each simulated concentration, implying that CEST may be less suited to quantify concentrations of exchanging species. However, CEST is potentially more sensitive to the presence of very low concentrations as MTR_{asym} was large compared to the very small $R_{1\rho}$ dispersions for both species below $p_b = 0.005$, shown in Figure 6.

Figure 7 illustrates the relative contributions to $R_{1\rho}$ dispersion of exchanging agents with disparate rates and chemical shifts in three-pool model simulations. Poly-L-lysine has a chemical shift of ~3.5 ppm and a slow chemical exchange rate of backbone amides of ~140 Hz. Sugars such as dextran have chemical shifts near 1 ppm and exchange rates an order of magnitude greater than amides. These relative differences may have pronounced effects on expected signal contrast. These typical rates were simulated in Figure 7 for both CEST and SL contrast. Additionally, Figure 7.a shows how the contrast may behave if the exchange of each species were reversed. The combined ^{-}OH and NH^{+} substance shown in Figure 7.b at biologically typical rates shows that ^{-}OH exchange will dominate $R_{1\rho}$ dispersion in mixtures, consistent with the findings of Reddy et al. who noted a larger contribution from ^{-}OH exchange to CEST than from NH^{+} sites in studies on chondroitin sulfate (9). This implies that a faster exchange rate in SL may be much more important for contrast than chemical shift. The composite dispersion curve shows little evidence of being separable into identifiable components or regimes. Figures 7.d and 7.e

demonstrates a main experimental difference between CEST and spin-locking techniques in that the peaks of the two exchanging species are clearly identifiable in the z-spectra and MTR asymmetry. The peaks are separated by about 2.3 ppm with little mutual overlap. Thus identification can be unambiguous based on the frequency offset of each peak even in a mixture.

There are several notable technical limitations for the simulations presented in this work that have ramifications for imaging experiments. For the CEST simulations, *cw*-shaped RF pulses were applied and MTR_{asym} values were calculated for two model systems. However, given specific absorption rate (SAR) limitations, it is difficult to implement such pulses clinically. Therefore the pulsed CEST technique is preferred for this application (33); however, there is no analytical solution to Bloch equations with shaped RF pulses. This makes the simulations very time-consuming, and thus direct comparisons of these simulations to the pulsed technique were not attempted. For spin locking, the limit on this technique's applicability to clinical imaging is given by the stable pseudo-*cw*-power achievable by the RF amplifier and also SAR considerations. This is typically in the ~10-20 kHz range on small animal systems and ~1-2 kHz for human imagers. A maximum B_1 of 10 kHz was used for the simulations here, and the effects are most notable in Figure 6.e where with a large chemical shift and high exchange rates, the contrast enhancement curves appear truncated at 10 kHz. The lower limit on power is typically given by the uniformity of the B_1 and B_0 fields (both of which also affect CEST) (2,28). Variations in B_1 affect the flip angle applied to the sample, and thus the average applied SLA. For B_0 variations, only nuclei whose line-width is less than γB_1 will be

"locked" and thus not experience dephasing effects. Typically, this lower limit is dictated by the sample of interest and is on the order of ~200 Hz in a clinical system. These effects may be mitigated by SL pulse sequence modifications that are employed in Part II (13). In addition, while it is difficult to directly compare calculated % contrast from Eq. 3 or the ratio in Eq. 4 to MTR_{asym} from Eq. 2, the available signal to noise ratio will be important to determining the feasibility of each method. Eqs. 2 and 3 rely on a normalized subtraction technique, whereas Eq. 4 uses a normalized difference in squared signal. Thus Eq. 4 may be expected to have reduced SNR as compared to the other techniques. These effects will be explored further in Part II.

CONCLUSIONS

We have demonstrated with simulations on model systems that CEST and spin locking are both sensitive to chemical exchange effects that scale with the main field at which the experiment is observed. We have shown that the CEST technique may be particularly suited to exploring contrast from systems in the slow-to-intermediate exchange regime and with low metabolite concentrations. SL is more suited to making dispersion measurements in an imaging context in the intermediate-to-fast regime where other approaches, such as CEST or CPMG, may be technically difficult. Therefore the techniques may be thought of as providing complementary information about chemically exchanging systems.

In Part I, we have demonstrated that a variety of structural and chemical factors can be modeled for their effects on $T_{1\rho}$ relaxation dispersion and CEST contrast enhancement. Part II will focus on the results of relaxation dispersion and CEST measurements on simple biologically relevant models of chemical exchange, with the goal of validating and further illuminating the simulations in Part I. The experiments in Part II will measure chemical exchange effects in simple polypeptide and sugar system that avoid many of the complexities of large heterogeneous tissue systems and allows for a more clear understanding of the effects of chemical exchange on rotating frame relaxation and CEST contrast.

ACKNOWLEDGEMENTS

NCRR 1S10 RR17799

NIH R01 EB000214

REFERENCES

1. Ward KM, Aletras AH, Balaban RS. A new class of contrast agents for MRI based on proton chemical exchange dependent saturation transfer (CEST). J Magn Reson 2000;143(1):79-87.
2. Zhou JY, van Zijl PCM. Chemical exchange saturation transfer imaging and spectroscopy. Prog Nucl Mag Res Sp 2006;48(2-3):109-136.
3. McMahon MT, Gilad AA, DeLiso MA, Berman SM, Bulte JW, van Zijl PC. New "multicolor" polypeptide diamagnetic chemical exchange saturation transfer (DIACEST) contrast agents for MRI. Magn Reson Med 2008;60(4):803-812.
4. Zhang S, Merritt M, Woessner DE, Lenkinski RE, Sherry AD. PARACEST agents: modulating MRI contrast via water proton exchange. Acc Chem Res 2003;36(10):783-790.
5. Woessner DE, Zhang S, Merritt ME, Sherry AD. Numerical solution of the Bloch equations provides insights into the optimum design of PARACEST agents for MRI. Magn Reson Med 2005;53(4):790-799.
6. Aime S, Calabi L, Biondi L, De Miranda M, Ghelli S, Paleari L, Rebaudengo C, Terreno E. Iopamidol: Exploring the potential use of a well-established x-ray contrast agent for MRI. Magn Reson Med 2005;53(4):830-834.
7. Longo DL, Dastru W, Digilio G, Keupp J, Langereis S, Lanzardo S, Prestigio S, Steinbach O, Terreno E, Uggeri F, Aime S. Iopamidol as a responsive MRI-chemical exchange saturation transfer contrast agent for pH mapping of kidneys: In vivo studies in mice at 7 T. Magn Reson Med 2010.

8. van Zijl PCM, Jones CK, Ren J, Malloy CR, Sherry AD. MR1 detection of glycogen in vivo by using chemical exchange saturation transfer imaging (glycoCEST). P Natl Acad Sci USA 2007;104(11):4359-4364.

9. Ling W, Regatte RR, Navon G, Jerschow A. Assessment of glycosaminoglycan concentration in vivo by chemical exchange-dependent saturation transfer (gagCEST). Proc Natl Acad Sci U S A 2008;105(7):2266-2270.

10. Wolff SD, Balaban RS. Magnetization transfer contrast (MTC) and tissue water proton relaxation in vivo. Magn Reson Med 1989;10(1):135-144.

11. van Zijl PCM, Yadav NN. Chemical exchange saturation transfer (CEST): What is in a name and what isn't? Magnet Reson Med 2011;65(4):927-948.

12. Sepponen RE, Pohjonen JA, Sipponen JT, Tanttu JI. A method for T1 rho imaging. J Comput Assist Tomogr 1985;9(6):1007-1011.

13. Witschey WR, 2nd, Borthakur A, Elliott MA, Mellon E, Niyogi S, Wallman DJ, Wang C, Reddy R. Artifacts in T1 rho-weighted imaging: compensation for B(1) and B(0) field imperfections. J Magn Reson 2007;186(1):75-85.

14. Hills BP. The Proton-Exchange Cross-Relaxation Model of Water Relaxation in Biopolymer Systems. Mol Phys 1992;76(3):489-508.

15. Hills BP. The Proton-Exchange Cross-Relaxation Model of Water Relaxation in Biopolymer Systems .2. The Sol and Gel States of Gelatin. Mol Phys 1992;76(3):509-523.

16. Duvvuri U, Goldberg AD, Kranz JK, Hoang L, Reddy R, Wehrli FW, Wand AJ, Englander SW, Leigh JS. Water magnetic relaxation dispersion in biological systems: the contribution of proton exchange and implications for the noninvasive

detection of cartilage degradation. Proc Natl Acad Sci U S A 2001;98(22):12479-12484.

17. Hills BP, Babonneau F. A quantitative study of water proton relaxation in packed beds of porous particles with varying water content. Magn Reson Imaging 1994;12(6):909-922.

18. Chopra S, Mcclung RED, Jordan RB. Rotating-Frame Relaxation Rates of Solvent Molecules in Solutions of Paramagnetic-Ions Undergoing Solvent Exchange. J Magn Reson 1984;59(3):361-372.

19. Goffeney N, Bulte JW, Duyn J, Bryant LH, Jr., van Zijl PC. Sensitive NMR detection of cationic-polymer-based gene delivery systems using saturation transfer via proton exchange. J Am Chem Soc 2001;123(35):8628-8629.

20. Jin T, Autio J, Obata T, Kim SG. Spin-locking versus chemical exchange saturation transfer MRI for investigating chemical exchange process between water and labile metabolite protons. Magn Reson Med 2010.

21. McMahon MT, Gilad AA, Zhou J, Sun PZ, Bulte JW, van Zijl PC. Quantifying exchange rates in chemical exchange saturation transfer agents using the saturation time and saturation power dependencies of the magnetization transfer effect on the magnetic resonance imaging signal (QUEST and QUESP): Ph calibration for poly-L-lysine and a starburst dendrimer. Magn Reson Med 2006;55(4):836-847.

22. Bloch F. Nuclear Induction. Physical Review 1946;70(7-8):460.

23. McConnell HM. Reaction Rates by Nuclear Magnetic Resonance. The Journal of Chemical Physics 1958;28(3):430-431.

24. Kogen F. Comparison of chemical exchange saturation transfer (CEST) and T1ρ MRI for measurement of proton chemical exchange between metabolites and water at 7T. Proc ISMRM 2010;3003(6499).

25. Hills BP. Water proton relaxation in dilute and unsaturated suspensions of non-porous particles. Magn Reson Imaging 1994;12(2):183-190.

26. Sun PZ, van Zijl PC, Zhou J. Optimization of the irradiation power in chemical exchange dependent saturation transfer experiments. J Magn Reson 2005;175(2):193-200.

27. Hills BP, Wright KM, Belton PS. Nmr-Studies of Water Proton Relaxation in Sephadex Bead Suspensions. Mol Phys 1989;67(1):193-208.

28. Hills B. Magnetic resonance imaging in food science. New York: Wiley; 1998. ix, 342 p. p.

29. Trott O, Palmer AG. Theoretical study of R-1p rotating-frame and R-2 free-precession relaxation in the presence of n-site chemical exchange. J Magn Reson 2004;170(1):104-112.

30. Hills BP, Cano C, Belton PS. Proton Nmr Relaxation Studies of Aqueous Polysaccharide Systems. Macromolecules 1991;24(10):2944-2950.

31. Trott O, Palmer AG, 3rd. R1rho relaxation outside of the fast-exchange limit. J Magn Reson 2002;154(1):157-160.

32. Liepinsh E, Otting G. Proton exchange rates from amino acid side chains - Implications for image contrast. Magnet Reson Med 1996;35(1):30-42.

33. Sun PZ, Benner T, Kumar A, Sorensen AG. Investigation of optimizing and translating pH-sensitive pulsed-chemical exchange saturation transfer (CEST) imaging to a 3T clinical scanner. Magn Reson Med 2008;60(4):834-841.

CHAPTER VI

EXCHANGE-MEDIATED CONTRAST MECHANISMS FOR CEST AND SPIN-LOCK IMAGING PART II: EXPERIMENTAL STUDIES ON MODEL SYSTEMS

ABSTRACT

Chemical exchange saturation transfer (CEST) and rotating frame ($R_{1\rho}$) dispersion measurements with spin-locking (SL) techniques both exploit novel sources of endogenous contrast in magnetic resonance imaging (MRI) and are particularly sensitive to chemical exchange effects. In Part I we presented simulations of the relaxation behaviors of two relevant biologic samples to investigate the influence of specific factors on MR signals. In Part II, we confirm and illustrate further these predictions with experimental studies on biologic samples of interest.

Measurements of rotating frame ($R_{1\rho}$) dispersion and CEST z-spectra were performed on biologically important polypeptides and sugars. Using these data, a novel imaging protocol based on rotating frame dispersion imaging, which emphasizes contrast originating from species that exchange at specific rates (as opposed to chemical shifts) is demonstrated.

We show that both CEST and SL imaging may generate contrast in MRI from chemically exchanging protons especially at high fields. The CEST technique may be particularly sensitive to species in the slow and intermediate exchange regimes with large chemical shifts (> 2ppm). The SL technique may produce greater contrast when the exchanging species has a small resonant frequency offset (< 2 ppm) and / or exchanges more rapidly in the intermediate to fast exchange regimes. SL contrast increases more than CEST effects with increasing main field (B_0), and may be more directly related to the concentration of exchanging protons. Both techniques provide a means to produce images sensitive to specific types of exchanging protons in biological media.

Key words: CEST, spin lock, $R_{1\rho}$, chemical exchange

INTRODUCTION

There is continuing interest in understanding and exploiting novel mechanisms that modulate proton signals in magnetic resonance imaging (MRI), and in the use of both endogenous and exogenous sources of contrast. Proton exchange between water and labile groups in other molecules is one such mechanism that may be sensitive to the presence and behaviors of specific chemical components within a mixture. Methods that monitor magnetization transfer such as chemical exchange saturation transfer (CEST) can provide direct measurements of exchange and rely on the ability to select labile protons based on their chemical shift. Other approaches, notably T_2 and $T_{1\rho}$ sequences, may also

be affected by exchange and rely on the ability to modify dephasing caused by exchange on specific time scales. The dynamics of protons in exchange with amide (RC(O)NR'R, abbreviated here as NH^{+}) and hydroxyl (^{-}OH) sites on polymers, peptides, or sugars, have been recently exploited to generate novel endogenous contrast in CEST experiments (1-3). Alternately, exogenous contrast agents incorporating paramagnetic metals such as europium have been used to shift proton precession frequencies to allow increased exchange effects (paraCEST) (4,5), while common x-ray contrast agents such as Iohexol (Omnipaque®, GE Healthcare) or Iopamidol (Isovue®, Bracco), which contain numerous amide and hydroxyl groups have also been shown to produce significant effects (6,7). Tissue constituents such as glycogen (glycoCEST) and gycosaminoglycan (gagCEST) have been used to generate contrast in a similar fashion(8,9). Polypeptides and sugars are important potential modulators of contrast in tissues, and they have recently been studied as potential CEST reporter agents *in vitro* (1,3) and as sources of chemical exchange contrast with spin lock imaging (10).

In Part I we performed simulations to investigate the factors that affect signals in CEST and spin lock imaging and to quantify how exchange parameters modify contrast. In Part II we experimentally validate the simulations of Part I and show how SL and CEST methods are differentially sensitive to exchange properties such that they have complementary abilities to characterize samples. The differences in sensitivity of CEST and SL techniques to chemical exchange effects that evolve in certain experimental regimes were predicted theoretically in Part I. The experiments in Part II are designed to

illustrate these regimes and to quantify endogenous contrast in simple polypeptide and sugar systems of biologic interest.

CEST methods employ radio frequency (RF) saturation of an exchanging species, which is then transferred to water, reducing the measured water MR signal. The change in water signal or image contrast depends mainly on the exchange rate and the relaxation times of the exchanging species. To maximize CEST contrast, a RF pulse may be applied at the resonance frequency offset of a specific metabolite (typically several ppm from the water peak (ω_0 = 0 ppm)). The saturated protons then exchange with the water peak and the reduced signal is then acquired. If the off-resonance irradiation pulse is swept across a range of frequencies surrounding the water peak, a spectrum of the resulting signal intensity at each frequency step is termed a "z-spectrum". Peaks in this z-spectrum identify resonance frequency offsets of specific exchanging species. However, the applied pulse may also alter the water signal because of direct saturation or non-specific magnetization transfer (11) with other broad resonances, making the measurement depend on other experimental parameters such as the pulse bandwidth relative to the frequency offset. Generally, two images at opposite frequency offsets are acquired for CEST imaging. The difference in the normalized saturation contrast on opposite sides of the water peak is then the magnetic transfer ratio asymmetry (MTR_{asym}).

An alternate method of exploring chemical exchange-based contrast uses spin-locking (SL) techniques. In a common implementation, a 90-degree adiabatic half-passage (AHP) pulse nutates longitudinal magnetization to the transverse plane, and is followed by a

hard pulse with a spin lock amplitude (SLA) and duration (SLT) along the y-axis. From there, another 90-degree reverse half-passage (RHP) pulse returns magnetization vector to the longitudinal axis, and the residual transverse magnetization is spoiled. An imaging sequence may then be used to read the $T_{1\rho}$-weighted signal. Recent improvements to this sequence such as the alternation of the phase of the applied SL pulse and the addition of a 180-degree refocusing pulse to reduce the effects of B_0 variations have been explored by Witschey et al. (12). Measurements of relaxation rates in the rotating frame ($R_{1\rho}$ and $R_{2\rho}$) with these techniques have been shown to be sensitive to molecular motions and interactions on the time scale of the locking field (13,14). Observed variations in $T_{1\rho}$ with locking-field strength ($T_{1\rho}$ dispersion) provides information on molecular motions and interactions such as chemical and diffusive exchange in tissues (15,16).

Quantitative measurements of $T_{1\rho}$ dispersion may be used to estimate the exchange rates of an exchanging species when the dispersion data are fit to an appropriate model (14,17-19). Although the contributions of chemical exchange to relaxation in simple peptide and monosaccharide systems have been studied previously, the contribution of various types of exchanging species (NH^+ vs. ^-OH, etc) on the origins of $T_{1\rho}$ dispersion in more complex biological samples have not been well studied, and there are few data describing important exchange parameters. Quantification of the concentrations of exchanging sites and their exchange rates would potentially allow distinctions to be made between different media *in vivo* and provide a way to tie specific biochemical tissue properties to image contrast.

CEST and SL techniques are both sensitive to chemical exchange effects, but they depend on different experimental aspects and influences. For example, CEST is most sensitive to slow CE interactions where the chemical shift of the exchanging species ($\delta\omega$) is greater than the exchange rate (k_{ba}). This sensitivity changes as k_{ba} increases relative to $\delta\omega$ into the "intermediate" exchange regime where $\delta\omega/k_{ba} \cong 1$ and line broadening begins to attenuate CEST's ability to select solely for the metabolite peak with an RF pulse while not simultaneously saturating the water peak. As the exchange rate increases into the fast-exchange regime ($\delta\omega/k_{ba} << 1$) the two peaks coalesce and the CEST technique becomes untenable. However, at these higher exchange rates chemical exchange may still modify $R_{1\rho}$ if the locking field frequency is sufficiently high. Fortuitously, exchange processes of biological interest occur at frequencies well within the range of practical B_1 fields achievable for imaging, at least for pre-clinical systems, so spin locking is a viable approach to modulate exchange based contrast (10,15).

Following the theoretical and simulation predictions of Part I, here we also demonstrate that $T_{1\rho}$ dispersion may be used in conjunction with a novel image subtraction method to emphasize the presence of nuclei characterized by specific exchange rates (rather than chemical shifts) and thereby used to generate novel image contrast. This approach is therefore complementary to CEST imaging, which provides image contrast based on nuclei that exchange at a particular resonance frequency offset to water. The experiments on endogenous sources of contrast such as polypeptides and sugars are designed to illustrate and verify the theoretical framework elucidated in Part I.

METHODS

Experimental Studies

Solutions of varied concentrations of polypeptides and sugars were created in 0.6 ml plastic tubes in 1X phosphate-buffered saline (PBS) and titrated to pH 7.4. All chemicals were purchased from Sigma-Aldrich (St. Louis, MO).

To test the effects of changing the exchangeable species, samples of poly-L-threonine (PLT, P8077), poly-L-arginine (PLR, P4663), and poly-L-lysine (PLK, P7890) at 10 mg/mL of molecular weight ~15 kDa were made. These three polypeptides have previously been identified in a study of a wide range of compounds as having a particularly large CEST effects by McMahon et al. (3). Their structures are shown in Figure 1 and were generated from the National Institutes of Health PubChem database (http://pubchem.ncbi.nlm.nih.gov/). The PLT molecule contains one backbone NH^+ and a single side-chain ^-OH exchangeable group per lysine sub-unit at chemical shifts of ~3.5 and ~0.8 ppm respectively. The PLR molecule contains two side-chain guanidyl NH_2 (gNH_2) groups and one backbone NH^+ per arginine sub-unit at ~1.8 and ~3.7 ppm respectively. The PLK molecule contains one side-chain NH_2 and a backbone NH^+ group at ~3.6 ppm.

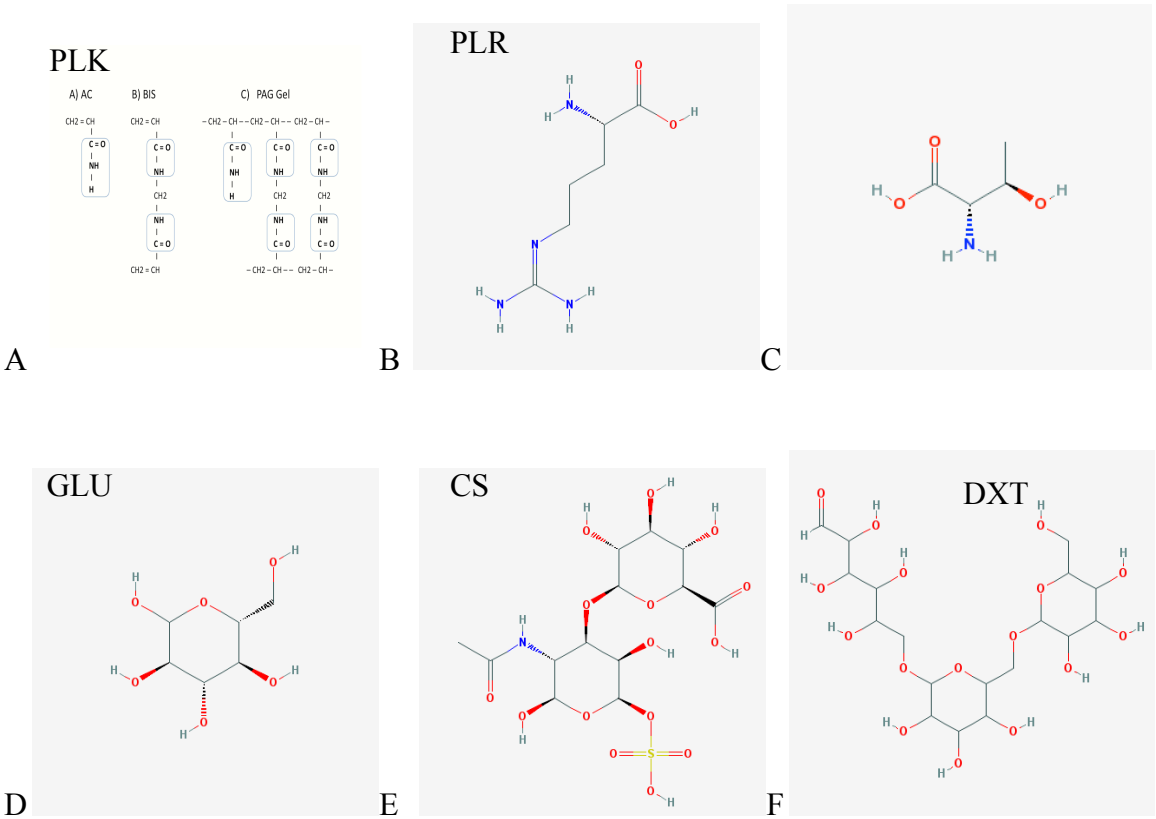

Figure 1. Models of chemical exchange in a biologic system. The images reference the corresponding National Center for Biological Information (PubChem) CID numbers.

1.a. Lysine (CID: 5962) sub-unit of poly-L-lysine with exchangeable amide (RC(O)NR'R) groups that resonate collectively near 3.69 ppm from water (0 ppm).

1.b. Arginine (CID: 6322) sub-unit of poly-L-arginine with exchanging guadinyl NH^+ (gNH_2) groups.

1.c. Threonine (CID: 6288) sub-unit of poly-L-threonine with exchanging NH^+ and ^-OH groups.

1.d. Glucose molecule (CID: 5793) with 3 distinct hydroxyl (^-OH) exchanging sites.

1.e. Chondroitin Sulfate (CID: 24766), a sulfated glycosaminoglycan, that carries multiple exchanging ^-OH and a single NH^+ site.

1.f. Dextran (CID: 4125253), a poly-glucose molecule that is formed from multiple glycosidic linkages at the α-1,6 or α-1,3 sites on the glucose sub-unit and carries exchanging $^{-}$OH sites that resonate near 1.2 ppm.

Samples of 40% (wt/wt) glucose (G8270), and dextran (D9260) were created both in distilled water and in 1X PBS at pH 7.4. Samples of 10% (wt/wt) chondroitin sulfate (CS, C4384) were also created in water and PBS, as they proved insufficiently soluble at and above a 20% concentration. Samples in PBS were diluted by half four times to create different concentrations. Samples in water were titrated to a pH range of 3 through 11 in 5 steps.

$T_{1\rho}$ dispersions were measured with Varian 9.4T and 4.7T spectrometers (Varian Medical Systems, Palo Alto, CA) each with a 10 mm loop-gap coil. The spin-locking sequence consists of an adiabatic 90-degree pulse (AHP), followed by on-resonance SL pulse and readout. Temperature was monitored by thermocouple connected to an animal physiologic monitoring system (SA Instruments, Stony Brook, NY). All measurements were maintained at 37 °C. The SL pulse was varied in time increments between 20 ms and 1 sec, and also in amplitude between 2π*(150 and 10 kHz). TR was set at ~5 times T_1 of the sample solutions.

CEST measurements were performed with a continuous wave (*cw*) method, which consists of an 8 second *cw* saturation pulse with TR of 20 sec. The RF saturation power

was set as 1μT. RF frequency offset was arrayed between +6 and -6 ppm, and stepped in 0.1 ppm increments.

Finally, magnetic resonance imaging (MRI) experiments were performed on the samples in a water bath prepared with 3 mM $MnCl_4$. The sequence consisted of a SL pulse as described by Witschey et al. followed by a fast spin-echo acquisition (20). Ten SLT were acquired as before at twelve spin lock amplitudes (SLA) between 2π*(150 Hz and 10 kHz). Other imaging parameters included: FOV = 25 x 25 x 1 mm, matrix = 64 x 128 x 1, TR = 4 sec, TE = 10 ms, ETL = 8, NEX = 1.

Data Analysis

The magnetization transfer ratio (MTR) and MTR_{asym} were calculated using the expressions:

$$MTR = 1 - \frac{S(\delta)}{S(0)} \qquad [1]$$

$$MTR_{asym} = \frac{S(-\delta) - S(+\delta)}{S(0)} \qquad [2]$$

$T_{1\rho}$ values were calculated using a three-parameter, least squares fit of signal vs. spin-lock time (SLT) to a monoexponential decay function for each spin-lock amplitude (SLA) in MATLAB using the Levenberg-Marquardt algorithm (21) as described by Eq. 3.

$$S(SLT) = S_0 esp \frac{-SLT}{T_{1\rho}} + C \qquad [3]$$

In this equation, $T_{1\rho}$ is the rotating frame decay constant, M_0 is the initial magnetization vector, the locking field duration is SLT, and C is a constant.

Chopra et al. modified the Bloch equations and showed how, under specific conditions, an experiment measuring $R_{1\rho}$ at different locking field strengths (B_1) may be used to determine solvent exchange rate (17). Over the limited range of locking frequencies usually available in MR imaging systems, there are negligible variations in the dipolar contributions to longitudinal relaxation, so Chopra's equation may adequately describe rotating frame relaxation in a two-pool system as given in Eq. 4.

$$R_{1\rho} = R_{2f} + p_b r_b \left(R_{2b} \left(R_{2b} + r_b \right)^{-1} \right) \left\{ \frac{\left(R_{1b} + r_b \right) \left(R_{2b} + r_b + \frac{\Delta\omega_b^2}{R_{2b}} \right) + \omega_1^2}{\left(R_{1b} + r_b \right) \left(R_{2b} + r_b + \frac{\Delta\omega_b^2}{R_{2b} + r_b} \right) + \omega_1^2} \right\} \qquad [4]$$

In Eq. 4, R_{2a} is the relaxation rate of free water, p_b is the ratio of populations of exchangeable sites, r_b is the exchange rate from the bound to free water pools (r_b in Chopra's notation corresponds to k_b in the Bloch Eqs. in part I, and k_{ba} in Part I, Figure 1), R_{1b} and R_{2b} are the relaxation rates of the bound sites, ω_1 is the spin lock amplitude, and the chemical shift is given as $\Delta\omega_b$. By substituting expressions for the limits of weak

($R_{1\rho}^{0}$ = R_2) and strong ($R_{1\rho}^{\infty}$ = R_1) locking fields into Eq. 4, the expression for the observed $R_{1\rho}$ reduces to:

$$R_{1\rho} = \left\{ \frac{R_2 + \frac{\left(R_{1\rho}^{\infty} * \omega_1^2\right)}{S_\rho^2}}{1 + \frac{\omega_1^2}{S_\rho^2}} \right\} \quad [5]$$

where $S_\rho^2 = (R_{1b} + r_b) / (R_{2b} + r_b) * \{ (R_{2b} + r_b)^2 + \Delta\omega_b^2 \}$. A non-linear least-squares fit of the variation of $R_{1\rho}$ with ω_1 to Eq. 5 may be used to estimate R_2, R_1, and S_ρ for cases of interest where $r_b > R_{1b}, R_{2b}$.

Then a study of $R_{1\rho}$ vs. ω_1 may be used to estimate exchange rates if $\Delta\omega_b$ is known (or negligible). Here, chemical shift values were taken from the maximum point of the measured CEST MTR asymmetry. Values for R_{1b} and R_{2b} for sugars and polypeptides in solution were taken from appropriate literature values (2,8,22,23) and are typically on the order of 1 s^{-1} for R_{1b} and 30 s^{-1} for R_{2b}. This approach has been used previously in an effort to quantify proteoglycans in bovine articular cartilage and to estimate amide exchange rates in polyacrylamide gels (24,25).

The novel contrast measurement proposed in Part I, was used to generate images in which contrast based primarily on specific ranges of exchange rates is emphasized, using Eq. 6 below. A 5% threshold mask was applied before subtraction to reduce the effects of background noise.

$$CE(\omega_1(ex),SLT) = 4 * \frac{\left(S_0(\omega_1(high),SLT) - S_0(\omega_1(ex),SLT)\right) * \left(S_0(\omega_1(ex),SLT) - S_0(\omega_1(low),SLT)\right)}{\left(S_0(\omega_1(high),SLT) - S_0(\omega_1(low),SLT)\right)^2} \quad [6]$$

where ω_1(high) is set to the maximum SLA acquired and ω_1(low) is set to the minimum SLA.

The term in the numerator gives a maximum value when the locking field ω_1(ex) is set equal to the mean exchange rate (k_{ex}). The terms in the denominator scale the numerator by the magnitude of the $T_{1\rho}$ dispersion (R_2, $R_{1\rho}^{\infty}$), thus minimizing the effect of a large dispersion on the resulting image. As the maximum value obtained from the ratio is ¼ when the exchange rate equals ω_1(ex) and zero when the exchange rate is far from ω_1(ex), thus a normalization factor of 4 was also used.

RESULTS

CEST and SL Results for Polypeptides

The experiments on polypeptides are designed to highlight how CEST and SL measurements depend on differences in the kinds of exchanging species contributing to contrast. Figure 2.a shows the measured CEST z-spectra of the 10 mg/mL ~15 kDa polypeptide solutions: poly-L-lysine (PLK), poly-L-arginine (PLR), and poly-L-threonine (PLT) measured at 400 MHz. PLK carries a backbone amide (NH^+) and a primary amine (NH_2) group that give a z-spectrum "peak" apparent at ~3.5 ppm as confirmed by the CEST MTR_{asym} in Figure 2.b. The PLR polypeptide carries a guanidyl amine (gNH_2) group in addition to backbone amide groups that resonate between 1.8 and 3.7 ppm. The

MTR asymmetry plot in Figure 2.b shows the wide frequency range of saturation for this substance at 400 MHz for B_1 of 1 µT. The PLT group carries an amide group resonating near 3.5 ppm and also a hydroxyl exchange site at 1 ppm, giving a wide spread in saturation effects as shown in the MTR asymmetry plot in Figure 2.b.

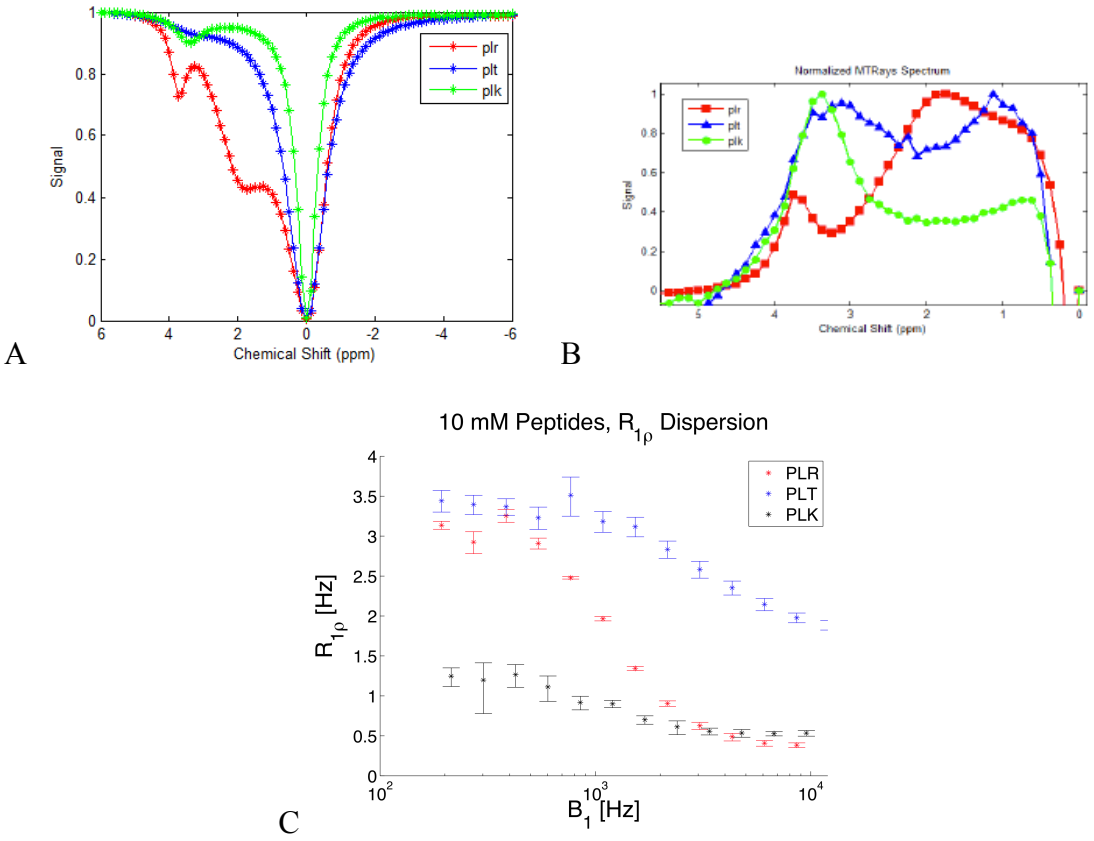

Figure 2. $R_{1\rho}$ dispersion of three 10 mM polypeptides: PLK, PLR, PLT. Note the three very different profiles from each species. The PLR, with its gNH_2 exchanging groups, has the greatest dispersion of $R_{1\rho}$ from 3.3 s^{-1} to 0.4 s^{-1} and carries a fitted mean exchange rate near 980 Hz. The PLK (NH_2) has much slower fitted exchange rates near 70 Hz and shows a smaller dispersion profile. The PLT has both ^{-}OH and NH^{+} exchanging sites and shows a small dispersion at much higher exchange rates >3 kHz.

2.a. CEST z-spectra of 3 peptides: PLK, PLR, PLT

2.b. MTR Asymmetry

2.c. $R_{1\rho}$ dispersion

The corresponding $R_{1\rho}$ dispersions for the polypeptides shown in Figure 2.a are plotted in Figure 2.c. The PLR showed the largest dispersion from a $R_{1\rho}$ value of 3.2 s^{-1} at a locking field of 150 Hz to 0.4 s^{-1} at 10 kHz with a fitted exchange rate from the Chopra model (Eq. 5) of ~930 Hz. PLK and PLT showed much smaller dispersions and showed fitted exchange rates that are ~70 Hz and ~3200 Hz. These and other fitted parameters are given in Table 1.

Table 1: Peptide Exchange Rates and Fitted Parameters:

	R_2 [s^{-1}]	$R_{1\rho}(\infty)$ [s^{-1}]	r_b [Hz]	LB [Hz]	UB [Hz]
PLK	1.6	0.4	69.8	28.8	110.8
PLR	3.3	0.3	928.0	863	993
PLT	3.4	1.8	3185	2815	3555

Note that no attempt was made to separate the individual contributions of the multiple exchanging species in PLR and PLT. Therefore the fitted rates are given as apparent average exchange rates as described previously by Hills and Jin et al. (10,26). Presumably PLR and PLT have R_2 (and $R_{1\rho}$) values much greater than PLK because of faster chemical exchange between exchanging sites, as the concentrations and chain lengths were kept constant. At high SLA the difference between PLR and PLK is negligible, whereas $R_{1\rho}$ for PLT is higher, which may be thought of as a difference in R_1

($1/T_1$). The values of $R_{1\rho}$ in between these two extremes in locking-field are dominated by changes in chemical exchange effects and therefore provide the opportunity to selectively modulate the measured $R_{1\rho}$ with the applied locking field (B_1).

CEST and SL Results for Sugars

The experiments on several commonly available sugars were designed to show the effects of different exchanging species, of concentration, and of field strength on measured $R_{1\rho}$ dispersion, CEST z-spectra, and MTR asymmetry as explored theoretically in Part I.

Figure 3.a shows the CEST z-spectra and 3.b shows the MTR_{asym} for glucose (GLU), dextran (DXT), and chondroitin sulfate (CS) at 5% (wt/wt) concentration. The z-spectra show that each sugar has a unique spectrum with peaks representing the exchanging sites on the molecule. The simplest spectrum in terms of apparent peaks is dextran. This substance shows a dominant peak at ~1.2 ppm with a smaller peak near 2.8 ppm. This smaller peak is attributed to residual sites on the dextran molecule that are not cross-linked to other glucose subunits. This 2.8 ppm peak is therefore much larger in the GLU z-spectrum that does not have such cross-links. The glucose molecule features three distinct exchangeable ^{-}OH sites that are clearly represented in the z-spectrum. The CS z-spectrum and MTR_{asym} shows a dominant peak at ~0.8 ppm that is attributed to exchangeable ^{-}OH sites and a smaller peak near ~3.5 ppm only visible at high concentrations that is attributed to the single NH^{+} site on the CS molecule.

Figure 3.c shows $R_{1\rho}$ dispersion profiles for glucose (GLU), dextran (DXT), and chondroitin sulfate (CS) at 5% (wt/wt) concentration. $R_{1\rho}$ values in the low spin lock amplitude (SLA) range from ~four s^{-1} for chondroitin sulfate (CS) to ~10 s^{-1} for glucose (GLU). At high SLA, the GLU and DXT samples show reduced $R_{1\rho}$ to near 0.5 s^{-1} with CS being slightly elevated from the other sugars. Fitted values for R_2, $R_{1\rho}^{\infty}$, and exchange rate (r_b) to the Chopra model (Eq. 5) for each of these substances are given in Table 2.

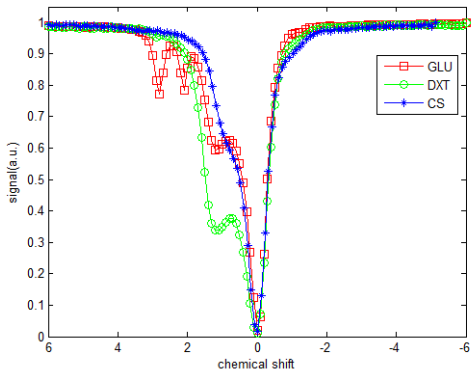

A

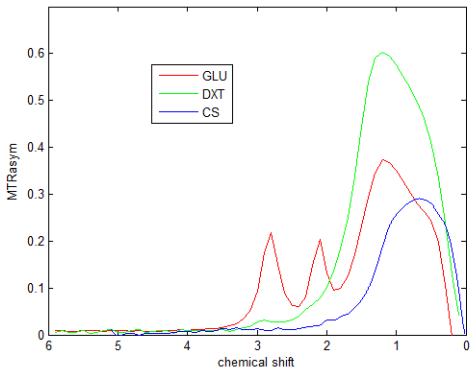

B

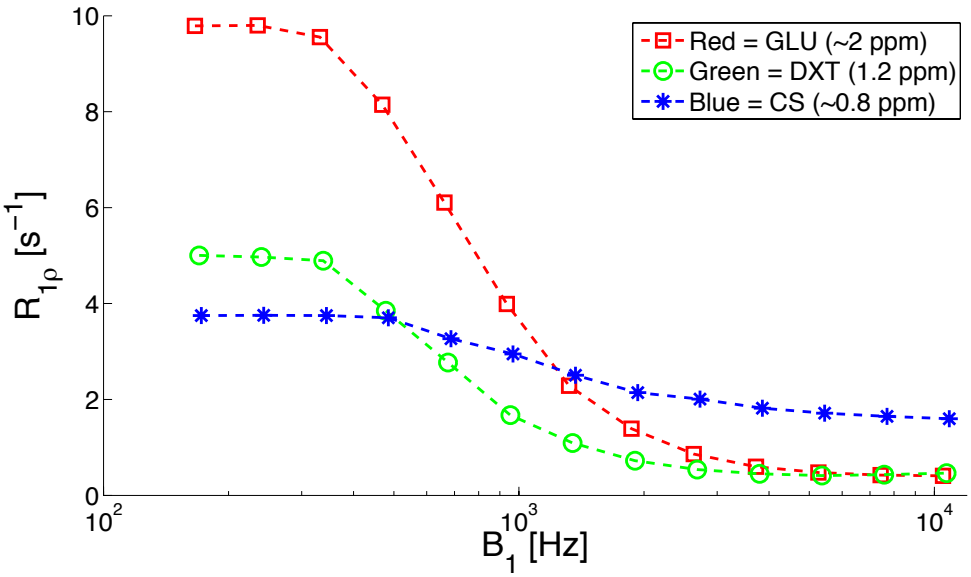

C

Figure 3. CEST z-spectra, MTR_{asym}, and $R_{1\rho}$ dispersion for 5% (wt/wt) concentrations of the sugars glucose (GLU), chondroitin sulfate (CS), and dextran (DXT).

3.a CEST z-spectra and 2.b is MTR_{asym} of CS, GLU, and DXT.

3.c $R_{1\rho}$ dispersion of sugars.

Figure 4 shows the effect of varying the concentration of dextran. The CEST spectrum of DXT was acquired at one μT with the sample concentration decreasing from 40% (wt/wt) to 5%. The CEST spectrum changes with increasing concentration. The dominant peak at 1.2 ppm becomes more distinct as the concentration decreases, though the smaller peak at 2.8 ppm, whose origins are discussed above, becomes less distinct as the sample concentration drops. Additionally, the MTR_{asym} does not vary in proportion to concentration.

The plots of $R_{1\rho}$ dispersion vs. dextran concentration in Figure 4.c show a nearly linear dependence of $R_{1\rho}$ at all SLA on concentration. $R_{1\rho}$ values in the low SLA range vary from about 5.5 s^{-1} for the 5% concentration sample to nearly 55 s^{-1} for the 40% sample. The dispersion curves drop steeply after ~500 Hz and all approach 1 s^{-1} at SLA frequencies greater than 3 kHz. Exchange rates and other fitted parameters from the Chopra model are given in Table 2.

Table 2: Sugar Exchange Rates and Fitted Parameters:

5% Sugar	R_2 [S^{-1}]	$R_{1\rho}(\infty)$ [S^{-1}]	r_b [Hz]	LB	UB
CS	3.7	1.6	6720.7	5706.9	7734.5
GLU	10.5	0.1	3716.9	3208.0	4226.0
DXT	5.7	0.3	466.3	157.0	575.0
GLY	8.9	0.7	4524.8	3441.6	5608.0

Dextran	1.2 ppm				
Conc	R_2 [S^{-1}]	$R_{1\rho}(\infty)$ [S^{-1}]	r_b [Hz]	LB	UB
0	1.0	0.3	0.0	0.0	0.0
5	5.7	0.3	466.3	257.0	675.0
10	11.6	0.3	634.7	176.0	1092.0
20	26.2	0.1	650.2	217.0	1083.0
40	60.0	0.0	386.7	148.0	625.0

Glucose	1.2 ppm				
Conc	R_2 [S^{-1}]	$R_{1\rho}(\infty)$ [S^{-1}]	r_b [Hz]	LB	UB
0	1.0	0.3	0.0		
5	10.5	0.1	3716.9	3208.0	4226.0
10	25.4	0.0	3913.4	3863.0	5184.0
20	54.4	0.0	4001.5	3282.0	4781.0
40	124.0	0.0	4400.0	3487.0	5432.0

CS	0.8 ppm				
Conc	R_2 [S^{-1}]	$R_{1\rho}(\infty)$ [S^{-1}]	r_b [Hz]	LB	UB
0	1.0	0.3	0.0		
1.2	1.7	0.6	3275.5	2653.4	3897.6
2.5	2.3	1.0	5647.5	4820.4	6474.7
5	3.7	1.6	6720.7	5706.9	7734.5
10	6.3	2.7	6371.0	5336.3	7405.7

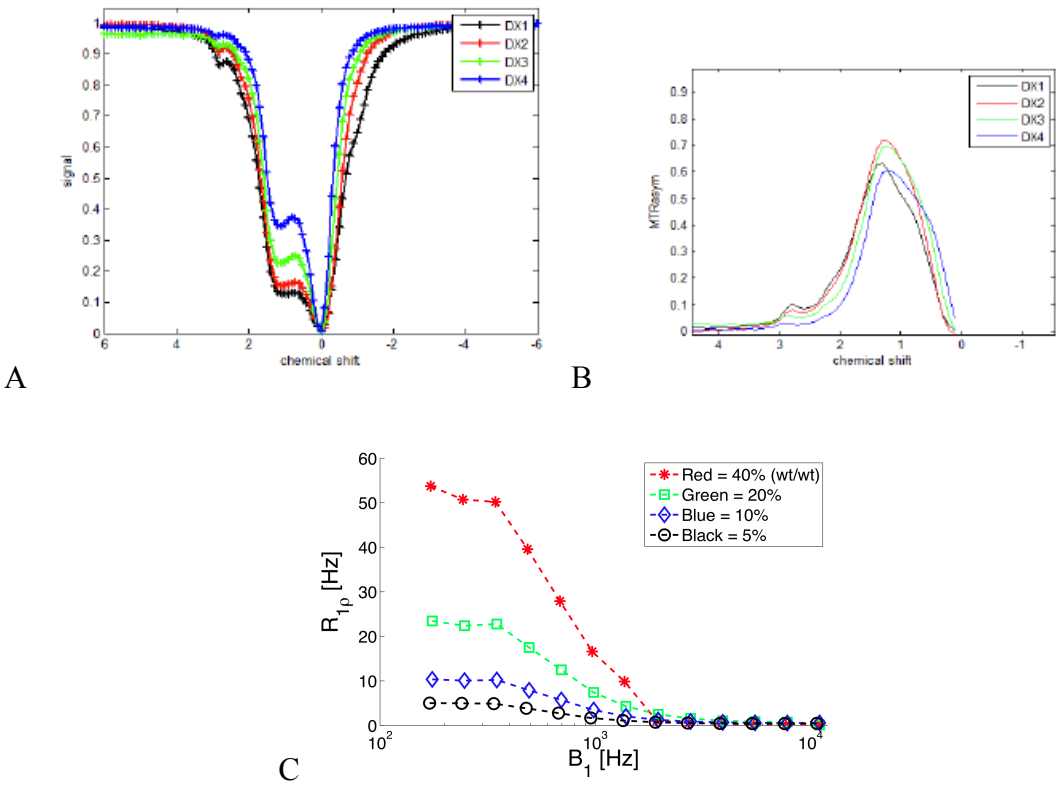

Figure 4. Demonstration of a 2-pool model of chemical exchange with dextran (DXT). Four concentrations were tested at 40, 20, 10, and 5 % (wt/wt).

4.a. CEST z-spectra and MTR_{asym} with concentration for Dextran. Note the single dominant peak at 1.2 ppm.

4.b. $R_{1\rho}$ dispersion with concentration for Dextran. Note that the lowest value of $R_{1\rho}$ (~= R_2) scales linearly with concentration.

The samples of CS shown in Figure 5 were designed to highlight differences in CEST and SL contrast for multi-pool models of chemical exchange as demonstrated in simulations in Part I. Figure 5.a gives the CEST z-spectra and MTR asymmetry of CS at multiple concentrations. CS has one exchanging NH^+ group that is apparent in the z-

spectrum at ~ 3.5 ppm only at the highest measured concentration of 10%. The large peak at ~0.8 ppm is attributed to the ˙OH groups on the molecule. The dominant peak decreases with sample concentration.

$R_{1\rho}$ dispersion plots for CS are shown in Figure 5.b. The values of $R_{1\rho}$ at low SLA show nearly linear concentration dependence. $R_{1\rho}^{0}$ values range from about 1.4 s^{-1} for the 1.2% concentration sample to nearly 6.5 s^{-1} for the 10% sample. At high SLA the samples show decreased $R_{1\rho}$ values that range from 0.8 s^{-1} for the 1.2% samples to nearly 3 s^{-1} for the 10% sample. Fitted values for exchange rates (assuming primarily hydroxyl exchange at 0.8 ppm) and other parameters from the Chopra fitting are given in Table 2.

A

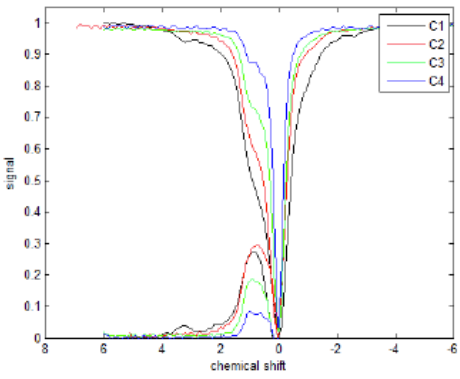

B

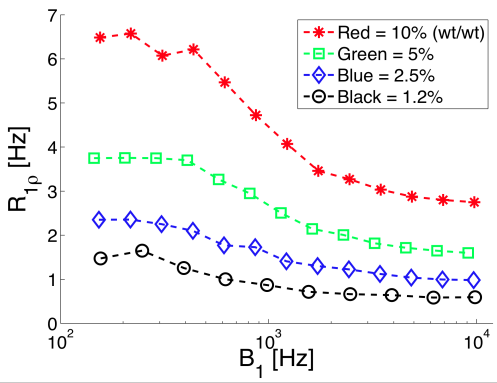

C

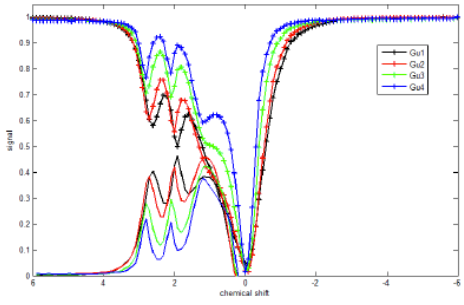

D

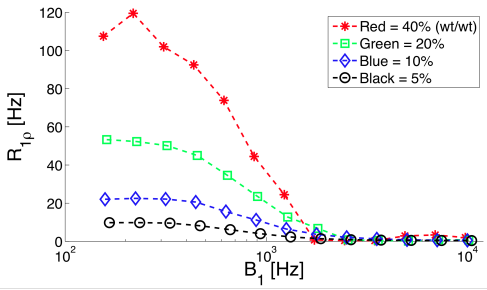

Figure 5. Demonstration of a 3-pool model with two types of exchanging sites in CS (NH^+ at 3.5 ppm & $^-$OH at 0.8 ppm), and a multi-pool system in Glucose with one type of exchanging site ($^-$OH) with multiple resonance offsets (3 peaks from ~1.2 to ~2.8 ppm).

5.a & b. CEST z-spectra, MTR_{asym}, and $R_{1\rho}$ dispersion with concentration for CS. Note that there are two distinct peaks in Fig. 5.a at 0.8 and 3.5 ppm, apparent at the highest concentration (CS1). The $R_{1\rho}$ dispersion profiles scale nearly linearly with concentration. Note that $R_{1\rho}$ at high locking field is also elevated, unlike the GLU samples in 5.d.

5.c & d. CEST z-spectra, MTR_{asym}, and $R_{1\rho}$ dispersion with concentration for GLU. Note the appearance of three distinct peaks in the z-spectrum, consistent with the presence of three exchanging $^-$OH groups on the GLU molecule. $R_{1\rho}$ dispersion at low locking filed scales linearly with concentration.

Glucose was also chosen as an example of a multi-pool exchanging species and the results are given in Figure 5.c and 5.d. However, as opposed to CS, GLU contains three distinct $^-$OH sites and no NH^+ groups. The number of exchanging $^-$OH peaks is confirmed in the CEST z-spectra and MTR_{asym} shown in Figure 5.c. This figure depicts the z-spectra of GLU at multiple concentrations with the peaks decreasing with sample concentration. Distinct peaks are noted near 1.2 ppm, 2 ppm, and 2.8 ppm at all concentrations. $R_{1\rho}$ dispersion plots for GLU are shown in Figure 5.d. The values of $R_{1\rho}$ at low SLA show nearly linear concentration dependence. $R_{1\rho}^0$ values range from about 10 s^{-1} for the 5% concentration sample to nearly 120 s^{-1} for the 40% sample. At high SLA the samples show decreased $R_{1\rho}$ values that converge to ~1 s^{-1} at frequencies greater than 2 kHz. Fitted values for apparent exchange rates, assuming a mean chemical shift of 2 ppm from

the central peak in the CEST spectra from Fig. 5.c, and other parameters from the Chopra fitting are given in Table 2.

The effect of main field (B_0) on CEST and $R_{1\rho}$ dispersion for simple systems was also investigated. The CEST and SL data for two concentrations of CS at two main field strengths are shown in Figure 6. The CEST z-spectrum in Figure 6.a shows all four spectra overlain, with the high concentration spectra appearing much broader than the low concentration spectra. The MTR_{asym} displayed in Figure 6.b shows that the high concentration sample at 9.4T features two distinct peaks as noted, consistent with Figure 5.b. However, the high concentration sample at 4.7T displays a very broad peak with a maximum at ~2.3 ppm. The two lower concentration samples in Figure 6.a and 6.b display very similar CEST peaks with a maximum near ~0.8 ppm for both samples.

$R_{1\rho}$ dispersion measurements were performed on the same low and high concentration samples of CS at 200 (4.7 T) and 400 MHz (9.4T), and they are shown in Fig. 6.c. Both samples demonstrate increased $R_{1\rho}$ dispersion with main field as predicted by simulation in Part I, Figure 4. The $R_{1\rho}^0 = R_2$ values indicate significant increases with field due to exchange effects. The 1.2% sample shows a $R_{1\rho}$ value at low SLA of 0.8 s^{-1} at 200 MHz ~ 1.6 s^{-1} at 400 MHz. The 10% sample dispersions at low and high field show a similar trend toward increasing dispersion, and the $R_{1\rho}$ values at high SLA level out around 2.5-3 s^{-1}.

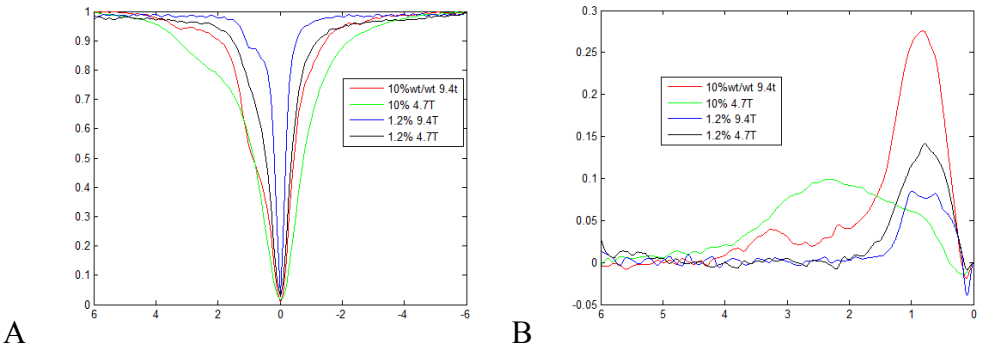

A B

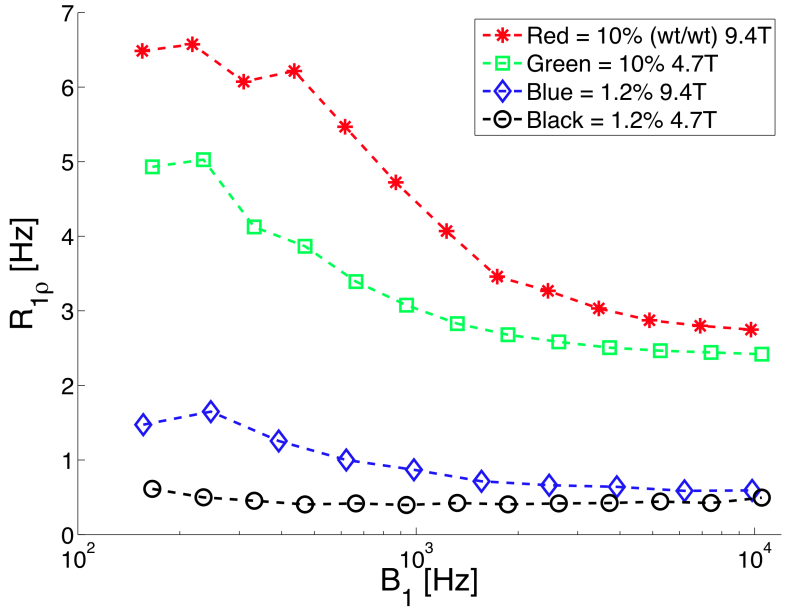

C

Figure 6. Demonstration of the effect of main field strength on chemical exchange and $R_{1\rho}$ dispersion. Note that dispersion is much greater at 400 MHz than at 200 MHz for both sample concentrations.

6.a. CEST z-spectrum and MTR_{asym} for 1.2 and 10 % (wt/wt) CS measured at 200 and 400 MHz. Note the increased MTR_{asym} for both samples at high field.

6.b. $R_{1\rho}$ dispersion of 1.2% and 10 % (wt/wt) CS at 200 and 400 MHz. Note the larger dispersion at high field for both samples.

The effect of variation of chemical exchange rate on $R_{1\rho}$ dispersion in a sample of a constant concentration is demonstrated in Figure 7. This experiment was performed to demonstrate the sensitivity of $R_{1\rho}$ dispersion to pH effects and to test the Chopra model for fitting increasing exchange rates. 10% concentrations of CS in deionized water were titrated from pH 3 to 11 and their $R_{1\rho}$ dispersions plotted in Figure 7.a. The values of $R_{1\rho}$ at low SLA were clustered together near 5.5 s^{-1} to which chemical exchange is a significant contribution. At higher SLA the curves separate, with the high pH samples showing less rapid dispersion than the low pH samples, and the inflection point of the dispersion curve moving to lower SLA values as pH drops presumably along with exchange rates. The fitted exchange rates are plotted in Figure 7.b and show a sharp increase in rate above pH 7.

A

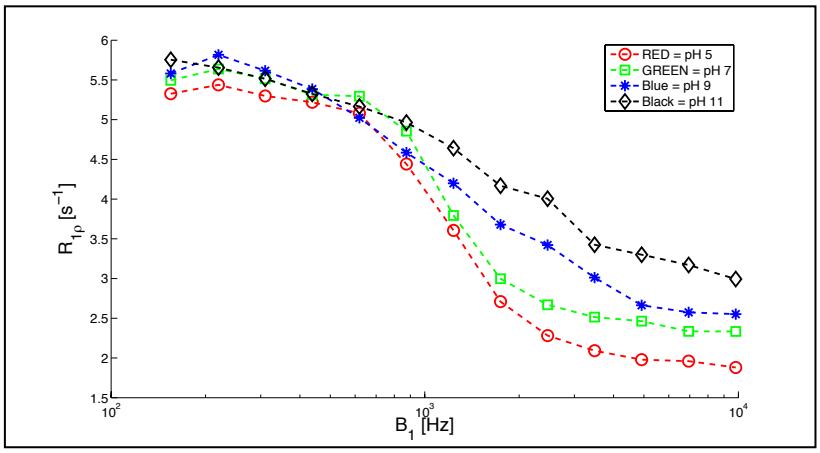

B

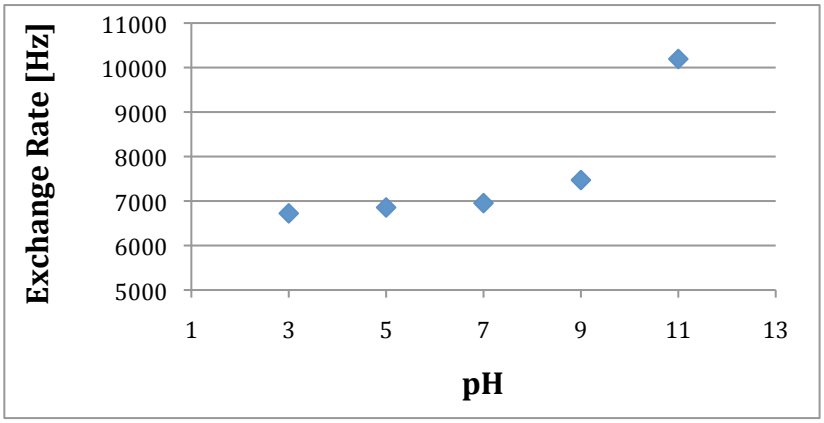

C

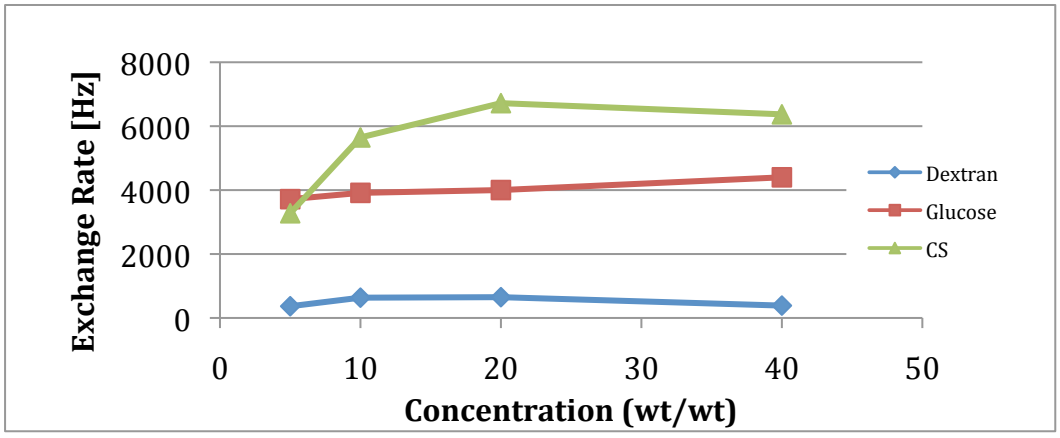

Figure 7. $R_{1\rho}$ dispersion of 10% CS (wt/wt) with pH at 400 MHz. Note the shift of the dispersion curves to greater mean frequency with increasing pH.

7.a. $R_{1\rho}$ dispersion of 10% CS with pH.

7.b. Fitted mean exchange rate (Hz) for CS from the Chopra fitting Eq. 8. Note how the mean exchange rate increases with pH.

7.c. Exchange rate stability vs. concentration. Note that the CS concentration is ¼ the plotted concentration for easier comparison to the other sugars. For CS, at 1.25% concentration, the fitting becomes less reliable.

The stability of the Chopra model in fitting rates across large concentration differences is shown in Figure 7.c. A nearly flat exchange rate is shown for the dextran and glucose samples across a wide range of concentrations. The CS concentrations are plotted at 4x the tested concentration for ease of comparison among the other substances. DXT has a mean chemical exchange rate of ~530 Hz, GLU has a mean chemical exchange rate of ~4 kHz, and CS has a mean exchange rate of ~5 kHz. This places DXT and GLU in the intermediate-to-fast exchange regimes and CS clearly in the fast exchange regime. The lowest concentration of CS (1.2%) had a 47% lower exchange rate than the larger concentrations. This may be attributed to errors in fitting a very flat dispersion curve to the Chopra model. The fitted parameter values and 1 STD confidence intervals are given in Table 2.

Imaging Results

$R_{1\rho}$ dispersion behavior may be used to create contrast based on sample exchange rates. Figure 8 shows the results of applying Eq. 6 to samples of CS whose pH has been varied to alter the average chemical exchange rate in the phantom. Figure 8.a shows an initial short-TE, T_2-weighted image at $\omega_1(\text{low}) = 2\pi*(150\text{ Hz})$ and SLT = 20 msec. The

phantoms are shown in counter-clockwise order from low pH to high with the top phantom = pH 5, left = pH 7, bottom = pH 9, and the right = pH 11. They appear equally bright at this value of SLT. Next, the ratio in Eq. 6 was used to yield contrast based mainly on exchange rates. Values for ω_1(ex) were taken from the fitted midpoints (S_ρ) of the dispersion curves from Figure 7.b which depend mainly on chemical shift and exchange rate. The nearest acquired SLA values to the fitted midpoints in Figure 7.b are 2π*(1200, 3450, 5250, and 8400 Hz) respectively. The resulting images are shown in Figure 8.b through 8.e. The phantom with maximum contrast cycles from the low pH sample to the high pH sample moving left to right from Figure 8.b through 8.e. Figure 8.d shows an artifact in the pH 5 phantom that is likely attributed to local variation in B_1 across the sample.

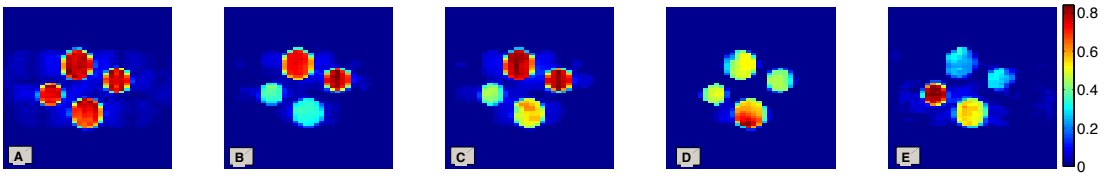

Figure 8. Using $R_{1\rho}$ dispersion for pH imaging. Top = pH 5, Right = pH 7, Bottom = pH 9, Left = pH 11. Note that while the fitted exchange rates are separated by approximately 2 kHz per pH unit, the ratio from Eq. 5 cannot exclusively select for that rate.

8.a. Reference "T2-weighted" image (SLT = 20 msec, SLA = 150 Hz). Top phantom = pH 5, Right = pH 7, Bottom = pH 9, Left = pH 11.

8.b. Exchange selective subtraction image with SLA = ~1200 Hz.

8.c. Exchange selective subtraction image with SLA = ~3450 Hz.

8.d. Exchange selective subtraction image with SLA = ~5250 Hz.

8.e. Exchange selective subtraction image with SLA = ~8400 Hz.

Figure 9 demonstrates imaging examples for both CEST and SL imaging as described by Eqs. 2 and 6, respectively. Images of the same 10 mg/mL polypeptide samples shown in Figure 2 were acquired. By appropriate selection of SLA and SLT, contrast from specific exchange rates may be emphasized by application of Eq. 6 to $R_{1\rho}$ dispersion imaging data. Figure 9.a shows an image of the three tested polypeptides acquired with SLA = 2π*(150 Hz) and SLT (20 msec) with fast spin-echo readout. This image is equivalent to a short-TE T2-weighted image. Figure 9.a shows PLK at top, PLT at right, and PLR at bottom with nearly equal brightness. Figure 9.b shows the result of selecting the image acquired with SLA = 2π*(300 Hz) as ω_1(ex), the next closest available acquired image to the fitted midpoint of the dispersion curve (S_ρ). For consistency, SLT = 678 msec was used for all subsequent calculations of Eq. 6 with only the ω_1 value being changed. This time point is close to the average time point of maximal signal contrast for ω_1(ex) in all three samples, but is probably not optimal for any individual sample. The time point is nearly twice the average $T_{1\rho}$ of all species, and allows sufficient time for spin-lock contrast to develop, but not so long as to allow signal to deteriorate into noise. Figure 9.b shows the results of filtering with the ratio in Eq. 6, with only the PLK sample being visible while contrast from the other species is well suppressed. The color bar indicates how closely the selected frequency matches the apparent chemical exchange rate, with an image scaled to unity representing a good match. In this figure the PLK has an average value of about 0.55 if the banding artifact at the top of the phantom is left out of the region of interest (ROI). Figure 9.c shows the result of selecting the image acquired at

2π*(1200 Hz) as ω_1(ex). With this selection, only the PLR sample is visible with an average intensity in the phantom of 0.5. Figure 9.d shows the result of selecting the image acquired at 2π*(7 kHz) as ω_1(ex). This last sub-figure shows only the PLT sample with average image intensity in the phantom of 0.95, indicating a close match to the apparent rate.

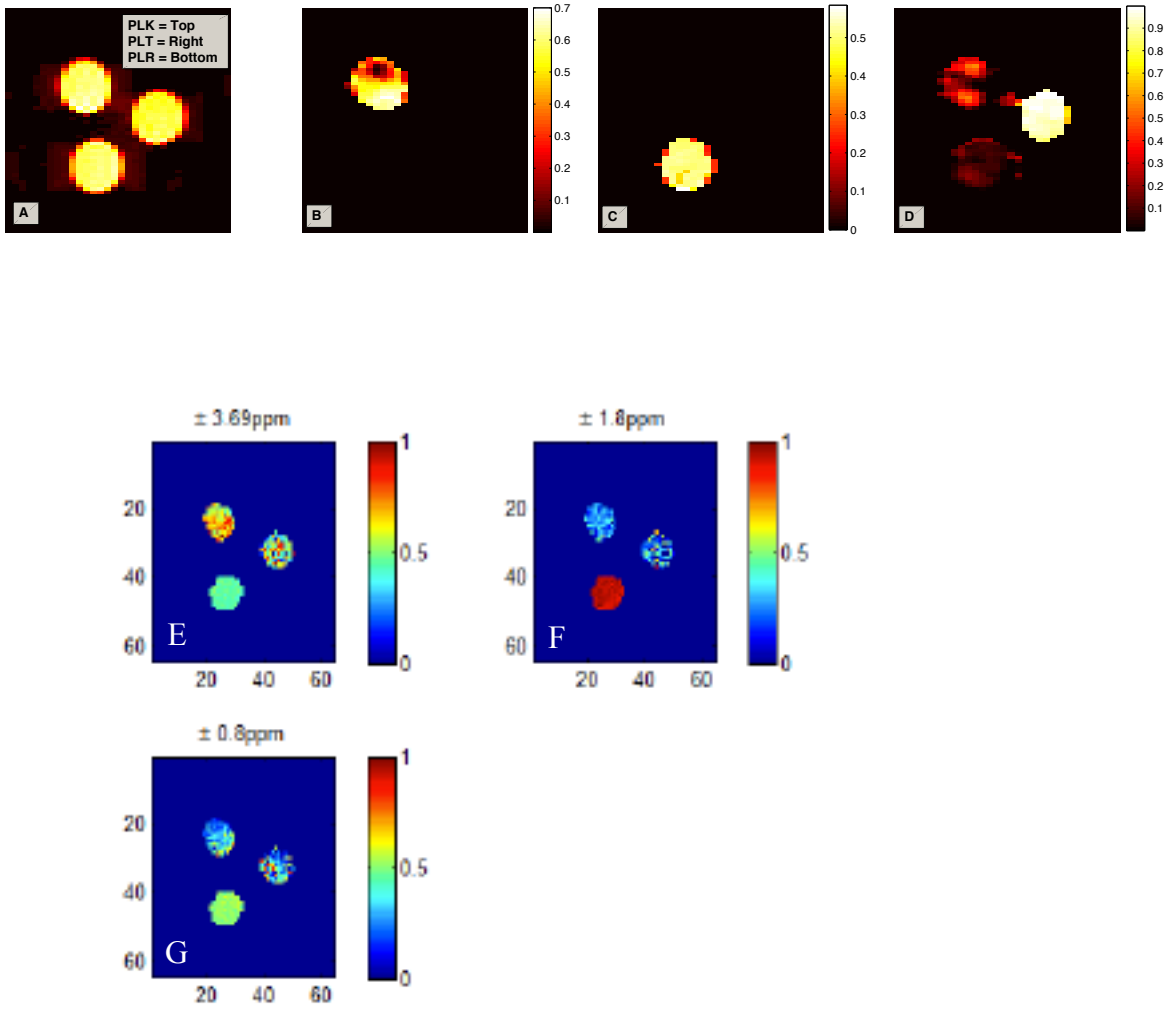

Figure 9. Exchange rate selective and chemical shift selective imaging using spin locking and CEST techniques. Note that for the exchange rate selective imaging technique using Eq. 5, the peptides are now in a slower exchange regime, and the ratio is better able to select for a given rate.

9.a. Original image of PLK (left), PLT (right), and PLR (bottom)

9.b. Exchange selective subtraction image with SLA = ~300 Hz.

9.c. Exchange selective subtraction image with SLA = ~1200 Hz.

9.d. Exchange selective subtraction image with SLA = ~4300 Hz.

9.e. Chemical shift selective image with saturation pulse offset = 3.69 ppm.

9.f. Chemical shift selective image with pulse offset = 1.8 ppm.

9.g. Chemical shift selective image with pulse offset = 0.8 ppm.

Figure 9.e through 9.g show the corresponding CEST subtraction images using Eq. 2. By appropriate selection of irradiation frequency offset and power, contrast based primarily on chemical exchange for specific offsets may be generated. Figure 8.e shows the subtraction image resulting from selective irradiation at ±3.69 ppm. All peptide species studied here have significant CEST MTR asymmetry (from Figure 2.b) near 3.69 ppm with PLK and PLT showing greater saturation effects than PLR. This is reflected in contrast in the images in Figure 9.e, where the contrast enhancement from PLK and PLT is greater than that shown in the PLR sample. Figure 9.f shows the image resulting from saturation at ±1.8 ppm. At this frequency, only the PLR sample has significant contrast as predicted by the MTR asymmetry from Figure 2.b. Figure 9.g shows the resulting image from saturation at ±0.8 ppm. At this frequency, the PLR and PLT samples show greater contrast as compared to PLK, as is consistent with Figure 2.b.

DISCUSSION

The experiments reported above were designed to test and validate the simulations from Part I and to illustrate factors that affect chemical exchange effects in CEST and spin lock imaging. Solutions of polypeptides and sugars were used to demonstrate how CEST and SL contrast provide complementary information about chemical exchange in biological samples. Variations in chemical exchange produced by changing the number and type of exchanging functional group, changes in concentration, pH, and main field demonstrate how each experimental technique is sensitive to the precise composition of samples. We also illustrate that specific features of SL contrast may be used to generate novel image contrast based primarily on exchange rate.

Figure 2 illustrates the behaviors of three common polypeptide molecules. Each molecule carries a different exchanging group each with its own exchange characteristics and chemical shift. This imparts to each polypeptide a unique $R_{1\rho}$ dispersion profile, and a unique z-spectrum. When comparing the $R_{1\rho}$ of the PLR, PLT, and PLK dispersion curves at low locking field, the differences can be thought of as a difference in R_2 ($1/T_2$). At high SLA, differences in $R_{1\rho}$ may be thought of as differences in R_1 (17,27). But the difference between the R_1 and R_2 rates may be largely determined by exchange between species of different chemical shifts, and the values of SLA at which the dispersion of $R_{1\rho}$ is steepest may mainly reflect the exchange rate of the sample (26). There have been no comparable $R_{1\rho}$ dispersion values reported previosly for the polypeptide samples measured here. The reported mean exchange rate for poly-L-lysine of 69.8 Hz is of the

correct order of magnitude with values for slow exchange reported by Englander et al. and Goffeney et al. who gave values on the order of ~100 Hz from line width measurements (28,29). There are no previous reports of the values of exchange rates for PLT and PLR taken from $R_{1\rho}$ dispersion, though the PLR rate should be near one kHz and the $^{-}$OH group of PLT should exchange near 700 Hz according to estimates by Liepinsh and Otting (30). Multiple species contribute to the behavior of $R_{1\rho}$ in these two polypeptides, so the PLT and PLR rates of ~3200 and ~930 Hz should be interpreted as weighted average rates, and no attempt has been made to separate the contribution of each exchanging species as the dispersion profiles contained no obvious double-inflection points, often indicative of two disparate rates (16). Those protons with larger chemical shift and higher exchange rates will contribute most to the average rate. PLT has relatively more $^{-}$OH groups than NH^{+} for a weighted effect on signal that is more representative of $^{-}$OH exchange than from NH^{+}. Also, the same weight percentage and comparable molecular weights were used, so for PLT there are more exchanging protons than for smaller molecules. This is consistent with the simulations in Part I, Figure 7. The large range of exchange rates displayed in these polypeptides provides the opportunity to selectively modulate contrast among all three samples based on exchange rate and locking field in conjunction with Eq. 6 as shown in Figure 9, with results similar to the CEST subtraction imaging technique.

The CEST and $R_{1\rho}$ dispersion experiments on sugar solutions shown in Figure 3 show the effect of variations in exchanging species on the measured data. The plots shown in Figure 3.a and 3.b show how each sugar has a characteristic CEST z-spectrum and MTR

asymmetry, which feature the presence of a different number of exchanging groups. Similar CEST z-spectra for GLU have been reported previously, confirming the presence of three peaks associated with different $^{-}$OH binding configurations on the molecule (9,10). The CEST z-spectra for CS are also consistent with previously reported spectra, confirming the association of the peak at ~3.5 ppm with the exchanging NH^{+} group and the peak at ~0.8 ppm with the exchanging $^{-}$OH group (9). There are no known published CEST spectra of dextran at high field, but the peaks are consistent with the chemical structure of glucose as shown in Figure 1 with cross-linking dramatically reducing the intensity of some peaks as suggested by Hills (31).

The $R_{1\rho}$ dispersion data for the sugars GLU, CS, and DXT are shown in Figure 3.c. Each sugar features $^{-}$OH exchange at a different chemical shift as evidenced by the CEST z-spectra in Figure 3.a. Therefore it is not expected that the dispersion profiles match even though exchange is primarily due to $^{-}$OH exchange in all species and even if the exchange rates were equivalent. There is a slight trend of increasing $R_{1\rho}$ at low locking field ($R_{1\rho}^{0} = R_2$) with the chemical shift of each species. The dispersion profiles are similar to those recently reported by other authors in terms of the range of the $R_{1\rho}^{0}$ values and points of inflection at particular locking fields (9,10,32). Figure 3.c shows DXT and GLU have very different dispersion profiles. This may appear surprising as dextran and glucose share many similar features, with DXT being made of long chains of glucose molecules that are chemically linked at the α(1,3) and α(1,6) positions as shown in Figure 1. At frequencies greater than ~ 3 kHz the profiles converge to near 0.5 Hz. For SLA values less than 3 kHz, and at equivalent concentrations (wt/wt), the GLU molecule

has $R_{1\rho}$ values that are over twice the rate of the equivalent amount of DXT. This is most likely due to the dextran glycolytic bonds reducing the availability of $^{-}$OH exchanging sites on the DXT molecule. This is perhaps confirmed by the very different CEST z-spectra shown in Figure 3.a. The GLU molecule has three distinct peaks ranging from ~0.8 to ~2.8 ppm, whereas the DXT z-spectrum has only one discernible peak at 1.2 ppm. The potential reduction in exchange from the $^{-}$OH sites with larger chemical shift may have reduced exchange effects on measured $R_{1\rho}$ dispersion. This hypothesis is supported by observations by Hills et al. (31) who comments on the availability of $^{-}$OH exchanging sites in dextran microspheres.

The CS dispersion profile appears distinctly different from the DXT and GLU profiles. An interesting feature of this profile is that the curve appears to be shifted to slightly higher frequency as compared to the other sugars. This is perhaps due to the presence of a NH^{+} exchanging site at ~3.5 ppm that may serve to scale the $R_{1\rho}$ dispersion curve to slightly higher frequency as predicted in Part I, Figure 7. An additional feature is the elevated $R_{1\rho}$ curve at high frequency as compared to the other two sugars. This perhaps due to the increased viscosity of the CS samples and will be discussed further below.

The exchange rates for sugars given in Table 2 reveal that, with the exception of dextran, the sugars have exchange rates in the kHz range. These rates, including those for dextran, agree with prior published rates (10,16). The fitted rates place the DXT and GLU samples in the intermediate-to-fast regime, which may explain why good CEST peak separation and moderate $R_{1\rho}$ dispersion (R_2-R_1) profiles were reported. CS z-spectra show poor peak

separation as expected when operating in the fast-exchange regime. Additionally, substances with higher chemical exchange rates typically have much higher R_2 values, implying that chemical exchange is a major contributor to R_2 at 400 MHz.

The effect of varying concentration of exchanging agent on a two-pool model of exchange was tested with dextran to validate the predictions of Part I, Figure 6, which shows the effect of increasing the metabolite pool. The $R_{1\rho}$ dispersion curves in Figure 4.c scale with concentration as expected. However, no such trend exists in CEST MTR_{asym}, so the CEST technique may not be well suited to indicating metabolite concentration difference under the irradiation conditions used here. The CEST z-spectrum verifies that exchange is predominantly governed by ^{-}OH exchange near 1.2 ppm. There are small peaks in the CEST z-spectrum at ~2 and ~2.8 ppm that are reminiscent of the GLU z-spectra shown in Figure 2.a. As mentioned previously, these residual peaks may be attributed to the dextran molecules not being fully cross-linked at the α(1,3) and α(1,6) positions.

Multi-pool models of chemical exchange were explored with CEST and SL imaging with samples of glucose and chondroitin sulfate in varying concentrations. Glucose features a single type of exchanging species at three distinct chemical shifts, whereas the CS experiments feature a slow NH^{+} exchanging site and a faster ^{-}OH site. The results of these experiments are given in Figure 5. The CEST z-spectra for CS are given in Figure 5.a and show that exchange is dominated by the peak at ~0.8 ppm and is attributed to ^{-}OH sites on the CS molecule (See Figure 1). At the highest concentration tested, a small NH^{+}

resonance is detected near ~3.5 ppm and is attributed to the single NH^+ site per CS sub-unit consistent with findings of Ling et Al (9). The corresponding $R_{1\rho}$ dispersion plots are shown in Figure 5.b. The dispersion curves scale linearly with concentration at $R_{1\rho}^0 = R_2$ as expected. Interestingly the curves do not converge to a single value at high SLA consistent with similar experiments by Duvvuri et al. at low field and Reddy et al. at similar field strengths (15,24). This may be attributed to increased viscosity as compared to the other sugars. These effects may alter the dispersion profiles in terms of observed $R_{1\rho}$ at high locking field, making them appear "flat" at high concentration as suggested by Matthews et al. and Hills (26,33). Fitted exchange rates and other parameters are given in Table 2 and range from ~3300 to ~6400 Hz. These values were fit assuming a predominant exchange contribution from the ^-OH site at 0.8 ppm, as the CEST z-spectra in Figure 5.a feature a prominent, but exchange-broadened peak at this frequency. The fitted rates shown in Fig. 7.c are fairly flat, except the lowest concentration tested of 1.2 %. Precise exchange rates for CS with spin locking techniques are difficult to compare with prior reports, e.g. Duvvuri et al. who made similar measurements at much lower field and made different assumptions as to the origins of $R_{1\rho}$ dispersion. Duvvuri et al. assumed NH^+ dominated exchange with relaxation rates of ~1400 Hz with no ^-OH relaxation component, and fit dispersion curves to a different exchange rate model than used here.

Glucose presents an alternate multi-pool system that features only one type of exchanging species, but contains resonance peaks at three different offsets from water. These peaks are attributed to three distinct configuration of ^-OH exchanging sites as shown in Figure

1, and this is reflected in the CEST z-spectra in Figure 5.c. Exchange at these relatively large chemical shifts appears to impart a very large $R_{1\rho}$ value at low SLA in Figure 5.d that nevertheless scales linearly with concentration. The $R_{1\rho}$ values range from 10 s^{-1} at the 10% concentration to over 100 s^{-1} at 40%. The dispersion profiles converge rapidly to a value less than one s^{-1} at SLA values greater than 2 kHz. The results from fitting the glucose curves at various concentrations average near ~4 kHz with an assumed average chemical shift of 2 ppm which was taken from the central peak of the CEST spectra in Fig. 5.c. A similar assumption was used recently by Jin et al. who reported similar exchange rates for GLU of between 4.5 and 5.5 kHz using the model of Trott and Palmer (10,18).

In Part I, simulations predicted a marked increase in CEST and SL contrast with increasing main field. Figure 6 shows the results on two concentrations of CS at 200 and 400 MHz. The two concentrations of CS behaved similarly to simulated data from the sugar model in Part I. At 4.7T, the CEST spectra appeared very broad with noticeable peaks near one ppm that are attributed to the $^{-}$OH site, but with the NH^{+} peak only becoming apparent at high concentration. At 9.4T, the peaks of the MTR asymmetry and z-spectra became narrower as predicted in simulation, and the NH^{+} and $^{-}$OH peaks separate. This is especially apparent with the 10% concentration at 9.4T. These spectra are comparable to those measured at 500 MHz by Ling et al (9).

The corresponding $R_{1\rho}$ dispersion plots of the two concentrations of CS at two different main fields are shown in Figure 6.c. The low concentration dispersion curves show a

marked increase of nearly 100% at low SLA when moving from 4.7 to 9.4T. The high concentration increased by a smaller ~50% in $R_{1\rho}$ at low SLA as the main field strength was doubled. This suggests that chemical exchange effects are a dominant contributor to $R_{1\rho}$ dispersion at high field. This increase is consistent with other authors' assertions in similar small molecules (13,15,34).

Figure 7 demonstrates the potential for SL techniques to be used to assess differences in pH and exchange rates. Variations in pH modulate the speed of proton exchange reactions, as the concentration of hydroxide and hydronium are varied (29,30). The CS solutions in Figure 7 demonstrated a large increase in fitted rates with increasing pH, consistent with the predictions of Leipinsch and Otting and consistent with recent results by Jin et al. for base-catalyzed proton exchange in sugars (10,30). Interestingly, the profiles for CS demonstrated only a very small increase of $R_{1\rho}$ with pH at the lowest SLA of about 0.5 s^{-1}. These values are essentially the same within experimental error. A larger increase in $R_{1\rho}$ values may have been expected at low SLA, where $R_{1\rho}^0 = R_2$. However an explanation may be found in simulations from Part I, Figure 5.b. At sufficiently high exchange rates, the $R_{1\rho}$ values reach a maximum and begin to decrease. The CS samples may be operating in this exchange region, and thus $R_{1\rho}$ values may stay relatively constant while the midpoint of the dispersion curve moves to higher SLA. This appears to be the case with Figure 7.a where most of the dispersive changes occurred at locking field frequencies > 1.5 kHz. The increase of the measured midpoint of the $R_{1\rho}$ dispersion curve with pH is consistent with the hypothesis that chemical exchange is accelerated when operating in a higher pH environment. The sites for chemical exchange in this model

system are the $^{-}$OH and NH^{+} protons in the CS molecule as demonstrated by the z-spectra in Fig. 5.a. Note that the dispersion profiles in Figure 7.a are not directly comparable to those in Figure 5 as the pH varied samples were created in deionized water and therefore lack contributions to exchange from the buffer solution that has been previously shown to be a mild exchange catalyst (30).

No attempt has been made to quantitatively separate the relative contributions of $^{-}$OH vs. NH^{+} with a multi-pool fitting for these species as no distinctive double-dispersion was noted in the $R_{1\rho}$ profiles(16,19). This implies that the contribution to $R_{1\rho}$ from NH^{+} exchange is either small or the rates are very similar. The CEST peak in Fig. 5.a at 3.7 ppm attributed to the NH^{+} group on the CS molecule was observable at the highest tested concentration, so we conclude that chemical exchange is dominated by $^{-}$OH exchange in CS. Additionally, it is typically not possible to precisely extract proton pool sizes from $T_{1\rho}$ dispersion measurements. Hills et al. and others (35,36) have demonstrated that these dispersion curves may be adequately fit with a significant range of values with the mean exchange rate being the most robustly fitted parameter. This is demonstrated in Figure 7.c that shows good stability of fitting across a broad range of concentrations, excepting the very lowest concentration of CS. This low concentration of CS resulted in a very flat $R_{1\rho}$ dispersion profile, suggesting there was insufficient macromolecular content to induce a large dispersion. This is consistent with Part I, Fig. 6, which shows only a slight $R_{1\rho}$ dispersion with $P_b = 0.001$. The exchange rates listed in Table 2 conform to the estimates of Leipinsh and Otting (30,37) and also to recently published rates on sugars and other peptides with similar techniques to those used here by Jin et al. (10).

Differences in fitted exchange rates with literature values may be driven primarily by differences in fitting technique (line-width measurements vs. CPMG vs. spin locking) and other issues such as subtle differences in temperature or sample preparation. As opposed to CPMG dispersion, where the ability to string together 180-degree pulses is limited to a relatively low frequency, spin-locking allows for ready translation to *in vivo* imaging, with the range of achievable locking fields being the primary limitation (13,14). Typically the lower limit of measurable exchange rates is given by the heterogeneity in the B_1 or B_0 fields generated in the tissue of interest. The upper limit is given by the stable pseudo-*cw*-power achievable by the RF amplifier or specific absorption rate considerations for human imaging. This limit is currently in the 20 kHz range for small animal systems and 2 kHz for human systems. With most biological exchange processes in the kHz range (1,14,15,30,38), $T_{1\rho}$ dispersion holds much promise for characterizing these processes in a variety of *in vivo* and *ex vivo* experiments.

Figure 8 shows the same samples of CS from Figure 6 imaged with the $T_{1\rho}$-FSE technique over a wide range of SLT and SLA and the resulting images analyzed with the ratio in Eq. 6. $T_{1\rho}$–weighted imaging may be used to create contrast based on the apparent average exchange rates for CS. The images shown in Figure 8 demonstrate this concept and show contrast from Eq. 6 changing as the frequency of interest, $\omega_1(ex)$, is increased from a low to a high SLA value. As predicted in Part I, Fig. 5, the exchange rates are too similar to uniquely select for a phantom with Eq. 6. However, the technique can select for a range of pH units as $\omega_1(ex)$ is stepped from low to higher frequency as seen from

Figure 8.b to 8.f. Figure 8.d also exhibits an artifact in the pH 5 phantom that is attributed to local variation in the applied B_1 field.

When evaluating the method proposed in Eq. 6, it is worth considering that the B_1 powers used were not explicitly tailored to the fitted apparent exchange rates. There is a dependence on the spacing of locking field frequencies that may need to be optimized in an iterative fashion for species of interest. Procedurally, this is analogous to the process of obtaining a z-spectrum in CEST to identify the position of exchanging peaks before imaging. For the exchange-rate sensitive imaging technique, a sweep from low to high SLA identifies the value for the apparent average exchange rate $\omega_1(ex)$. This process may also need to be performed to optimize the locking time (SLT) for best results. Due to the large number of samples and wide range of fitted rates observed, iterative adjustment of locking field was not attempted for these experiments.

Figure 9 demonstrates a novel imaging application where images can be made whose contrast reflects the presence of exchanging protons with specific exchange rates with spin-locking methods as opposed to CEST techniques that emphasize contrast from particular chemical shifts. Each polypeptide demonstrates a characteristic $R_{1\rho}$ dispersion curve indicative of chemical exchange at one or more of the ^{-}OH or NH^{+} sites on the molecule with surrounding water. The rates of the PLT polypeptide occur at much higher rates than those for PLR and again for those of PLK. It is important to reiterate that the fitted rates are apparent average rates and may include distributions of exchange rates from multiple sites. This may be particularly true for PLR and PLT that have multiple

exchanging species as shown in Figure 2.a. However, by appropriate selection of the spin lock field amplitudes in conjunction with Eq. 6, maximal contrast can be derived from nuclei whose dispersion (exchange rate) occurs near the locking frequency. Figure 9.a through 9.d shows the dramatic effect of the presence of the exchanging species on $R_{1\rho}$ dispersion and the ability to selectively manipulate contrast even if the $R_{1\rho}$ dispersions (R_1 - R_2) among the various species are similar. Figure 9.b shows the results of selecting ω(ex) nearest to the acquired locking field frequency of the apparent exchange rate of PLK. The PLK phantom is clearly identified while contrast in the other two phantoms is suppressed. This is due to a feature of Eq. 6 where because the PLR and PLT species exchange at much higher rates, the ratio results in signal from those phantoms subtracting to near zero. This result contrasts to Figure 8, where the rates were more closely spaced, and the ratio could not uniquely separate the phantoms. Average pixel values in the PLK phantom are 0.55 for Figure 9.b if the banding artifact at the top of the phantom is excluded. Banding artifacts are attributable to variations in B_1 and B_0 across a sample and are common artifacts in spin-locking experiments at low SLA. These effects may be reduced by alternating SL phase and by the addition of a 180-degree refocusing pulse at the center of the SL preparation pulse as demonstrated by Witschey et al. (12) and used here to acquire images. The PLK value of 0.55 demonstrates that the closest measured SLA could be improved with better selection of locking field frequencies. For instance, the fitted exchange rate for PLK is ~70 Hz, while the closest available ω_1(ex) for use in Eq. 6 was 300 Hz as ω_1 (low) used the lowest acquired value of 150 Hz. This frequency mismatch is also true for Figure 9.c, which clearly shows the PLR phantom, but has an

average pixel value of ~0.5. The PLT sample in Fig. 9.d shows much better exchange rate selection, as its average pixel value is 0.95.

CONCLUSIONS

We have demonstrated with simulations and experiments on model systems that CEST and spin locking are sensitive to chemical exchange effects and typical perturbations such as increasing the metabolite pool, altering pH, and scaling exchange effects with main field. We have shown that the CEST technique may be particularly suited to exploring contrast from systems in the slow-to-intermediates exchange regime and with low metabolite concentrations, but CEST contrast does not provide a clear indication of the concentration of a species. SL is more suited to making dispersion measurements in an imaging context in the intermediate-to-fast regime where other approaches, such as CEST or CPMG, may be technically difficult. The contrast scales with concentration, but identifies disparate species by exchange rate and offset frequency rather than chemical shift alone. Additionally, we have demonstrated that a variety of structural and chemical changes affect $T_{1\rho}$ relaxation and may be emphasized with a novel image subtraction technique. Each technique demonstrates strengths in a particular exchange regime, and therefore the two techniques may be thought of as providing complementary information about chemically exchanging systems.

ACKNOWLEDGEMENTS

NCRR 1S10 RR17799

NIH R01 EB000214

REFERNCES

1. Ward KM, Aletras AH, Balaban RS. A new class of contrast agents for MRI based on proton chemical exchange dependent saturation transfer (CEST). J Magn Reson 2000;143(1):79-87.
2. Zhou JY, van Zijl PCM. Chemical exchange saturation transfer imaging and spectroscopy. Prog Nucl Mag Res Sp 2006;48(2-3):109-136.
3. McMahon MT, Gilad AA, DeLiso MA, Berman SM, Bulte JW, van Zijl PC. New "multicolor" polypeptide diamagnetic chemical exchange saturation transfer (DIACEST) contrast agents for MRI. Magn Reson Med 2008;60(4):803-812.
4. Zhang S, Merritt M, Woessner DE, Lenkinski RE, Sherry AD. PARACEST agents: modulating MRI contrast via water proton exchange. Acc Chem Res 2003;36(10):783-790.
5. Woessner DE, Zhang S, Merritt ME, Sherry AD. Numerical solution of the Bloch equations provides insights into the optimum design of PARACEST agents for MRI. Magn Reson Med 2005;53(4):790-799.
6. Aime S, Calabi L, Biondi L, De Miranda M, Ghelli S, Paleari L, Rebaudengo C, Terreno E. Iopamidol: Exploring the potential use of a well-established x-ray contrast agent for MRI. Magn Reson Med 2005;53(4):830-834.
7. Longo DL, Dastru W, Digilio G, Keupp J, Langereis S, Lanzardo S, Prestigio S, Steinbach O, Terreno E, Uggeri F, Aime S. Iopamidol as a responsive MRI-chemical exchange saturation transfer contrast agent for pH mapping of kidneys: In vivo studies in mice at 7 T. Magn Reson Med 2010.

8. van Zijl PCM, Jones CK, Ren J, Malloy CR, Sherry AD. MR1 detection of glycogen in vivo by using chemical exchange saturation transfer imaging (glycoCEST). P Natl Acad Sci USA 2007;104(11):4359-4364.

9. Ling W, Regatte RR, Navon G, Jerschow A. Assessment of glycosaminoglycan concentration in vivo by chemical exchange-dependent saturation transfer (gagCEST). Proc Natl Acad Sci U S A 2008;105(7):2266-2270.

10. Jin T, Autio J, Obata T, Kim SG. Spin-locking versus chemical exchange saturation transfer MRI for investigating chemical exchange process between water and labile metabolite protons. Magn Reson Med 2010.

11. Wolff SD, Balaban RS. Magnetization transfer contrast (MTC) and tissue water proton relaxation in vivo. Magn Reson Med 1989;10(1):135-144.

12. Witschey WR, 2nd, Borthakur A, Elliott MA, Mellon E, Niyogi S, Wallman DJ, Wang C, Reddy R. Artifacts in T1 rho-weighted imaging: compensation for B(1) and B(0) field imperfections. J Magn Reson 2007;186(1):75-85.

13. Hills BP. The Proton-Exchange Cross-Relaxation Model of Water Relaxation in Biopolymer Systems. Mol Phys 1992;76(3):489-508.

14. Hills BP. The Proton-Exchange Cross-Relaxation Model of Water Relaxation in Biopolymer Systems .2. The Sol and Gel States of Gelatin. Mol Phys 1992;76(3):509-523.

15. Duvvuri U, Goldberg AD, Kranz JK, Hoang L, Reddy R, Wehrli FW, Wand AJ, Englander SW, Leigh JS. Water magnetic relaxation dispersion in biological systems: the contribution of proton exchange and implications for the noninvasive

detection of cartilage degradation. Proc Natl Acad Sci U S A 2001;98(22):12479-12484.

16. Hills BP, Babonneau F. A quantitative study of water proton relaxation in packed beds of porous particles with varying water content. Magn Reson Imaging 1994;12(6):909-922.

17. Chopra S, Mcclung RED, Jordan RB. Rotating-Frame Relaxation Rates of Solvent Molecules in Solutions of Paramagnetic-Ions Undergoing Solvent Exchange. J Magn Reson 1984;59(3):361-372.

18. Trott O, Palmer AG, 3rd. R1rho relaxation outside of the fast-exchange limit. J Magn Reson 2002;154(1):157-160.

19. Trott O, Palmer AG. Theoretical study of R-1p rotating-frame and R-2 free-precession relaxation in the presence of n-site chemical exchange. J Magn Reson 2004;170(1):104-112.

20. Witschey WR, Borthakur A, Elliott MA, Mellon E, Niyogi S, Wang C, Reddy R. Compensation for spin-lock artifacts using an off-resonance rotary echo in T1rhooff-weighted imaging. Magn Reson Med 2007;57(1):2-7.

21. Marquardt DW. An Algorithm for Least-Squares Estimation of Nonlinear Parameters. SIAM Journal on Applied Mathematics 1963;11(2):431-441.

22. Hills BP, Wright KM, Belton PS. Proton Nmr-Studies of Chemical and Diffusive Exchange in Carbohydrate Systems. Mol Phys 1989;67(6):1309-1326.

23. Sun PZ, van Zijl PC, Zhou J. Optimization of the irradiation power in chemical exchange dependent saturation transfer experiments. J Magn Reson 2005;175(2):193-200.

24. Regatte RR, Akella SV, Borthakur A, Reddy R. Proton spin-lock ratio imaging for quantitation of glycosaminoglycans in articular cartilage. J Magn Reson Imaging 2003;17(1):114-121.

25. Cobb JG, Xie J, Gore JC. Contributions of chemical exchange to T1ρ dispersion in a tissue model. Magnet Reson Med 2011:n/a-n/a.

26. Hills B. Magnetic resonance imaging in food science. New York: Wiley; 1998.

27. Swift TJ, Connick RE. NMR-Relaxation Mechanisms of O[sup 17] in Aqueous Solutions of Paramagnetic Cations and the Lifetime of Water Molecules in the First Coordination Sphere. The Journal of Chemical Physics 1962;37(2):307-320.

28. Goffeney N, Bulte JW, Duyn J, Bryant LH, Jr., van Zijl PC. Sensitive NMR detection of cationic-polymer-based gene delivery systems using saturation transfer via proton exchange. J Am Chem Soc 2001;123(35):8628-8629.

29. Englander SW, Downer NW, Teitelbaum H. Hydrogen exchange. Annu Rev Biochem 1972;41:903-924.

30. Liepinsh E, Otting G. Proton exchange rates from amino acid side chains - Implications for image contrast. Magnet Reson Med 1996;35(1):30-42.

31. Hills BP, Wright KM, Belton PS. Nmr-Studies of Water Proton Relaxation in Sephadex Bead Suspensions. Mol Phys 1989;67(1):193-208.

32. Gray ML, Burstein D, Kim YJ, Maroudas A. 2007 Elizabeth Winston Lanier Award Winner. Magnetic resonance imaging of cartilage glycosaminoglycan: basic principles, imaging technique, and clinical applications. J Orthop Res 2008;26(3):281-291.

33. Mathews MB. Isomeric Chondroitin Sulphates. Nature 1958;181(4606):421-422.

34. Makela HI, Grohn OH, Kettunen MI, Kauppinen RA. Proton exchange as a relaxation mechanism for T1 in the rotating frame in native and immobilized protein solutions. Biochem Biophys Res Commun 2001;289(4):813-818.

35. Hills BP, Takacs SF, Belton PS. The Effects of Proteins on the Proton Nmr Transverse Relaxation-Times of Water .1. Native Bovine Serum-Albumin. Mol Phys 1989;67(4):903-918.

36. Chen EL, Kim RJ. Magnetic Resonance Water Proton Relaxation in Protein Solutions and Tissue: T-1p Dispersion Characterization. Plos One 2010;5(1).

37. Otting G, Wuethrich K. Studies of protein hydration in aqueous solution by direct NMR observation of individual protein-bound water molecules. J Am Chem Soc 1989;111(5):1871-1875.

38. Virta A, Komu M, Kormano M. T-1 rho of protein solutions at very low fields: Dependence on molecular weight, concentration, and structure. Magnet Reson Med 1997;37(1):53-57.

CHAPTER VII

CONTRIBUTIONS OF CHEMICAL AND DIFFUSIVE EXCHANGE TO $T_{1\rho}$ DISPERSION

ABSTRACT

Variations in local magnetic susceptibility may induce gradients in magnetic fields that affect the signals acquired for MR imaging. Under appropriate diffusion conditions though, such inhomogeneous fields produce effects similar to slow chemical exchange. These diffusive effects may be found in combination with other chemical exchange effects processes with multiple time scales. We investigate these effects with simulations and measurements to determine their relative contributions to relaxation in the rotating frame ($R_{1\rho}$) in model systems.

Simulations of slow diffusive and rapid chemical exchange were performed using Bloch equations modified for chemical exchange. $R_{1\rho}$ was measured in suspensions of Sephadex beads and latex beads with varying locking frequencies at 9.4T. The second derivative of the resulting dispersion data was used to identify the number of apparent inflection points corresponding to specific exchange rates. These inflection points were then iteratively fit to a model of chemical exchange proposed by Chopra et al. to determine apparent average exchange rates.

Simulations of slow diffusive exchange resulted in single-inflection dispersion profiles that scale with exchange rate and chemical shift. The addition of rapid chemical exchange to the model resulted in double-inflection dispersion profiles. Consistent with these predictions, measurements of $R_{1\rho}$ for suspensions of latex beads showed only one inflection point, attributed to diffusion through external susceptibility gradients. The large diameter Sephadex beads showed multi-exponential relaxation and were excluded from further analysis. The smaller Sephadex beads showed two inflection points where the slow rate may be attributed to a combined contribution diffusion through external susceptibility gradients, diffusive exchange between regions of different fields with the same characteristic time, and faster chemical exchange between labile protons and water, which may be attributed to rapid $^{-}$OH exchange. The chemical and diffusive exchange rates responded to perturbations in temperature and pH, consistent with simulations.

Key Words: T1rho, dispersion, diffusion, chemical exchange

INTRODUCTION

Within a heterogeneous medium, variations in the local magnetic susceptibility may induce gradients in magnetic field that affect the signals acquired for MR imaging. The decay of transverse magnetization is then accelerated, but the precise effects depend on several factors including the sizes of the field perturbations, their spatial extent and geometry, the rate of spin diffusion in their vicinity, and the pulse sequence. One theoretical description that affords useful insights into how these factors interplay is the

Anderson-Weiss Mean Field approach previously applied to transverse relaxation in MRI by Kennan et al. (1). Spin-lattice relaxation in the rotating frame with rate $R_{1\rho}$ is also sensitive to variations in the local magnetic field experienced by nuclei that vary on the time scale of an applied radiofrequency spin-locking field that is under experimental control. Values of $R_{1\rho}$ generally decrease from R_2 to R_1 as the locking field increases, and the dispersion reflects the characteristic time scale of irreversible dephasing effects (2). In principle, measurements of $R_{1\rho}$ dispersion may be used to estimate some intrinsic properties of the medium. Of particular note, in biological media, if the intrinsic diffusion coefficient D is of order 2×10^{-5} cm^2s^{-1}, the time required to move 2 μm is 1 msec. If variations of field are present on this spatial scale we may expect to observe significant $R_{1\rho}$ dispersion around locking fields of 1 kHz, well within the regime readily accessible in practical MRI experiments. When the scale is much larger, dispersion will occur at correspondingly lower frequencies. Potentially, therefore diffusion dephasing within a magnetically inhomogeneous medium may contribute to $R_{1\rho}$ dispersion measurements, and appear similar to a chemical exchange process.

A second major potential contributor to $R_{1\rho}$ dispersion is more rapid chemical exchange between water protons and labile groups in solute molecules. This dispersion depends, amongst other factors, on the exchange rate and the chemical shift of the exchanging species. In biological samples, $R_{1\rho}$ dispersion may be typically dominated by the chemical exchange of hydroxyl, amine, and / or amide protons. In a medium containing variations in bulk susceptibility and chemically exchanging protons, the $R_{1\rho}$ dispersion will reflect the integrated effects of both diffusion and chemical exchange. Here we

consider some simple systems that demonstrate these behaviors and show how these different mechanisms may be separately identified. By using an appropriate theory and analysis, useful parameters that describe the samples may be quantified.

Although a precise description of diffusion through gradients requires a computation of the continuous dephasing that occurs over time due to random motions, we show below how in practice we can use the approximation that diffusion may be represented as slow exchange between regions of discrete frequencies, which simplifies the analysis considerably.

Intrinsic field gradients in tissues caused by variations in bulk magnetic susceptibility ($\Delta\chi$) have a spatial scale that reflects the size of the inhomogeneity. For example, micron-scale effects may arise around deposits of iron or calcium or because of the influence of microvascular changes in blood oxygenation, the basis of the blood level oxygen dependence (BOLD) effect on R_2* (1). Diffusion around such inhomogeneities causes dephasing and effective relaxation. The time scale over which the local field varies significantly corresponds to the time required to diffuse distances on the order of the size of the inhomogeneity.

Here we consider and contrast the $R_{1\rho}$ dispersion characteristics of water in the presence of packed arrays of small spherical beads. Latex beads represent the situation where the field is disturbed by the susceptibility mismatch between latex and water. Sephadex® beads consist of cross-linked dextran sugars that swell when hydrated and are a useful

model system to explore the combined effects of susceptibility, diffusion, and chemical exchange (3,4). They are commercially available in a variety of sizes and cross-link densities. The beads are permeable to the extent that water may freely diffuse between the inner dextran and outside water pools. Quantitative measurements of these effects have previously been made with Carr-Purcell-Meiboom-Gill (CPMG) techniques and result in enhanced transverse relaxation at a rate proportional to the pulse spacing (1,4,5).

Proton relaxation inside Sephadex beads is dominated by hydroxyl ($^{-}$OH) chemical exchange as reported by Hills et al. (4,6). However, Hills noted that under certain experimental conditions, diffusive exchange behaves like slow chemical exchange and a double-dispersion is observable in CPMG experiments in which the pulse rate is varied (6,7). Hills proposed a model that attributes the observed low frequency dispersion to a combination of diffusive exchange from within the beads to the solvent and diffusion through the intrinsic susceptibility gradients. This diffusive exchange model is characterized by protons moving between two spatially uniform parts of a sample (e.g. between water and Sephadex bead) where their spins experience different relaxation rates or are imparted with a different resonant frequency as shown in Figure 1. The characteristic rate for diffusive exchange is expected to be $\sim D/r^2$, where 'D' is the diffusion coefficient and 'r' is the mean bead radius (4). The same time scale is relevant for the case of diffusion among susceptibility gradients external to the beads, as is the case for latex.

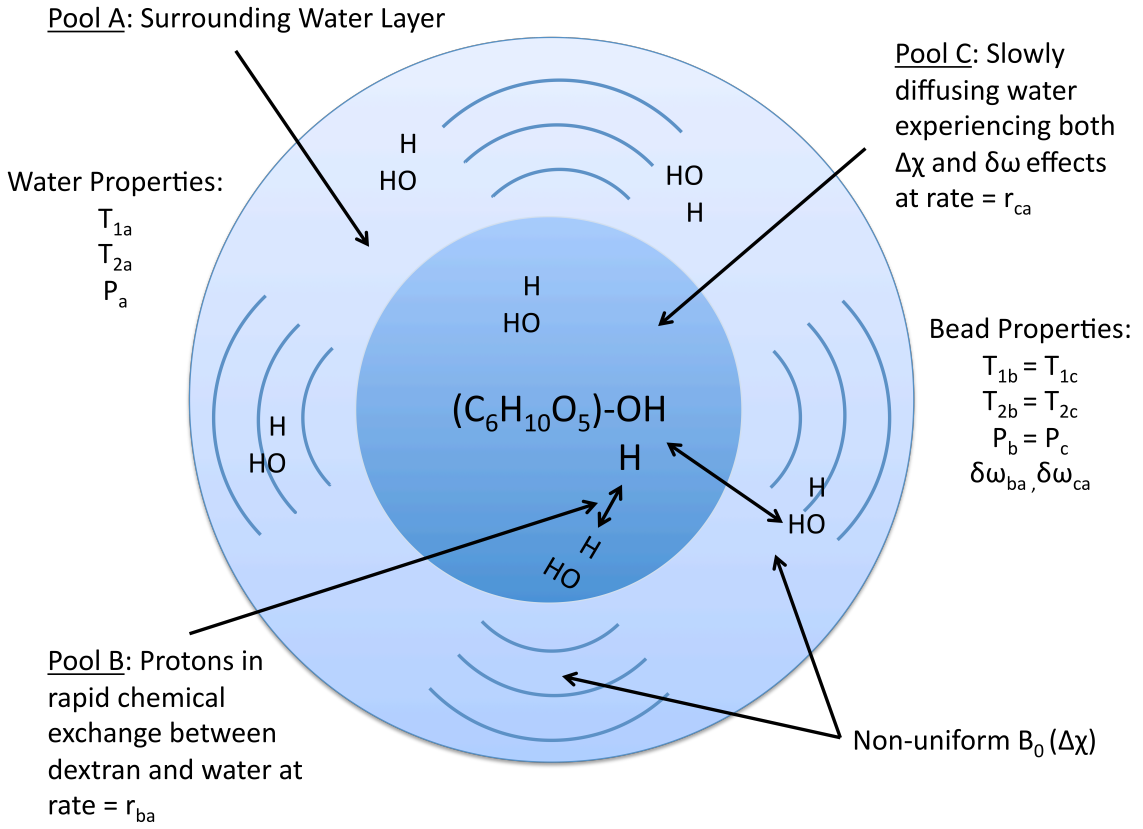

Figure 1. A model of chemical and diffusive exchange. The Sephadex bead approximates a sphere on the order of tens of microns in radius, and is composed of cross-linked dextran with numerous ¯OH exchange sites. Pool A represents free water, Pool B represents surface ¯OH groups in rapid exchange with water at rate k_{ba}, Pool C represents interior ¯OH groups in diffusive exchange from within the bead to the surrounding water at rate k_{ca}.

While Hills and others have measured CPMG dispersions, it is often technically easier to measure a greater range of spin lock frequencies than equivalent CPMG pulse rates. Therefore, dispersive effects due to exchange may be apparent over a wider range of locking fields as compared to CPMG dispersion. We demonstrate that slow diffusive exchange may be approximated as slow chemical exchange with simulations of the Bloch-McConnell equations (as opposed to the traditionally used Bloch-Torrey equations

governing diffusion). To fit simulated and experimental $R_{1\rho}$ data to a model that contains both diffusive and chemical exchange, we propose extending the model of chemical exchange under spin-locking conditions by Chopra et al. to fit a double-dispersion curve (8). We show how this fits the simulated data and evaluate its suitability for estimating chemical and diffusive exchange rates in experiments on relevant model samples.

THEORY

Dispersion data in porous beads containing labile protons are characterized by three dynamic processes, of which two depend on the resonant frequency difference between the inside of the bead and the exterior solvent. If this frequency difference is larger than the inverse of the time required to sample each spatial domain this corresponds to a "fast" diffusion regime and the net result is conceptually similar to chemical exchange between phases with rate $\sim D/r^2$ (6,9). When the rate of diffusion is much slower and the exchange rate is less than the frequency difference, nuclei do not sample all spatial areas. This results in different degrees of dephasing and more complex multi-exponential relaxation (6).

A second diffusion-related process is water diffusion through locally induced field gradients caused by susceptibility differences (1). For sphere-shaped objects, the gradients occur externally to the particles, and Eq. 1 gives the average field gradient generated,

$$G_{avg} = \mu_0 B_0 \Delta\chi / (4R) \qquad [1]$$

where μ_0 is the magnetic permeability of free space, B_0 is the main field strength, $\Delta\chi$ is the magnetic susceptibility difference between substances, and R is the object radius (10).

For transverse relaxation, this mechanism contributes an additional diffusion-related term shown in Eq 2.

$$R_{2,obs} = R_2 + D(\gamma G\tau)^2/3 \qquad [2]$$

where R_2 is the intrinsic spin-spin relaxation rate, D is the diffusion coefficient, γ is the gyromagnetic ratio, G is the induced field gradient, and τ is the interval between refocusing pulses in a CPMG measurement that defines the time scale for irreversible spin dephasing.

For rotating frame relaxation we can identify τ instead as the inverse of the locking frequency $\tau = (\gamma B_1)^{-1}$ so that an equivalent expression for rotating relaxation may be expressed as Eq 3.

$$R_{1\rho} = R_{1\rho}^0 + \frac{DG^2}{3B_1^2} \qquad [3]$$

where $R_{1\rho}$ is the rotating frame relaxation rate, $R_{1\rho}^0$ is the rotating frame relaxation rate at 0 Hz locking field ($R_{1\rho}^0 = R_2$), and B_1 is the applied locking field strength.

Hills et al. attribute a midpoint of a region of dispersion to the relevant mean diffusive or chemical exchange rate (6). However, if other parameters such as the relativities and chemical shifts of the exchanging species are known, Chopra, Hills, Woessner and others have shown that more precise estimates of chemical exchange may be fitted from rotating frame or CPMG dispersion data (3,8,11).

METHODS

Simulations of Diffusive and Chemical Exchange Effects on $R_{1\rho}$

In order to evaluate potential contributions of chemical and diffusive exchange to $R_{1\rho}$ measurements, simulations were performed using reference values for dextran and Sephadex beads (3,12) in combination with the Bloch equations modified for chemical exchange in a manner described by Hills with minor corrections for consistency of notation (13). We model the system as three pools of protons. Pool A represents the free water outside the beads that experience the external field gradients. Pool B is the rapidly exchanging hydroxyl sites on the surface and interior of the dextran bead, and pool C represents those water molecules that diffuse from the inside to the outside of the beads and experience a shift in field and resonance frequency as shown in Figure 1. The equations governing the simulations have been published previously by several authors (14,15), and are listed in the Appendix. Note that both Pools A and C experience field perturbations with the time scale $\sim r^2/D$ and will appear like water in relatively slow exchange.

Simulated data were generated to illustrate the effects of increasing the mean diffusive exchange rate or the scale of the local magnetic field gradients (k_{ca}) and to separately scale the mean chemical exchange rate (k_{ba}) to generate double-dispersion relaxation profiles. The chemical exchange rate was increased from 1 to 10 kHz while keeping the diffusive rate equal to 5 Hz. This rate is in the typical range for rapid hydroxyl exchange in sugar solutions (16). The diffusive exchange rate (k_{ca}) was increased from 5 to 50 Hz, which is consistent with other observations of such rates (3), with an accompanying chemical exchange rate that is well separated at 10 kHz to simulate the effect of increasing the magnitude of local field gradient strength. The data were simulated at main fields of $\omega_0 = 2\pi*$(200 and 400) MHz over a range of locking fields (ω_1) easily achievable experimentally from $2\pi*$[1 Hz to 10 kHz]. The remaining model characteristics were kept constant at T_{1a} = 3 sec, T_{2a} = 2 sec, $T_{1b} = T_{1c}$ = 1 sec, $T_{2b} = T_{2c}$ = 30 msec, p_a = 0.99, $p_b = p_c$ = 0.005, $\Delta\omega_{ba}$ = 1.23 ppm, $\Delta\omega_{ca}$ = 1.23 ppm or 0.123 ppm. Two values of $\Delta\omega_{ca}$ were used in simulation to model a range of systems whose slow diffusive exchange component (Pool C to A) is dominated by either a ~1 ppm frequency shift that is typical of a hydroxyl resonance or is dominated by a susceptibility-induced field that is typically an order of magnitude less for latex or ~0.1 ppm. Additionally, T_{2b} times are expected to change with bead density, and the values used here are approximate for G100-50 and were taken from fitted CPMG dispersion experiments by Hills et al. (3).

Zero-mean, Gaussian white noise was added to the simulated double-dispersion relaxation data, and the noisy data were subsequently fit to the double dispersion model of chemical and diffusive exchange described in the data analysis section below using a

Levenberg-Marquardt based non-linear least squares fitting algorithm implemented in MATLAB (R2010a, MATLAB, Natick, MA).

Materials

Samples of Sephadex® were obtained from Sigma-Aldrich in the following sizes and densities: G100-50, G100-120, G25-300, and G25-50; where the density scales as (1000 / X) and the mean bead radius is given in μm (Y), as in GX-Y on the product label. Thus the concentration of dextran inside a G100-50 bead is much lower (~10 % wt/wt) than in a G25-50 bead (~40%), which affects relaxation times of water within the beads. Phantoms of close packed, fully saturated beads were prepared by addition of distilled and deionized Milipore® water to a known dry weight of Sephadex beads. The bead and water mixtures were transferred to 5mm NMR tubes, and gently stirred to create an even mixture. The tubes were sealed and allowed to rest for 24 h before being used in any experiment.

Additional samples of G100-50 and G25-50 were prepared over a pH range of 6 to 9 in 1X PBS buffer to selectively accelerate chemical exchange by the addition of HCL or NaOH to the 0.6 mL microtubes. The total amount of liquid was held constant as compared to the unmodified samples.

A similarly sized bead phantom, without interior water or a chemically exchanging species, was created from 47-micron diameter latex beads (07314-5) that were obtained

from PolySciences (Warrington, PA) and centrifuged to create a close-packed mixture similar to the Sephadex beads.

NMR Experiments

All NMR experiments were performed on a Varian 9.4T magnet at 400 MHz (Varian Medical Systems, Palo Alto, CA) with a 5- or 10-mm loop-gap coil. Temperature was monitored by thermocouple connected to an animal physiologic monitoring system (SA Instruments, Stony Brook, NY) and was maintained at 25 or 40° C.

$T_{1\rho}$ dispersion was measured with a spin-locking sequence consisting of an adiabatic 90-degree pulse (AHP), followed by an on-resonance spin-locking (SL) pulse for half of the spin lock time (SLT), then a 180 degree refocusing pulse, followed by the other half of the spin lock pulse with reversed phase, and signal readout as described by Sepponen et al. and Witschey et al. (17,18). The SL pulse was varied logarithmically in 10 time increments between 10 msec and 2 sec and also in amplitude (SLA) in 21 increments between 2π*[1 Hz and 10 kHz]. The maximum allowed spectral line width with first and second order shims was 35 Hz for G25-Y beads, 25 Hz for G100-Y beads, and 12 Hz for the latex beads. TR was set at 5 times the estimated T_1 for each solution.

Data Analysis

$R_{1\rho}$ values were calculated by fitting the signal variation with SLT to a three-parameter mono-exponential decay function in MATLAB (The MathWorks, Inc., Natick, MA).

$$S(t) = S_0 \exp\left(-t * R_{1\rho}\right) + C \qquad [4]$$

We propose fitting double-dispersion data iteratively to the Chopra equation for chemical exchange contribution to $R_{1\rho}$ ($1/T_{1\rho}$) dispersion, shown in Eq. 5 (8)

$$R_{1\rho} = \left\{ \frac{R_2 + \frac{\left(R_{1\rho}^{\infty} * \omega_1^2\right)}{S_\rho^2}}{1 + \frac{\omega_1^2}{S_\rho^2}} \right\} \qquad [5]$$

where, $S_\rho^2 = (R_{1b} + k_{ex}) / (R_{2b} + k_{ex}) * \{ (R_{2b} + k_{ex})^2 + \Delta\omega_b^2 \}$. [6]

A non-linear least squares fit of the variation of $R_{1\rho}$ with ω_1, ($\omega_1 = \gamma B_1$), to Eq. 5 may be used to obtain best fits of R_2, $R_{1\rho}^{\infty}$ ($R_{1\rho}^0 \simeq R_1$), and S_ρ^2, where S_ρ is the midpoint between the R_2 and $R_{1\rho}^{\infty}$ values. For systems where multiple exchange processes are sufficiently separated in frequency we expect distinct double-dispersion profiles in measured $R_{1\rho}$. By taking the second derivative of the double-dispersion data, the three resulting zero crossings are assumed to define the boundaries of the low frequency diffusive exchange regime, the transition point from the diffusion dominated regime to chemical exchange dominated regime, and finally the higher frequency chemical exchange regime of the curve. With the exchange regimes thus separated, the data in the slow exchange regime are fit to Eq. 5, where the slow diffusion exchange rate ($k_{ex} = k_{ca}$) is expected to correspond to a midpoint in the dispersion curve (S_ρ), consistent with the observations of

Hills (4). In the fast chemical exchange region the $R_{1\rho}$ values are fit are fit to the full Chopra model (by including Eq. 6) to give the fast exchange component ($k_{ex} = k_{ba}$). The necessary chemical shift and other relaxation parameters are identical to those used in the simulations. This approach to fitting for fast chemical exchange rates has been previously used in cartilage systems and also in poly-acrylamide gels (21,22). By measuring the change in observed $R_{1\rho}$, G_{avg} in the solution can be estimated and then subsequently the mean $\Delta\chi$ using Eqs. 3 and 1 respectively, assuming a spherical geometry.

RESULTS

Simulation Results

Initial simulations of rapid diffusive exchange approximating chemical exchange explored the role of the frequency shift between pools C and A. The frequency ω_{ca} was varied from the chemical shift of dextran, ~1.23 ppm, to a frequency shift an order of magnitude lower, or ~25 Hz at main field strength of 200 MHz, representing a system with only diffusion through susceptibility gradients and no chemical exchange. The results are shown in Fig. 2.a. The larger frequency shift represents a system dominated by diffusive exchange approximating slow chemical exchange and is shown in Figure 2.b. The $R_{1\rho}$ dispersion profile scales with the exchange rate, k_{ca}, with an inflection point near ~250 Hz that corresponds roughly to the sum of the simulated chemical shift and exchange rate.

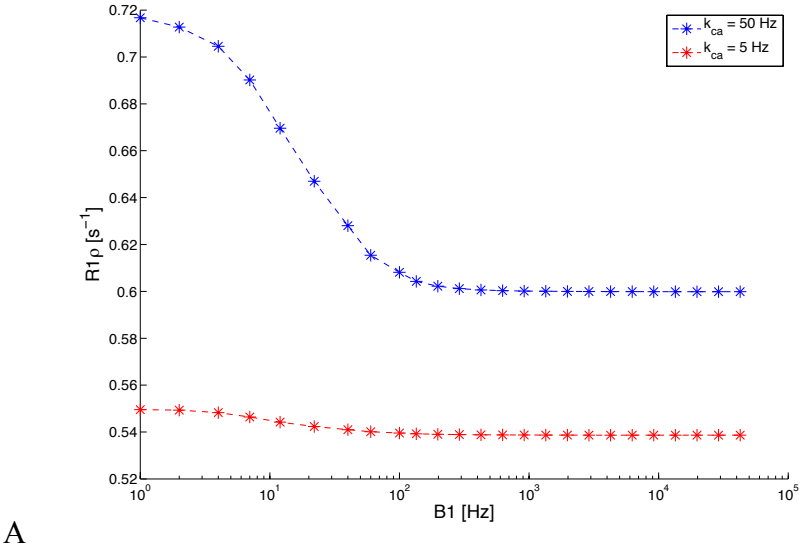

A

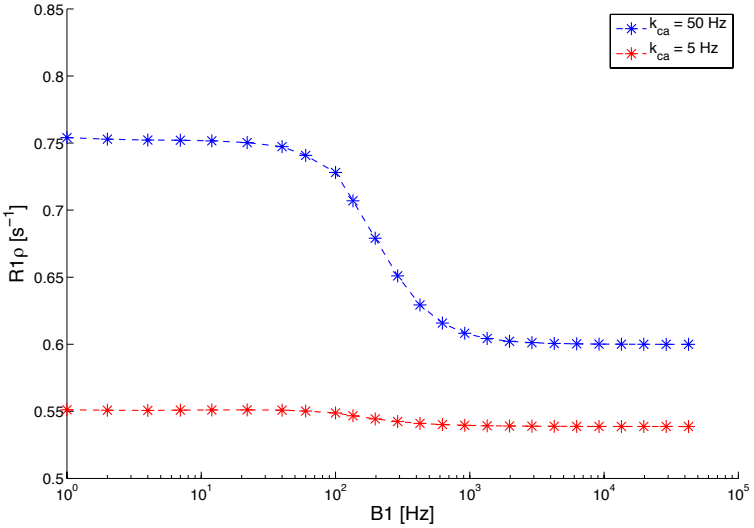

B

Figure 2. Simulations of diffusive exchange approximating slow chemical exchange (2.a) or diffusion related dephasing as spins encounter susceptibility-induced gradients (2.b).

2.a. Simulation of increasing the observed diffusive exchange rate (k_{ca}) from 5 to 50 Hz with $\delta\omega_{ca}$ = 1.23 ppm or ~250 Hz at 200 MHz. Note a single inflection point near ~250 Hz that scales with the increased exchange rate.

2.b. Simulation of increasing the observed diffusive exchange rate from 5 to 50 Hz with $\delta\omega_{ca}$ = 0.123 ppm or ~25 Hz at 200 MHz. Note a single inflection point near ~25 Hz that scales with the increased exchange rate.

Simulations of combined chemical and diffusive exchange were performed to create $R_{1\rho}$ double-dispersion profiles across a range of exchange rates, locking fields, and spectrometer frequencies. The effect of increasing the diffusive exchange rate from 5 to 50 Hz at $\omega_0 = 2\pi*200$ MHz, with chemical exchange rate of 10 kHz, is shown in Figure 3.a. Here the double dispersion profile is clearly demonstrated at low SLA, with $R_{1\rho}^0$ increasing from 2.4 to 2.7 s^{-1}. Figure 3.b. shows the effect of increasing chemical exchange rate from 1 kHz to 10 kHz at a constant diffusive exchange rate of 5 Hz at $\omega_0 = 2\pi*400$ MHz. This figure demonstrates the effect of increased separation of exchange rates of the two exchanging processes, with the 10 kHz profile showing the double-dispersion more clearly than the 1 kHz profile.

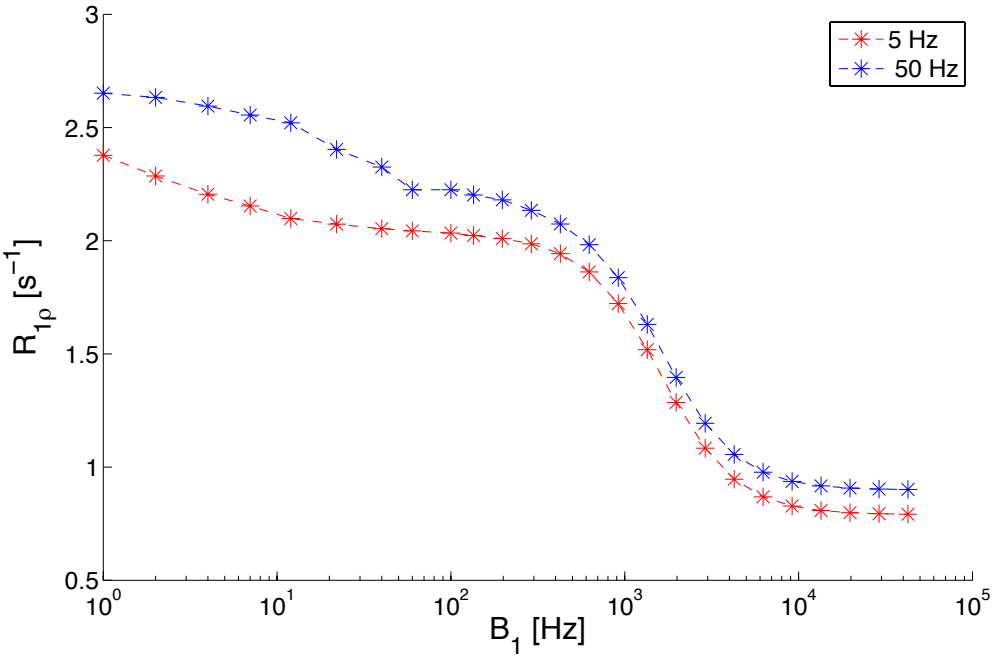

A

400 MHz

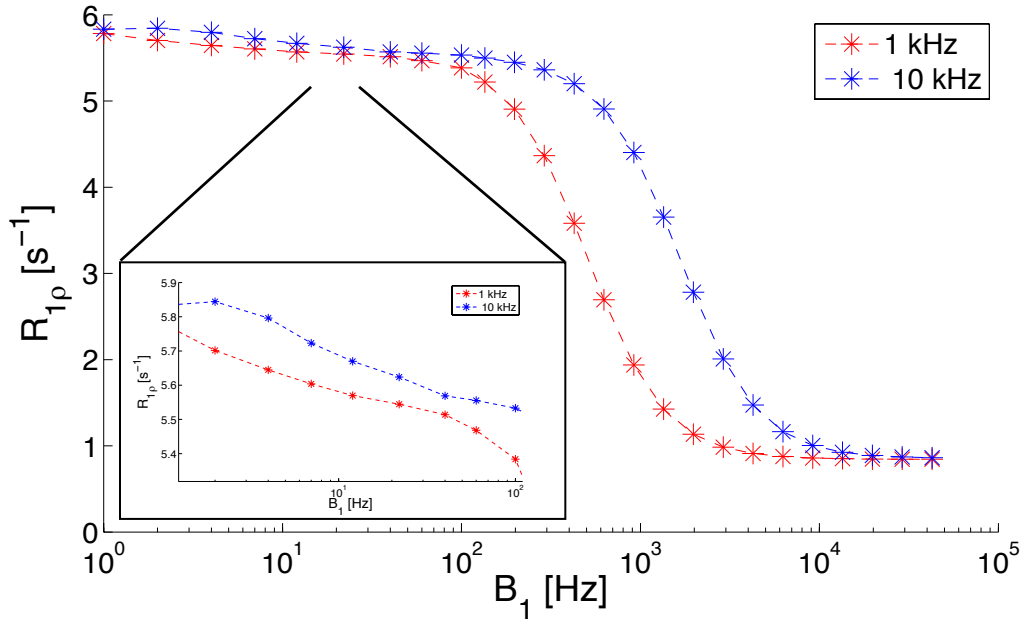

B

Figure 3. Simulations of Chemical and Diffusive Exchange

3.a. A simulation of $R_{1\rho}$ dispersion at 200 MHz with an increasing diffusive exchange rate (from 5 Hz to 50 Hz) and a constant chemical exchange rate. Note the subtle rise in $R_{1\rho}$ dispersion at SLA < 100 Hz.

3.b. A simulation of $R_{1\rho}$ dispersion at 400 MHz with an increasing chemical exchange rate (from 1 kHz to 10 kHz) and a constant diffusive exchange term of 5 Hz. Note the large increase in $R_{1\rho}$ dispersion at SLA > 100 Hz. The inset figure shows the dispersion within below 100 Hz SLA.

These simulated data were then used to test the ability of the Chopra expression to fit for the two exchange processes. The results of progressively adding noise to the closely spaced curve (5 Hz diffusive rate, and 1 kHz chemical exchange rate, at 400 MHz main field) are given in Table 1. The fitting for the chemical exchange rate is accurate within 8% of the simulated rate until the signal to noise ratio (SNR) drops below 20:1. The diffusive exchange rate is only accurate within 40% of the simulated rate until the SNR also drops below 20:1, at which point the double-dispersion is lost in noise and the fitting fails.

Table 1: Fitting Methods Compared

		SNR = 100:1	80	60	40	20	10
Chopra Fits	ChemEx	960.2 (± 17)	969.7 (± 21)	1054.5 (± 38)	924.7 (± 82)	806.6 (± 61)	829.2 (± 370)
	DiffEx	3.0 (± 2.7)	3.5 (± 2.8)	4.0 (± 5.8)	6.3 (± 5.5)	5.3 (±8.3)	n/a
		SNR = 100:1	80	60	40	20	10
% Variance	ChemEx	3.98%	3.03%	5.45%	7.53%	19.34%	17.08%
	DiffEx	39.40%	29.82%	19.13%	26.03%	5.66%	n/a

Sample noisy data fits with SNR = 80:1 with simulated data points, and fitted parameters from the fitting procedure shown in Figure 4. The chemical exchange fit is shown with a solid red line and the diffusive exchange fit is shown in solid blue. The range of fitted values was extended to higher and lower values to demonstrate where the fits would extend to over the whole range of simulated locking fields. The second derivative is shown as a dashed black line and illustrates where the zero crossings intersect the fitted data. Given the large range of y-values the second derivative encompasses it was difficult to normalize for plotting purposes, and so the overall shape is given on the inset figure in 4.a for reference.

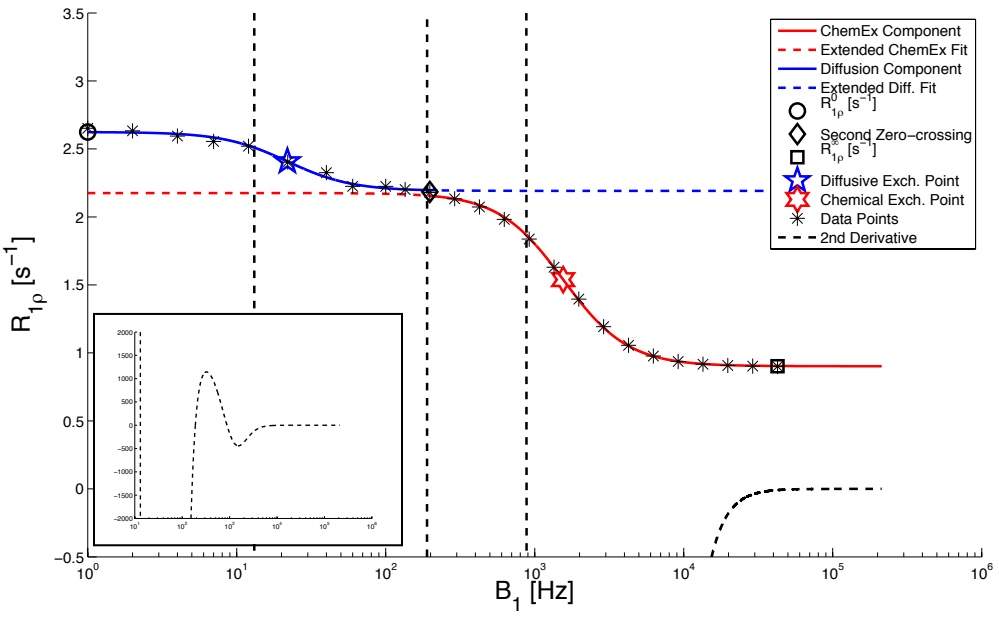

A

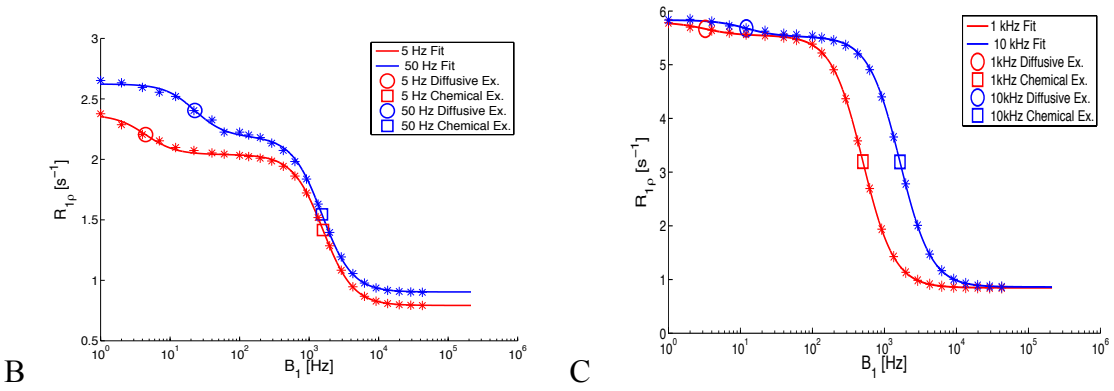

Figure 4. Model Fitting

4.a. Iterative fitting of simulated $R_{1\rho}$ double-dispersion due to chemical and diffusive exchange with the Chopra Eq. 5. The second derivative of the $R_{1\rho}$ dispersion data was calculated and the second zero crossing used to identify the inflection point between the chemical and diffusive exchange regimes (~200 Hz). The full second derivative is plotted in the inset figure. The Chopra equation was applied in an iterative fashion between SLA 0 and 200 Hz, and again between 200 Hz and 10 kHz. The midpoints of the diffusive and chemical exchange portions of the curve (S_ρ in Eq. 5) are shown with a 5- and 6-pointed star respectively.

4.b. Fitting of simulated $R_{1\rho}$ double-dispersion curves with the iterative Chopra technique. Figure 4.b shows the fittings from a 5 Hz diffusive component increased to 50 Hz with a chemical exchange rate of 10 kHz. Note that the mid-point of the chemical exchange portion of the curve (S_ρ in Eq. 5) remains relatively constant with increased diffusion.

4.c. shows the fittings from a simulation of a 5 Hz diffusive component and a chemical exchange rate that was increased from 1kHz to 10 kHz. Note that the increase in chemical exchange rate also increases the fitted diffusion component.

Sample fits of the plots in Figure 3.a. and 3.b. are given in Figure 4.b. and 4.b. respectively. Note that the increase in diffusive rate in Figure 4.b. has little effect on the fitted chemical exchange rate, whereas the increase in chemical exchange rate in Figure 4.c pulls the fitted diffusive rate to slightly higher frequency. The chemical exchange portion of the curve is accurate to within 8% of the simulated value across the range of simulated noise, and the diffusive value is accurate within 40% over the same range.

Experimental Results

NMR experiments on different size and density beads were performed to verify that $T_{1\rho}$ decay was predominantly monoexponential, implying fast chemical and diffusive exchange. All large diameter beads (> 120 μm) displayed multi-exponential behavior at 25C and were excluded from further analysis. The smaller diameter beads (50 μm) displayed predominantly mono-exponential behavior, confirming fast exchange processes at 25C.

Further experiments on latex and Sephadex beads of similar, small sizes were made to determine if their $R_{1\rho}$ dispersion profiles displayed obvious signs of multiple frequency components. Figure 5.a shows the G25-50 bead $R_{1\rho}$ dispersion plotted vs. the 47-μm latex bead dispersion. The second derivative of the latex dispersion resulted in only a single zero crossing at low frequency, consistent with the lack of an exchanging species on the latex bead. Thus the fitting results in a single frequency component at 42.1 Hz. The remaining fitted parameters are given in Table 2. Knowing the change in observed $R_{1\rho}$, G_{avg} can be estimated in the solution and the $\Delta\chi$ using Eqs. 3 and 1 respectively. Using

Eq. 3, if $\Delta R_{1\rho}$ is ~3.5 Hz, D is ~$2.5*10^{-9}$ m^2/s, γB_1 is 10 Hz, then G_{avg} is approximately 15 mT/m. Using this value we estimate $\Delta\chi$ for a spherical geometry with radius 23 μm, at 9.4T, to be 0.152 ppm or 61 Hz at 400MHz B_0. This value seems reasonable in light of the small changes in $R_{1\rho}$ observed.

Table 2: Fitted Data from Figures 5 and 6

Fig. 5.a.	Substance	Diffusive Exch. Rate [Hz]	Chemical Exch. Rate [Hz]
	47 μM Latex	42.1 (± 1.8)	n/a
	G25-50	19.2 (± 1.9)	2270 (± 520)

Fig. 5.b.	Substance	Diffusive Exch. Rate [Hz]	Chemical Exch. Rate [Hz]
	G100-50	13.2 (± 1.4)	1393 (± 330)
	G25-50	19.2 (± 1.9)	2270 (± 520)

Fig. 6.a.	Substance	Diffusive Exch. Rate [Hz]	Chemical Exch. Rate [Hz]
	G100-50 25C	13.2 (± 1.4)	1393 (± 330)
	40C	36.3 (± 9.0)	4140 (± 136)

Fig. 6.b.	Substance	Diffusive Exch. Rate [Hz]	Chemical Exch. Rate [Hz]
	G100 pH6	13.2 (± 1.4)	1365 (± 280)
	pH7	13.1 (± 1.4)	4596 (± 404)
	pH9	14.8 (± 1.4)	8650 (± 2385)

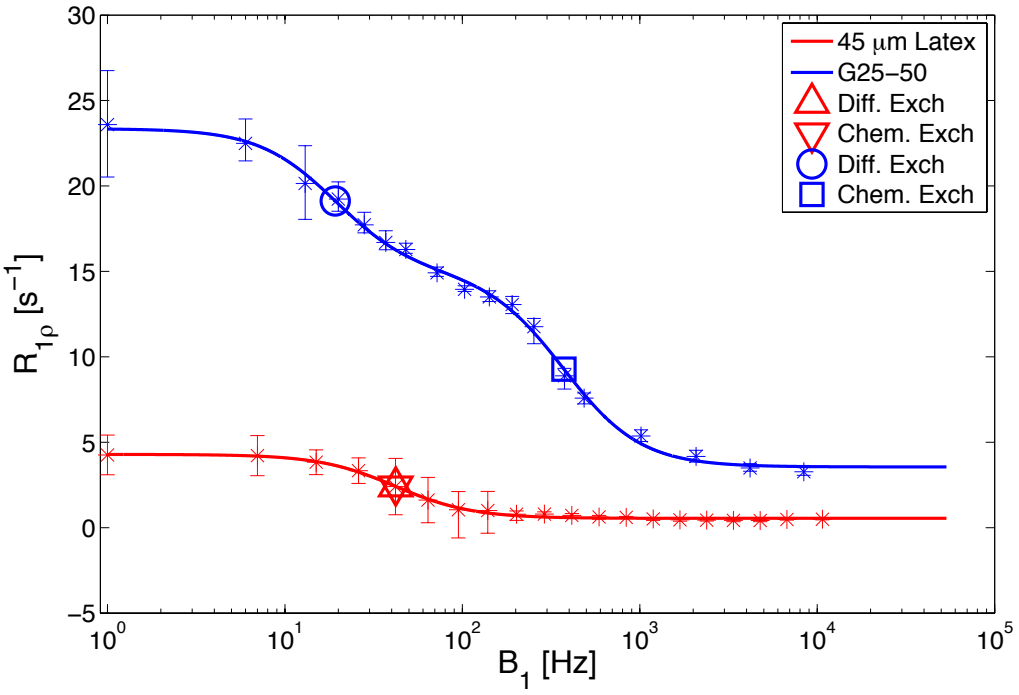

A

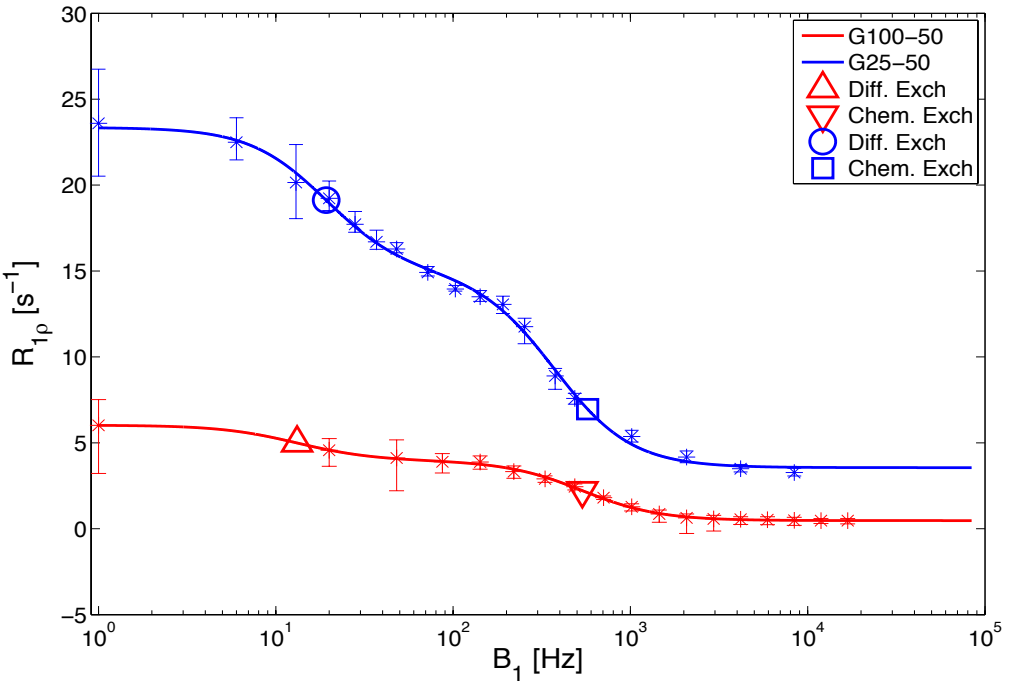

B

Figure 5. 5.a. The G25 bead shows a double dispersion, characteristic of chemical and diffusive and or susceptibility induced exchange. The latex bead's second derivative only contains one zero transition at low

frequency, indicating a lack of a chemically exchanging species. 5.b. Figure 5.b shows the characteristic double $R_{1\rho}$ dispersion curves for the G25-50 and G100-50 beads. The increased density of the G25-50 bead results in an increase in $R_{1\rho}$ values across the entire dispersion curve. The iterative fits to the Chopra equation [Eq. 5] are shown along with the mid-points (S_ρ) for both chemical and diffusive exchange.

This is contrasted to the G25-50 bead that shows an obvious double-dispersion with midpoints near 20 Hz and 400 Hz, which are attributed to diffusive and fast chemical exchange respectively. The combination of the two diffusive processes and fast chemical change result in a large increase in measured $R_{1\rho}$ at all SLA values. At low SLA the additional exchange processes present in the dextran bead result in an $R_{1\rho}$ value nearly 5 times that of the latex bead of similar size.

Figure 5.b shows the results of measured $R_{1\rho}$ dispersion curves for similarly sized 50-micron diameter beads with different densities. The G25-50 beads contain a greater concentration of dextran (~40% vs. ~10%) and display a range of $R_{1\rho}$ values approximately 5x that of the G100-50 bead. Interestingly the fitted rates for diffusive exchange are very similar and are given in Table 2.

The results of increasing both the chemical and diffusive exchange rate with temperature are plotted in Figure 6.a. For the G100-50 bead the two fitted midpoints of dispersion increase to higher frequencies by approximately 3-fold. The results of the double-dispersion fitting are given in Table 2. The effect of selectively increasing the chemical exchange rates is shown in Figure 6.b. As the pH is increased from 6 to 9, the fitted

chemical exchange rate increases with pH, whereas the fitted diffusive exchange rate remains fairly constant. The fitted parameters for Figure 6.b are also given in Table 2.

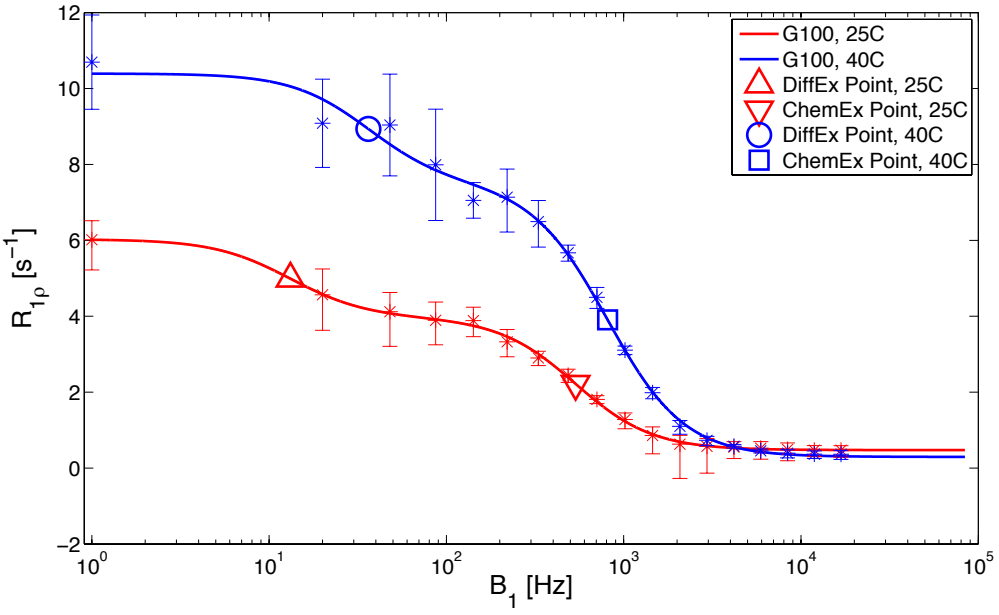

A

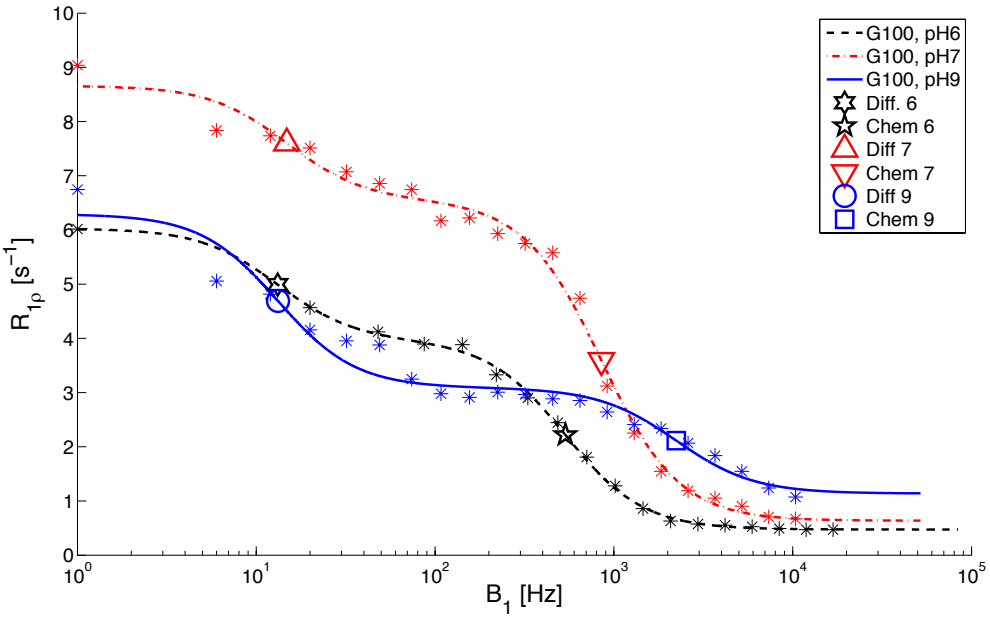

B

Figure 6. Shows the sensitivity of chemical and diffusive exchange rates to changes in temperature and pH.

6.a. $R_{1\rho}$ dispersion for G100-50 at 25 and 50 deg. C. Note that both the chemical and diffusive rates are sensitive to temperature perturbation.

6.b. $R_{1\rho}$ dispersion for G100-50 at pH 6,7,9. Note that the fitted mid-point (S_ρ term) for chemical exchange rate increases with increasing pH, while the diffusive exchange term remains fairly constant.

DISCUSSION AND CONCLUSIONS

Diffusion and chemical exchange may be important contributors to NMR relaxation and to MR image contrast, though their relative contributions have been seldom reported in the MR literature. Hills et al. published a series of papers exploring these contrast effects on transverse relaxation with CPMG dispersion on a model system of Sephadex beads. Spin-locking techniques may also be used to explore these processes, as they are technically much easier to implement in an imaging context. Therefore we investigated a similar model system to determine if the relative contributions of chemical and diffusive exchange in spin-locking experiments are separable and to determine their relative contributions to measured $R_{1\rho}$. The distinct exchange processes of diffusive exchange from water and hydroxyl protons within the bead to free water, of diffusion through susceptibility gradients, and of chemical exchange are depicted in Figure 1.

Numeric simulations of double dispersion data with a three-pool model of chemical exchange verified that the exchange processes of diffusion and chemical exchange result

in a double-dispersion $R_{1\rho}$ profile if the two processes have sufficiently separated mean frequencies. Figure 2 depicts the effect of modulating the magnitude of the frequency step of either diffusive exchange between the interior and exterior of the Sephadex or migration of spins through susceptibility gradients. The frequency step was decreased from a high rate of the chemical shift, representing no contribution from susceptibility effects, down an order of magnitude to a rate of $0.1*\delta\omega$, representing a dephasing contribution from susceptibility effects only. The upper rate is consistent with the chemical shift of dextran and the lower rate is consistent with prior reports of the contribution of susceptibility gradients to T_2 contrast in CPMG experiments (6). Therefore, Figure 2 demonstrates the range of frequencies (midpoints of the dispersion curves) that may reasonably be expected for both types of diffusive exchange in a model system of Sephadex beads in the absence of rapid chemical exchange. The midpoint of the dispersion curve is seen to scale with chemical shift and exchange rate as expected by Chopra et al. and others (8,22). The magnitude of $R_{1\rho}$ dispersion for Figure 2.a should be considered somewhat arbitrary, as the figure is designed to demonstrate how slow diffusion through susceptibility gradients may approximate chemical exchange at a particular rate near the midpoint of the dispersion curve, and as the Bloch equations modified for exchange do not directly model susceptibility effects. Protons traversing locally induced gradients incur gradually accruing phase changes, not the instantaneous jump between two discrete frequencies used here as a simplification. Therefore it is difficult to scale these effects with the exchange rate or "chemical shift" in a way that can be directly tied to the magnitude of a susceptibility gradient. Susceptibility contributions to relaxation are best modeled with Monte Carlo or other alternate methods, and several

excellent reviews have been published on these methods (1,23,24). Figure 2.b demonstrates the expected slow diffusive contribution of protons moving from within the bead to the surrounding water layer. Here, the midpoint of the dispersion curve moves to the right near the sum of the exchange rate and chemical shift. This is also consistent with the work of Chopra et al. and Hills et al. who state that the midpoint of a dispersion curve scales with the mean chemical exchange rate of a species (2,8). This slow chemical exchange process is more consistent with the Bloch equation simulations as the model and physical processes are more closely related (25). Therefore, the expected contribution to $R_{1\rho}$ relaxation has more relevance, and Figure 2.b shows that only a slight contribution of 0.1 s^{-1} is expected at the simulated rates and chemical shift.

Figure 3 shows the result of adding rapid chemical exchange to the model simulations, and demonstrates the extremes of dispersion midpoints that may be expected from rapid chemical exchange of hydroxyl protons in combination with slow diffusive exchange (3,19,26) at two field strengths. The effect of increasing the diffusive exchange rate by a factor of 10, in Figure 3.a, showed an increase in simulated $R_{1\rho}$ of ~0.2 s^{-1} at 200 MHz main field strength. There is some variation in fitted $R_{1\rho}$ values at locking fields < 30 Hz as the line width of the exchanging species is now greater than the locking field. This induces oscillations in the measured signal from off-resonance spin locking and is represented in the figure as increased fitting error. Figure 3.b shows the effect of increasing the chemical exchange rate from 1 kHz to 10 kHz with a constant diffusive exchange rate of 5 Hz at 400 MHz main field strength. The $R_{1\rho}$ dispersion curve moved to relatively higher frequency as expected, and resulted in a slightly more apparent

diffusive exchange component near 5 Hz. This is expected as the separation between the chemical and diffusive rates is now significantly greater and is consistent with the observations of Hills (4).

Figure 4 shows the results of iteratively fitting the simulated data to the Chopra model. The key feature to observe when selecting the range of frequencies to allocate to each process is the second derivative of the double-dispersion curve. The three resulting zero-crossings correspond specifically to the inflection point of the diffusion component, the transition point between the two processes, and the inflection point of the chemical exchange component. Each component is plotted in Figure 4.a along with an inset depicting the full second derivative. This method results in stable fittings for both chemical and diffusive exchange as long as the SNR remains above 20:1 as shown in Table 1. The chemical exchange portion of the curve is accurate to within 8% of the simulated value across the range of simulated noise, and the diffusive value is accurate within 40% over the same range. Thus the technique is potentially more sensitive to changes in the chemical exchange portion of the double-dispersion curve than the diffusive exchange region. However, given that the expected values for the diffusion portion of the curve are on the order of 5 to 10 Hz, the fitting of these values within a range of a few Hz is potentially very useful. Figure 4.b shows that an order of magnitude change in the diffusive exchange rate is observable in the simulated and fitted results, with little observed change in the fitted chemical exchange rate. The same is not true for the fitting to simulated data in Figure 4.c, which shows the fitted diffusive exchange rate

moving to higher frequency (~3 to ~18 Hz) when the simulated exchange rate is increased by an order of magnitude.

Spin locking NMR experiments on a model Sephadex system where the bead radius and densities were varied resulted in multi-exponential behavior for the large radius beads (> 120 um) at 25C. This is consistent with previous studies by Hills et al (6). This behavior is attributed to the slow rate of diffusion at 25C where all regions of the phantom are not sufficiently sampled, resulting in multi-exponential decay. As a result, these beads were excluded from the dispersion analysis. The small diameter beads showed predominantly monoexponential behavior at 25C and thus were used for the temperature and pH variation studies.

Figure 5.a shows a comparison of the effects of a latex bead of similar diameter is compared to the G25-50 bead. Only a single dispersion is noted in the latex bead data, indicating the lack of a chemical exchange component. The second derivative is consistent with this observation, showing only a single zero crossing. Given the lack of a chemically exchanging species on or within the latex molecule, the observed $R_{1\rho}$ dispersion is hypothesized to be from susceptibility induced dephasing alone. The mean frequency of this dispersion is 42 Hz and the remaining fitted parameters are given in Table 2. Our $\Delta\chi$ estimate of ~0.152 ppm, or 61 Hz at 400 MHz, is roughly 6.6 times the 0.023 ppm or 9.2 Hz $\Delta\chi$-induced dephasing component Hills et al. estimated for 50 micron Sephadex beads (4), which is consistent with the simulation in Fig. 2.a.

Figure 5.b shows the $R_{1\rho}$ dispersion data for the two 50 μm diameter Sephadex beads studied. The $R_{1\rho}^0$ value for the G100-50 bead, dextran density of roughly ~10 % (wt/wt), is 6.1 s^{-1}. The $R_{1\rho}^0$ value for the G25-50 bead, roughly 40% (wt/wt) dextran, is 23.9 s^{-1}. These values are consistent with CPMG dispersion data by Hills et al. who gave R_2 values of ~5 and 25 s^{-1} respectively (6). It's notable that the fitted diffusive and chemical exchange rates are within the same order of magnitude of each other, given the large difference in bead density. Also note that the fitted $R_{1\rho}$ rates became less precise at low SLA as is reflected in the larger error bars (1 SD). This is most likely due to inefficient locking at low rates as was noted in the simulation data. The line width of the high-density bead was ~35 Hz and so it may be expected that the applied B_1 field would fail to lock magnetization in the transverse plane below this frequency, resulting in oscillations.

In order to test the ability to fit for chemical and diffusive exchange across a range of variation, the G100-50 sample was measured at two temperatures. Both rates are expected to be sensitive to this perturbation with hydroxyl chemical exchange rates expected to increase by a factor of 2.5 per 10 degrees C as predicted by Englander et al. (25). For the 15-degree rise induced, an expected increase in hydroxyl exchange rates of 3.7 times is expected. Both fitted exchange rates increased by a factor of nearly three, consistent with these predictions. The fitted rates are given in Table 2 and the double-dispersion plots are shown in Figure 6.a. The fitted $R_{1\rho}$ value at low SLA increased from a value of 6.1 s^{-1} to 10.2 s^{-1} while at high locking field, little change was noted.

Figure 6.b. shows the results of selectively modulating the rapid chemical exchange rate by altering the pH of the sample. The samples were prepared at three pH values of 6, 7.4, and 9 and showed markedly different dispersion profiles. The pH 6 sample had a $R_{1\rho}^0$ value of 6 s^{-1} and dropped to 0.5 s^{-1} at high SLA. The pH 7.4 sample showed much greater $R_{1\rho}$ dispersion at low frequencies, with a $R_{1\rho}^0$ value of 9 s^{-1}. The pH 9 sample showed a decreased $R_{1\rho}^0$ of 6.8 s^{-1}, however the chemical exchange inflection point moved to significantly higher frequencies, consistent with a large increase in chemical exchange rate. These chemical exchange trends are also reflected in Table 2, where the fitted chemical exchange rate increases by a factor of six. Interestingly the fitted diffusive exchange rate remains relatively constant near 15 Hz, consistent with the simulations in Figure 3. It was thought that the diffusive exchange rate might be increased by pH modification as well, possibly separating the effects of diffusive exchange and susceptibility-related dephasing into three distinct inflection points. However, this was not observed. The increase and subsequent decrease in measured $R_{1\rho}$ as the chemical exchange rate rises is consistent with simulations and may be explained by referring to Eq. 7, an analytic expression of $R_{1\rho}$ dispersion, which is a simplification of the Bloch equations given certain assumptions (8,27). The expression for $R_{1\rho}$ dispersion as derived by Chopra et al. may be simplified under the reasonable conditions of $R_{1b}<R_{2b}<<r_b$ as:

$$R_{1\rho,\text{obs}} \cong R_{2,A} + P_B R_{2B}\left[1 + \frac{\frac{r_B}{R_{2B}} * \Delta\omega_B^2}{r_B^2 + \Delta\omega_B^2 + \omega_1^2}\right] \quad [7]$$

where P_b is the size of the B pool, $\Delta\omega_b$ is the chemical shift, r_b is the exchange rate from pool B to A, and ω_1 is the locking field amplitude.

As r_b becomes extremely high, the second term in brackets approaches zero and $R_{1\rho,obs}$ decreases and becomes exchange insensitive. However, these rates are typically outside the range of physiologic relevance (19). This effect has also been recently demonstrated by Jin et al. in sugar solutions (28).

The most significant experimental limitation of this experiment is the departure from mono-exponential decay observed at low locking field. As the locking field strength drops below the sample line width, spin locking begins to fail. This is mitigated by the use of a B_0 and B_1 compensating SL pulse (18), but as shown experimentally, the $T_{1\rho}$ fits demonstrate more uncertainty at low SLA. This is reflected in the 1-SD error bars used in Figs. 5 and 6, and contributes to the increased size of the confidence intervals shown for both the simulated and experimental data. However, the technique appears to be sensitive enough to show trends with a controlled set of experiments. It may be more efficient and accurate to stop acquiring data when $T_{1\rho}$ fitting drops below some set R^2 value and extrapolate a fit line to lower locking field frequencies.

It would be interesting to compare the simulation and experimental results from the Bloch-McConnel equations to similar parameters using the finite element or Monte Carlo methods required for the Bloch-Torrey equations. Additionally, it may be more efficient

to fit these double-dispersion data in one step with Halle's model-free analysis techniques for multiple dispersion curves, rather than the iterative approach used here (29).

In conclusion, we have demonstrated that combined chemical and fast diffusive exchange may be approximated as a fast and slow chemical exchanging component in $R_{1\rho}$ dispersion curves with simulations and experiments on a simple system of Sephadex beads. The resulting double-dispersion curves may be fit with an extension of Chopra's chemical exchange model. These data may be of use for investigating systems where diffusion effects are an important contributor relaxation.

ACKNOWLEDGEMENTS

NCRR 1S10 RR17799

NIH R01 EB000214

APPENDIX

This notation corresponds to a three-pool system of free water A and exchange processes due to chemical exchange in pool B and diffusive exchange in pool C. Variations in the rates of k and κ are used to modulate exchange among pools.

$$\dot{\mathbf{M}} = \mathbf{A} \bullet \mathbf{M} + \mathbf{M}', \qquad [1]$$

where

$$M = \begin{bmatrix} M_a \\ M_b \\ M_c \end{bmatrix} \text{ and } M_i = \begin{bmatrix} M_x^i \\ M_y^i \\ M_z^i \end{bmatrix}, \text{ i = a,b,c}$$

and A is the 9 x 9 matrix

$$A = \begin{bmatrix} a & \prod(k_b + \kappa_b) & \prod \kappa'_{-c} \\ \prod(k_a + \kappa_a) & b & \prod \kappa_{-c} \\ \prod \kappa'_c & \prod \kappa_c & c \end{bmatrix} \qquad [2]$$

where Π is the 3 x 3 identity matrix and

$$a = \begin{bmatrix} -(R_{2a} + k_a + \kappa_a + \kappa'_c) & (\omega - \omega_a) & \omega_1 \\ -(\omega - \omega_a) & -(R_{2a} + k_a + \kappa_a + \kappa'_c) & 0 \\ -\omega_1 & 0 & -(R_{1a} + k_a + \kappa_a + \kappa'_c) \end{bmatrix} \qquad [3]$$

$$b = \begin{bmatrix} -(R_{2b} + k_b + \kappa_b + \kappa'_b) & (\omega - \omega_b) & \omega_1 \\ -(\omega - \omega_b) & -(R_{2b} + k_b + \kappa_b + \kappa'_b) & 0 \\ -\omega_1 & 0 & -(R_{1b} + k_b + \kappa_b + \kappa'_b) \end{bmatrix} \qquad [4]$$

$$c = \begin{bmatrix} -\left(R_{2c} + \kappa'_{-c} + \kappa_{-c}\right) & \left(\omega - \omega_c\right) & \omega_1 \\ -\left(\omega - \omega_c\right) & -\left(R_{2c} + \kappa'_{-c} + \kappa_{-c}\right) & 0 \\ -\omega_1 & 0 & -\left(R_{1a} + \kappa'_{-c} + \kappa_{-c}\right) \end{bmatrix} \qquad [5]$$

This notation corresponds to a three-pool system of free water (A) and two exchangeable proton pools (B and C). The rate terms of k and κ are used to modulate exchange among pools. $\mathbf{M}'$ is the equilibrium vector:

$$\mathbf{M}' = \begin{bmatrix} M_a^0 R_{1a} \\ M_b^0 R_{1b} \\ M_c^0 R_{1c} \end{bmatrix} \text{where } \mathbf{M}_i^0 = \begin{bmatrix} 0 \\ 0 \\ M_z^{i0} \end{bmatrix} \text{ i = a,b,c} \qquad [6]$$

Resonance frequency offsets may be explicitly accounted for with the following expressions:

$$\omega - \omega_a = \omega_z + \left(1 - P_a\right)\delta\omega + P_c\delta\Omega \ , \quad [7]$$

$$\omega - \omega_b = \omega_z + P_a\delta\omega + P_c\delta\Omega \, , \qquad [8]$$

$$\omega - \omega_c = \omega_z - P_a\delta\omega - \left(P_a + P_b\right)\delta\Omega \, , \quad [9]$$

where $\delta\omega = (\omega_b - \omega_a)$, $\delta\Omega = (\omega_c - \omega_b)$, and the rf offset $\omega_z = (\omega - \omega_{avg})$, where ω_{avg} is the weighted average of the resonance frequency of all three pools. Mass balance still holds in the rotating frame, so the typical flux equalities of $P_a k_a = P_b k_b$, $P_a \kappa_a = P_b \kappa_b$,

$P_c\kappa'_{-c} = P_a\kappa'_c$ and $P_b\kappa_c = P_c\kappa_{-c}$ remain valid. Simulations for two-pool models may be performed by simply removing pool "C" from the model.

REFERENCES

1. Kennan RP, Zhong J, Gore JC. Intravascular susceptibility contrast mechanisms in tissues. Magn Reson Med 1994;31(1):9-21.
2. Hills B. Magnetic resonance imaging in food science. New York: Wiley; 1998.
3. Hills BP, Babonneau F. A quantitative study of water proton relaxation in packed beds of porous particles with varying water content. Magn Reson Imaging 1994;12(6):909-922.
4. Hills BP, Wright KM, Belton PS. Proton Nmr-Studies of Chemical and Diffusive Exchange in Carbohydrate Systems. Mol Phys 1989;67(6):1309-1326.
5. Meiboom S, Gill D. Modified Spin-Echo Method for Measuring Nuclear Relaxation Times. Rev Sci Instrum 1958;29(8):688-691.
6. Hills BP, Wright KM, Belton PS. Nmr-Studies of Water Proton Relaxation in Sephadex Bead Suspensions. Mol Phys 1989;67(1):193-208.
7. Hills BP, Takacs SF, Belton PS. The Effects of Proteins on the Proton Nmr Transverse Relaxation-Time of Water .2. Protein Aggregation. Mol Phys 1989;67(4):919-937.
8. Chopra S, Mcclung RED, Jordan RB. Rotating-Frame Relaxation Rates of Solvent Molecules in Solutions of Paramagnetic-Ions Undergoing Solvent Exchange. J Magn Reson 1984;59(3):361-372.
9. Beall PT, Amtey SR, Kasturi SR. NMR data handbook for biomedical applications. New York: Pergamon Press; 1984. xviii, 198 p. p.

10. Glasel JA, Lee KH. Interpretation of Water Nuclear Magnetic-Resonance Relaxation-Times in Heterogeneous Systems. J Am Chem Soc 1974;96(4):970-978.

11. Woessner DE. Brownian motion and its effects in NMR chemical exchange and relaxation in liquids. Concept Magnetic Res 1996;8(6):397-421.

12. Harvey JM, Symons MCR, Naftalin RJ. Proton Magnetic-Resonance Study of Hydration of Glucose. Nature 1976;261(5559):435-436.

13. Hills BP. Water proton relaxation in dilute and unsaturated suspensions of non-porous particles. Magn Reson Imaging 1994;12(2):183-190.

14. Hills BP. The Proton-Exchange Cross-Relaxation Model of Water Relaxation in Biopolymer Systems .2. The Sol and Gel States of Gelatin. Mol Phys 1992;76(3):509-523.

15. Woessner DE, Zhang S, Merritt ME, Sherry AD. Numerical solution of the Bloch equations provides insights into the optimum design of PARACEST agents for MRI. Magn Reson Med 2005;53(4):790-799.

16. Molday RS, Englande.Sw, Kallenrg. Primary Structure Effects on Peptide Group Hydrogen-Exchange. Biochemistry-Us 1972;11(2):150-&.

17. Sepponen RE, Pohjonen JA, Sipponen JT, Tanttu JI. A method for T1 rho imaging. J Comput Assist Tomogr 1985;9(6):1007-1011.

18. Witschey WR, 2nd, Borthakur A, Elliott MA, Mellon E, Niyogi S, Wallman DJ, Wang C, Reddy R. Artifacts in T1 rho-weighted imaging: compensation for B(1) and B(0) field imperfections. J Magn Reson 2007;186(1):75-85.

19. Liepinsh E, Otting G. Proton exchange rates from amino acid side chains - Implications for image contrast. Magnet Reson Med 1996;35(1):30-42.

20. Hills BP, Takacs SF, Belton PS. The Effects of Proteins on the Proton Nmr Transverse Relaxation-Times of Water .1. Native Bovine Serum-Albumin. Mol Phys 1989;67(4):903-918.

21. Regatte RR, Akella SV, Borthakur A, Reddy R. Proton spin-lock ratio imaging for quantitation of glycosaminoglycans in articular cartilage. J Magn Reson Imaging 2003;17(1):114-121.

22. Cobb JG, Xie J, Gore JC. Contributions of chemical exchange to T1ρ dispersion in a tissue model. Magnet Reson Med 2011:[Epub ahead of release].

23. Hardy P, Henkelman RM. On the Transverse relaxation rate enhancement induced by diffusion of spins through inhomogeneous fields. Magnet Reson Med 1991;17(2):348-356.

24. Pathak AP, Ward BD, Schmainda KM. A novel technique for modeling susceptibility-based contrast mechanisms for arbitrary microvascular geometries: The finite perturber method. Neuroimage 2008;40(3):1130-1143.

25. Englander SW, Downer NW, Teitelbaum H. Hydrogen exchange. Annu Rev Biochem 1972;41:903-924.

26. Hills BP, Cano C, Belton PS. Proton Nmr Relaxation Studies of Aqueous Polysaccharide Systems. Macromolecules 1991;24(10):2944-2950.

27. Trott O, Palmer AG, 3rd. R1rho relaxation outside of the fast-exchange limit. J Magn Reson 2002;154(1):157-160.

28. Jin T, Autio J, Obata T, Kim SG. Spin-locking versus chemical exchange saturation transfer MRI for investigating chemical exchange process between water and labile metabolite protons. Magn Reson Med 2010.

29. Halle B, Johannesson H, Venu K. Model-free analysis of stretched relaxation dispersions. J Magn Reson 1998;135(1):1-13.

CHAPTER VIII

CONCLUSIONS

SUMMARY OF MANUSCRIPTS

This work comprises a series of studies that attempt to move beyond qualitative measurements with magnetic resonance imaging towards a more quantitative understanding of the mechanisms by which protons relax in heterogeneous tissues. The experiments attempt to explain how molecular properties of model tissue systems influence proton relaxation and how they may be employed to generate useful contrast in images. The experiments emphasized measurements of spin-lattice relaxation in the rotating frame at high field, model fitting to extract exchange parameters, and image subtraction techniques to generate novel contrast based on selecting for specific exchange rates.

The experiments performed to address the goals of the first aim resulted in the implementation of multiple variations of $T_{1\rho}$ relaxation measurement sequences on the clinical and pre-clinical imaging systems at the Vanderbilt Institute for Imaging Science. For clinical imaging, quantitative $T_{1\rho}$ measurements were made *in vivo* on epiphyseal cartilage in children at 3T and the results are detailed in Chapter II. Student's t-tests were performed to compare means among anatomic regions of interest. Significant differences were found within subjects among all cartilage types compared ($p < 0.02$). The study concluded that it is feasible to acquire quantitative $T_{1\rho}$ data *in vivo*, and in addition,

normative $T_{1\rho}$ values for epiphyseal and articular cartilage in children were evaluated. It was determined that there are quantifiable differences in LB and NLB epiphyseal cartilage within a subject. Thus, spin-locking techniques may hold promise as a non-invasive method of studying normal and abnormal developmental states of cartilage in children.

The manuscript in Chapter III gives the results of making $T_{1\rho}$ dispersion measurements of a tissue model on a pre-clinical imaging system. Data were acquired on phantoms of polyacrylamide gel with a variance in the type of exchanging NH^+ group and in pH. The resulting $T_{1\rho}$ dispersion data were fit to a model of chemical exchange and the results compared with a novel simplification of this model that does not rely on assumptions about the exchanging pool relaxation parameters. For low stiffness gels, the calculated exchange values increased by a factor of 4 as pH increased, consistent with chemical exchange being the dominant contributor to $T_{1\rho}$ dispersion. Interestingly, calculated chemical exchange rates also increased with stiffness, likely due to modified side-chain exchange kinetics as the composition varied. This chapter demonstrates a new method to assess the structural and chemical effects on $T_{1\rho}$ relaxation dispersion with a suitable model under specific conditions. These phenomena may be exploited in an imaging context to emphasize the presence of nuclei of specific exchange rates, rather than chemical shifts. The simplification proposed in this paper may also be used to significantly reduce the amount of acquired data needed to make exchange rate measurements with spin locking techniques. This may prove especially useful for making quantitative exchange rate estimates on clinical systems where RF power limits reduce the amount of $T_{1\rho}$ dispersion data that may be acquired.

In Chapter IV we developed a novel approach to exchange rate selective imaging based on measured $T_{1\rho}$ dispersion with applied locking field strength, and demonstrated the method on samples containing the X-ray contrast agent Iohexol (IO) with and without cross-linked bovine serum albumin (BSA). $T_{1\rho}$ dispersion of water in the phantoms was measured with a Varian 9.4T magnet by an on-resonance SL pulse with fast spin-echo readout, and the results used to estimate exchange rates. The IO phantom alone gave a fitted exchange rate of ~1 kHz, BSA alone was ~11 kHz, and in combination gave rates in between. Thus, the addition of Iohexol to a tissue phantom of BSA resulted in large changes in apparent exchange rates, and thus $T_{1\rho}$ dispersion profiles. A novel image subtraction method was used to generate contrast based primarily on differences in exchange rates and reduced the effects of differences in R_2 and R_1 on image contrast. By using these estimated rates, we demonstrated how a novel SL imaging method may be used to enhance contrast due to the presence of a contrast agent whose protons have specific exchange rates.

Chapters V and VI compared spin locking techniques theoretically and experimentally to CEST techniques on a number of biologically relevant tissue constituents. The contribution of chemical exchange to $T_{1\rho}$ decay and to CEST contrast was modeled with the Bloch equations and the differences in sensitivity evaluated. In Chapter V, Simulations of rotating frame dispersion and CEST contrast were performed on two model systems. Poly-L-lysine, a simple polypeptide of known relaxation parameters, was chosen as a model of amide (NH^+) exchange. Dextran, a simple poly-glucose molecule,

was selected as a model of hydroxyl ($^{-}$OH) exchange. These were chosen because of the simplicity of their CEST z-spectra and their moderate exchange rates (< 1 kHz).

The simulations reveal that for systems in which appropriate exchange occurs, both CEST and $R_{1\rho}$ measurements depend on similar exchange parameters but they manifest themselves differently in their effects on MRI contrast. CEST contrast may be larger in the slow and intermediate exchange regimes for protons with large resonant frequency offsets (> 2ppm). On the other hand, the SL technique produces larger contrast enhancement when resonant frequency offsets are small (< 2 ppm) and exchange is in the intermediate to fast regime. Both techniques benefit from increasing main field (B_0), and each provides a useful approach to producing images that emphasize protons undergoing chemical exchange under specific experimental conditions.

In Chapter VI, measurements of rotating frame ($R_{1\rho}$) dispersion and CEST z-spectra were performed on biologically important polypeptides and sugars. Using these data, a novel imaging protocol based on rotating frame dispersion imaging, which emphasizes contrast originating from species that exchange at specific rates (as opposed to chemical shifts) was demonstrated.

We showed that both CEST and SL imaging may generate contrast in MRI from chemically exchanging protons especially at high fields. The CEST technique may be particularly sensitive to species in the slow and intermediate exchange regimes with large chemical shifts (> 2ppm). The SL technique may produce greater contrast when the

exchanging species has a small resonant frequency offset (< 2 ppm) and / or exchanges more rapidly in the intermediate to fast exchange regimes. SL contrast increases more than CEST effects with increasing main field (B_0), and may be more directly related to the concentration of exchanging protons. Both techniques provide a means to produce images sensitive to specific types of exchanging protons in biological media.

Chapter VII describes studies on a model system of Sephadex and latex beads. Variations in local magnetic susceptibility may induce gradients in magnetic fields that affect the signals acquired for MR imaging. Under appropriate diffusion conditions, such inhomogeneous fields produce effects similar to slow chemical exchange. These diffusion effects may be found in combination with other chemical exchange effects with multiple time scales. We investigated these effects with simulations and measurements to determine their relative contributions to relaxation in the rotating frame ($R_{1\rho}$) in model systems.

Simulations of slow diffusive and rapid chemical exchange were performed using Bloch equations modified for chemical exchange. To validate these simulations, $R_{1\rho}$ was measured in suspensions of Sephadex beads and latex beads with varying locking frequencies at 9.4T. In a manner similar to the method explored in Chapter III, the second derivative of the resulting dispersion data was used to identify the number of apparent inflection points corresponding to specific exchange rates. These inflection points were then iteratively fit to a model of chemical exchange.

Simulations of slow diffusive exchange resulted in single-inflection dispersion profiles that scale with exchange rate and chemical shift. The addition of rapid chemical exchange to the model resulted in double-inflection dispersion profiles. Consistent with these predictions, measurements of $R_{1\rho}$ for suspensions of latex beads showed only one inflection point, attributed to diffusion through external susceptibility gradients. The smaller Sephadex beads showed two inflection points where the slow rate may be attributed to a combined contribution diffusion through external susceptibility gradients, diffusive exchange between regions of different fields with the same characteristic time, and faster chemical exchange between labile protons and water, which may be attributed to rapid $^{-}$OH exchange. The chemical and diffusive exchange rates responded to perturbations in temperature and pH, consistent with simulations. We concluded that spin-locking techniques may be used to investigate systems where diffusion effects are an important contributor relaxation.

APPLICATIONS OF ROTATING FRAME RELAXATION MEASUREMENTS IN BIOLOGY AND MEDICINE

We demonstrated the ability to generate images in a clinical context as reported in Chapter II, where spin-locking techniques were used to identify different cartilaginous regions in children at 3T. Since spin-locking techniques are sensitive to several relaxation processes, such as chemical exchange and diffusion, $T_{1\rho}$ measurement is a potentially rich source of contrast. However, it is important to isolate as many relaxation parameters as possible to avoid sensitivity to multiple or conflicting effects. For this reason, the sensitivity of SL techniques to exchange rate based contrast agents may prove especially useful. The presence of an exogenous agent may simplify the analysis of SL contrast changes in complex tissues considerably *in vivo*, where multiple relaxation effects may be present.

We show that rotating frame relaxation measurements may be particularly suitable for making quantitative MRI measurements of substances with large concentrations of chemically exchanging species. In particular, many biologically relevant substances such as peptides and sugars contain large concentrations of NH^+ and ^-OH groups, respectively. It may be particularly useful to apply spin locking techniques in conjunction with an appropriate subtraction method to generate contrast based on changes in the local pH in a tissue of interest. Changes in local pH have been associated with many normal and abnormal cellular processes. The techniques developed here may be applicable to large changes in base-catalyzed exchange rates as shown in Chapters III through VI.

The reduced data acquisition technique reported in Chapter III may be useful for detecting changes in concentration of an exchanging agent *in vivo*. An important limitation of spin lock imaging is the available B_1 power that may be used to make dispersion measurements. This is a particularly large obstacle to the use of SL techniques in clinical imaging where the use of large B_1 powers is limited by specific absorption rate restrictions. However, the reduced data acquisition technique may allow for lower power B_1 values to be used while still giving reasonable exchange rate estimates under specific conditions. This may be of clinical relevance for sugars such as glycosaminoglycans that are of interest for their potential role in cartilage disease processes.

An additional application is the detection of an exogenous contrast agent such as the Iohexol x-ray contrast agent used in Chapter IV. These types of agents have large concentrations of exchanging $^{-}$OH groups, to which SL techniques are particularly sensitive as shown in Chapters V and VI. These types of agents induce large dispersions in $R_{1\rho}$ that may be successfully modulated with spin locking techniques may potentially generate novel contrast.

Finally, Chapter VII demonstrated the sensitivity of SL techniques to susceptibility agents in a model system. Susceptibility effects caused by agents such as calcium or iron deposits in the brain are associated with several neurodegenerative disease processes, and the results of these experiments may be useful in determining appropriate parameters for imaging these tissues with SL techniques.

FUTURE STUDIES

The experiments performed here reveal several potentially fruitful avenues for future study. The manuscript in Chapter II features normative values for epiphyseal cartilage in children, and it was determined that it is feasible to make $T_{1\rho}$ measurements *in vivo*. It may be possible to combine the reduced data acquisition technique proposed in Chapter III with the techniques used in Chapter II to make dispersion measurements *in vivo*. There is considerable interest in the ability to observe concentrations and distributions of glocosaminoglycans within epiphyseal cartilage as it matures. If the exchanging species of the predominant tissue constituents of epiphyseal cartilage are well separated, it may be possible to make exchange-rate sensitive images of individual tissue components as outlined in Chapters IV-VI. This ability may be particularly useful for monitoring normal and abnormal development of the cartilage epiphysis in children.

The experiments in Chapter IV briefly introduce the concept of exchange-rate sensitive image subtraction with $T_{1\rho}$ dispersion measurements. However, the range of rates to which the technique is sensitive is rather large. It may be useful to explore alternate versions of this technique that can narrow this sensitivity to a smaller range of exchange rates.

Since the experiments in Chapters V and VI were performed, an alternate model of the contribution of chemical exchange to $T_{1\rho}$ dispersion has been used in similar studies of tissue components by Jin et al. (116). This paper uses a derivation of Trott and Palmer's (19) method of fitting for exchange rates with $T_{1\rho}$ dispersion, which makes different

assumptions in the simplification of the Bloch equations than does Chopra et al (18). It may be useful to perform a theoretical or quantitative comparison of these two models to identify the conditions where each model is most appropriately used.

The experiments performed here focus exclusively on spin locking techniques on-resonance. However, many substances such as iron may shift the water proton resonance frequency. It may be useful to perform off-resonance experiments to identify conditions where this proton shift provides useful contrast. This possibility was explored for paramagnetic agents in a series of papers by Zhang et al. (117-120) and they were also evaluated briefly by Jin et al. for chemically exchanging species(116). These off-resonance techniques may be particularly useful for improving sensitivity to small concentrations of exchanging species that resonate far from water at low rates.

PROTECTION OF RESEARCH SUBJECTS

The Vanderbilt University Institutional Review Board (IRB) approved all studies involving human subjects. The subjects were provided with written and verbal informed consent. The consent forms and script for obtaining consent were tailored to the age of the subject. Dr. Herman Kan was charged with maintaining the IRB protocol and managing any private health information that was obtained through these studies. The IRB protocol number used was 0802223ICD.

SOCIETAL IMPLICATIONS

As one of the few clinical imaging modalities not to use ionizing radiation, magnetic resonance imaging (MRI) is as a compelling resource for biomedical research. Its relative safety coupled with a rich variety of available research techniques makes it an ideal platform for performing studies on human tissues. The physics governing MRI date back to the work of Bloch and Purcel who first coupled quantum mechanics theory to nuclear spin physics in the late 1940s, giving rise to the field of nuclear magnetic resonance (NMR) (23). Since then, foundational techniques have been developed to generate novel information about biologic tissue structure and function, revolutionizing the fields of chemistry, physics, and biology. The novel application of a spatially varying magnetic field over a sample in the 1970s by Lauterbur and others provided the ability to gather spatial information by separating the frequency components of the resulting signal (24). This development led to the realization that as a non-invasive imaging modality, MRI could be safely applied to humans by providing diagnostically useful tomographic information. Much of the subsequent research efforts in this field have been to develop meaningful contrast mechanisms for use in image formation. By seeking a more complete and quantitative description of these tissues in the normal state, hypotheses may be developed to probe for signal alterations as a function of physiological state, disease state, damage, or other perturbation.

This work fits into this research framework by attempting to further understanding of the contributing factors to rotating frame relaxation. The study of spin locking techniques on children's cartilage may lead to the use of MRI to monitor the normal and abnormal

development of the skeletal epiphysis. Abnormal developments such as constrictions of epiphyseal water channels may restrict normal growth, and the techniques such as spin locking may prove useful in monitoring changes in cartilage constituents and water content.

The study of chemical exchange effects on a tissue model with acrylamide, given in Chapter III, may lead to the ability to measure exchange rates with reduced fitting and data acquisition. This may overcome a traditional limitation of SL techniques in clinical settings, where only limited B_1 powers are available. However, the reduced data technique may allow a lower range of B_1 powers to be used while still resulting in reasonable exchange rate estimates for substances with large exchange rates and small chemical shifts such as sugars. Therefore this technique may improve the usefulness of MRI in diagnosing and monitoring cartilaginous diseases and other diseases feature changes in the amount of an exchanging species.

The study of the exogenous contrast agent Iohexol, in Chapter IV, may lead to the use of agents with large numbers of exchanging protons for exchange rate based imaging. The methods presented here represent a new class of contrast agents that may be useful in a variety of applications where the exchange rate is an important biomarker of physiologic state. These effects may be probed with SL techniques in an imaging context, thus allowing for choice in contrast based upon exchange rate as opposed to chemical shifts from CEST techniques.

The experiments comparing CEST and SL techniques on biologically relevant molecules, in Chapters V and VI, highlight the differences and complementary features of each exchange-sensitive technique. Knowledge of these features may increase understanding of the dynamic range of endogenous chemical exchange agents.

The Sephadex experiments in Chapter VII quantify the relative contributions of chemical exchange and diffusion through susceptibility gradients to rotating frame relaxation. Diffusion through these gradients is hypothesized to be a major contributor to relaxation in heterogeneous tissues, and its effects on image contrast are poorly understood. The study in Chapter VII helps to quantify these effects in a controlled experimental setting. It may be feasible for spin-locking techniques to determine the presence of susceptibility agents such as calcium or iron deposits in the brain, which have been associated with multiple disease processes. The results presented here will be of particular help in developing optimized spin-locking techniques for these purposes *in vivo*.

APPENDICES

Appendix 1: Role of the Student in the Manuscript

Jared Cobb prepared and formatted all manuscript materials with the exception of the first half of the introduction of Chapter VII, which was prepared by Dr. Gore. Dr. Gore acted as an editor and recommended changes to the other manuscript sections to improve clarity and to ensure that the content was of appropriate scope.

Appendix 2: Relaxation Simulations

It is often important when studying relaxation phenomena to employ the use of models to better understand and predict the behavior of proton relaxation under a variety of scenarios. Therefore rotating frame relaxation was modeled utilizing the Bloch equations modified for exchange. These equations are useful for predicting the relative role of exchange in rotating frame relaxation and dispersion. Following the demonstration of Hills et al. (31), the following equations for rotating frame relaxation and exchange were solved in MATLAB utilizing an ordinary differential equation solver. Slight corrections have been made for errors in notation from the original text. These simulations were used as a guide for the experimental parameters used in the experiments in the following chapters.

$$\dot{\mathbf{M}} = \mathbf{A} \bullet \mathbf{M} + \mathbf{M}', \qquad [1]$$

where

$$M = \begin{bmatrix} M_a \\ M_b \\ M_c \end{bmatrix} \text{ and } M = \begin{bmatrix} M_x^i \\ M_y^i \\ M_z^i \end{bmatrix}, \text{ i = a,b,c}$$

and A is the 9 x 9 matrix

$$A = \begin{bmatrix} a & \prod(k_b + \kappa_b) & \prod \kappa'_{-c} \\ \prod(k_a + \kappa_a) & b & \prod \kappa_{-c} \\ \prod \kappa'_c & \prod \kappa_c & c \end{bmatrix} \qquad [2]$$

where Π is the 3 x 3 identity matrix and

$$a = \begin{bmatrix} -(R_{2a} + k_a + \kappa_a + \kappa'_c) & (\omega - \omega_a) & \omega_1 \\ -(\omega - \omega_a) & -(R_{2a} + k_a + \kappa_a + \kappa'_c) & 0 \\ -\omega_1 & 0 & -(R_{1a} + k_a + \kappa_a + \kappa'_c) \end{bmatrix} \qquad [3]$$

$$b = \begin{bmatrix} -(R_{2b} + k_b + \kappa_b + \kappa'_b) & (\omega - \omega_b) & \omega_1 \\ -(\omega - \omega_b) & -(R_{2b} + k_b + \kappa_b + \kappa'_b) & 0 \\ -\omega_1 & 0 & -(R_{1b} + k_b + \kappa_b + \kappa'_b) \end{bmatrix} \qquad [4]$$

$$c = \begin{bmatrix} -(R_{2c} + \kappa'_{-c} + \kappa_{-c}) & (\omega - \omega_c) & \omega_1 \\ -(\omega - \omega_c) & -(R_{2c} + \kappa'_{-c} + \kappa_{-c}) & 0 \\ -\omega_1 & 0 & -(R_{1a} + \kappa'_{-c} + \kappa_{-c}) \end{bmatrix} \qquad [5]$$

This notation corresponds to a three-pool system of free water (A) and exchangeable proton pools (B and C). The rate terms of k and κ are used to modulate exchange among pools. $\mathbf{M}'$ is the equilibrium vector:

$$\mathbf{M}' = \begin{bmatrix} M_a^0 R_{1a} \\ M_b^0 R_{1b} \\ M_c^0 R_{1c} \end{bmatrix} \text{where } \mathbf{M}_i^0 = \begin{bmatrix} 0 \\ 0 \\ M_z^{i0} \end{bmatrix} \text{ i = a,b,c} \qquad [6]$$

Resonance frequency offsets may be explicitly accounted for with the following expressions:

$$\omega - \omega_a = \omega_z + (1 - P_a)\delta\omega + P_c\delta\Omega \ , \quad [7]$$

$$\omega - \omega_b = \omega_z + P_a\delta\omega + P_c\delta\Omega \, , \quad [8]$$

$$\omega - \omega_c = \omega_z - P_a\delta\omega - (P_a + P_b)\delta\Omega \, , \quad [9]$$

where $\delta\omega = (\omega_b - \omega_a)$, $\delta\Omega = (\omega_c - \omega_b)$, and the rf offset $\omega_z = (\omega - \omega_{avg})$, where ω_{avg} is the weighted average of the resonance frequency of all three pools. Mass balance still holds in the rotating frame, so the typical flux equalities of $P_a k_a = P_b k_b$, $P_a \kappa_a = P_b \kappa_b$, $P_c \kappa'_{-c} = P_a \kappa'_c$ and $P_b \kappa_c = P_c \kappa_{-c}$ remain valid. Simulations for two-pool models are performed by simply removing pool "C" from the above-mentioned model.

Appendix 3: Experimental Materials and Ancillary Data

Iohexol Samples
63 mM Iohexol in TRIS Buffer

pH Variations

Tube number	Substance
1 - 16 mM Iohexol in TRIS buffer	pH 5.5
2	pH 6.5
3	pH 7.4

32 mM IO (1/2 dilution) and 10% BSA

Tube number	Substance
B1 –	TRIS buffer
B2 - Iohexol in TRIS buffer	32 mM Iohexol
B3 – 10% BSA	10% GA X-linked (1%) BSA
B4 – IO + BSA	32 mM IO + 10% GA XL BSA

16 mM IO in D_20

Tube number	Substance
1 - 1:0:3 ->1 part 63mM IO: 0 D_2O: 3 water, pH 7	16 mM Iohexol in water
2 – 1:1.5:1.5. 1 part IO:1.5 D_20:1.5 water	16 mM IO in water/D_20
3 – 1:4:0. 1 part IO:3 D_20:0 water	16 mM IO in D_20

Peptide and Sugar Samples:
Group A

Tube Number (0.6 mL microtubes)	Substance
1 – Lysine, (mid wt) in 1X PBS, pH 7.4	10 mg/mL
2 -	5
3 -	2.5
4 -	1.25
5 -	0

Group B

Tube Number	Substance
1 – Glycogen in 1X PBS, pH 7.4	500 µM ~= 200mg/mL ~= 20% (wt/wt)
2 - G8876-500MG	250
3 -	125
4 -	63
5 -	0

Group C

Tube Number	Substance
1 – Dextran in H_20, pH 7	40 % (wt/wt)
2 - D9260-10G	20
3 -	10
4 -	5
5 -	0

Group D - Glu

Tube Number	Substance
1 – Glucose in H_20, pH 7	40 % (wt/wt)
2 – G8270 – 100 g	20
3 -	10
4 -	5
5 -	0

Group E - CS

Tube Number	Substance
1 – Chondroitin Sulfate in 1X PBS, pH 7.4	10 % (wt/wt)
2 – C4384	5
3 -	2.5
4 -	1.25
5 -	0

Group F

Tube Number	Substance
1 – Collagen in 1X PBS, pH 7.4	20 % (wt/wt)
2 -	10
3 -	5
4 -	2.5
5 -	0

Group G

Tube Number	Substance
1 – P4761 Poly-L-glutamic acid	10 mg/mL
2 – 25 mg (15-50kDa)	5
3 – in 1X PBS, pH 7.4	2.5
4 -	1.25
5 -	0

Group H

Tube Number	Substance
1 – P7890 Poly-L-lysine (15-30 kDa)	10 mg/mL

2 – in 1X PBS, pH 7.4	5
3 –	2.5
4 -	1.25
5 -	0

pH Variations
Group I

Tube Number	pH
pC1 – 10 % CS in H20	3
pC2 – Chondroitin Sulfate	5
pC3 –	7
pC4 -	9
pC5 -	11

Group J

Tube Number	pH
pG1 – 10 % Glucose in H20	3
pG 2 –	5
pG 3 –	7
pG 4 -	9
pG 5 -	11

Group K

Tube Number	pH
pK1 – P7890 Poly-L-lysine (15-30 kDa)	3
pK 2 – 2.5 mg / mL	4
pK 3 – in H20	5
pK 4 -	7
pK 5 -	9

Appendix 4: MATLAB Code

Bloch Simulation Code:

```
%% RFdemo of 2 or 3 pool Bloch Simulation w/ Exchnage
% v.042511
% (c) Jared G. Cobb, 2011
% VUIIS, Vanderbilt University
% requires BlochSim_ODE.m, lsq_mono_fit.m


clear all, close all
clc

%relax terms
R1a = 1/3; %3 seconds [Hz]
R2a = 1/2;
R1b = 1; %~1 sec
R2b = 1/(33e-3); %~30 ms
R1m = 1/(10e-6); %10 us
R2m = 1/(10e-6);

%Note: frequency terms are all IN HZ!!!

f0 = 400e6; %Hz
B1 = 100; %Hz

w0 = 2*pi()*f0;
w1 = 2*pi()*B1;

ppm = 3.69;          %~3.5ppm for PLK amides

delw = w0*ppm/10^6; %freq offset [Hz] pool b from a, (wb - wa)
delOmega = 0;        %freq offset [Hz] pool m from b, (wm - wb)
delOmega = w0*delOmega/10^6;
wz = 0;              %rf offset [Hz] (w-w_avg)

%rates 'k or K'
kb = 1000; % proton exchange rate from pool b to a[Hz]
Km = 0; % cross-relax rate from pool b to m
Kb = 0; % cross-relax rate from pool b to a
Kpr_m = 0; % cross-relax rate from pool a to m

%Pool sizes

Pb = 0.01;
Pa = 1-Pb; %Pool size free water;
Pm = 1 - Pa - Pb; %Pool solid;


% START STUFF TO SEND TO FUNCTION

for i = 1:1
% SL pulse, start w/ M in transverse plane
X = 0;
Y = 0;
Z = 0;

% define intial magnetization vector M = [Mx;My;Mz]
```

```
% Along Y
Ma = [X;Pa;Z];
Mb = [X;Pb;Z];
Mm = [X;Pm;Z];
M0 = [Ma;Mb;Mm];

% (i = a,b,m);
Ma0 = [0;0;Pa];
Mb0 = [0;0;Pb];
Mm0 = [0;0;Pm];

Mpr = [Ma0*R1a;... %MPrime, equilibrium vector. Eq 29
    Mb0*R1b;...
    Mm0*R1m];

%Flux equalities
% Pa*ka = Pb*kb;
% Pa*Ka = Pb*Kb;
% Pm*Kpr_negm = Pa*Kpr_m;
% Pb*Km = Pm*K_negm;

ka = (Pb/Pa)*kb;
Ka = (Pb/Pa)*Kb;
Kpr_negm = (Pa/Pm)*Kpr_m;
K_negm = Pb*Km/Pm;

%Independent Variables
%kb, Kb, Km, Kpr_m
%wz, delw, delOmega, w1

%consolidate freq offset terms per p 503.
del_wm = wz - Pa*delw - (Pa + Pb)*delOmega;%E1 32
del_wb = wz - Pa*delw + Pm*delOmega;%Eq 31
del_wa = wz + (1 - Pa)*delw + Pm*delOmega;%Eq 30

%Hills way
c = [-(R2m + Kpr_negm + K_negm), del_wm, w1;... %Eq 28
    -del_wm, -(R2m + Kpr_negm + K_negm), 0;...
    -w1, 0, -(R1m + Kpr_negm + K_negm)];

b = [-(R2b + kb + Kb + Km), del_wb, w1;...%Eq 27
    -del_wb, -(R2b + kb + Kb + Km), 0;...
    -w1, 0, -(R1b + kb + Kb + Km)];

a = [-(R2a + ka + Ka + Kpr_m), del_wa, w1;...%Eq 26
    -del_wa, -(R2a + ka + Ka + Kpr_m), 0;...
    -w1, 0, -(R1a + ka + Ka + Kpr_m)];

nu = eye(3,3); % Identity Matrix

A = [a, nu*(kb + Kb), nu*Kpr_negm;...
    nu*(ka + Ka), b, nu*K_negm;...
    nu*Kpr_m, nu*Km, c];  % Eq 25
end

% END STUFF TO SEND TO FUNCTION

% START ODE PARMS

% set pulse duration [Tau] and phase angle [phi] of B1
Tau = 3; %[seconds]
pts = 1e3;
tx = linspace(0,Tau,pts); % pts sampling SL pulse

% Send to ode45
```

```
[t,M] = ode45(@BlochSim_ODE, tx, M0, [], A, Mpr);

% END ODE PARMS

% START PARSE AND PLOT SUB-COMPONENTS

% Parse M vector

Ma_v = M(:,1:3); %1 = X, 2 = Y, 3 = Z;
Mb_v = M(:,4:6);
Mm_v = M(:,7:9);

% Subdivide M species to plot:
Ma_x = M(:,1);
Ma_y = M(:,2);
Ma_z = M(:,3);

Mb_x = M(:,4);
Mb_y = M(:,5);
Mb_z = M(:,6);

Mb_t= abs(Mb_v(:,1)+1i*Mb_v(:,2));
Ma_t= abs(Ma_v(:,1)+1i*Ma_v(:,2));


% START FIT T1rho

sig_v = Ma_t;
echoes = t; %seconds
const = [sig_v(1) 0.9 0.1]; % initial guess of [M0 T1rho(sec) offset]

%lsqcurvefit

options = optimset('lsqcurvefit');
options =
optimset(options,'MaxIter',10000,'LevenbergMarquardt','on','TolFun',1e-
12,'TolX',1e-12);
lb = [0 0 0];
ub = [10e9 10e4 10e6];

[fit,resnorm, residual] = lsqcurvefit(@lsq_mono_fit, const, ...
    echoes,sig_v, lb,ub,options);

S0 = fit(1);
t1_rho = fit(2);
C = fit(3);
r1_rho = 1/fit(2); %in Hz
tshow = linspace(echoes(1),1.0*max(echoes),pts);
xshow = S0*exp(-tshow/t1_rho)+C;

disp(r1_rho);
close all;

% end lsqcurvefit


figure(3)
hold on
plot(echoes, sig_v,'b*','MarkerSize',2)
hold off
legend('fit','signal')
xlabel('time (s)','FontSize', 14)
ylabel('Magnetization (AU)','FontSize',14);
title('T1{\rho} Fit','FontSize',14);
```

```
%%
%incrememnt B1_v
close all;

lenc = 12;

B1_v = logspace(log10(150),log10(10000),lenc);  %Cobb

w1_v = 2*pi().*B1_v;  %Convert f to w;

%create new A mtx for parfor

B = zeros(9,9,lenc);
for i = 1:lenc
    B(:,:,i) = A;
    w1_i = w1_v(i);

    B(1,3,i) =  w1_i;
    B(3,1,i) = -w1_i;
    B(4,6,i) =  w1_i;
    B(6,4,i) = -w1_i;
    B(7,9,i) =  w1_i;
    B(9,7,i) = -w1_i;
end

% use parallel toolbox
% h = waitbar(0,'Hold your horses...');
matlabpool open;

parfor i = 1:lenc

    [t,M] = ode45(@BlochSim_ODE, tx, M0, [], B(:,:,i), Mpr);
    %pick out all of Y vector for pool A at ea. B1 into M_v
    M_v(:,i) = M(:,2); %Pool Ax = 1, Ay = 2, Az = 3;
    t_v(:,i) = t;
%     waitbar(i/lenc);
end


parfor i = 1:lenc;

    sig_v = M_v(:,i);
    echoes = t_v(:,1); %seconds

    const = [1 0.7 0.1]; % initial guess of [M0 T1rho(msec) C]
    [fit, resnorm, residual, exitflag, output, lambda, jacobian] = ...
        lsqcurvefit(@lsq_mono_fit, const, echoes,sig_v, lb,ub,options);
    beta = fit;
    alpha = 0.32;  %0.32 = 1 stdev, 0.05 = 2 stdev (95% conf int)
    ci = nlparci(beta,residual,'jacobian',jacobian,'alpha',alpha);

    ci_v(i,:) = ci(2,:);

    M0(i) = fit(1);
    t1rho(i) = fit(2);
    r1rho(i) = 1/fit(2); %in Hz
    C(i) = fit(3);

end

matlabpool close;

r1rho_std = 1./ci_v;  %conv to r1rho;
```

```
fpf = 1;
numSLA = length(B1_v);

X = B1_v(fpf:numSLA);
Y = r1rho(fpf:numSLA);
L = r1rho_std(fpf:numSLA,1);
U = r1rho_std(fpf:numSLA,2);
for i = 1:length(L);
    L_v(i) = Y(i)-L(i);
    U_v(i) = U(i)-Y(i);
end

close all;

figure(2),
errorbar(X,Y,L_v,U_v);
h = gca;
set(h,'XScale','log');
title('R_1_{\rho} vs SLA','FontSize', 14)
xlabel('SLA [Hz]','FontSize', 14)
ylabel('R_1_{\rho} [s^-^1]','FontSize', 14)

B1_v2 = round(B1_v);

disp(r1rho); %Hz


figure(3)
semilogx(B1_v2,r1rho,'b*');
set(gca,'FontSize',14);
title('R_1_{\rho} vs B_1','FontSize',18)
xlabel('B_1 [Hz]','FontSize',18)
ylabel('R_1_{\rho} [s^-^1]','FontSize',18)


Required Functions:
%%%%%%%%%%%%%%%%%%%%%%%%%%%%%%%%%%%%%%%%%%%%%%%%%%%%%%%%%%%%%%%%%%%

function dM = BlochSim_ODE(t, M, A, Mpr)
% Bloch Equations
% dM = A*M+Mpr
% t: time in seconds
% M: column vector (9 x 1)
% M0: M at thermal equilibrium to use for Mpr
% R_s = struct of relax rates (Hz)
% F_s = struct of frequency terms & offsets (Hz)
% K_s = struct of MT rates (Hz)
% P_s = struct of pool sizes
% Tau = time base (seconds)
% B1a = B1 amplidude (Hz)
% phi = B1 phase (deg)
%%%%%%%%%%%%%%%%%%%%%%%%%%%%%%%%%%%%%%%%%%%%%%%%%%%%%%%%%%%%%%%%%%%

dM = A * M + Mpr;  %Eq 24
return

%%%%%%%%%%%%%%%%%%%%%%%%%%%%%%%%%%%%%%%%%%%%%%%%%%%%%%%%%%%%%%%%%%%
function sig = lsq_mono_fit(x0, te);
% Calculate mono decay for a curve fitting using s(TE).
%USE
%x0 = [1 0.7 0.1]; % initial guess of [M0 T2 C]
% tshow=linspace(0,1.0*max(te),100);
t=te; %x=s'; %make sure t and x are columns
```

```
M0 = x0(1); T2 = x0(2); C = x0(3);
sig = M0*exp(-t/T2) + C; %evaluate your x
% er_norm=norm(xnew-x); % compute with data and compute error
end

%%%%%%%%%%%%%%%%%%%%%%%%%%%%%%%%%%%%%%%%%%%%%%%%%%%%%%%%%%%%%%%%%%%%%%%
```

Noise Generation

```
% ADD NOISE TO SIMULATED DATA
% v.042511
% (c) Jared Cobb, 2011
% Fit noisy data to Chopra eq
% VUIIS, Vanderbilt University
% requires: lsq_mono_fit.m, chopra_sig.m, chopra_fit.m


clear all, close all, clc;

%Initial exp data and plot
load('BSim_SLA_250_8000.mat'); %vect of SLAs
SLA = B1_v;

% Load M_v for SLAs above.

% load('M_v_250_8k_100kb_94T.mat');
% load('M_v_250_8k_500kb_94T.mat');
% load('M_v_250_8k_500kb_94Tb.mat');
% load('M_v_250_8k_1000kb_94T.mat');
 load('M_v_250_8k_2000kb_94T.mat');
% load('M_v_250_8k_5000kb_94Tb.mat');
% load('M_v_250_8k_7000kb_94T.mat');
% load('M_v_250_8k_10000kb_94T.mat');
% load('M_v_250_8k_10000kb_2T.mat');
% load('M_v_250_8k_20000kb_94T.mat');
% load('M_v_250_8k_50000kb_94T.mat');

% now have vector of signal decay at ea. SLA at 1kHz kb
[numEcho numSLA] = size(M_v);


% Select desired SNR

% nPer = 0.01; % SNR of 100
% nPer = 0.02; %SNR of 50
% nPer = 0.025; %SNR of 40
  nPer = 0.0333; % SNR of 30
% nPer = 0.05; % SNR of 20
% nPer = 0.10; % SNR of 10
% nPer = 0.2; % SNR of 5

rNum = 0 + nPer .* randn(numEcho,numSLA); %zero mean, nPer STD
M_v2 = M_v + rNum;  %Add gwn to M_v

% TEST adding random noise, specific mean and var

% 5x5 matrix of mean 0.6 and std = 0.1
% rNum = 0.6 + sqrt(0.1) * randn(5,5);

% Test adding random white noise
% t = 0:.1:10;
% x = sawtooth(t); % Create sawtooth signal.
```

```
% rNum = 1+ sqrt(0.05) * randn(1,length(t));
% y = rNum.*x;
% % y = awgn(x,10,'measured'); % Add white Gaussian noise.
% plot(t,x,t,y) % Plot both signals.
% legend('Original signal','Signal with AWGN');

% END TEST

% Fit for R1rho values.
h = waitbar(0,'Hold your horses...');


%Fit sim data w/ noise for T1rho values
for j = 1:numSLA;

    options = optimset('lsqcurvefit');
    options =
optimset(options,'MaxIter',10000,'LevenbergMarquardt','on','TolFun',1e-
15,'TolX',1e-12);
    lb = [0 0 0];
    ub = [10e9 10e4 10e6];
    const = [1 0.5 0.1]; % initial guess of [M0 T1rho(msec)]

    x = linspace(0,5,1000)'; %1000 pts. during 5 sec SL pulse
    y = M_v2(:,j);

    %fit
    [fit, resnorm, residual, exitflag, output, lambda, jacobian] = ...
        lsqcurvefit(@lsq_mono_fit, const, x,y, lb,ub,options);

    %generate ci
    beta = fit;
    alpha = 0.32;  %0.32 = 1 stdev, 0.05 = 2 stdev (95% conf int)
    ci = nlparci(beta,residual,'jacobian',jacobian,'alpha',alpha);

    ci_v(j,1) = ci(2,1);    % lower ci bound
    ci_v(j,2) = ci(2,2);    % upper ci

    M0(j) = fit(1);
    t1rho(j) = fit(2);
    r1rho(j) = 1/fit(2); %in Hz
    C(j) = fit(3);

    waitbar(j/numSLA);

end

close(h);

r1rho_std = 1./ci_v;  %conv CI to r1rho;

i = 1;  %select a series to plot

tshow = linspace(0,1.2*5,1000);
xshow = M0(i).*exp(-tshow/t1rho(i))+C(i);

% disp(r1_rho);

close all;

figure(1)
hold on
plot(tshow,xshow,'r','LineWidth',1)
plot(x, M_v2(:,i),'b*','LineWidth',1)
hold off
```

```
legend('fit','signal')
xlabel('time (s)','FontSize', 14)
ylabel('Magnetization (AU)','FontSize',14);
title('T1{\rho} Fit','FontSize',14);

fpf = 1;

X = SLA(1,fpf:numSLA);
Y = r1rho(1,fpf:numSLA);
L = r1rho_std(fpf:numSLA,1);
U = r1rho_std(fpf:numSLA,2);
for i = 1:length(L);
    L_v(i) = Y(i)-L(i);
    U_v(i) = U(i)-Y(i);
end

figure(2),
errorbar(X,Y,L_v,U_v,'Linewidth',1.5);
h = gca;
set(h,'XScale','log');
grid on
title('R1{\rho} vs SLA','FontSize', 14)
xlabel('SLA [Hz]','FontSize', 14)
ylabel('R1{\rho} [Hz]','FontSize', 14)

% END MONO FIT
```

Model Fitting

```
%Continued from noise sim above
%BEGIN Chopra Fit
%%
clc;
fpf = 1;

R1m = 1/(10e-3); %R1 of macro pool [Hz]
R2m = 1/(10e-3); %R2 of macro pool (ie 10 ms) [Hz]
f0 = 400e6; %Hz
w0 = 2*pi()*f0;
ppm = 2/10^6;             %2ppm
delf_m = f0*ppm; %Chemical Shift in [Hz].
delw_m = 2*pi()*delf_m;


% Define initial values for beta
rm = 500; %exchange rate [Hz]
R2 = r1rho(1); %R2 value in [Hz],
R1rhoinf = r1rho(end); %R1rho at infinite SLA in [Hz]

Delta = [R1m R2m delf_m]; %things we may need to transfer to fit func
beta0 = [R2 R1rhoinf rm]; %[R2 R1rhoinf rm];

%define lower and upper bounds for beta
lb = [ 0   0   100    ];
ub = [ 100 100 1e6 ];

%redefine vars for transfer to Chopra_fit func.

x = SLA(1:numSLA); %send in Hz
y = r1rho(1:numSLA);

flag = '';
```

```
% Fit to Chopra Model
[Chopcoeff,resnorm_b,residual,exitflag,output,lambda,jacobian,ci]= ...
     chopra_fit(x, y, beta0, lb, ub, flag, Delta) ;


Chopcoeff(3)
Chopcoeff(4) = ci(3,1);
Chopcoeff(5) = ci(3,2);


%Create new vector of fit parms for plotting
tshow = linspace(10,3*max(x),1000);
yfit = chopra_sig(Chopcoeff,tshow, Delta); % input = (beta, x, Delta)

X = SLA;
Y = r1rho;

L = r1rho_std(:,1);
U = r1rho_std(:,2);
for i = 1:length(L);
    L_v(i) = Y(i)-L(i);
    U_v(i) = U(i)-Y(i);
end

close all;

figure(3),
hold on
% plot(X,Y,'b*');
errorbar(X,Y,L_v,U_v,'b*');
plot(tshow,yfit,'r');
h = gca;
set(h,'XScale','log');
title('B_1 vs R_1_{\rho}','FontSize',18),
xlabel('B_1 [Hz]','FontSize',18),
ylabel('R_1_{\rho} [s^-^1]','FontSize',18);
%%%%%%%%%%%%%%%%%%%%%%%%%%%%%%%%%%%%%%%%%%%%%%%%%%%%%%%%%%%%%%%%%%%%%%%%
```

Required functions:
@chopra_fit.m

```
function [beta,resnorm,residual,exitflag,output,lambda,jacobian,ci] =
chopra_fit(x, y, beta0, lb, ub, flag, Delta)

options=optimset('lsqcurvefit') ;
options=optimset(options,'LevenbergMarquardt','on','Display','off',...
    'TolFun',1e-11,'TolX',1e-11,'MaxFunEvals',5e6*length(x),'MaxIter',2e6) ;

if strcmp(flag, 'linear')
    [beta,resnorm,residual,exitflag,output,lambda,jacobian] = ...
        lsqcurvefit(@chopra_sig_linear, beta0, x, y, lb, ub, options, Delta) ;
elseif strcmp(flag, 'reddy')
    [beta,resnorm,residual,exitflag,output,lambda,jacobian] = ...
        lsqcurvefit(@reddy_sig, beta0, x, y, lb, ub, options, Delta) ;
elseif strcmp(flag, 'sierra')
    [beta,resnorm,residual,exitflag,output,lambda,jacobian] = ...
        lsqcurvefit(@sierra_sig, beta0, x, y, lb, ub, options, Delta) ;
elseif strcmp(flag, 'pool')
    [beta,resnorm,residual,exitflag,output,lambda,jacobian] = ...
        lsqcurvefit(@chopra_poolsize, beta0, x, y, lb, ub, options, Delta) ;
elseif strcmp(flag, 'simple')
    [beta,resnorm,residual,exitflag,output,lambda,jacobian] = ...
        lsqcurvefit(@chopra_sig_simple, beta0, x, y, lb, ub, options, Delta) ;
elseif strcmp(flag, 'T1')
```

```
    [beta,resnorm,residual,exitflag,output,lambda,jacobian] = ...
        lsqcurvefit(@chopra_sig_T1, beta0, x, y, lb, ub, options, Delta) ;
elseif strcmp(flag, 'T1_simple')
    [beta,resnorm,residual,exitflag,output,lambda,jacobian] = ...
        lsqcurvefit(@chopra_sig_simple_T1, beta0, x, y, lb, ub, options, Delta)
;
elseif strcmp(flag, 'double')
    [beta,resnorm,residual,exitflag,output,lambda,jacobian] = ...
        lsqcurvefit(@chopra_double, beta0, x, y, lb, ub, options, Delta) ;
else
    [beta,resnorm,residual,exitflag,output,lambda,jacobian] = ...
        lsqcurvefit(@chopra_sig, beta0, x, y, lb, ub, options, Delta) ;
end
alpha = 0.32;  %0.32 = 1 stdev, 0.05 = 2 stdev (95% conf int)
ci = nlparci(beta,residual,'jacobian',jacobian,'alpha',alpha);

%%%%%%%%%%%%%%%%%%%%%%%%%%%%%%%%%%%%
function sig  = chopra_sig( beta0, x, Delta)
%Chopra Signal eq

% R1rho = (R2 + (R1rhoinf*w1^2)/Srho^2)/(1+ w1^2/Srho^2);

% beta = initial conditions
% beta = [R2 R1rhoinf rm]; %[Hz Hz Hz];
% Delta = constants
% Delta = [R1m R2m delf_m]; % [Hz Hz Hz];

w1          = 2*pi*x; %vector of SLA's in [Hz]

R1m         = Delta(1);
R2m         = Delta(2);
delw_m      = 2*pi*Delta(3);

R2          = beta0(1);
R1rhoinf    = beta0(2);
rm          = beta0(3);

A = (R1m + rm)/(R2m + rm); %First part of Srho
B = ((R2m + rm)^2 + delw_m^2); %Second part of Srho
Srho2 = A*B;

%Signal Equation
sig = (R2+(R1rhoinf.*w1.^2)./Srho2)./(1+ w1.^2./Srho2); %Chopra signal eq


end
```

Spectroscopic Dispersion Analysis

```
% Varian Dispersion Meas Spectro
% Cobb, JG. VUIIS, Vanderbilt
% v.4/13/11
% Requires Mono_fit, lsq_mono_fit;


%Part 1, load Varian Spectro Data

clear;clc;close all;


path = '/GORE_DATA/PLK_New/t1rho_PLK_t4n';

[re im]=load_fid(path);
```

```
data=complex(re,im);
re_FT = abs(fftshift(fft(re(:,1))));
im_FT = abs(fftshift(fft(im(:,1))));
fs = linspace(-1024,1024,2048)';


slt=queryPP(path,'tl');
tp=queryPP(path,'tpwr4');
p180=queryPP(path,'tpwr5');
comment = queryPP(path,'comment');
t180 = queryPP(path,'tinv');

fd = zeros(size(data));
tdata=zeros(length(tp),length(slt));
for ii=1:length(slt)*length(tp)
    fd(:,ii)=fftshift(fft(data(:,ii)));
%     tdata(ii)=trapz(abs(fd(:,ii)));
%     fd(:,ii) = fftshift(fft(data(:,ii)));
    tdata(ii) = max(abs(fd(:,ii)));
end

parms.slt = slt;
parms.tp = tp;
parms.t180 = t180;  % 80 us or so
parms.p180 = p180;  % 45 dB or so
parms.comment = comment;
% calc SLA in Hz

dB_off = -1.*(p180-tp);
dB_off = (dB_off./20) + log10(0.5/t180);
parms.sla = round(10.^dB_off);

% END PART 1

% part 2, fit stuff

[numSLA numSLT] = size(tdata);

SLT = parms.slt;
SLA = parms.sla;

ii = 1; %pick series to plot (1 = 0 Hz, 10 = 10 kHz);
X = SLT';
Y = tdata(ii,:);

% test fit one data series

options = optimset('fminsearch');
options = optimset(options,'MaxFunEvals',5e4,'MaxIter',10000,'TolFun',1e-
15,'TolX',1e-12);


const = [tdata(1,1) 0.07 0]; % initial guess of [M0 T1rho(msec)]

fit = fminsearch(@Mono_fit,const, [],X,Y);

tshow = linspace(0.001,2*max(SLT),1000);
yfit = lsq_mono_fit(fit,tshow);
disp(fit(2)) %decay time in sec


figure(3),
hold on
plot(X,Y,'b*');
plot(tshow,yfit,'r');
```

```
h = gca;
set(h,'FontSize',14);
xlabel('time [sec]','FontSize',20),
ylabel('signal [au]','FontSize',20);

%% Fit all data


%fit for T1rho vals

fp = 1; %first time point to fit
lp = length(SLT); %last time pt to fit
fpf = 1; %first SLA to plot
lpf = numSLA; %last SLA to plot

xx = zeros(1,numSLT);
yy = zeros(numSLA,numSLT);
xx = SLT';
yy = tdata;

options = optimset('fminsearch');
options = optimset(options,'MaxFunEvals',1e5,'MaxIter',1e5,'TolFun',1e-
15,'TolX',1e-12);


% START FMINSEARCH
for i = 1:numSLA
    const = [yy(1,1) 0.7 0]; % initial guess of [M0 T1rho(msec)]
    fit = fminsearch('Mono_fit', const, [],xx(fp:lp),yy(i,fp:lp));
    M0(i) = fit(1);
    t1rho(i) = fit(2);
    r1rho(i) = 1/fit(2);
end
% END FMINSEARCH

X = SLA(fpf:numSLA);
Y = r1rho(fpf:numSLA);

figure(4),
hold on
plot(X,Y,'b*');
h = gca;
set(h,'XScale','log');
set(h,'FontSize',14);
set(h,'YLim',[0 3]);
title('R_1_{\rho} vs B_1','FontSize',20),
xlabel('B_1 [Hz]','FontSize',20),
ylabel('R_1_{\rho} [s^-^1]','FontSize',20);
```

Imaging Dispersion Analysis

```
% Varian Dispersion Meas from ROI
% Cobb, JG. VUIIS, Vanderbilt, v.4/13/11
% Requires @Mono_fit.m
% Requires @lsq_mono_fit.m

%Part 1, save Varian data to .mat file
```

```
clear;clc;close all;

% Path to data
path='/Users/cobbjg/Documents/MATLAB/GORE_DATA/PLK/t1rho_fse_kl_11a'; % 3
tubes, more SLAs


numIM   = queryPP_IMG(path,'acqcycles');
tp      = queryPP_IMG(path,'tpwrSL');
tl      = queryPP_IMG(path,'tl');
p180    = 54;
comment = queryPP_IMG(path,'comment');
t180 = 7.2e-5;

parms.slt = tl;
parms.tp = tp;
parms.t180 = t180;  % 80 us or so
parms.p180 = p180;  % 62 dB or so
parms.comment = comment;
% calc SLA in Hz

dB_off = -1.*(p180-tp);
dB_off = (dB_off./20) + log10(0.5/t180);
parms.sla = round(10.^dB_off);

for ii = 1:numIM
    IM(:,:,ii) = load_fdf_image(path,ii);
end


% Prepare data for Fitting

close all;
% pick ROI

figure(1), imagesc(IM(:,:,1));
ROI = roipoly;

max1 = max(max(max(IM)));
IM2 = IM./max1;

for ii = 1:numIM
    mask_stack(:,:,ii) = ROI .* IM(:,:,ii);

end

signal_v = zeros(1,numIM);
std_v = zeros(1,numIM);
for i = 1:numIM
    a = mask_stack(:,:,i);
    signal_v(i) = mean(a(a > 0));
    std_v(i) = std(a(a > 0));
end


numSLT = length(parms.slt);
numSLA = length(parms.sla);
SLT = parms.slt;
SLA = parms.sla;
sig = reshape(signal_v,numSLA,numSLT);


tdata  = sig;
ii = 1; %pick series to plot (1 = 0 Hz, 10 = 20 kHz);
```

```
% test fit one data series

% START FMINSEARCH

options = optimset('fminsearch');
options = optimset(options,'MaxFunEvals',5e4,'MaxIter',10000,'TolFun',1e-
15,'TolX',1e-12);


const = [tdata(1,1) 0.07 0]; % initial guess of [M0 T1rho(msec)]


for ii = 1:numSLA;

    X = SLT';
    Y = tdata(ii,:);

    fit = fminsearch(@Mono_fit,const, [],X,Y);

    M0(ii) = fit(1);
    t1rho(ii) = fit(2);
    r1rho(ii) = 1/fit(2); %in Hz
    C(ii) = fit(3);
    tshow(ii,:) = linspace(0.001,1.5*max(SLT),1000);
    yfit(ii,:) = lsq_mono_fit(fit',tshow(ii,:)');

end

% END FMINSEARCH

% CALC POWER from dB and t180

pwr = numSLA; %numSLA for max
y = tdata(1,:); %low power series typically 1 = 150 Hz
yy = tdata(pwr,:); %high power, max = 10kHz

diff = yfit(pwr,:)-yfit(1,:);
max_diff = max(diff);
x_diff = find(diff == max_diff);

% END POWER CALC

% PLOT LOW AND HIGH POWER PLOTS

figure(2),
hold on
plot(X,y,'b*');  % low power
plot(X,yy,'k*');    % high power
plot(tshow,yfit(1,:),'r');
plot(tshow,yfit(pwr,:),'g');
plot(tshow,diff,'b');
plot(tshow(x_diff),max_diff,'r*','MarkerSize',15);
h = gca;
legend('low power','high power', 'LP fit','HP Fit','Difference','Max Contrast
Pt.');
title('signal vs time','FontSize',20),
xlabel('time [sec]','FontSize',20),
ylabel('signal [au]','FontSize',20);
XLim([0 1.5]);


% PLOT DISPERSION CURVES

figure(3)
```

```
plot(SLA,r1rho,'b*')
h = gca;
set(h,'XScale','log');
set(h,'FontSize',14);
title('R_1_{\rho} vs B_1','FontSize',20),
xlabel('B_1 [Hz]','FontSize',20),
ylabel('R_1_{\rho} [s^-^1]','FontSize',20);
% YLim([0 20])
```

Philips T1ρ Mapping

```
% T1rho-FSE Fit v.2.x  ca. 12/9/10
%
% Functions: calculates map and ROI from Philips .PAR/.REC
% Requires: T2fit.m, 3-parm monoexp decay function
%
% Jared Cobb, VUIIS

clear all; close all; clc;


dir = '/Users/cobbjg/Documents/MATLAB/GORE_DATA/Manus/';


pref = 'Welch_2519_WIP_T1rho_TSE_';
mid = 'ms_CLEAR_';
suf = '_1.PAR';
start = 3;
stop = 4;

inc = start:stop; %scans to include
n = stop-start+1; %number of SLTs. 60,40,20

SLT = [60 40]; %be sure order is correct

sl = 5; %Slice num to use

%concat strings to get full paths
for i = 1:n;
    a = num2str(inc(i));
    b = num2str(SLT(i));
    c{i} = strcat(dir,pref,b,mid,a,suf);
end

for i = 1:n
    IM = vuOpenImage(c{i});
    stack(:,:,i) = IM.Data(:,:,5); %central slice from 3D method for Exp3 ONLY
end


%%
close all; clc;

% slice is chosen above for simplicity
[nRows nCols numEcho] = size(stack);


%create threshold mask
firstImage_m = squeeze(stack(:,:,numEcho));
maxValue = max(firstImage_m(:));
mask_m = (firstImage_m > 0.05 * maxValue ); % 5% mask
```

```
figure(1), imagesc(mask_m), colormap(gray);  %display mask

% COBBJG : START Single Parm MonoExponential Fit MAP
warning off all
%Initial Conditions & Settings


t2_m = zeros(nRows, nCols);
s0_m = zeros(nRows, nCols);
R_m = zeros(nRows,nCols);
t2lim = 150;  %upper limit based on type o scan / tissue
echoes = SLT';



for row = 1:nRows
    for col = 1:nCols
        if (mask_m(row,col) == 1)
            signal_v = squeeze(stack(row, col, :));
            coeff_v = polyfit(echoes, log(signal_v), 1);
            slope = coeff_v(1);
            logS0 = coeff_v(2); % Intercept.
            fit = polyval(coeff_v, echoes);
            R_squared = corrcoef(signal_v, fit);
            t2 = -1 / slope;
            % Force a lower limit on the slope:
            if (t2 > t2lim)
                t2 = t2lim;
            end
            if (t2 < 0)
                t2 = 0;
            end
            %end slope limit
            t2_m(row,col) = t2;
            s0_m(row,col) = exp(logS0);
            R_m(row,col) = R_squared(2);
        end
    end
end
warning on all

%Test view map
figure(2),
imagesc(t2_m(:,:)),
colorbar,
colormap(jet);
h = gca;
set(h,'FontSize',16);
xlabel('pix');
ylabel('pix');
title('Mid-Brain T_1_{\rho} map [ms]','FontSize',18)


%% select ROI

clc;close all;

figure(3), imagesc(stack(:,:,1));
title('Magnitude IM: Create ROI for signal vector','FontSize',16);
mask = roipoly;
for i = 1:n;
    mask_stack(:,:,i) = mask .* stack(:,:,i);
end

figure(4), imagesc(mask_stack(:,:,1));
```

```
title('Signal Mask','FontSize',16);

signal_v = zeros(1,n);
std_v = zeros(1,n);
for i = 1:n
    a = mask_stack(:,:,i);
    signal_v(i) = mean(a(a > 0));
    std_v(i) = std(a(a > 0));
end

figure(5)
hold on
plot(SLT,signal_v,'r');
h = gca;
set(h,'FontSize',16);
title('Signal Plot: Sig vs. SLT','FontSize',16)
xlabel('SLT [ms]','FontSize',16)
ylabel('Signal [AU]','FontSize',16)
hold off


%Fminsearch curve fit for T1rho
close all
y = signal_v;
x = SLT;
%initial guesses of MO and T1rho
M0 = y(1);
T1rho = 100;
constants = [M0 T1rho]; % initial guess of [M0 T1 (sec)]
%Fit to 3 parm mono-exp decay @T2fit
fit = fminsearch('T2fit', constants, [],x,y);
M0 = fit(1);
T1rho = fit(2);  %ms
R1rho = 1000/T1rho; %gives R1 in Hz
yfit = M0*exp(-x./T1rho);

figure(6),
hold on
plot(SLT,y,'b*','MarkerSize',20,'LineWidth',2)
plot(SLT,yfit,'r','LineWidth',2)
title('Sig vs. fit','FontSize',16)
xlabel('SLT [ms]','FontSize',16)
ylabel('Signal [AU]','FontSize',16)
h = gca;
set(h,'FontSize',16);
xlim([0 2*max(SLT)]);
hold off

disp(T1rho); %ms
disp(R1rho); %hz
```

Gochberg Subtraction Method

```
% Varian Dispersion Meas w/ Gochberg Image Ratio
%
% (c) Jared Cobb
% v.042511
% requires: @lsq_mono_fit.m
```

```
% VUIIS, Vanderbilt University

%Part 1, save Varian data to .mat file


clear;clc;close all;

% IO BSA
%
path='/Users/cobbjg/Documents/MATLAB/GORE_DATA/Iopamidol/IO_BSA/t1rho_fse_BSA_I
O_Disp2';

numIM   = queryPP_IMG(path,'acqcycles');
tp      = queryPP_IMG(path,'tpwrSL');
tl      = queryPP_IMG(path,'tl');
p180    = 54;
comment = queryPP_IMG(path,'comment');
t180 = 7.2e-5;

parms.slt = tl;
parms.tp = tp;
parms.t180 = t180;  % 80 us or so
parms.p180 = p180;  % 62 dB or so
parms.comment = comment;
% calc SLA in Hz

dB_off = -1.*(p180-tp);
dB_off = (dB_off./20) + log10(0.5/t180);
parms.sla = round(10.^dB_off);

for ii = 1:numIM
    IM(:,:,ii) = load_fdf_image(path,ii);
end
%% part 2, fit stuff

% All this first section does is pick out ROI for two vectors
% to illustrate contrast.
close all;

figure(1), imagesc(IM(:,:,1));
ROI = roipoly;

max1 = max(max(max(IM)));
IM2 = IM./max1;

for ii = 1:numIM
    mask_stack(:,:,ii) = ROI .* IM(:,:,ii);

end

signal_v = zeros(1,numIM);
std_v = zeros(1,numIM);
for i = 1:numIM
    a = mask_stack(:,:,i);
    signal_v(i) = mean(a(a > 0));
    std_v(i) = std(a(a > 0));
end


numSLT = length(parms.slt);
numSLA = length(parms.sla);
SLT = parms.slt;
SLA = parms.sla;
sig = reshape(signal_v,numSLA,numSLT);
```

```
tdata  = sig;
ii = 1; %pick series to plot (1 = 0 Hz, 10 = 20 kHz);


% test fit one data series

options = optimset('lsqcurvefit');
options = optimset(options,'MaxIter',1e5,'LevenbergMarquardt','on','TolFun',1e-
15,'TolX',1e-12);
lb = [0    0    0];
ub = [10e9 10e4 10e6];


beta0 = [tdata(1,1) 0.5 tdata(1,end)]; % initial guess of [M0 T1rho(sec) C]
for ii = 1:numSLA;
    X = SLT';
    Y = tdata(ii,:);

    [fit, resnorm_a, residual, exitflag, output, lambda, jacobian] = ...
        lsqcurvefit(@lsq_mono_fit, beta0, X, Y, lb,ub,options);

    beta = fit;
    alpha = 0.32;  %0.32 = 1 stdev, 0.05 = 2 stdev (95% conf int)
    ci = nlparci(beta,residual,'jacobian',jacobian,'alpha',alpha);

    ci_v(ii,:) = ci(2,:);

    M0(ii) = fit(1);
    t1rho(ii) = fit(2);
    r1rho(ii) = 1/fit(2); %in Hz
    C(ii) = fit(3);



    tshow = linspace(0.001,2*max(SLT),1000);
    yfit(ii,:) = lsq_mono_fit(fit,tshow);
end
%conv to r1rho for s values;
r1rho_std = 1./ci_v;

fpf = 1;

%generate confidence intervals for figure
XX = zeros(1,fpf:numSLA);
YY = zeros(1,fpf:numSLA);
L = zeros(1,fpf:numSLA);
U = zeros(1,fpf:numSLA);
L_v = zeros(1,fpf:numSLA);
U_v = zeros(1,fpf:numSLA);


XX = SLA(fpf:numSLA);
YY = r1rho(fpf:numSLA);
L = r1rho_std(fpf:numSLA,1);
U = r1rho_std(fpf:numSLA,2);
for i = 1:length(L);
    L_v(i) = YY(i)-L(i);
    U_v(i) = U(i)-YY(i);
end
% END LSQ CURVE FIT

% CALC POWER from dB

pwr = 10; %10 = 2700 Hz for IO + BSA;
```

```
y = tdata(1,:); %low power series typically 1 = 150 Hz
yy = tdata(pwr,:); %exch power, max = 10kHz
yyy = tdata(numSLA,:);%max power


diff = yfit(pwr,:)-yfit(1,:);
max_diff = max(diff);
x_diff = find(diff == max_diff);

% END POWER CALC

figure(2),
hold on
plot(X,y,'b*');  % low power
plot(X,yy,'ko');    % exch power
plot(X,yyy,'rd');    % max power
plot(tshow,yfit(1,:),'r');
plot(tshow,yfit(pwr,:),'g');
plot(tshow,diff,'b');
plot(tshow(x_diff),max_diff,'r*','MarkerSize',15);
h = gca;
legend('low power','high power', 'LP fit','HP Fit','difference');
% title('Time Point of Maximum Contrast','FontSize',20),
xlabel('time [sec]','FontSize',20),
ylabel('signal [au]','FontSize',20);
xlim([0 1.0]);

figure(3)
% plot(SLA,r1rho,'b*')
errorbar(XX,YY,L_v,U_v,'b*');
h = gca;
set(h,'XScale','log');
set(h,'FontSize',14);
title('B_1 vs R_1_{\rho}','FontSize',20),
xlabel('B_1 [Hz]','FontSize',20),
ylabel('R_1_{\rho} [Hz]','FontSize',20);
% YLim([0 20])


%%
close all; clc;

% Create Difference Image

[nRows nCols aa] = size(IM);


IM3 = reshape(IM,[nRows nCols numSLA numSLT]);
%IM3 = [nRows nCols numSLA numSLT];


% SET UP SUBTR VARIABLES
low = 2; %SLA Low, i.e. first point fit
high = numSLA; %SLA High


% max contrast from IO:
kex = 7;  %10 = 2700 Hz, IO+BSA, %13 for BSA, 7 for IO alone.
time1 = 6; %time point

maxValue = max(max(IM3(:,:,high,1)));
mask_m = (IM3 > 0.05 .* maxValue ); % 1% mask
IM3 = (mask_m .* IM3)./maxValue;

%subtracted image
```

```
IM_1 = IM3(:,:,kex,time1); % IM at exch SLA

IM_2 = IM3(:,:,low,time1); %IM at low SLA

IM_3 = IM3(:,:,numSLA,time1); % IM at high SLA

subIM = imsubtract(IM_1,IM_2); %IM(ex) - IM(low)
subIM2 = imsubtract(IM_3,IM_1); %IM(high) - IM(ex)
subIM3 = immultiply(subIM,subIM2); %diff * diff
subIM4 = imsubtract(IM_3,IM_2); % high - low
subIM4 = immultiply(subIM4,subIM4);

% Gochberg method

% 4 is normalization factor
filt_im = 4*imdivide(subIM3,subIM4);


% figure, imagesc(subIM3);colorbar;

% cancel < 0 values
for ii = 1:nRows
    for jj = 1:nCols
        if filt_im(ii,jj) <= 0
            filt_im(ii,jj) = 0;
        end
    end
end
% IM is flipped top to bottom!
filt_im = flipud(filt_im);

figure(6)
hold on

imagesc(filt_im);
title('Exchange-Rate Based Image','FontSize',14);
colormap(hot);
h = gca;
set(h,'Visible','off');
colorbar
hold off

io = filt_im;
```